THE ROLE OF DISLOCATION CHANNELING IN IASCC INITIATION OF NEUTRON IRRADIATED AUSTENITIC STAINLESS STEEL

by

Kale Jennings Stephenson

A dissertation submitted in partial fulfillment
of the requirements for the degree of
Doctor of Philosophy
(Materials Science and Engineering)
in The University of Michigan
2016

Doctoral Committee:

Professor Gary S. Was, Chair
Adjunct Associate Professor Jeremy T. Busby
Associate Professor Samantha H. Daly
Professor J. Wayne Jones

To Sarah

ACKNOWLEDGEMENTS

My advisor, Dr. Gary Was, deserves great thanks for the countless hours of guidance, the support, and the means to be able to complete this work. The experience I've gained as a member of his research group has benefitted me immensely. I would also like to thank the members of my dissertation committee, Dr. Jeremy Busby, Dr. Samantha Daly, and Dr. Wayne Jones for their assistance and insight.

Many thanks are due to my colleagues in the Was research group for their encouragement, assistance, and valuable discussion. The friendship and help offered by my fellow group members: Elaine West, Anne Campbell, Cheng Xu, Mike McMurtrey, Tyler Moss, Justin Hesterberg, Wenjun Kuang, Shyam Dwaraknath, Stephen Raiman, Elizabeth Getto, Anthony Monterrosa, Drew Johnson and Clyde "Josh" Beers, was paramount to my progress and experience. Thanks also to Sean Gray, for the assistance and the experience I gained through his instruction. And especially, thanks to Alex Flick for the countless favors and hours of assistance in the Irradiated Materials Testing Laboratory.

Credit is due to the professionals at the Oak Ridge National Laboratory for their assistance and guidance with the project. Dr. Jeremy Busby and Dr. Maxim Gussev have been excellent mentors, providing both leadership and meaningful discussion. Thanks also to the LAMDA laboratory staff (Alta Marie Williams, Janie Myers, Patricia Tedder, and Kennith Curtis) for the assistance with sample handling, preparation, and shipment.

Many other colleagues at the University of Michigan are also deserving of thanks. Dr. Jwo Pan provided valuable assistance and discussion related to mechanical behaviors. Members of the Radiation Safety Services division of the Occupational Safety and Environmental Health department including Shannon Weger, Rob Blackburn, Phil Simpson, Phil Keavey, and Dr. Joe Miklos provided much assistance. Staff in the Lurie Nanofabrication Facility (Pilar Herrera-Fierro and Sandrine Martin) gave assistance with surface characterization. Staff at the Center for Statistical Consultation and Research, especially Corey Powell, supplied knowledge regarding statistical issues encountered in this work.

Finally, none of this would have been possible without the patience and support of my girlfriend, Sarah Dolan, my family (Bryce, Nancy, and Breya Stephenson) and the Dolan family (Patrick, Cindy, Jennifer, and Alexis Poitrasson-Rivière). Their constant emotional support and encouragement through this process was a constant that kept me going through the difficult times.

Support for this project was provided by funding from the Electric Power Research Institute (contract number 10003872) and the United States Department of Energy Light Water Reactor Sustainability Program (contract number 4000136608).

TABLE OF CONTENTS

LIST OF TABLES

LIST OF FIGURES

LIST OF APPENDICES

ABSTRACT

THE ROLE OF DISLOCATION CHANNELING IN IASCC INITIATION OF NEUTRON IRRADIATED AUSTENITIC STAINLESS STEEL

by

Kale Jennings Stephenson

Chair: Gary S. Was

The objective of this study was to understand the role of dislocation channeling in the initiation of irradiation-assisted stress corrosion cracking (IASCC) of neutron irradiated austenitic stainless steel. Constant extension rate tensile (CERT) experiments in a simulated normal water chemistry (NWC) environment (288°C, 2 ppm dissolved oxygen, 0.2 μS/cm) compared cracking behavior amongst a set of stainless steels after irradiation in the BOR-60 fast reactor at 320 °C. Based on the results, several alloys with a range in IASCC susceptibility were selected for study, including a commercial purity 304L stainless steel irradiated to 5.5, 10.2, and 47.5 dpa and two high purity stainless steels, Fe-18Cr-12Ni and Fe-18Cr-25Ni, irradiated to ~10 dpa. CERT test results determined that irradiation hardening correlated strongly with increased IASCC, and the average height of steps formed by dislocation channels intersecting the sample surface was larger on conditions with high IASCC susceptibility.

To isolate key factors affecting IASCC initiation, a miniature four-point bend test was developed and performed in NWC conditions on samples created from irradiated tensile bars used in the CERT tests. Four-point bend tests were performed in small stress or strain increments to

characterize the development of dislocation channeling and observe intergranular cracks with limited propagation. For the same alloys, the four-point bend test produced the same relative IASCC susceptibility as CERT experiments, and observations determined several key controlling factors of IASCC initiation.

IASCC initiation was induced by the dissolution of MnS inclusions in high temperature water, which forms sulfate ions (SO_4^{2-}) and Mn_2O_3. At all locations where IG cracking occurred, an oxide cap had formed, occluding the inclusion site and creating a local environment with a high potential for crack initiation. Local stress concentration at this site due to a favorably oriented grain boundary, the dissolved inclusion, and an intersecting discontinuous dislocation channel caused intergranular crack initiation. The stress necessary to initiate IASCC decreased with irradiation dose, and as dislocation channeling preceded crack initiation, it is likely that dislocation channeling controlled crack initiation. The HP Fe-18Cr-12Ni alloy was less susceptible to IASCC than the CP 304L alloy due to a lack of MnS inclusions, but stress concentration at locations where dislocation channels intersected grain boundaries still was sufficient to initiate cracking. Alternatively, the high Ni alloy was not susceptible to IASCC initiation because it also did not contain MnS inclusions, but it had much higher propensity to transmit dislocation channels across grain boundaries, relieving stress accumulation at locations where dislocation channels and grain boundaries intersect.

CHAPTER 1 - INTRODUCTION

Nuclear energy is a major contributor to the United States and world energy supply, accounting for 19.5% (797 billion kWh in 2014) of U.S. domestic electricity production [1]. Despite the density of energy production, safety, and carbon-free emissions of light water reactors (LWRs), very few new reactors have been constructed in recent years and the number operating in the U.S. has been diminishing since the 1990s [1]. Many existing LWRs in the U.S. are aging, and reactor lifetime extensions would allow the continued generation of abundant, cheap, and clean electricity.

A major concern when extending the lifetime of existing LWRs is irradiation-assisted stress corrosion cracking (IASCC); a degradation phenomenon which has been observed in a variety of reactor designs, materials, components, and operating water chemistries as shown in Table 1.1 [2]. The probability of IASCC increases as LWRs operate for longer time periods, and could eventually cause safety concerns or lead to diminishing returns on the additional energy produced due to the high cost of reactor shutdowns and maintenance. Therefore, understanding the mechanisms causing IASCC and establishing mitigation strategies are of high priority.

Similar to stress corrosion cracking (SCC), IASCC has three primary requirements: a corrosive environment, a susceptible material, and an applied stress. Inside a LWR core, however, the radiation field increases both material susceptibility (due to radiation-induced defect formation) and the corrosive nature of the environment (due to radiolysis). IASCC nucleates on the water-

side of components, following the path along the grain boundaries in an intergranular (IG) cracking mode [3].

Austenitic stainless steels are used as structural components in operating LWR cores, causing them to receive high levels of radiation exposure during their lifetime, thus increasing their susceptibility to intergranular stress corrosion cracking (IGSCC). Irradiation causes stainless steels to form dislocation loops, precipitates, and voids, while also causing radiation-induced segregation (RIS) of solute elements at grain boundaries; which evolve as a function of irradiation dose, as shown in Figure 1.1 [4]. These micro-scale changes are believed responsible for the enhancement of susceptibility to IGSCC, but isolating the cracking mechanism is difficult due to their simultaneous evolution.

Irradiation causes a transition in the deformation mode from homogeneous to highly localized slip, confined to narrow slip bands called dislocation channels. Once dislocation movement (i.e., slip) occurs, irradiation-induced defects are annihilated in the slip pathway, creating a 'cleared channel' for subsequent dislocation movement. Cracks have been observed to preferentially initiate where dislocation channels intersect grain boundaries [5–8], and recently, a study by Jiao and Was [9] showed that the average height of steps on the surface of proton irradiated SS (created by dislocation channels) had a stronger correlation with IASCC susceptibility than a wide range of other variables. Closer examination revealed that grain boundaries unable to transmit dislocation channels into adjacent grains accumulate local stress and are more susceptible to SCC [10,11].

This study aims to be the first to quantify dislocation channeling in neutron irradiated stainless steels and determine its effect on IASCC initiation. Measurements of dislocation channeling in

neutron irradiated stainless steels are limited [12], and most cracking analyses are made only after complete failure using traditional SCC experiments such as constant extension rate tensile (CERT) (also called the slow strain rate tensile (SSRT)) tests or constant load tests [13–18]. The brittle nature of neutron irradiated SS typically causes the initial IG crack to propagate to failure, and consequentially, the only metrics to describe SCC susceptibility are %IG, total elongation, reduction in area and fracture stress. Therefore, a novel four-point bend experiment was developed to provide more information on the IASCC initiation process [19]. The bend test creates a stress gradient through the sample thickness such that cracks grow into a progressively decreasing tensile stress, slowing crack propagation and preserving the sample beyond formation of the first crack. Furthermore, the four-point bend test creates an area at the surface of nearly constant tensile stress and strain, enhancing the possibility of observing multiple crack initiation sites on a single sample. Combined with periodic unloading and inspection, loading conditions (stress, strain) and surface conditions (oxidation, dislocation channeling) were monitored up to and after IASCC initiation. These novel observations of IASCC initiation sites created by the four-point bend test have created a much clearer view of factors affecting IASCC initiation in the analyzed materials and a wealth of new understanding.

This study utilizes several stainless steel alloys created during the CIR (Cooperative IASCC Research) I and II programs and irradiated in the BOR-60 liquid sodium fast reactor to doses ranging from 4.4 to 47.5 dpa [20–27]. To assess susceptibility to IASCC initiation, constant extension rate tensile (CERT) tests were performed in simulated LWR environments. The results determined which variables affected IASCC initiation, including (in order of decreasing priority) irradiation hardening, alloy purity, grain boundary composition, cold work, and test environment

[28]. These determinations helped to determine the focus of this study and the selection of alloys to include.

Chapter 2 presents background information including an overview of irradiation effects, deformation in stainless steel, and IASCC along with the current objective and experimental approach. Chapter 3 elaborates on experimental techniques and analytical methods employed to achieve the objective. Chapter 4 describes experimental results obtained, and Chapter 5 provides interpretation of the results and correlations. The conclusions of this study are summarized in Chapter 6.

Table 1.1. IASCC occurrences from LWR service experience. From [2].

Component	*Material*	*Reactor type*	*Possible sources of stress*
Fuel cladding	304SS	BWR	Fuel swelling
Fuel cladding	304SS	PWR	Fuel swelling
Fuel cladding[a]	20% Cr–25% Ni–Nb	AGR	Fuel swelling
Fuel cladding ferrules	20% Cr–25% Ni–Nb	SGHWR	Fabrication
Neutron source holders	304SS	BWR	Welding and Be swelling
Instrument dry tubes	304SS	BWR	Fabrication
Control rod absorber tubes	304/304L/316L SS	BWR	B4C swelling
Fuel bundle cap screws	304SS	BWR	Fabrication
Control rod follower rivets	304SS	BWR	Fabrication
Control blade handle	304SS	BWR	Low stress
Control blade sheath	304SS	BWR	Low stress
Control blades	304SS	PWR	Low stress
Plate type control blade	304SS	BWR	Low stress
Various bolts[b]	A-286	PWR and BWR	Service
Steam separator dryer bolts[b]	A-286	BWR	Service
Shroud head bolts[b]	600	BWR	Service
Various bolts	X-750	BWR and PWR	Service
Guide tube support pins	X-750	PWR	Service
Jet pump beams	X-750	BWR	Service
Various springs	X-750	BWR and PWR	Service
Various springs	718	PWR	Service
Baffle former bolts	316SS cold work	PWR	Torque, differential swelling
Core shroud	304/316/347/L SS	BWR	Weld residual stress
Top guide	304SS	BWR	Low stress (bending)

[a]Cracking in AGR fuel occurred during storage in spent fuel pond.

[b]Cracking of core internal occurs away from high neutron and gamma fluxes.

AGR, Advanced gas-cooled reactor

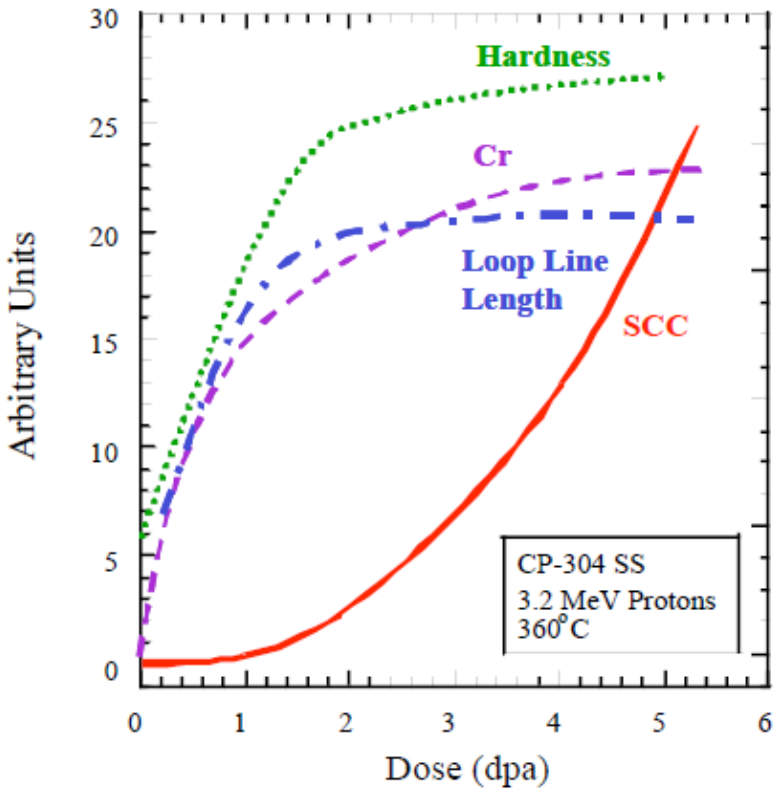

Figure 1.1. Irradiation-induced material changes and susceptibility to IGSCC as a function of increasing dose. From [4].

CHAPTER 2 - BACKGROUND

Before discussing irradiation-assisted stress corrosion cracking (IASCC) and its possible mechanisms, it is first necessary to introduce austenitic stainless steel (SS) and deformation of this alloy under LWR relevant conditions. Radiation effects in SS are then discussed, including the evolution of microstructure, mechanical properties and the deformation mode. IASCC is then introduced followed by a discussion of possible crack initiation mechanisms. Finally, the known correlations between deformation in irradiated SS and IASCC are presented, followed by the objective and approach to this study.

2.1 Metallurgy and mechanical behavior of austenitic stainless steel

Type 304 austenitic stainless steel is an iron-base alloy typically containing ~18 wt% Cr and ~8 wt% Ni. Because of the combined strength and corrosion resistance, austenitic SS alloys are widely used as structural material in LWR cores. Austenitic SS is solid solution strengthened, not heat treatable, and therefore not susceptible to over-aging as a result of long periods of exposure at reactor operating temperatures ~300 °C [29]. However, the susceptibility of these alloys to SCC is well known, often following grain boundary (GB) paths, implying a link between the SCC process and microstructure.

2.1.1 Composition and microstructure

Cr content in SS alloys causes passivation through the formation of a chromium rich oxide layer, which establishes resistance to aqueous corrosion and high temperature oxidation [30]. Direct correlations exist between GB Cr depletion and IGSCC in high temperature water, showing that IGSCC susceptibility increases sharply once GB Cr concentration drops below ~13.5 wt% [31]. Furthermore, Cr depletion profiles as narrow as 5 nm can cause significant susceptibility to IGSCC [31].

Although Cr content in SS is beneficial to corrosion resistance, its presence reduces stability of the austenite phase, a face-centered cubic (FCC) structure. Conversely, it enhances stability of the body-centered cubic (BCC) ferrite phase, the amount of which can be approximated by the use of a Schaeffler diagram, as shown in Figure 2.1 [32]. Other solute elements such as Mo, Si and Nb additionally stabilize the ferrite phase, represented by their contribution to the Cr equivalent as shown on the x-axis of Figure 2.1. BCC phases typically increase the yield and tensile strength of the steel [33], however, ferrite is typically less desirable than austenite in LWR structural materials as it is less corrosion resistant and does not maintain its yield strength as well at high temperature [34].

Ni is added to SS alloys to stabilize the austenite phase [30,32]. Other solute elements such as C, N, and Mn also act as austenite stabilizers, represented by their contribution to the Ni equivalent as shown on the y-axis of Figure 2.1. Ni also has an effect on SCC susceptibility [29], although its effect is less dramatic than that of Cr. For example, a 16 wt% Cr Fe-Cr-Ni steel has comparable corrosion resistance at Ni contents of 1, 4, and 8 wt% [35].

C concentration greatly enhances austenite stability, as indicated by the large coefficient associated with its contribution to the Ni equivalent, however, C concentrations are typically low

in SS to prevent the formation of carbides. C diffusion towards GBs commonly causes chromium carbide precipitation, depleting Cr concentration in regions near GBs and enhancing IGSCC susceptibility in oxygenated high temperature water (this process is commonly referred to as 'sensitization'). To counteract this effect, L grade stainless steels are commonly used, which have very low C content, ~0.03 wt% [34]. Despite the general agreement that carbide precipitation at grain boundaries is detrimental to IGSCC resistance, experiments in hydrogenated water (with low electrochemical potential) have shown that carbide distributions at GBs can enhance IGSCC resistance in these types of environment [36].

A third phase commonly observed in SS alloys is martensite, which has a body-centered tetragonal (BCT) structure and can greatly improve alloy strength because of its deformation resistance [37]. This phase typically forms upon cooling, but will redissolve upon sufficient thermal annealing. The temperature at which martensite transformation occurs is governed by the C, N, and Ni composition of the alloy [38].

Several types of inclusions and secondary phases are commonly observed in stainless steel including carbides, nitrides, MnS and oxides [38–41]. Secondary intermetallic phases typically include σ or χ phases, which only form after long periods at high temperature (700-850 °C) [38]. Carbides are most commonly $M_{23}C_6$, although MC or M_6C may also form. M commonly is represented by Fe, Mo, Cr or Ni, although carbides are predominantly Cr rich (~65%) [38]. As mentioned previously, carbide formation can cause sensitization and enhance IGSCC susceptibility, however, carbide distributions at GBs also can reduce IGSCC susceptibility by preventing GB sliding in hydrogenated high temperature water environments [36]. MnS inclusions are often observed as the sites of pit formation when SS is exposed to an aqueous

environment [40–42]. Oxide inclusions commonly include Cr, Ti, Al, and Mn oxides with possible traces of MnS, and have the hypothesized structure: TiO_2-MnO-Al_2O_3-Cr_2O_3 [39,43].

2.1.2 Deformation behavior

Plastic deformation in austenitic SS occurs in $\langle 110 \rangle$ directions on $\{111\}$ crystallographic planes, of which, there are a total of 12 variants in FCC crystal structures. The application of stress initially causes an elastic response ($\sigma = E\varepsilon$, where σ is stress, E is the elastic modulus and ε is strain) until the resolved shear stress on a slip plane exceeds a critical value, causing dislocation glide (slip) to occur. Resolved shear stress depends upon the applied stress and the orientation of the slip system with respect to the direction of stress.

It is energetically favorable for a single atomic slip step in FCC materials (vector b_1 in Figure 2.2) to dissociate into two Shockley partial dislocations (vectors X and Y in Figure 2.2) [44,45]. Shockley partials repel each other due to their combined edge and screw character, forming a region between the steps called a stacking fault, which have an associated interfacial energy called the stacking fault energy (SFE). Low SFE materials (such as austenitic SS, SFE <10 mJ/m^2) have widely separated partial dislocations, while high SFE materials have narrow stacking faults [44]. The SFE of austenitic SS depends heavily upon C, Cr, and Ni concentration, and is commonly estimated using the Pickering's formula [46]:

$$\begin{aligned} SFE\left(mJm^{-2}\right) = {} & 25.7 + 2\left(\%Ni\right) + 410\left(\%C\right) \\ & - 0.9\left(\%Cr\right) - 77\left(\%N\right) - 13\left(\%Si\right) - 1.2\left(\%Mn\right), \end{aligned} \qquad (1.1)$$

SFE affects deformation, as partial dislocations must be brought together before cross-slip (the transfer of slip from one plane to another) can occur [47]. Increasing SFE causes the nature of

slip to transition from planar to wavy [4], as it requires less energy for Shockley partials to combine and cross slip or jog formation to occur [48].

A variety of deformation microstructures are possible in austenitic SS, depending upon material condition, test temperature, and the applied strain rate. Wide stacking faults (with Shockley partial spacing >1 μm) and twin bands are formed after deformation at cryogenic temperatures [49], at high speed, or after a large amount of plastic deformation [50]. As temperature increases to room temperature and up to 450 °C, stacking faults become increasingly narrower, allowing cross-slip to dominate. This results in an equiaxed dislocation cell structure at low levels of strain [51], followed by dislocations becoming progressively more tangled [50,52]. Differences in the deformation microstructure formed in varying deformation conditions can be attributed to the equivalent stress level necessary for deformation to occur. Dislocation tangles are dominant below 400 MPa, isolated stacking faults (<1 μm wide) and perfect dislocations form between 400 to 600 MPa, and large stacking faults/twin bands dominate at greater than 600 MPa [50]. The equivalent stress level necessary to cause deformation is increased by strengthening through increasing the strain level, decreasing the deformation temperature, or through irradiation [53]. Representative images showing the difference in deformation microstructure due to the application of strain at different test temperatures are shown in Figure 2.3 [50].

Deformation in austenitic SS may also cause a stress-induced phase transformation of austenite to α' martensite [37,54]. Martensite forms due to dislocation motion on $\{111\}$ planes, when suitable dislocation configurations favor the occurrence of this stress-induced phase transformation [49]. Martensite lamellae have been observed as a result of deformation between

room temperature and 450 °C [51], which increase work-hardening capacity, but decrease the ductility of the steel [54].

Polycrystallinity complicates deformation, as deformation in each grain must be accommodated by that in adjacent grains. It is typically assumed that all grains undergo the same shape change as the bulk material, requiring the activation of at least five of the possible twelve slip systems in an FCC crystal [55]. GBs further influence deformation by affecting slip transfer between grains, and model results have shown that high stress concentrations can occur as a result of microstructural irregularities such as triple points (locations where three adjacent grains meet) [56]. The Hall-Petch relationship shows that as grain size becomes smaller (i.e., GB area increases), material strength increases as GBs act as barriers to dislocation motion [57].

2.2 Defect formation and microstructural evolution during irradiation

When a material is exposed to radiation, energetic particles (i.e., neutrons) displace lattice atoms from their original positions, creating vacancy and interstitial point defects. Radiation damage is quantified in displacements per atom (dpa), the average number of lattice sites each atom has been displaced from its original position. Average dpa can be calculated using the Norgett, Torrens and Robinson (NRT) model integrated over the recoil spectrum and time [58].

During the initial stage of irradiation, both vacancy and interstitial concentrations increase rapidly as their concentrations are initially too low for annihilation due to recombination or interaction with defect sinks (such as GBs, phase boundaries, dislocations, and free surfaces). Under irradiation at low temperature, a quasi-steady state regime occurs after initial defect buildup, due to mutual recombination as the limited mobility of interstitials prevents immediate

diffusion to sinks. As time progresses, interstitial concentration begins to decrease due to interstitial annihilation at sinks, because the interstitial diffusion rate is greater than the vacancy diffusion rate. This causes vacancy concentration to increase until steady state concentrations of both interstitials and vacancies are achieved. At high irradiation temperatures, defect diffusion rates increase, and fast interstitial diffusion causes rapid annihilation at sinks which eliminates the quasi-steady state regime where annihilation due to mutual recombination occurs. Regardless of irradiation temperature, steady state interstitial concentrations are orders of magnitude lower than vacancy concentrations due to their enhanced mobility and ease of transport to sinks. However, it is important to note that both defect concentrations under irradiation are orders of magnitude higher than thermal equilibrium concentrations. All following discussions will only address material changes due to LWR relevant irradiation temperatures near 300 °C, where vacancy mobility is effectively negligible.

Irradiation causes microstructural changes as well as elemental segregation. Microstructural formations include small defect clusters, dislocation loops, network dislocations, cavities (bubbles and/or voids), and precipitates [4], with faulted dislocation loops being the dominant feature [9]. Elemental segregation (called radiation-induced segregation (RIS)) occurs at vacancy and interstitial sinks such as GBs, phase boundaries, dislocations, and free surfaces.

2.2.1 Microstructure evolution

Irradiation near 300 °C is considered the low temperature regime, where small defect clusters (‘black spots,’ typically <2 nm) and faulted dislocation loops (Frank loops) are the most commonly formed microstructural features [4,59]. Black spots have been observed by transmission electron microscopy (TEM) to be faulted, interstitial-type dislocation loops [60].

Faulted dislocation loops can be either interstitial or vacancy in character, and have a Burgers vector equal to $a_o/3\langle 111\rangle$, where a_o is the FCC unit cell length. Loop sizes evolve with dose from an initially narrow distribution to a much broader, asymmetrical distribution [61], with a low density of loops 30-40 nm in diameter. In general, loops larger than 10 nm are interstitial in nature, lying on $\{111\}$ planes. Voids and large precipitates are not typically observed during low temperature irradiation, although fine-scale precipitation [59,61] and void formation have been observed after irradiation at 325 °C [59].

The size and number density of microstructural features increase with irradiation dose until saturation, which generally occurs at less than 5 dpa, as shown in Figure 2.4 for 275 °C neutron irradiated SS [61]. As irradiation damage progresses, defect clusters grow by interstitial absorption until they become faulted loops and eventually unfault into perfect loops or interact with network dislocations [62]. Faulted dislocation loops saturate with an average size near 10 nm and number density ~10^{23} m^{-3}, as indicated in Figure 2.5. Small defect clusters saturate with a density of 2-4 × 10^{24} m^{-3} after approximately 0.1 dpa [59,61].

Alloy chemistry affects dislocation loop evolution during irradiation, due to the fact that chemistry controls SFE and faulted dislocation loops are similar in character to stacking faults [63]. Muroga et al. [64] observed loop density to vary with Ni content in austenitic SS irradiated at high temperatures (>500 ºC), with a maximum density occurring at approximately 30 wt%. A similar dependence is possible at LWR operating temperatures, due varying dislocation sink strength with Ni content [64].

Radiation-induced precipitates also commonly form in SS during irradiation. Precipitation has been observed after irradiation in a PWR to approximately 10 dpa [65], and after fast reactor irradiation [66,67], however, precipitates typically only form after irradiation in the temperature range between 300 and 800 °C [59]. Precipitates formed in SS during BOR-60 irradiation have a size on the order of several nm, but an order of magnitude lower number density than dislocation loops (~10^{22} m^{-3}) [23,27]. Precipitate phases typically formed in austenitic SS during irradiation are Si-containing phases such as γ' (Ni_3Si) or G-phase ($M_6Ni_{16}Si_7$) [59]. Characterization of 10 dpa proton irradiated commercial purity (CP) 304 SS by atom probe tomography showed a high density of Ni and Si atomic clusters (with an atomic ratio of ~3:1, indicating likelihood of γ' formation) typically associated with dislocation loops [68]. Precipitation of Si containing phases sometimes does not occur until high irradiation doses are achieved, near 50 dpa [59].

2.2.2 Microchemical evolution

Diffusion of point defects (especially interstitials) formed during irradiation can cause local chemistry changes at defect sinks. Defect sinks include GBs, free surfaces, and to a lesser extent, dislocations (both network and loops), precipitates, and voids. The process of local chemistry change during irradiation, RIS, occurs in narrow regions near sinks, typically 5-10 nm FWHM after 3-5 dpa near 300 °C [4].

Diffusion depends upon the association of solute elements in SS alloys with a vacancy or interstitial flux [69]. Ni, Si, and to a lesser extent, P typically enrich by the interstitial drag mechanism, while over-sized elements such as Cr and Mo deplete due to the inverse-Kirkendall vacancy diffusion mechanism [4,59]. Fe segregation depends on the magnitude of the diffusion coefficient relative to other solute elements, and depletion occurs in most austenitic SSs [4,70].

The magnitude of segregation varies depending upon alloy composition and radiation exposure. BOR-60 irradiation of SS caused Ni enrichment of more than 10 wt% and Cr depletion of more than 5 wt% relative to the bulk composition [23,27,71].

2.2.3 Mechanical behavior evolution

Irradiation-induced defect clusters cause mechanical property changes such as an increase in hardness and yield strength [72–74]. Strength typically saturates at 3-5 times that of the unirradiated yield stress after several dpa, as shown in Figure 2.6. Several attempts have been made to relate irradiation hardening to the irradiated microstructure, including the dispersed-barrier hardening (DBH) and the cascade-induced source hardening (CISH) models. Despite the different methods used to describe hardening from irradiation, it is indisputable that irradiation hardening is caused by the formation of defect clusters.

The DBH model expresses a change in yield strength ($\Delta\sigma_{total}$) due to dislocation interactions with both short and long range obstacles:

$$\Delta\sigma_{total} = \sqrt{\sum_i \left(\Delta\sigma_{SR,i}\right)^2} + \Delta\sigma_{LR}, \qquad (1.2)$$

where $\Delta\sigma_{LR}$ is the change due to long range obstacles and $\Delta\sigma_{SR,i}$ is the change due to the i^{th} short range obstacle [62]. Dislocation networks are long range obstacles, while irradiation-induced defect clusters are considered short range obstacles. The total change in yield strength resulting from multiple short range sources (i.e., dislocation loops and precipitates) is determined by summing their effect in quadrature [62,75], although simulations have shown that this method becomes less adequate as defect strengths become more dissimilar [75].

The stress to move a dislocation through a field of obstacles is derived after the original Orowan strengthening model [76]:

$$\Delta\sigma_{SR} = M\alpha\mu b\sqrt{Nd} \quad , \qquad (1.3)$$

where $\Delta\sigma_{SR}$ is the change in the yield strength due to obstacles of size d and number density N. α is a parameter defining the obstacle strength, determined by measuring the angle between adjacent dislocation segments when the dislocation breaks free of the obstacle [77]. α values for faulted loops are typically between 0.25 and 0.5, while α values for precipitates can vary considerably depending on their size and coherency with the matrix, but are generally higher than those for faulted loops [62]. These values are inferred based on the mechanical behavior of irradiated materials, as very few measurements of α have been made in irradiated microstructures [78]. M is an upper limit for the ratio of uniaxial yield strength to resolved shear strength (the Taylor factor) and has a value 3.06 for FCC lattices [72,78,79]. μ is the shear modulus (78 GPa [80]), and b is the Burgers vector (2.52×10^{-10} m in SS [81]).

Comparison between the DBH model and experimental data indicate that strengthening is due to network and loop dislocations, while the saturation in yield strength is associated with the saturation of defect size and density in the irradiated microstructure, with additional increases only occurring because of void growth [82]. The DBH model reasonably predicts changes in yield strength for austenitic stainless steel, as shown by Yoshida at doses <0.1 dpa [60], and by Lucas [62] at doses up to ~20 dpa. However, disagreement of the model has been observed at LWR relevant irradiation temperatures [83], likely because the model is dependent upon accurate defect detection, and those smaller than 2 nm (i.e., defects not resolvable via TEM such as black dots) must not be neglected due to their high density [83,84]. The model further incorrectly

assumes that strength is uniform for a particular defect, when variations in size and character cause different dislocation interactions [72].

Alternative to the DBH model, the CISH model was created to better represent hardening observed in neutron irradiated materials. In brief, this model suggests that Frank-Read (F-R) sources (dislocations pinned at two points) become locked during irradiation due to their decoration by small clusters and dislocation loops [85]. This prevents activation of F-R sources until stresses much higher than $\mu b/l$ are achieved (the force required to cause dislocation bowing between two pinning points separated by length l, where μ is the shear modulus). The main hypothesis of the CISH model is that hardening should be treated in terms of the Cottrell atmosphere mechanism and not the Orowan hardening mechanism [85]. The stress necessary to unlock dislocations is given by:

$$\tau = 0.1\mu\left(\frac{b}{l}\right)\left(\frac{d}{y}\right)^{1/2}, \qquad (1.4)$$

where y is the distance from the line dislocation to the loop population and l is the distance between loops in the atmosphere [72].

2.3 Deformation in irradiated stainless steel

As SS reactor components harden under irradiation, the deformation mode transitions from homogeneous to highly localized slip. In irradiated SS, deformation becomes similar to that during unirradiated deformation at cryogenic temperatures [50], where slip is confined to narrow, planar bands. However, there is less of a tendency for twin band formation at LWR relevant conditions, and it is more favorable for dislocation channeling to occur [7].

Dislocation channels (DCs) form in materials where hardening is caused by removable, nanometer size defect clusters [86], typically in the form of a high dislocation loop density [48]. The radiation-induced defect network causes Shockley partial dislocations to increase in spacing, because the leading Shockley partial in a gliding dislocation creates a jog in a dislocation loop which impedes the motion of the trailing partial [51]. The increase in Shockley partial spacing suppresses cross-slip and causes planar deformation to occur on widely spaced $\{111\}$ planes [51]. DCs are formed once a sufficient number of dislocations on adjacent slip planes cut, annihilate, and/or combine with radiation-induced defects in their path [48,79]. A single dislocation interaction is not always sufficient to annihilate an irradiation-induced defect [72], and hundreds to thousands of dislocations are typically necessary to create a cleared channel [45,86]. DCs are defect-free pathways in the irradiated microstructure (shown in Figure 2.7 [87]) which allow subsequent dislocations to follow the same path with ease.

GBs or twin boundaries are the likely sites of channel formation [72,88], as dislocations can be formed at micro-scale ledges in the boundaries [89]. Only certain irregular sites with the capability of emitting large numbers of dislocations can initiate the channels [5]. In heavy ion irradiated Cu, no dislocation sources were observed at grain interiors (from F-R sources) during in-situ TEM observation [72]. Formation of new channels continues with increasing plastic strain, without F-R sources becoming active between existing channels [88].

DCs are characterized by their width, spacing, and the amount of strain contained within the channel [87]. Both channel widths and spacings vary grain-to-grain and within individual grains [86]. Channels likely widen as a result of repeated cross slip of dislocations within the channel. Mobile dislocations interact with dislocation loops, causing jogs in the loops and making them

more resistant to annihilation, which force dislocations to cross slip around them [90,91]. Hashimoto et al. [79] determined that channel width varied with resolved shear stress, although the dependence was small in neutron-irradiated 316 SS. Channels represent only a very small fraction of the specimen volume [85], yet include nearly all of the deformation, where local shear strain can be greater than 100% [6]. Locations where deformation channels intersect a free surface show visible steps which increase in density with increasing strain [48]. Channel density and the height of steps formed by their interaction at surfaces become homogenized as more dislocation emission sites activate [5].

DC formation has several impacts upon the stress-strain behavior of irradiated SS during deformation. A major consequence is the formation of an upper and lower yield point, which is likely caused by the combined formation of a high density of DCs and reduced amount of stress required to move dislocations once channels have formed [92]. Channeling does occur independent of macroscopic yielding, however, as cleared channels are observed before the yield point (although small and few in number), and in very low dose (0.01 dpa) samples without yield point formation [88]. Channeling also reduces strain hardening capability, because DCs are regions of local plastic instability [93]. As defects are annihilated or reduced in size within the channels, strain softening occurs [72].

2.3.1 Factors controlling dislocation channeling

Dislocation channeling is primarily controlled by irradiation dose, becoming the dominant deformation mode after ~0.1 dpa [86,94]. Deformation becomes increasingly localized as irradiation dose increases in proton irradiated SS, indicated by increased slip step spacing [7,52] and step height magnitude [5,9]. The increased localization is caused by the evolution of

radiation-induced defects, which increases the separation of gliding Shockley partial dislocations thus preventing cross-slip [51]. Channel step height increased with dislocation loop density, while loop size, void size, and void density had relatively little effect on channeling in proton irradiated SS [95]. Generally, higher hardness increased deformation localization (as measured by surface step height), however exceptions do exist [9].

Channeling also depends upon deformation temperature, and is typically observed at LWR operating temperatures near 300 °C. At 300 °C, glide can occur before the critical twinning stress is achieved [96], while twinning is more likely at lower temperatures [48]. Byun et al. [86] created a deformation mode map for irradiated 316 SS at room temperature, shown in Figure 2.8. At irradiation dose less than 0.1 dpa, the yield stress increases but deformation occurs as in unirradiated materials, in dislocation tangles after yielding occurs. After sufficient irradiation damage, the yield strength becomes sufficiently high and simultaneous twinning and channeling can occur after yielding. Alternate studies confirmed the existence of twins after low temperature deformation in both ion irradiated [96] and neutron irradiated [79] austenitic stainless steel.

Strain rate is another factor affecting the formation of DCs. The kinetics of channel formation can be interpreted from the Taylor-Orowan equation for strain rate, from ref. [97]:

$$\frac{d\varepsilon}{dt} = \beta b \rho_d^m \frac{\lambda}{\theta_w} \quad , \qquad (1.5)$$

where β is the generalized Schmidt factor (estimated at 1/3), b is the Burgers vector, ρ the mobile dislocation density (~10^{10} cm^{-2}), λ the effective spacing between glide obstacles ($7x10^{-6}$ cm^{-1}), and θ the effective wait time for a glide dislocation at an obstacle before it reacts and is free to glide. If the strain rate is slower than the rate defined by the Taylor-Orowan equation, channeling

can occur, otherwise twinning will be the deformation mode [97]. This theory is supported by experimental observations such as those by Hashimoto et al. [98], which show more twinning at higher strain rates.

Channeling is also mildly dependent upon SFE. Jiao et al. [5] observed that alloys with lower SFE had increased deformation in slip channels at comparable irradiation dose and strain, however at higher doses, the effect of SFE is diminished [99]. SFE controls planarity of slip in unirradiated materials, therefore also likely affects irradiated material deformation, but the effect is complex and not well understood.

Finally, channeling is dependent upon strain. As strain increases, both the strain within channels and the channel density increase [9].

2.4 Irradiation-assisted stress corrosion cracking

Irradiation-assisted stress corrosion cracking (IASCC) is a degradation phenomenon that affects austenitic stainless steels (SS) used as core component materials in light water reactors (LWRs). IASCC manifests as an intergranular (IG) type crack, which propagates along GBs. This gives the crack a faceted appearance, as exemplified in Figure 2.9. Similar to SCC, IASCC requires the existence of an applied stress, a corrosive environment, and a susceptible material; however, irradiation exacerbates SCC by altering both the environment *and* material.

Despite substantial research efforts, a mechanistic understanding of IASCC remains unknown. Difficulty in its understanding stems from the fact that IASCC susceptibility increases simultaneously with microstructural and microchemical evolution during irradiation, as shown previously in Figure 1.1. The cracking mechanism is further complicated by the fact that the

microstructural changes cause secondary effects such as hardening and dislocation channeling, which also correlate with cracking susceptibility. In the following sections, the primary dependencies of IASCC are reviewed and possible IASCC mechanisms are summarized.

IASCC susceptibility is often studied using a constant extension rate tensile (CERT) test (also sometimes referred to as a slow strain rate tensile (SSRT) test). These tests are similar to conventional tensile tests, but are performed at very slow strain rates on the order of 10^{-7} s^{-1}. The slow strain rate allows time for corrosion processes to affect the test specimen, as CERT tests are commonly performed in an aggressive environment. For the case of IASCC testing, the test environment typically simulates that of a LWR. CERT test results provide analysis of mechanical properties (yield strength, ultimate tensile strength, and elongation), as well as a comparison of cracking behavior via post-test fractography. IASCC susceptibility is typically quantified by the percentage of IG cracking (%IG) on the fracture surface after the CERT test is completed. Although it is difficult for CERT experiment results to provide an exact measure of material susceptibility to SCC (due to cracking dependence on strain rate [100]), it is often used to provide a relative measure of susceptibility among material conditions, and is generally accepted as a method to compare crack initiation susceptibility as CERT results are governed by the crack initiation event [4].

2.4.1 Environmental dependence of IASCC

IASCC depends strongly on the corrosive nature of the environment, as IG cracking initiates at the material surface exposed to the operating environment [3]. LWRs use high temperature, high pressure water as coolant, and LWR water chemistry has a known effect on IASCC susceptibility. More aggressive environments (compared by their electrochemical potential

(ECP)) increase IASCC susceptibility in CERT tests, as seen by reduced strain to failure and increased %IG [28,101,102]. Regardless of ECP, strain to failure and %IG are inversely correlated for irradiated alloys tested by CERT [28]. Similar effects of water chemistry are observed in crack growth rate (CGR) test results, showing that CGR increases with ECP for both unirradiated as well as irradiated stainless steel, exemplified in Figure 2.10. A pronounced increase in CGR occurs as potential increases above ~100 mV vs. the standard hydrogen electrode (SHE) [103].

Three LWR environments are most common: boiling water reactor (BWR) normal water chemistry (NWC), BWR hydrogenated water chemistry (HWC), or primary water reactor (PWR) primary water (PW). The main difference among these environments is the dissolved gas content, which directly affects ECP. NWC typically has a low concentration of dissolved oxygen (DO), which creates a relatively high ECP (>200 mV vs. SHE). Alternatively, HWC and PW contain dissolved hydrogen (DH), which lowers ECP. HWC typically has a concentration of several hundred ppb DH (ECP <500 mV vs. SHE), while PW generally has a concentration of ~3 ppm DH (ECP <800 mV vs. SHE).

Radiation can enhance the corrosive nature of high temperature water through radiolysis, which forms free radicals and molecules (e.g., H^+, OH^-, H_2O_2, etc.) [3]. The formation of these products can increase ECP, however the effect of radiolysis on IASCC is outside the scope of this study. Experiments in the present study have all been performed in simulated LWR environments without the presence of a radiation field.

Despite the influence of ECP on IASCC, several instances of IG cracking have been observed on irradiated materials in inert environments [7,14,101,104–106]. These observations provide

evidence that crack initiation is possible without the effect of the corrosive environment, although the effects of high temperature water on CERT results are undeniable. Previous work has been unable to determine whether similar mechanisms cause IASCC initiation in simulated LWR environments and GB separation during experiments in high temperature inert environments.

2.4.2 Microstructural dependence of IASCC

IASCC has a known dependence on the irradiated microstructure. As discussed previously, irradiation-induced defect clusters cause irradiation hardening, which correlates with IASCC susceptibility. Figure 2.11 includes CERT results from several authors showing that IASCC susceptibility increases after the irradiated yield strength (YS) achieves ~400 MPa. Although the irradiated microstructure can account for irradiation hardening, it does not directly correlate with IGSCC susceptibility [107]. West et al. showed that hardening, dislocation loops, and void distribution did not define IASCC susceptibility by comparing multiple irradiated austenitic alloys (both Fe- and Ni-base) [84]. Furthermore, the large scatter in %IG observed at high YS values indicates that irradiation hardening is not the only factor controlling IASCC.

Post-irradiation annealing (PIA) studies further analyzed irradiated microstructure and hardening as the cause of IASCC [108,109]. The total dislocation loop line length (determined by multiplying the circumferential length of dislocation loops by their number density) remains relatively unchanged by the time IASCC susceptibility has been completely removed [108], although the recovery in irradiation hardening scales with a reduction in IASCC susceptibility [109]. Some irradiation hardening remains after IASCC susceptibility has been completely

removed by PIA [108], indicating that a critical amount of hardening may be necessary for the occurrence of IASCC.

Hash et al. also established that hardness alone does not correlate directly with IASCC susceptibility, and that irradiation-induced hardening is essential to IASCC initiation [110]. Comparing CP 304 SS with different levels of CW and irradiation (to yield the same total hardness), only samples with the greatest amount of irradiation damage (>0.55 dpa) were susceptible to IGSCC. Therefore, it was established that the hardening source plays an important role in IASCC susceptibility.

2.4.3 Microchemical dependence of IASCC

Many IASCC studies have focused on RIS effects at GBs. Cr depletion was a primary focus, as Cr controls corrosion resistance in austenitic SS alloys and IASCC occurs at GBs. Cr depletion by RIS was expected to cause a similar SCC response as sensitization. Sensitization causes depletion of Cr in GB regions due to the formation of chromium carbides, rendering GBs susceptible to brittle cracking once local Cr concentration depletes below a critical concentration required for repassivation [4]. Figure 2.12 shows that IASCC susceptibility occurs in materials with GB Cr concentration below ~17%, however the large scatter in the cracking response between GB Cr concentrations of 12% to 17% indicates that GB Cr depletion is not a controlling factor for IASCC susceptibility [111].

GB Si concentration is also a potential detriment to IASCC resistance, and RIS causes severe enrichment of Si at GBs to levels as high as 15-20 wt% [4]. Irradiated high Si alloys generally have increased susceptibility to IG corrosion, likely due to combined Si enrichment at GBs and the high solubility of Si in high temperature water [15,112]. Various effects of Si segregation

have been observed, including increases [113,114], decreases [15], and indeterminate effects [115,116] on IASCC susceptibility. From the results available in literature, it can also be concluded that Si enrichment does not control IASCC susceptibility.

PIA studies have shown that IASCC susceptibility decreases while RIS remains unchanged until longer annealing times [108,109]. Busby et al. [108] determined that IG cracking susceptibility was completely removed before any change occurred in GB Cr or Ni content. Both Si and P segregation were removed during annealing at a similar rate as IASCC susceptibility [108], however it is difficult to conclude that Si segregation is a defining factor for IASCC due to the conflicting results from the literature. P segregation has been observed to either have no effect or a slightly beneficial effect on IASCC resistance [117,118].

2.4.4 Potential mechanisms of IASCC

Water chemistry, irradiation hardening (caused by irradiation induced defect formation), and RIS all affect IASCC susceptibility, although direct attribution cannot be given to any one factor. Existing evidence shows that the mechanism is likely related to irradiation hardening rather than changes in GB chemistry, while increasing the corrosion potential of the environment further enhances cracking susceptibility. Based on this knowledge, research has focused on a secondary effect of irradiation: the transition from homogenous deformation to highly localized deformation involving the formation of DCs.

DCs create high local strains and may terminate at GBs, which, according to Was [4], cause GB cracking by either of two processes. The first involves dislocation accumulation within a DC impinged at a GB, which accumulates stress at the DC-GB intersection (ahead of the dislocation pileup). Cracking may occur when local stress exceeds a critical value (i.e., the GB cohesive

strength), resulting in the formation of a wedge or Zener-Stroh type crack [119]. Was proceeds to mention that this cracking process could initiate without the influence of a corrosive environment [4], thus explaining the observation of IGSCC initiation in irradiated materials deformed inert environments [7,12,101,104,105,120].

The second cracking process implicates deformation within the GB as the cause of crack initiation [4]. GB deformation (also called GB sliding) in irradiated materials could be caused by dislocation absorption by the GB when DCs intersect the GB. This mechanism was observed by Alexandreanu [121] in Ni-base alloys tested in 360 °C primary water, where deformed GBs cracked more often than those that did not.

Both processes described by Was [4] are consistent with the more general mechanism proposed by Jones for SCC type cracking: the first step involved is rupture of a protective oxide film by slip bands created from an applied stress which expose underlying bare metal surfaces [122]. As rupture of a protective oxide may be the only necessity for IASCC initiation, several authors have suggested IASCC initiation to have a mechanical basis [5,97,123]. It is possible that the amount of deformation necessary to cause rupture of the protective oxide film creates the environmental dependence, yet the mechanism of rupture may be the independent of environment.

2.5 Localized deformation and IASCC

Recent studies have focused on gaining a better understanding of dislocation channeling in irradiated SS and how they relate to cracking [4,5,8–12,14,95,103,106,124–126]. When straining neutron irradiated SUS 316 in 320 °C Ar, Nishioka et al. only observed GB separation in

samples strained at slow strain rates [12], and a similar same strain rate dependence was also observed by Fukuya et al. [14,127]. Because DCs only form under deformation at high temperatures and slow strain rates, DCs are implicated as a necessity for IGSCC initiation. Jiao and Was [9] showed that when looking at a wide range of variables, the average height of deformation steps on the surface of proton irradiated stainless steels showed the strongest correlation with IASCC susceptibility. A 'threshold' step height was observed between ~300 and ~350 nm, such that samples with average step heights below 300 nm did not form IASCC, and above 350 nm all samples formed IASCC, Figure 2.13. Cracking sites were observed to initiate preferentially where slip lines intersect GBs [5–8], and in locations where DCs are present in only one grain adjacent to the separated boundary [6,8,12].

Despite observations indicating DCs as a cause of IASCC, there is still much to consider due to the complexity of deformation in polycrystalline materials. Different types of interaction occur between DCs and GBs depending upon factors such as the angle of interaction, the orientation of adjacent grains, and the character of the boundary. For example, Dropek et al. [128] showed that significant differences in cracking can occur in similar SSs after thermo-mechanical processing to enhance the ratio of coincident site lattice (CSL) boundaries to high angle boundaries (HAB), Figure 2.14. The following section will discuss the different types of DC-GB interaction (summarized in Figure 2.15) and their effect on IASCC.

2.5.1 Dislocation channel-grain boundary interactions

Several researchers including Bloom [129] and Nishioka [12] have postulated that IG crack initiation sites in irradiated austenitic SS result from intersections between DCs and GBs. Was et al. [130] also stated that the GB resistance to deformation and/or slip accommodation may

control SCC susceptibility. Because IASCC is IG in nature, it is important to consider how DCs and GBs interact. Generally, a GB will either accommodate slip or cause slip discontinuity, depending upon which occurrence results in the largest decrease in free energy [131]. Each interaction is examined, including: slip transmission, dislocation absorption and GB sliding, and slip discontinuity.

Slip transmission (GB3 in Figure 2.15) causes DC formation in an adjacent grain. This type of DC accommodation requires relatively small misorientation between adjacent crystals [6,130], and CSL boundaries are more likely to meet this criterion than HABs [10,132]. CSL boundaries having low Σ values (i.e., those with the highest degree of coincidence between grains) exhibit the highest degrees of slip continuity [133]. As strain increases within individual DCs, the propensity for slip transmission across a GB increases (as shown in three proton-irradiated alloys with different SFE [99]). Also, GBs with a surface trace at a low angle with respect to the tensile axis are more likely to transmit slip [10].

After slip transmission occurs, dissimilar Burgers vectors orientations in adjacent grains causes some deformation to remain at the GB, which creates a geometrically necessary step [134] (also referred to as a "deformation ledge" [12,131]). The step can be characterized by an effective Burgers vector, *B*:

$$B = n\left(b_1 - Qb_2\right), \qquad (1.6)$$

where b_i are the Burgers vectors in adjacent grains, Q is a rotation matrix, and n is the number of dislocations that slip [131]. Ledges are associated with a strain field [99,129] that can be relieved by the initiation of accommodating plastic flow in areas surrounding the ledge, or by the opening of a crack [131]. Grains that transmit slip relieve large amounts of stress and induce low levels of

deformation at the GB, rendering them less susceptible to SCC [99], as shown by the results of McMurtrey [10].

The second type of interaction, dislocation absorption and GB sliding, is shown at GB1 in Figure 2.15. Generally, GB deformation occurs by sliding or migration [5], however, migration is a diffusional process that occurs only at high temperatures and will be omitted from further discussion. GB sliding occurs when GB dislocations climb or glide [130]. GB dislocations can originate from GB dislocation sources, but most are produced by the interaction of lattice dislocations with the boundary [135]. In the case of irradiated materials, GB dislocations are supplied by DCs [5]. GBs are efficient sinks for dislocations due to elastic energy reductions during their dissociation into GB dislocations, especially when the boundary has a large Σ value (i.e., boundaries with high degrees of misorientation) [136]. As more lattice dislocations become GB dislocations, GB stress increases until dislocations are emitted into the adjacent grain or GB dislocations start gliding. Sliding is localized to portions of a grain rather than shearing the entire boundary [137], and may cause decohesion of GBs or oxide film rupture leading to IG crack initiation. Alexandreanu and Was [121] established that GB sliding affects IGSCC initiation in Ni-base alloys, as observed in Figure 2.16.

GB deformation may also be affected by RIS. GBs form a narrow region free of dislocation loops after irradiation, thus promoting GB sliding because the matrix is hardened by irradiation-induced defects [48,97]. It is also possible that RIS affects GB cohesive force [120].

The third type of interaction (GB2 in Figure 2.15), DC discontinuity, results in dislocation pile-ups at a GB without slip transfer [48]. High local stresses result, causing the GB to emit dislocations, create deformation twins, or crack [48]. Channel strain at this type of intersection is

generally less than other interaction types [11]. Observations show this type of interaction to be linked to points of IGSCC initiation [10,106], as shown in Figure 2.17.

2.5.2 Stress at discontinuous dislocation channel – grain boundary intersections

A non-transmitting DC creates a region of high local stress and can lead to the opening of a crack. Fukuya et al. [8,138] showed that in regions where coarse steps intersect a GB, a high degree of local misorientation exists as evidenced by electron backscatter diffraction analysis. Local misorientation indicates the existence of local strain fields [8], which could exceed GB cohesive energy and lead to cracking. Finite element model results confirm that a region of high stress forms within ~100 nm of a DC-GB intersection, causing GB normal stress in excess of 3 times the applied stress [139]. The magnitude of shear stress at these points is approximately 70% of the normal stress, which indicates that normal stress controls crack formation. Figure 2.18 indicates that GB inclination with respect to the tensile direction has a negligible effect on the normal stress near the intersection.

Despite model results, GB normal stress is likely related to IASCC susceptibility based on the observations of Fukuya [6], Nishioka et al. [12] and West and Was [106,140], who only observed IGSCC at GBs with a surface trace nearly normal to the tensile axis. Observations of IGSCC at these GB types led to the development of the Schmid Modified Grain Boundary Stress (SMGBS) model, which assumes a critical GB normal stress is necessary to cause IG crack nucleation [140]. GB normal stress is calculated based upon the Schmid factor of an adjacent grain and the inclination of the GB plane with respect to the applied tensile stress. A critical GB normal stress for crack initiation was determined by comparing the stress distribution and the crack distribution as functions of the GB angle distribution. Irradiation was observed to broaden

the cracking distribution, indicating a lower critical normal stress required for IGSCC initiation [140]. This model, however, neglects the effect of dislocation channeling.

2.6 Objective and approach

Stress at a GB has a likely role in the IASCC initiation mechanism, however, it is unclear whether stress due to impingement of a DC at a GB or GB normal stress is the most important factor. Further, DCs in neutron irradiated alloys have only been characterized in a limited number of studies, especially in terms of their relation to IASCC susceptibility. ***Therefore, the primary objective of this research was to determine the role of dislocation channeling in the IASCC initiation of neutron irradiated stainless steel.*** To achieve this objective, several neutron irradiated alloys were compared based on their susceptibility to crack initiation, and crack initiation sites created in a novel deformation experiment were examined in close detail. Analysis of the microstructure and deformation in regions near IGSCC initiation sites allowed identification of key factors affecting the IASCC initiation process.

This study was predicated on recent comparisons of the IASCC susceptibility of austenitic SSs created and irradiated during the previous CIR I and II programs. Based on the findings, several irradiated alloys were chosen for further study. The dependence of dislocation channeling on irradiation dose necessitated the selection of an alloy with different levels of irradiation dose, and two similar alloys were also included in the study with low IASCC susceptibility and IASCC resistance under the test conditions of interest.

A novel experiment was designed and performed under comparable conditions as those in the previous SCC experiments. These conditions included: a region of uniaxial tensile strain, a

similar strain rate (3.5×10^{-7} s^{-1}), and the ability to be performed in a simulated LWR environment. Finally, it was necessary that the experiment be possible with the limited amount of available irradiated material. A miniaturized four-point bend test fit these criteria, and allowed observation of crack initiation sites without propagation due to the stress/strain gradient through the sample thickness.

Four-point bend tests were performed in a simulated BWR NWC environment. To create cracks near the initiation stage, stress or strain increments were applied to bend samples, observing the bend surface for cracks and surface deformation after each increment. Once crack initiation sites had formed, local features were compared near cracking locations. The resulting observations allowed dependencies to be determined and a mechanism for the IASCC initiation process to be proposed.

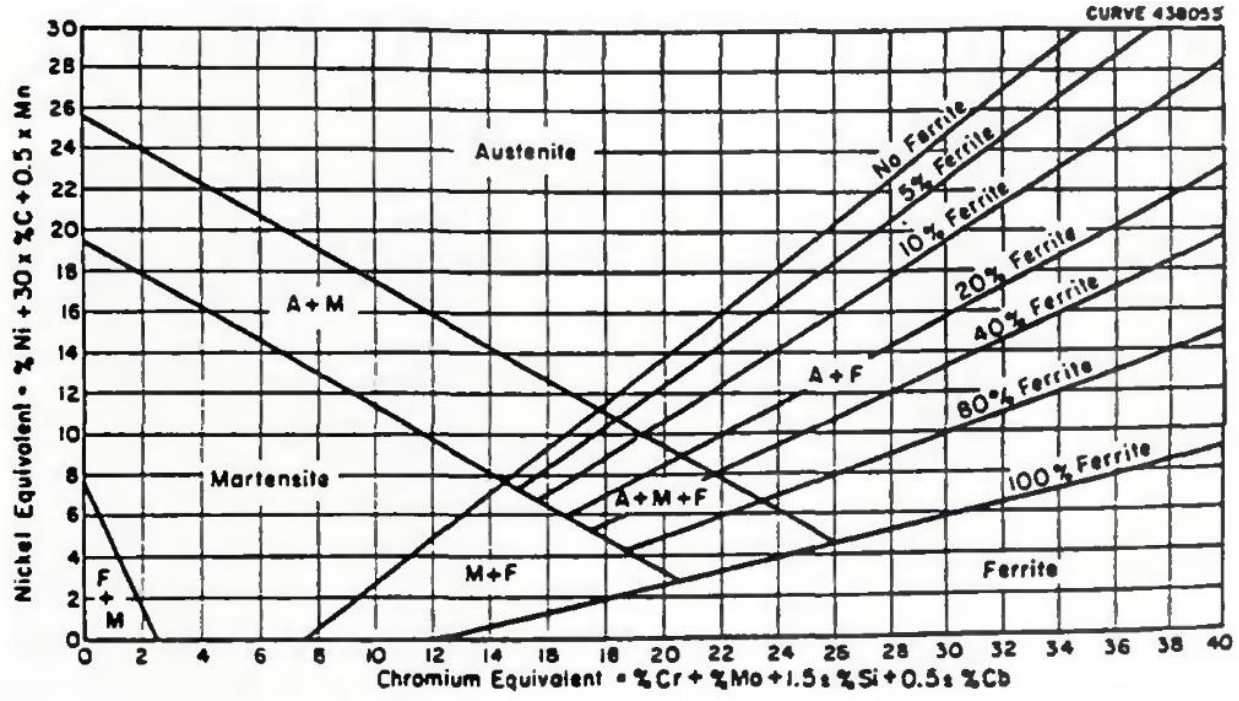

Figure 2.1. Schaeffler diagram for stainless steel, from [32].

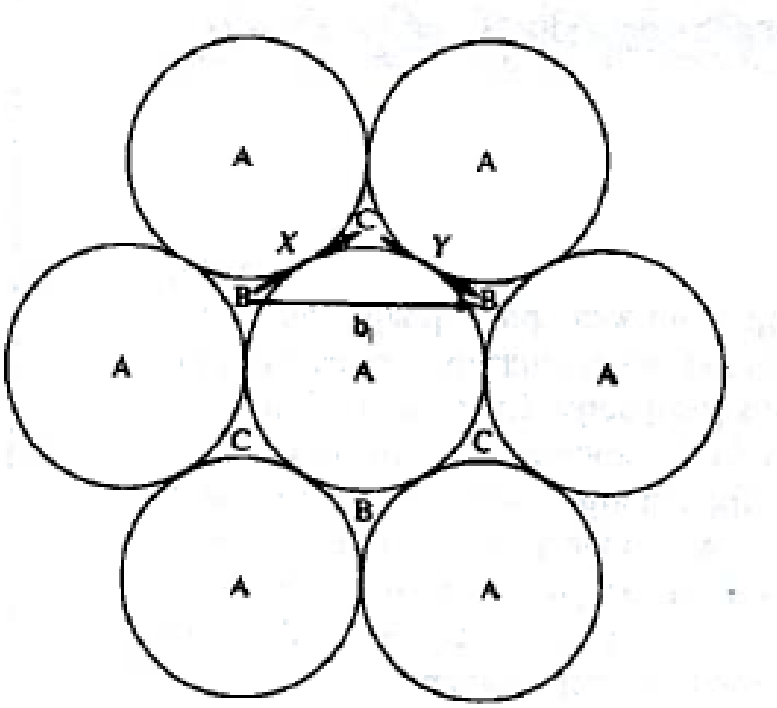

Figure 2.2. A portion of atoms from a (111) plane in an FCC crystal, displaying a full atomic displacement burgers vector b_1, and its two partials X and Y. From [44].

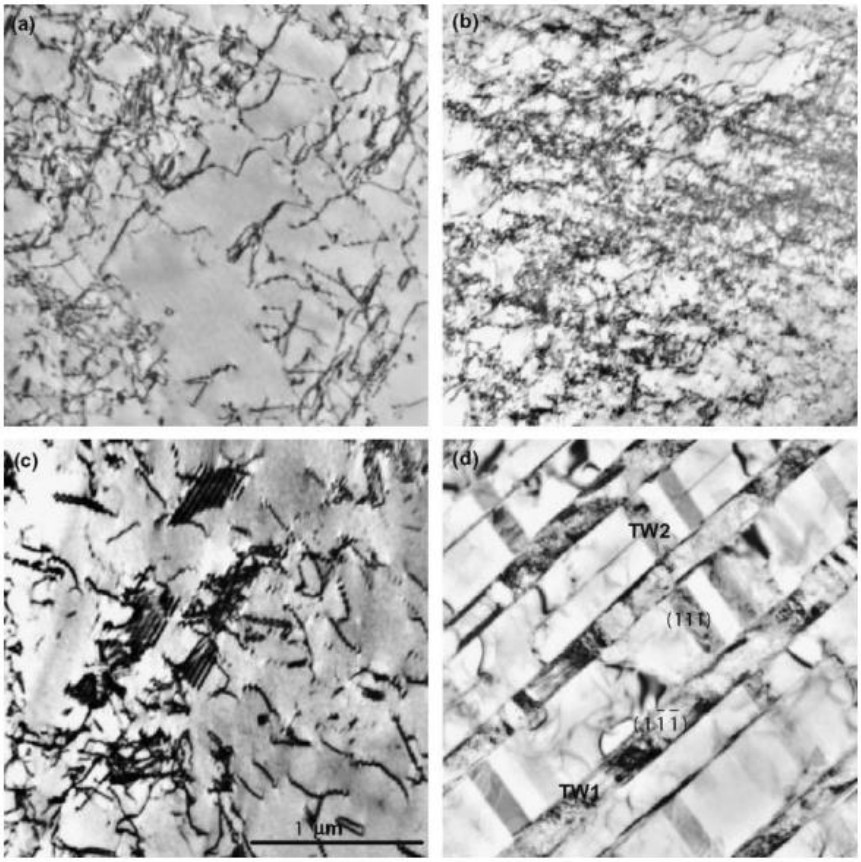

Figure 2.3. Deformation microstructures of 316LN SS after deformation to ~15% at a) 400 °C, b) 200 °C, c) room temperature, and d) -100 °C. From [50].

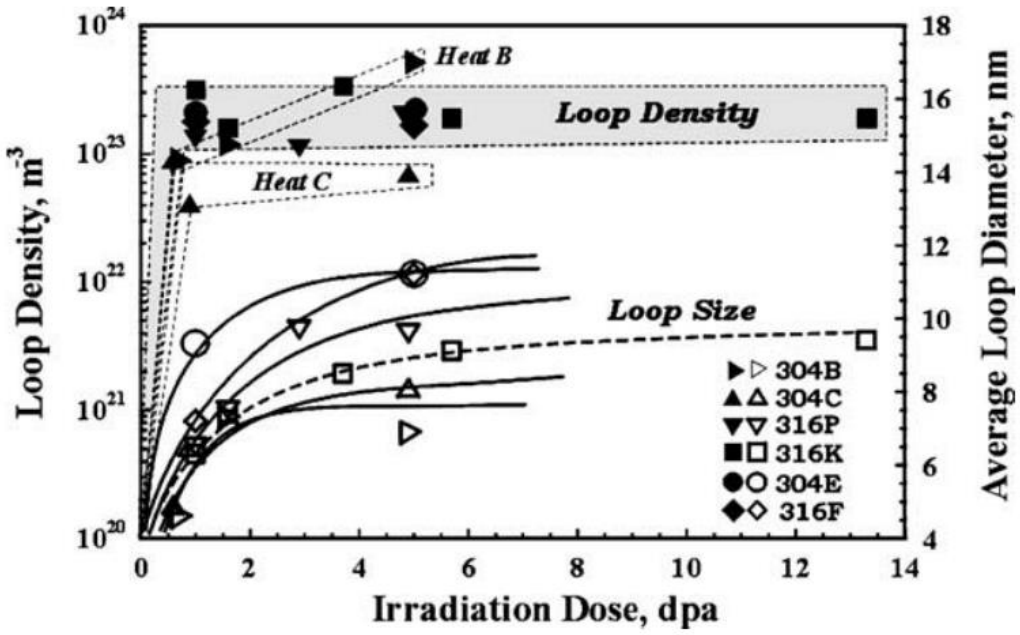

Figure 2.4. Average size and density of dislocation loops in austenitic SS as a function of irradiation dose, after 275 °C irradiation. Saturation typically occurs after ~2 dpa. From [61].

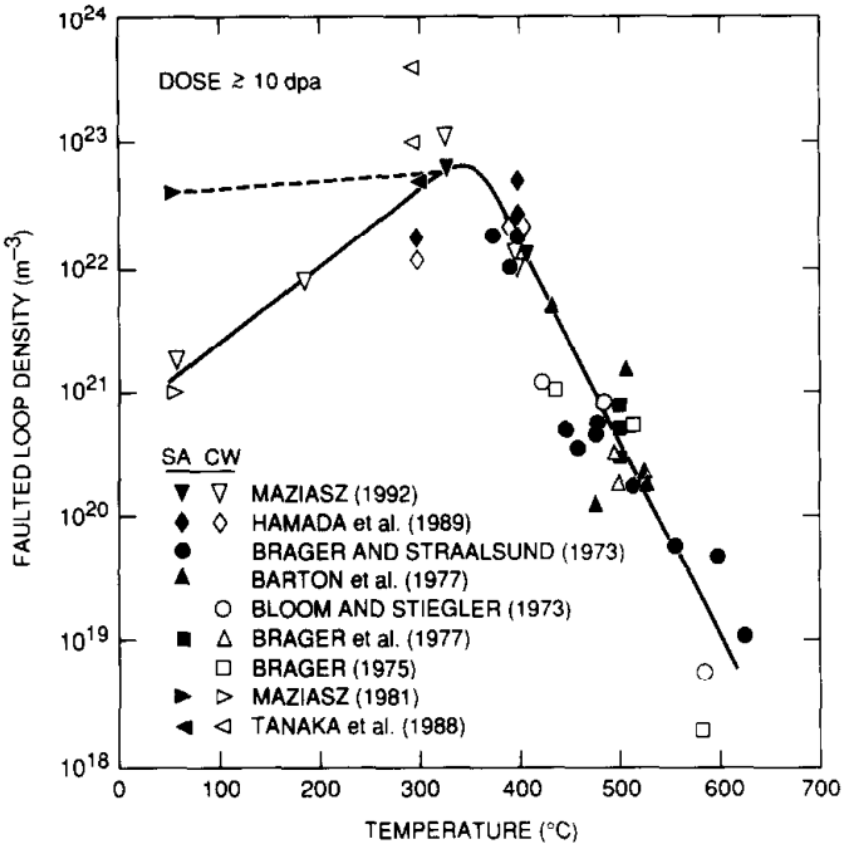

Figure 2.5. Temperature dependence of faulted dislocation loop density in neutron-irradiated austenitic SS. From [59].

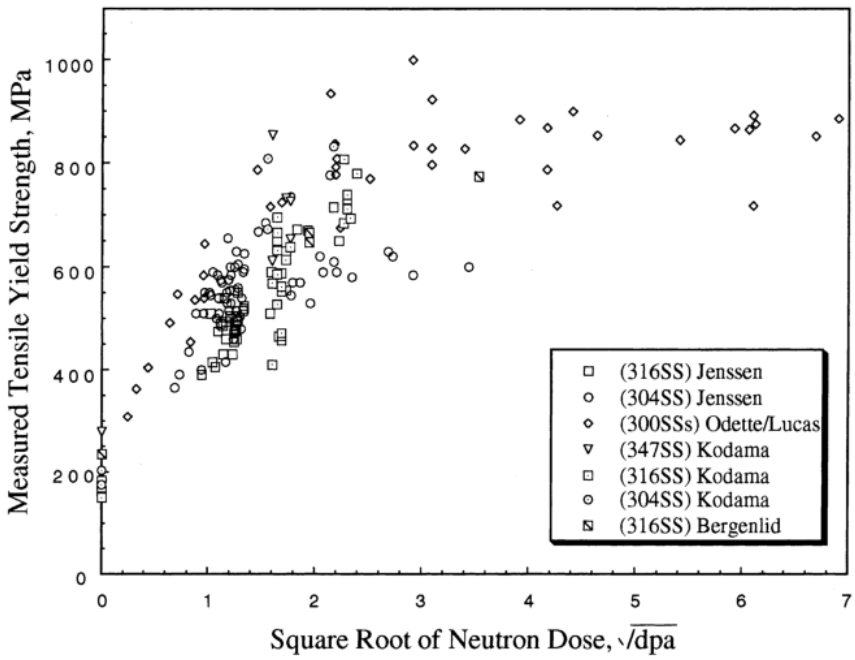

Figure 2.6. Irradiation dose dependence of tensile yield strength for austenitic SS, from [74].

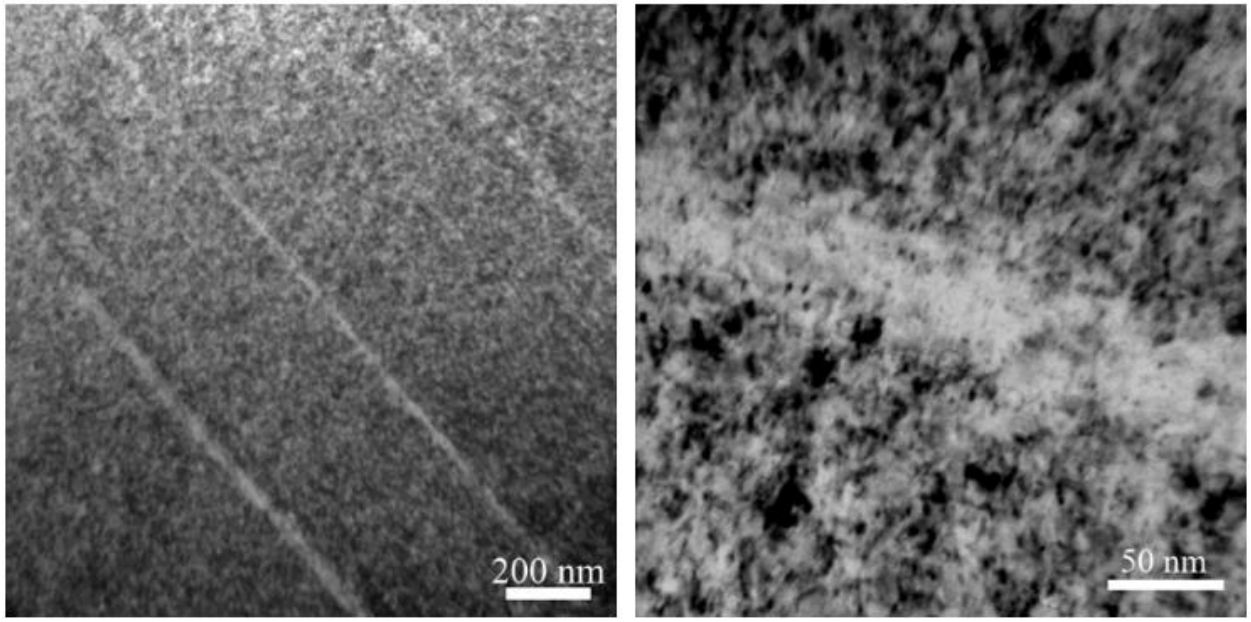

Figure 2.7. TEM micrographs of cleared DCs in proton irradiated stainless steel deformed in CERT tests at 288 °C, from [87].

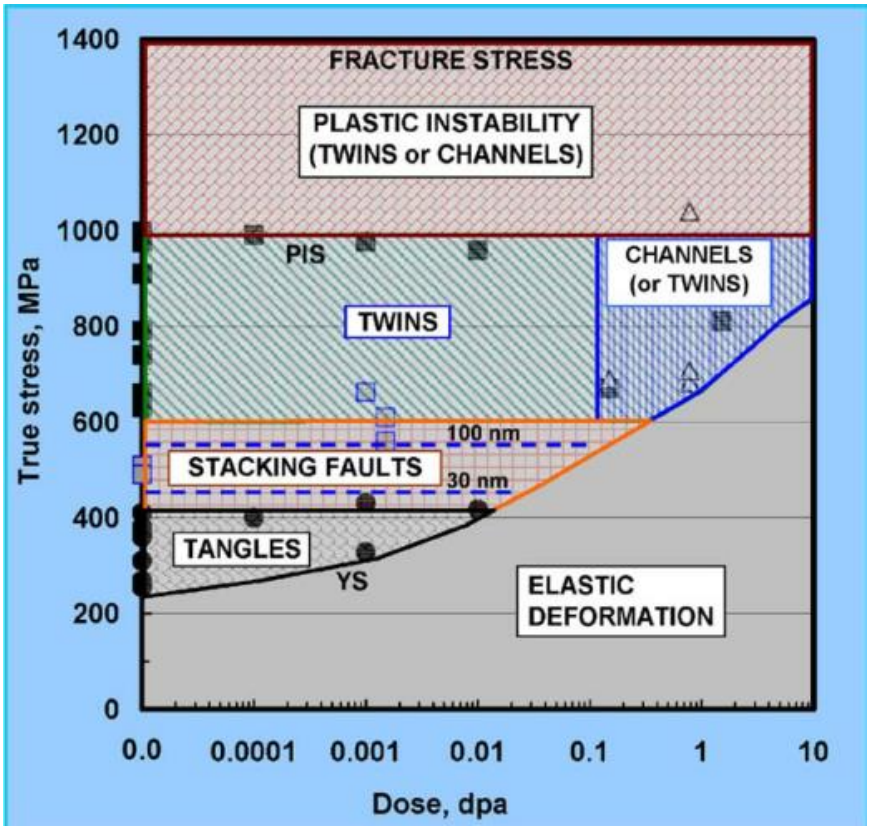

Figure 2.8. Room temperature deformation mode map as a function of irradiation dose for 316 SS, from [86].

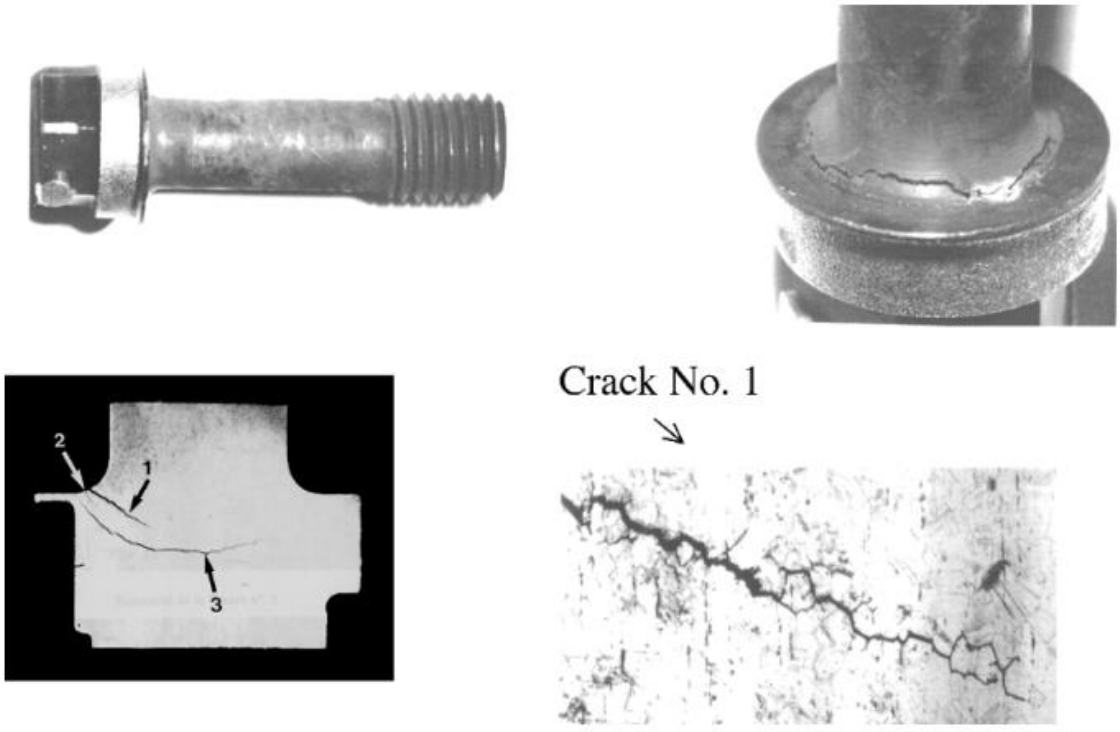

Figure 2.9. IGSCC type cracks observed in an irradiated, cold worked type 316 stainless steel baffle bolt removed from an operational LWR. From [87].

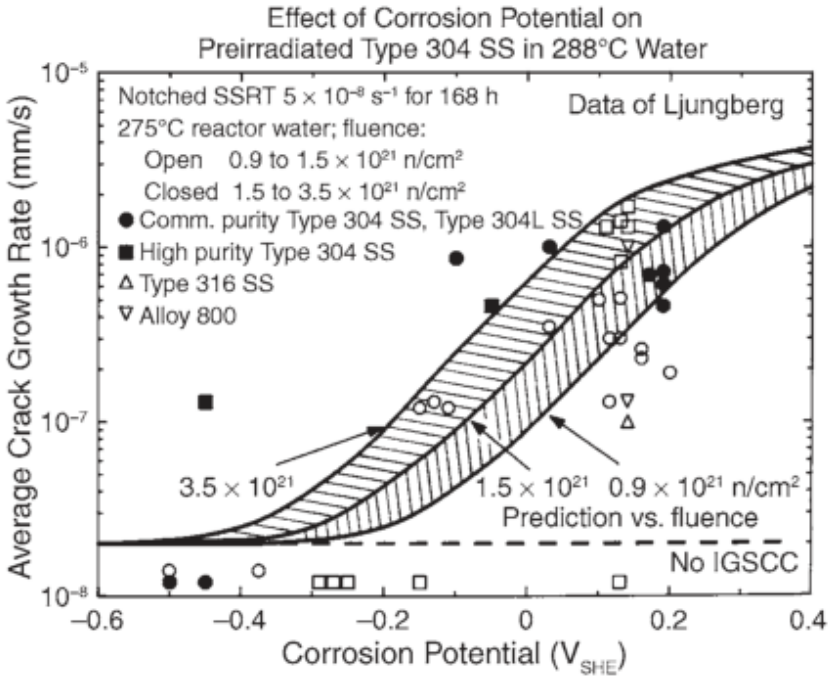

Figure 2.10. ECP dependence of CGR in irradiated stainless steel. From [103].

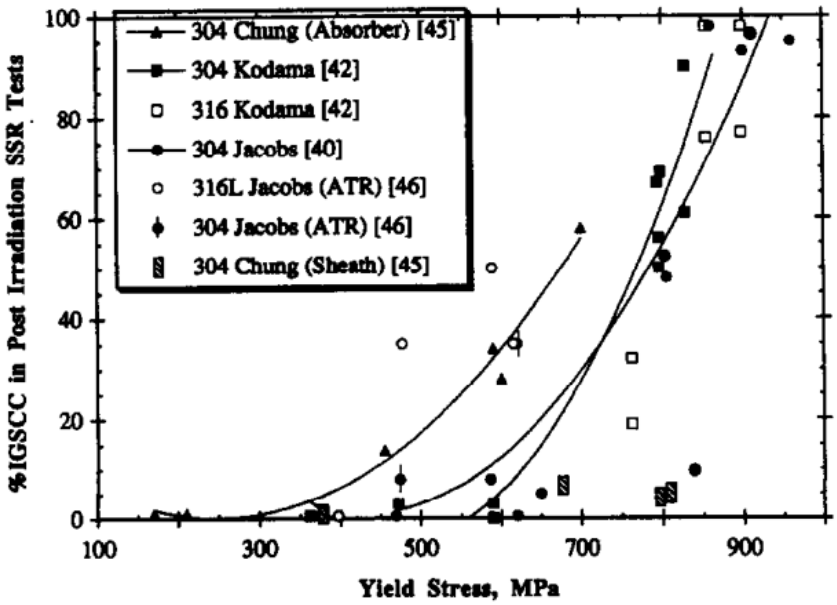

Figure 2.11 IGSCC susceptibility as a function of irradiated yield stress in neutron irradiated stainless steels, as determined from CERT tests. From [141].

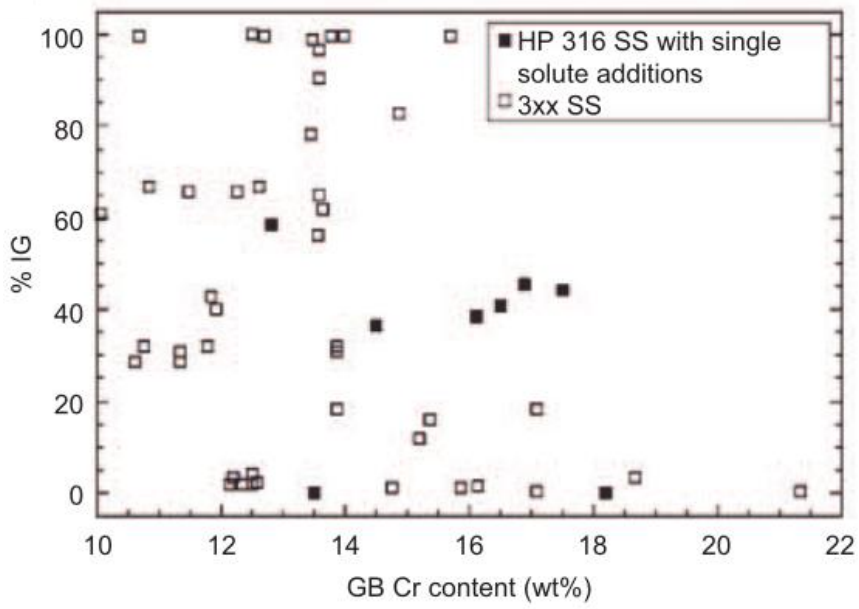

Figure 2.12. IASCC susceptibility (%IG) from CERT experimental results plotted as a function of GB Cr concentration. From [113].

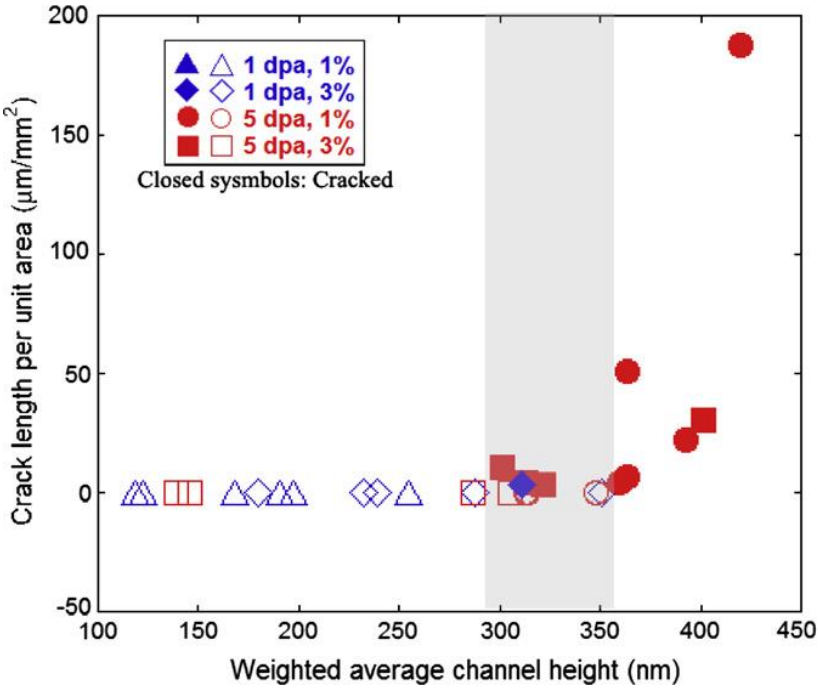

Figure 2.13. The impact of DC step height on cracking susceptibility measured on proton irradiated stainless steel after deformation by CERT in simulated NWC. From [9].

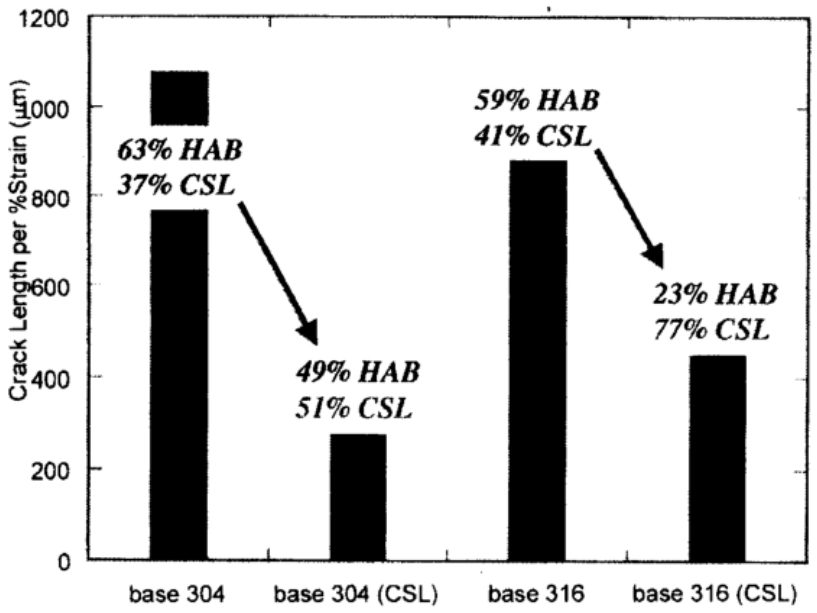

Figure 2.14. Effect of grain boundary character on cracking susceptibility for 304 and 316 SS deformed by CERT in BWR conditions. From [130].

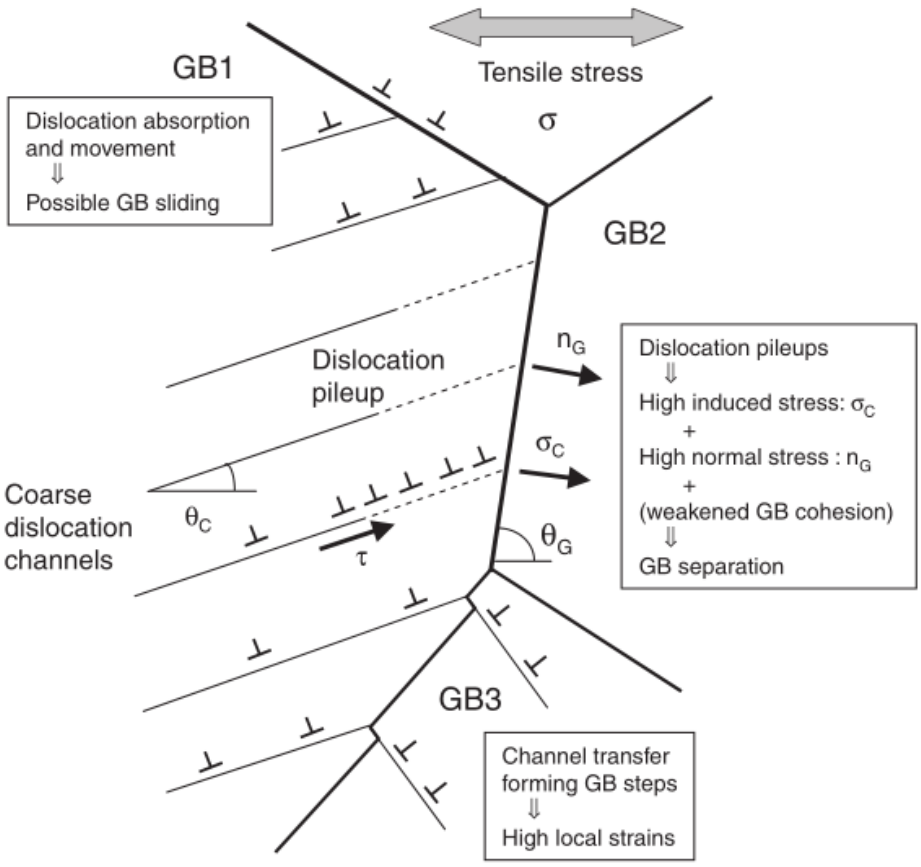

Figure 2.15. A schematic showing possible DC-GB interaction types. From [12].

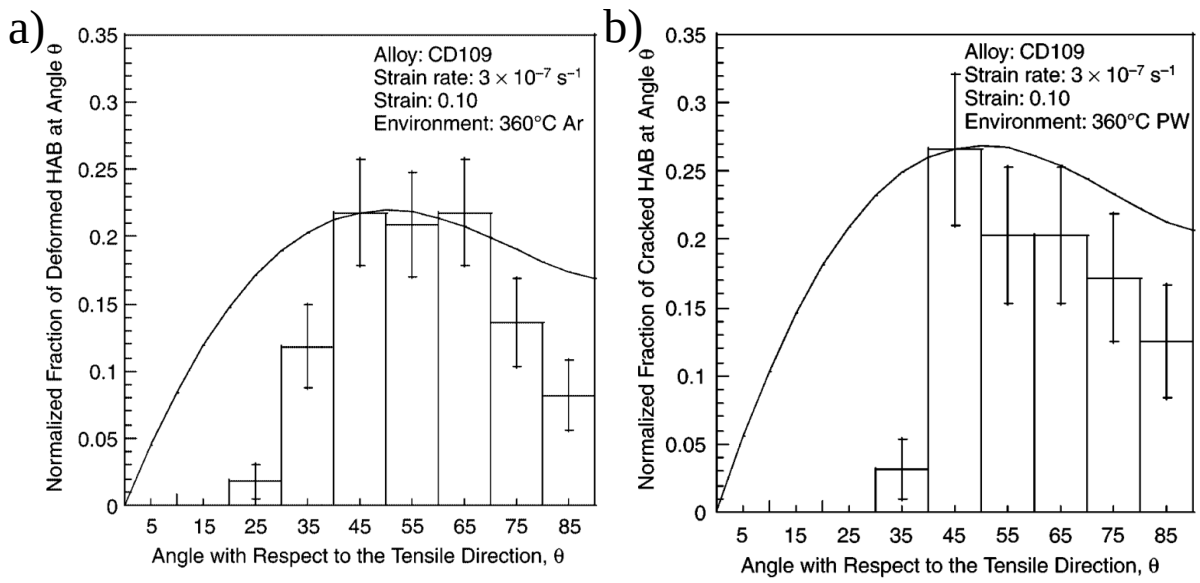

Figure 2.16. a) Fraction of deformed HABs as a function of GB inclination to the tensile direction and b) fraction of cracked boundaries versus the same inclination. The curve in each figure represents the average normalized shear stress on the GB plane. From [121].

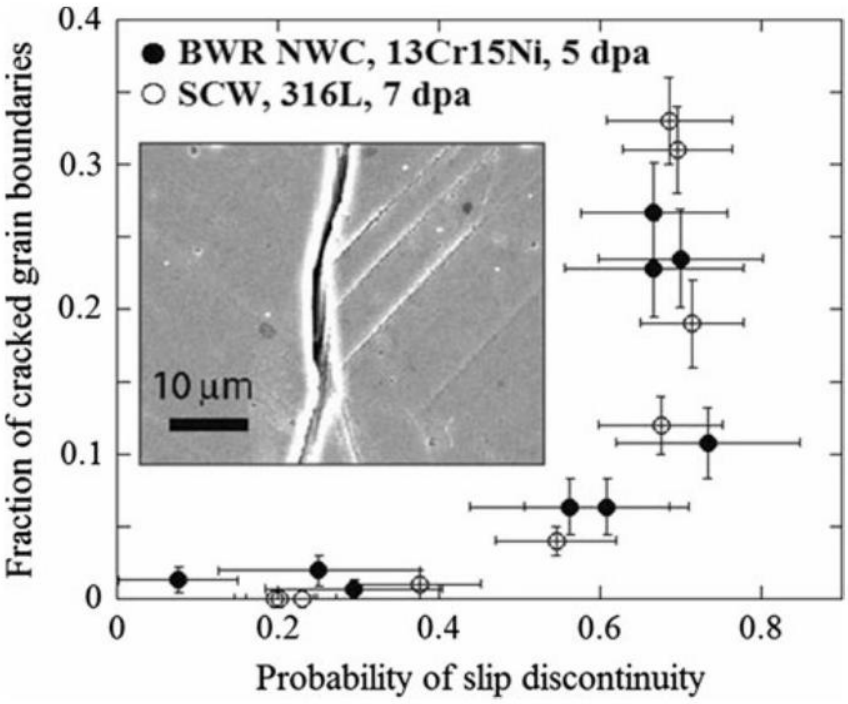

Figure 2.17. Correlation between cracking susceptibility and probability of slip transmission at GBs in proton irradiated SS. From [106].

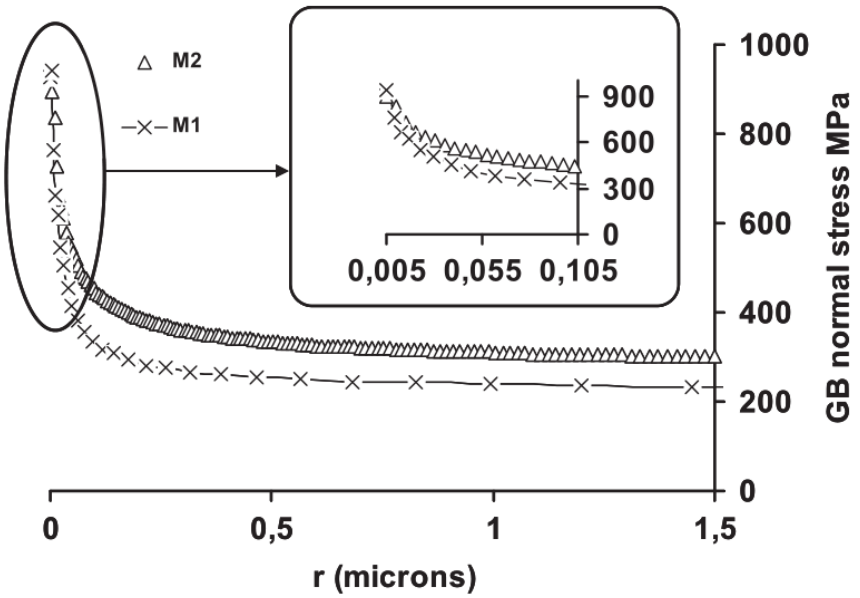

Figure 2.18. GB normal stress as a function of distance away from the DC-GB intersection. Cases M1 and M2 refer to GBs with a normal oriented 35° and 0° with respect to the tensile direction. In both cases, the channel is inclined 45° with respect to the tensile direction. From [139].

CHAPTER 3 - EXPERIMENTAL PROCEDURES

To determine the role of dislocation channeling in IASCC initiation of neutron irradiated SS, several irradiated SS alloys were compared. CERT tests were initially performed to determine general susceptibility to IASCC initiation under certain test conditions and compare dislocation channeling near IGSCC initiation sites. To better isolate factors that affect IASCC initiation, a four-point bend experiment was developed to create sites of IGSCC initiation with limited crack propagation. Four-point bend tests were performed in small stress or strain increments to analyze the sample surface up to and after the point of IASCC initiation. After crack initiation, the local microstructure and sample surface state near crack sites were carefully examined and compared. To compare dislocation channeling among the alloys of interest, four-point bend tests were also performed to similar levels of strain in a 288 °C Ar gas environment. Tests in the inert environment prevented oxide film formation and cracking, allowing a more accurate deformation comparison.

3.1 Alloy description

Three austenitic stainless steel alloys were chosen for analysis in this study: alloys AS, ES, and KS. Alloy AS was a commercial purity (CP), low carbon (L) 304 stainless steel designated CP 304L SS. Alloy ES was a high purity (HP) 18Cr-12Ni SS also with a low carbon content and a similar composition as alloy AS. Alloy KS was a HP 18Cr-25Ni SS created by re-melting a

sample of alloy ES and adding pure Ni to the melt. The compositions of these three alloys are given in Table 3.1. Additional details pertaining to the fabrication of these alloys can be found in a previous report [26].

Also included in Table 3.1 is the composition of a CP 304L alloy (heat 3E748) used for practice experiments. This material was supplied by Alro Steel Corporation as a cold drawn ¾ inch square bar. To create similar mechanical properties as irradiated alloys, this bar was further cold worked at ORNL via 2-high rolling mill with a 12 inch work face and 5 ¾ inch diameter work rolls. Sections of the material in the as-received (AR) condition and after 16.9% cold work were used for practice tests. The tensile yield strength of these conditions were 510 ± 77 MPa and 752 MPa ± 69, respectively.

The grain size of alloys AS, ES, and KS were 32 ± 5 μm, 29 ± 4 μm, and 25 ± 6 μm, respectively, corresponding to an ASTM grain size of ~7. Representative images of the microstructure of each alloy are shown in Figure 3.1. Grain structures of irradiated samples were characterized with electron backscatter diffraction (EBSD) imaging at the Oak Ridge National Laboratory (ORNL) High Temperature Materials Laboratory. A small amount of δ ferrite was observed in Alloy AS, which was not unexpected because of the increased Cr and decreased Ni content in this alloy (~5% ferrite is to be expected based on the Schaeffler diagram in Figure 2.1). Alloys were intended to be solution annealed prior to irradiation, however, deformation twins and traces of residual strain were visible in alloy ES, Figure 3.1b.

Inclusions were observed in each alloy as a result of processing, with average size and density shown in Table 3.2. Representative images of inclusions in each alloy are shown in Figure 3.2. Inclusions in alloy AS were often elongated and much larger than in HP alloys ES and KS. The

standard deviation of inclusion size was also large for alloy AS, and inclusions larger than 100 μm^2 were not uncommon. The number density of inclusions was similar for all alloys.

Inclusion composition was measured via x-ray energy dispersive spectroscopy (XEDS) in a Philips XL30 scanning electron microscope (SEM) on unirradiated samples of each alloy. Two types of inclusion were observed in alloy AS: MnS with high concentrations of Mn and S and a small amount of Cr, and oxide inclusions with similar concentrations of Mn, Cr, Ti, O and trace amounts of Al (the structure of which is hypothesized as TiO_2-MnO-Al_2O_3-Cr_2O_3 [39,43]). Both MnS and oxide inclusions are commonly observed in austenitic stainless steel [39–41]. The presence of S (in MnS inclusions) and Ti (in the oxide inclusions) were mutually exclusive to the two inclusion types, and MnS inclusions were typically larger in size than oxide inclusions (66 μm^2 vs. 25 μm^2, respectively, for 24 characterized inclusions). All inclusions in HP alloys ES and KS were oxide inclusions, and had similar compositions containing O, Cr, and Fe with traces of Mn, Ni and in some cases Si. A complete analysis of inclusion composition is included in Appendix A.

3.2 Sample irradiation

Samples of each alloy were originally fabricated as cylindrical gage tensile bars at Pacific Northwest National Laboratory (PNNL). After fabrication, samples were shipped to Dimitrovgrad, Russia, where irradiation was performed in the BOR-60 reactor.

Irradiations in the BOR-60 liquid sodium fast reactor were completed between 2001 and 2004 at an irradiation temperature of 320 °C. Neutron flux was ~1.8×10^{15} $n \cdot cm^{-2} \cdot s^{-1}$ (E > 0.1 MeV), corresponding to a damage rate of 9.4×10^{-7} $dpa \cdot s^{-1}$ (E > 0.1 MeV) calculated using the NRT

model [24]. Tensile bar sample IDs and doses used in this study are listed in Table 3.3, and further details of the irradiation procedure are specified in ref. [24]. After irradiation, samples were shipped to ORNL for post-irradiation sample preparation.

3.3 Autoclave system and test conditions

SCC tests were performed in the IM1 autoclave system in the Irradiated Materials Testing Laboratory (IMTL) at the University of Michigan. Samples were deformed at a slow strain rate ($3.5x10^{-7}$ s^{-1}) to provide adequate time for corrosion processes to cause SCC susceptibility.

The high pressure Inconel 625 autoclave (supplied by Cortest, Inc.) and water loop for SCC testing are diagrammed in Figure 3.3, and images of the IM1 test system are shown in Figure 3.4. Water flows from the primary water column where chemical solutions are added with a peristaltic pump and gas overpressures are applied. Water is pressurized with a Pulsafeeder® high pressure pump and flows at 200 mL/min through the autoclave. The autoclave is heated by two 1800 W Watlow® heating bands at the autoclave surface. Water exiting the autoclave heats the inlet water by flowing through a tube-in-tube heat exchanger and is further cooled by a second tube-in-tube heat exchanger connected to a chiller system. Pressure in the autoclave is maintained by a Tescom® back pressure regulator before returning to atmospheric pressure and flowing back to the primary water column. Temperature is monitored and controlled within the autoclave using a K-type thermocouple. Inlet and outlet water dissolved oxygen (DO) and conductivity are monitored continuously with Orbisphere® 31110 oxygen sensors and conductivity sensors supplied by Omega®, respectively.

The IM1 loading system is capable of straining up to four samples simultaneously. Load is applied by a 5K Interactive Instruments servo-motor which displaces the system crosshead. Crosshead displacement is measured with a Solartron® linear variable differential transformer (LVDT). Four independent Inconel 718 pull rods connected to the crosshead apply load to each sample and are sealed at the inlet to the autoclave with self-energizing graphite Bal® seals. Load at each pull rod is measured with Transducer Techniques® 1000 lbf load cells. Because load is applied to all samples with the same crosshead, individual sample failures can cause small load shifts on adjacent samples.

The autoclave is sealed by lowering the body onto the head assembly. A deformable Inconel 625 gasket between the autoclave had and body creates the seal. A hydraulic Pivicat™ flange tensioner applies pressure of 70-90 MPa to reaction nuts threaded to the tops of 12 Nitronic 50 bolts, which pass through two flanges on both the autoclave head and body. This pressure compresses the deformable gasket, and allows flange nuts threaded also to the Nitronic bolts to be tightened equally before releasing the Pivicat pressure.

For the duration of each experiment, all data was recorded once per minute using a LabView™ data acquisition program. Recorded data includes inlet and outlet pressure, inlet and outlet water conductivity, inlet and outlet dissolved oxygen, vessel internal and surface temperature, LVDT displacement, and the load at each pull rod. Electrochemical potential (ECP) was measured between a Cu/Cu_2O reference electrode and two working electrodes: a 1 cm^2 Pt flag, and a type 304L SS tensile bar. Raw potential measurements between each working electrode and the reference were converted to the potential versus the standard hydrogen electrode by subtracting 0.273 V.

Experiments were performed in a simulated 288 °C BWR NWC environment as detailed in Table 3.5 or in pure 288 °C Ar. For water tests, system pressure was maintained at ~10.3 MPa, to keep water in the liquid phase. The target outlet conductivity was maintained by adding dilute H_2SO_4 to the primary water column. The target dissolved oxygen concentration was achieved by adding a mixture of 4.9% O_2/Ar gas in the main water column with ~0.1 atm overpressure. Tests in 288 °C Ar utilized 99.999% purity Ar gas that was further purified with a 27601-U Supelco® purifier at the autoclave inlet. No system pressure was applied in the Ar environment, and gas flow was regulated to achieve visible flow through an airlock at the autoclave outlet.

3.4 Constant extension rate tensile test procedure

CERT tests were used to assess relative IASCC susceptibility of each alloy in NWC. Tensile bar samples for CERT tests were fabricated prior to irradiation with the geometry shown in Figure 3.5. Before SCC testing, sample surfaces were polished to a mirror finish at the Low-Activity Materials Development and Analysis (LAMDA) Lab at ORNL. Mechanical polishing was performed by hand using 320 grit SiC grinding paper to remove residual surface contamination from irradiation. Electrochemical polishing was then performed in the A2 solution supplied by Struers™ (9% distilled water, 73% ethanol, 10% ethylene glycol monobutyl ether, and 8% perchloric acid), cooled to below 20 °C in an ice bath. Electrochemical polishing was performed at an applied potential of 30 V between the sample and a stainless steel cathode submersed in the A2 solution. Four separate 15 sec intervals were applied to each sample to achieve the final finish.

After sample surface preparation, tensile bars were loaded into Inconel 625 loading fixtures (shown in Figure 3.6) installed in the IM1 test system. The loading fixtures applied load at the tensile bar shoulders to avoid premature SCC failure at pinhole loading locations, and were electrically insulated from the pull rod with zirconia washers supplied by Coorstek® Ceramics. After loading the samples, sealing the autoclave, and achieving NWC conditions, the environment was allowed to stabilize for 72 hrs. Prior to straining, a pre-load of ~20 MPa was applied to each specimen by manually tightening pull rod connections at the crosshead. Tensile bar samples were strained in tension until failure without interruption. A crosshead displacement rate of 1.65×10^{-7} in/s was used for CERT experiments, corresponding to a sample strain rate of 3.5×10^{-7} s^{-1}.

3.4.1 Stress-strain analysis

Plots of engineering stress vs. engineering strain were created to compare the mechanical behavior of each sample. Before comparison, load and crosshead displacement data were adjusted to account for system pressure and compliance, respectively. These steps were necessary because direct sample measurements were not possible in the high temperature environment.

To correct tensile load for system pressure, tare stress was added to each load cell measurement. The value of the tare stress, 58.6 MPa, was determined by calculating the force applied to the 4.76 mm diameter pull rod by the 10.3 MPa system pressure.

To correct system compliance, the raw stress-strain curve was plotted to determine the apparent modulus, generally ~10,000 MPa. Crosshead displacement values were converted to strain by dividing the change in displacement by the original specimen gage section length (12 mm). The

apparent modulus was determined by fitting a linear trend line in the linear elastic region of the curve. A good linear fit (i.e., R^2 value minimum of 0.999) was created by eliminating data points at low stress. The apparent modulus was then divided by the reported modulus for type 304 SS at 300 °C, 166.3 GPa [142]. The resulting ratio was multiplied by the apparent strain up to the yield point. This method is consistent with the general definition of compliance: the change in length due to compliance is equal to the observed change in length less the force divided by the system stiffness, where stiffness is equal to either: force divided by the change in length, or system modulus multiplied by cross sectional area divided by original length [143]. Plastic strain data was continued from the yield point by subtracting the difference in strain between the original strain and the compliance corrected strain, and no compliance correction was applied during plastic elongation. A comparison between raw and compliance corrected stress-strain curves is shown in Figure 3.7.

After correcting for system pressure and compliance, several values were determined from the stress-strain curve. Yield stress (YS) was recorded as the 0.2% offset YS if strain hardening was observed. In the case of strain softening, YS was taken to be the maximum stress. Uniform elongation (UE) was recorded as the strain at which the maximum stress occurred. Total elongation (TE) was recorded as the strain at the point of fracture.

3.4.2 Fractography

Fractography was performed following CERT testing using a JEOL JSM-6480 SEM. Tensile bar gage and fracture surfaces were examined in detail, and the nature of failure was characterized. Samples showed combinations of ductile, intergranular (IG), transgranular (TG), or mixed mode

IG/TG cracking. Areas of IG, TG or mixed IG/TG fracture were determined and expressed as an area-based percentage of the total fracture surface.

3.4.3 Oxide removal

Corrosion product formed during SCC testing was removed to accurately characterize surface topography. The procedure consisted of two subsequent soaks in water-based solutions: 100 g/L sodium hydroxide with 30 g/L potassium permanganate, and 100 g/L ammonium oxalate. Both solutions were heated to ~95 °C and samples were soaked for 5 minutes in each, rinsing and ultrasonically cleaning after each step. The process was repeated until all oxide was visibly removed, and had a minor effect on surface feature height, causing a 17 ± 33 nm variation for features ranging 300 – 3000 nm.

3.4.4 Step height measurement

To measure step height on irradiated samples, replicas were made of tensile bar surfaces using the Microset® 202 replication compound. The difference in feature height between the replica and original sample was 11 ± 23 nm for features in the height range of 100 – 600 nm. Surface topography was measured with an Olympus® LEXT OLS4000 3D laser confocal microscope in the Lurie Nanofabrication Facility at the University of Michigan. Areas close to the IG fracture edge (the assumed point of crack initiation) were analyzed including grains with only one visibly active slip system, as the step height is typically smaller in grains with multiple active slip systems. Areas within the necked region of the tensile bar were avoided, where excessive deformation was present. A minimum of 10 grains were measured on each sample, unless fewer

channels were observed. In most grains, several measurements were taken over the length of a single channel averaged for accuracy.

Using a technique similar to Jiao [9], the weighted average step height, $\bar{h}$, was calculated from the individual step height measurements:

$$\bar{h} = \frac{\sum_{i=1}^{n} h_k^2}{\sum_{i=1}^{n} h_k} , \qquad (3.1)$$

where *h* is the height of the *k*th DC. This value emphasizes larger channels and typically yields a value higher than the mathematical average. Larger channels were highlighted because of their likely influence on cracking.

To determine error in $\bar{h}$, the central limit theorem was applied by generalizing the equation for $\bar{h}$:

$$\bar{\mathrm{h}} = \frac{\overline{\mathrm{h}^{\mathrm{n+1}}}}{\overline{\mathrm{h}^{\mathrm{n}}}}, \quad \mathrm{n} = 1 \qquad (3.2)$$

where $\overline{\mathrm{h}^{\mathrm{n}}}$ and $\overline{\mathrm{h}^{\mathrm{n+1}}}$ are the mean values of *h*:

$$\overline{\mathrm{h}_{\mathrm{K}}^{\mathrm{n}}} = \frac{1}{\mathrm{K}} \sum_{\mathrm{k}=1}^{\mathrm{K}} \mathrm{h}_{\mathrm{k}}^{\mathrm{n}} , \qquad (3.3)$$

$$\overline{\mathrm{h}_{\mathrm{K}}^{\mathrm{n+1}}} = \frac{1}{\mathrm{K}} \sum_{\mathrm{k}=1}^{\mathrm{K}} \mathrm{h}_{\mathrm{k}}^{\mathrm{n+1}} , \qquad (3.4)$$

and *K* and *k* represent the total number of measurements and the *k*th measurement, respectively. Standard deviations of each $\overline{h^{n}}$ and $\overline{h^{n+1}}$ could then be calculated using the traditional definition of the sample standard deviation:

$$\sigma_{n,K}^{2} = \frac{1}{K-1}\sum_{1}^{K}\left(h_{k}^{n} - \overline{h_{K}^{n}}\right)^{2} , \qquad (3.5)$$

$$\sigma_{n+1,K}^{2} = \frac{1}{K-1}\sum_{1}^{K}\left(h_{k}^{(n+1)} - \overline{h_{K}^{n+1}}\right)^{2} . \qquad (3.6)$$

Using the following inequalities derived from the central limit theorem, the confidence interval of $\bar{h}$ was derived:

$$\left|\overline{h_{k}^{n}} - \overline{h^{n}}\right| \leq \frac{\sigma_{n,K}}{\sqrt{K}} , \qquad (3.7)$$

$$\left|\overline{h_{k}^{n+1}} - \overline{h^{n+1}}\right| \leq \frac{\sigma_{n+1,K}}{\sqrt{K}} , \qquad (3.8)$$

Using the definition of $\bar{h}$ (equation 3.1), equation 3.8 was substituted as the numerator, and equation 3.7 as the denominator. The range of error was then calculated by expanding the central limit theorem to derive the confidence window for $\bar{h}$:

$$\frac{\overline{h_{K}^{n+1}} - \frac{\sigma_{n+1,K}}{\sqrt{K}}}{\overline{h_{K}^{n}} + \frac{\sigma_{n,K}}{\sqrt{K}}} < \bar{h} < \frac{\overline{h_{K}^{n+1}} + \frac{\sigma_{n+1,K}}{\sqrt{K}}}{\overline{h_{K}^{n}} - \frac{\sigma_{n,K}}{\sqrt{K}}} \qquad (3.9)$$

3.5 Four-point bend test procedure

The four-point bend test procedure was selected to perform additional SCC tests and form a better understanding of factors affecting the IASCC initiation process. The bend test creates a stress gradient through the sample thickness such that cracks grow into a progressively decreasing tensile stress, slowing crack propagation and preserving the sample beyond formation of the first crack. This test type was selected over similar bend test types (3 point bend, shear punch), as it creates a region of uniform uniaxial strain [144], similar to the state induced in the uniaxial CERT test. Furthermore, the area of uniform strain enhances the possibility of observing multiple crack initiation sites on a single sample.

3.5.1 Sample preparation

Four-point bend samples were created from the ends of tensile bars in the LAMDA facility. Samples ~1 mm thick were cut perpendicular to the tensile bar length using a Buehler™ slow speed saw with an abrasive diamond blade, as indicated in Figure 3.8. Samples were mechanically thinned to a target thickness of 800 µm and electro-polished on one side prior to SCC testing. A Buehler Mini-met 1000™ sample grinding and polishing tool performed sample thinning to a target thickness of 800 µm; using 120, 180, and 340 grit SiC grinding paper on each side to achieve a uniform thickness (final thickness variations were less than 10 µm). One side of each sample was then polished with a 3 µm nylon pad in the Mini-met™ and subsequently electrochemically polished in a Struers LectroPol-5™ system. One electrochemical polishing step was applied for 15 sec at a potential of 30 V at 20 °C in the A2 solution. Parent tensile bar ID, bend sample ID, dose, and thickness are presented in Table 3.4.

3.5.2 Finite element analysis

Abaqus™ finite element analysis (FEA) software was used to design an optimized four point bend loading fixture and determine the expected stress-strain distribution on the sample surface. A simplified model of the four-point bend setup was created using Solidworks™ computer-aided design (CAD) software. Loading points and supports were assumed as round cylinders with a length of 4 mm, extending beyond the bend sample width. Below-sample supports were spaced 3.5 mm apart, just less than the maximum allowable spacing based on the sample geometry.

Several assumptions were made when creating boundary conditions for the FEA model. Loading points and below-sample supports were created as un-deformable rigid bodies, and a coefficient of friction equal to 0.36 was applied to all interaction locations. The coefficient of friction was unable to be measured experimentally, therefore it was chosen such that strain distributions in the FEA model were comparable with those measured in practice tests. The FEA model mesh size was chosen for optimized accuracy and efficiency by comparing model results when using a mesh size of 10, 18, and 22 elements per mm. As mesh size decreases, stress and strain values converge, but the simulation slows due to the increased number of calculations. A 2.2% difference in strain between the smallest two mesh sizes was observed, therefore a mesh size of 18 elements per mm (~56 μm per element) was used for all simulations.

Two material conditions were compared in the simulation, based on the tensile stress-strain behavior of the unirradiated AR and 16.9% cold worked 304L SS alloy. The modulus of these two conditions was that for type 304 SS at 300 °C, 166.3 GPa [142], the Poisson's ratio was 0.3, and the density was 7.8 g/cm^3. The respective yield strength and strain hardening coefficients were determined from tensile tests performed in the IM1 test system. The AR and 16.9% CW

conditions had yield strength of 445 and 783 MPa, and strain hardening coefficients 4.5 and 7.5 GPa, respectively.

Simulations compared the effects of varying the diameter of the loading points and their spacing to determine the optimal fixture design. The final loading geometry was capable of creating a region of uniaxial tensile strain up to ~3%, an amount sufficient to induce cracking in the neutron-irradiated conditions based on the results from CERT tests [28]. Additional simulations assessed the effects of experimental errors including: an off-centered sample, off-centered central loading points, and variations in sample thickness.

3.5.3 SCC test procedure

A loading fixture was fabricated in accordance with the schematic in Figure 3.9. Fixture components were fabricated out of solution annealed Inconel 718, which was heat treated after fabrication to achieve a hardened state and prevent deformation during bend testing. Heat treatment was performed in 99.999% purity Ar gas by aging for 8 hours at 720 °C, furnace cooling to 620 °C and aging at this temperature for another 10 hours. After aging, parts were cooled in air. The heat treatment caused the hardness of the fixture material to increase from 199 HV to 443 HV.

Bend tests were performed in the IM1 test system described previously. Although the system is capable of straining up to four samples at once, bend tests were performed individually. Samples were loaded into the fixture using tweezers with the mirror-finish surface facing downward, between four centering pins which prevented rotational misalignment. Set screws centered the

sample laterally, the load train was manually tightened, and the set screws were retracted prior to the experiment to prevent constraint.

The autoclave was sealed, pressurized (if performing an experiment in NWC) and heated to 288 °C for experiments in either Ar or NWC. The system was allowed to stabilize for a six hour period after temperature stabilization. During this period, conductivity control (for experiments in NWC) was initialized once the vessel conductivity dropped below 0.1 µS/cm. After stabilization, the connection of the pull rod at the loading crosshead was tightened manually, and straining was started. A crosshead displacement rate of $1.3x10^{-7}$ in/s created a sample strain rate of $3.5x10^{-7}$ s^{-1}.

A series of practice tests were performed on unirradiated 304L samples to ensure that the intended stress-strain condition was created prior to performing experiments on neutron irradiated samples. Practice bend tests were first performed in room temperature (RT) air on samples at both levels of CW, utilizing direct sample deflection measurement as well as DIC for surface strain measurement. One sample of each unirradiated condition (AR and after 16.9% CW) was tested, stopping the experiment after pre-determined increments to record surface strain. Increments were stopped at sample deflections of 20, 30, 40 and 50 µm on an AR condition sample, and at deflections of 30, 40, 50, and 60 µm on a 16.9% CW condition sample. Three additional bend tests (each using previously un-tested samples) on the unirradiated 16.9% CW condition were performed to a nominal sample deflection of 40 µm. These three bend tests were performed in RT air, 288 °C Ar, and 288 °C NWC to confirm strain distributions in the three environments, and compare strain distributions with those from the incremented bend tests.

Bend tests on irradiated samples were only conducted in 288 °C Ar gas or 288 °C NWC. All tests were initially stopped at ~40%-70% of the irradiated yield strength, and the sample was removed from the test system to characterize the surface for cracks. Additional stress or strain increments were applied in subsequent tests up to the point of crack initiation. The magnitude of stress (for tests pre-macroscopic yield) or strain (for tests beyond macroscopic yield) increments were based on prior knowledge of IASCC behavior [28], i.e., smaller increments were applied for materials with high IASCC susceptibility. After achieving target stress or strain, the sample was unloaded. Tare load was measured prior to cooling the autoclave for each experiment in NWC, by moving the loading points out of contact with the bend sample. The compressive load due to water pressure was then measured, which typically had a value between 155-175 N. The autoclave was then cooled to room temperature and the sample removed for examination. If additional straining was necessary, the bend test procedure was repeated.

3.5.4 Bend deflection measurement

Sample bend deflection was measured during experiments in RT air with a microminiature DVRT® (differential variable reluctance transducer) supplied by LORD Microstrain®. The operation of the DVRT is similar to an LVDT, and sample deflection was measured by mounting the DVRT vertically with a spring-loaded plunger in contact with the center of the bend sample.

Direct sample bend deflection measurement was not possible in high temperature Ar or NWC environments due to limitations of the DVRT, therefore estimations of sample deflection were made by subtracting a load dependent compliance correction factor from the crosshead deflection measurement. A compliance correction factor was determined in both 288 °C Ar and 288 °C NWC, by loading a ~10 mm thick ‘bend’ sample with the same cross-sectional geometry as

actual bend test samples. Due to its large thickness, it was assumed that no sample deflection occurred during loading, and compliance correction curves were determined by fitting a second order polynomial to the resulting load vs. crosshead displacement curve in each test environment. The thick sample was loaded three times in each environment, and data was averaged for accuracy. The following correction factors were determined in 288 °C Ar:

$$\mathrm{CF_{Ar}} = -6.57\times10^{-5}\mathrm{P}^2 + 0.493\mathrm{P} - 15.8\ , \qquad (3.10)$$

and in 288 °C NWC:

$$\mathrm{CF_{NWC}} = -5.56\times10^{-5}\mathrm{P}^2 + 0.460P - 24.6\ , \qquad (3.11)$$

where P is the applied load in N and CF_i is the correction factor in environment i in μm. The correction factor subtracted from the crosshead deflection yields the sample bend deflection.

3.5.5 Stress measurement

Applied load during four-point bend tests was used to determine the effective stress at the bend sample surface when testing irradiated samples. FEA results were considered to determine the stress state at the bend sample surface. During elastic bending, the stress state was not purely uniaxial, especially in the center of the sample, where stress in the transverse direction (σ_{yy}, as designated according to Figure 3.10) was approximately 30% of the tensile stress (σ_{xx}). As a result, the effective stress (σ_{eff}) on the bend sample surface was calculated according to the von Mises formulation:

$$\sigma_{eff} = 1/\sqrt{2}\left[\left(\sigma_{xx}-\sigma_{yy}\right)^2+\left(\sigma_{yy}-\sigma_{zz}\right)^2+\left(\sigma_{zz}-\sigma_{xx}\right)^2+6\left(\sigma_{xy}^2+\sigma_{yz}^2+\sigma_{xz}^2\right)\right]^{1/2}\ , \qquad (3.12)$$

where σ_{ii} represent stresses in the principal directions and σ_{ij} represent shear stresses [57]. Analyzing σ_{eff} on the bend surface in the FEA model revealed that its value was relatively constant in the region between the two loading points across the entire sample width, with standard deviation less than 2% of σ_{eff} during elastic bending. Therefore, the correlation between σ_{eff} and P_b was used to determine the applied stress during elastic bending, shown in Figure 3.11:

$$\sigma_{eff} = m \cdot P_b \,, \qquad (3.13)$$

where m is the slope of the correlation (1.53 MPa/N), and P_b is the load applied in the bend test.

Error bounds on the effective stress were determined by considering factors affecting the stress on the bend sample surface: elastic modulus, geometry of the loading fixture, and sample dimensions. Elastic modulus and loading fixture geometry were constant, therefore sample width and sample thickness were the only parameters considered to affect σ_{eff}. Sample width did not drastically effect σ_{eff}, as small variations (±50 µm) only caused minor variation in effective stress (±~1.5%) at any value of P_b. Therefore, sample width was not factored into the magnitude of the error bounds. Sample thickness had a more considerable effect. A standard deviation in sample thickness was calculated based on the bend sample thicknesses in Table 3.4, 26.5 µm, which resulted in a variation of ±6.2% in σ_{eff} at all values of P_b. This variation, being the most prominent source of error, constituted the error bounds in Figure 3.11. Error due to limitations in load cell non-repeatability (4.4 N) and tare load measurement (~9.4 N) were considered to be negligible.

The four-point bend test was repeated on multiple samples of the same condition to confirm factors affecting crack initiation and improve statistics, therefore, it was necessary to average the stress for crack initiation for a particular sample condition. Four-point bend tests were conducted

in discrete stress intervals, therefore, the stress required for crack initiation on a sample was estimated by averaging the stresses of bend tests ended before and after observation of a crack:

$$\sigma_{CI,sample} = \frac{\sigma_{pre-crack} + \sigma_{crack}}{2}, \qquad (3.14)$$

where $\sigma_{CI,sample}$ is the crack initiation stress for a particular sample and $\sigma_{pre\text{-}crack}$ and σ_{crack} are the maximum stress applied before crack initiation and the stress applied when a crack formed, respectively. Error on the crack initiation stress was calculated for each sample by applying the error propagation technique, also including a term for the error due to the size of the increment between observations:

$$\varphi_{CI,sample} = \sqrt{\frac{1}{2^2}\varphi^2_{pre-crack} + \frac{1}{2^2}\varphi^2_{crack} + \varphi^2_{interval}}, \qquad (3.15)$$

where $\varphi_{CI,sample}$ is the total error considering errors in the stress before crack initiation, $\varphi_{pre\text{-}crack}$, after crack initiation, φ_{crack}, and the magnitude of the stress increment $\varphi_{interval}$ ([σ_{crack} - $\sigma_{pre\text{-}crack}$]/2). Covariance was not considered as the stress error and interval magnitude error were independent.

When considering multiple samples of the same material condition, crack initiation stresses were averaged to determine the average crack initiation stress for a particular condition, $\sigma_{CI,condition}$:

$$\sigma_{CI,condition} = \frac{1}{N}\sum_{i=1}^{N}\left(\sigma_{CI,sample}\right)_i. \qquad (3.16)$$

Error on $\sigma_{CI,condition}$ was calculated using the error propagation technique, but also considering the standard deviation among $\sigma_{CI,sample}$ for each condition:

$$\varphi_{CI,condition} = \sqrt{\frac{1}{N^2}\sum_{i=1}^{N}\left(\varphi_{CI,sample}\right)_i^2 + \varphi_{stdev}^2} \quad . \qquad (3.17)$$

3.5.6 Strain measurement

Digital image correlation (DIC) was used to measure permanent strain on bend sample surfaces in four-point bend tests on unirradiated materials in RT air and 288 °C Ar. The DIC technique determined local strains by comparing images (taken under identical imaging conditions) of a high contrast speckle pattern recorded before and after deformation. Speckle patterns were applied using high-temperature RustOleum™ spray paint (exemplified in Figure 3.12), and images of bend sample surfaces were recorded with a Fujifilm® Finepix™ S7000 digital camera through a 4x magnification stereoscope. A Matlab® script created by McMurtrey et al. [14] was used to create strain maps from the images, and average surface strain was determined by averaging strain measurements in the center 500 x 500 μm region of the bend sample (where uniform strain was expected based on FEA results).

An alternative DIC method was used for measuring surface strain in bend tests performed in NWC, due to instability of the paint speckle pattern in the high temperature water environment. An array of microhardness indents was applied to the bend sample surface prior to deformation, spaced ~100 μm apart. Relative indent locations were compared before and after deformation, to determine associated strain between indentations.

Neither speckle pattern DIC nor the indent spacing DIC technique was used on irradiated samples to prevent altering material-environment interactions and avoid the creation of surface defects that could possibly have formed SCC initiation. Therefore, surface strain was estimated by determining a correlation between the xx component of plastic strain (indicated in Figure

3.10) and post-yield sample deflection. This correlation was validated by results of FEA analysis, as the majority of strain on the bend sample surface was concentrated in the xx direction. Results from practice four-point bend tests on the unirradiated 16.9% CW 304L SS were used to determine the correlation shown in Figure 3.13. A least squares fitting technique was applied to determine the slope of the fit, forcing the fit through the origin, as only plastic strain and post-yield deflection were considered (which both approach zero simultaneously), which resulted in the following relationship:

$$\varepsilon_{xx} = m \cdot \delta_p \tag{3.18}$$

where ε_{xx} is the plastic strain, δ_p is the plastic deflection, and m is the slope of the fit (0.00119/μm).

A confidence interval on the plastic strain estimated in this manner, φ_ε, was determined using the error propagation method on Equation 3.16:

$$\varphi_\varepsilon = \sqrt{\left(\frac{\partial \varepsilon_{xx}}{\partial m}\right)^2 \varphi_m{}^2 + \left(\frac{\partial \varepsilon_{xx}}{\partial \delta}\right)^2 \varphi_\delta{}^2} \tag{3.19}$$

where φ_m is the error on the fit of the slope (±0.000144/μm , calculated using the 95% confidence interval on the linear fit calculated using the linear regression tool in Microsoft Excel), and φ_δ is the error in the deflection measurement (3 μm, the difference between the measured sample deflection and that calculated from the compliance correction factor). The following equations represent the respective upper and lower bounds of the confidence interval:

$$\varepsilon_{xx} = 0.00125P_b + 0.00357 \quad \textit{and} \tag{3.20}$$

$$\varepsilon_{xx} = 0.00113P_b - 0.00357 . \tag{3.21}$$

3.5.7 Bend sample imaging

After each bend test, the bend surface was imaged with a JEOL JSM-6480 SEM. Examination was performed with the sample oriented as shown in Figure 3.10, where strain (ε_{xx}) was primarily concentrated along the longitudinal axis. Both secondary electron (SE) and backscatter electron (BSE) imaging modes were used to record the center ~1500 μm of the sample along the length of the transverse axis at a low magnification setting, 250x. Crack locations and regions of interest were recorded at higher magnification (typically, ~1000x). Several samples were subjected to the oxide removal procedure described in section 3.4.3 to more carefully observe crack initiation sites.

Channeling was clearly visible when imaging the bend sample surface in the BSE mode, allowing quantification of channel and slip transmission site density. Slip transmission sites were recognizable by a sharp change in the DC at a GB, exemplified in Figure 3.14. Channels that did not transmit across a GB were termed 'discontinuous channels.' Channel characterization was performed in the center 500 μm of the sample along the length of the transverse axis.

Steps formed by DC intersection with sample surfaces were analyzed on several samples using a similar technique as described previously in section 3.4.4. Step heights were measured on replicas created from bend sample surfaces with Microset® 202 replication compound.

XEDS was used to characterize surface oxidation on several samples. Unirradiated material was characterized using the JEOL XL30 SEM at the Electron Microscopy Analysis Laboratory at the University of Michigan. Irradiated material was characterized in the FEI™ Versa 3D SEM in LAMDA at ORNL.

Table 3.1. Chemical compositions of alloys for study, in wt%.

Heat ID	Material	Fe	Cr	Ni	Mn	Mo	Si	C	Ti	P	S	N	Nb	O	Co	Cu
AS	CP 304L SS	bal.	19.95	10.80	1.82	0.53	0.56	0.023	0.02	0.02	0.015	0.072	<0.001	0.011	0.22	0.29
ES	HP 304 SS	bal.	18.76	12.37	0.94	0.04	0.04	0.021	0.01	<0.01	0.003	0.000	0.005	0.004	0.01	<0.01
KS	HP 304 SS (+Ni)	bal.	18.21	25.08	1.00	0.02	0.03	0.020	0.01	<0.01	0.002	0.001	<0.001	0.003	0.01	<0.01
3E748	CP 304L SS	bal.	18.10	8.01	1.68	0.15	0.34	0.021		0.03	0.027	0.084				

Table 3.2. Inclusions in alloys used in this study.

Alloy	No. Density, mm^{-2}	Avg. Size, μm^2	Type
AS	126 ± 2	16.1 ± 7.9	MnS, Oxide
ES	125 ± 5	3.4 ± 1.5	Oxide
KS	155 ± 6	3.5 ± 1.6	Oxide

Table 3.3. Tensile bar samples and irradiation doses.

Sample ID	Dose, dpa
AS14	5.5
AS17	10.2
AS18	10.2
AS19	10.2
AS22	47.5
AS23	47.5
ES16	10.2
ES21	10.7
KS13	9.6

Table 3.4. Samples for four-point bend SCC testing.

Parent Tensile Sample ID	Bend Sample ID	Dose, dpa	Thickness, μm
AS14	AS01	5.5	825
AS14	AS02	5.5	797
AS14	AS03	5.5	839
AS14	AS04	5.5	801
AS18	AS05	10.2	813
AS19	AS06	10.2	796
AS17	AS07	10.2	791
AS19	AS08	10.2	777
AS22	AS09	47.5	807
AS23	AS10	47.5	729
ES16	ES01	10.2	770
ES21	ES02	10.7	804
KS13	KS01	9.6	806
KS13	KS02	9.6	815

Table 3.5 BWR NWC test conditions.

Parameter	Value
Temperature	288 °C
Conductivity	0.2 µS/cm
O_2 concentration	2000 ppb
ECP (SHE)	> 140 mV_{SHE}

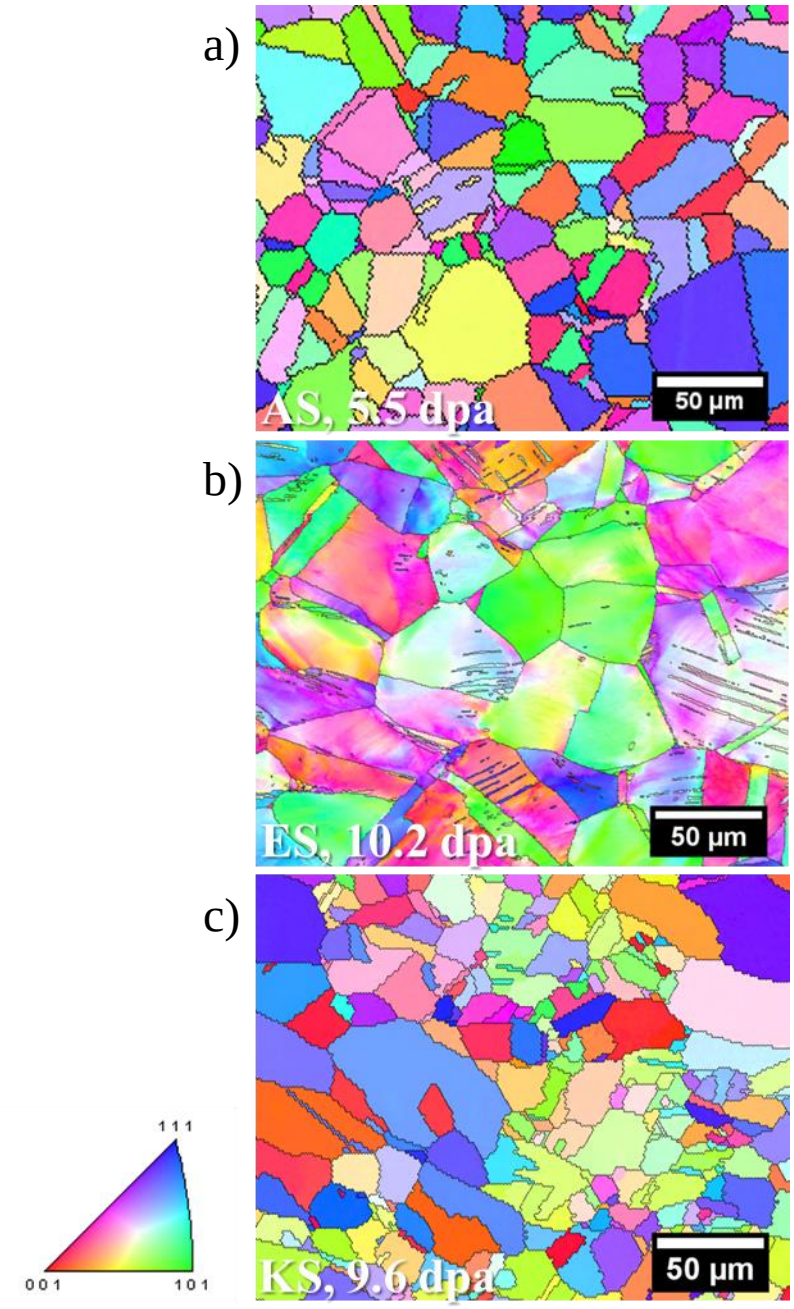

Figure 3.1. Representative images of alloy microstructures as well as inclusions present in a) alloy AS (CP 304L), b) alloy ES (HP 304L), and c) alloy KS (HP 304L+Ni).

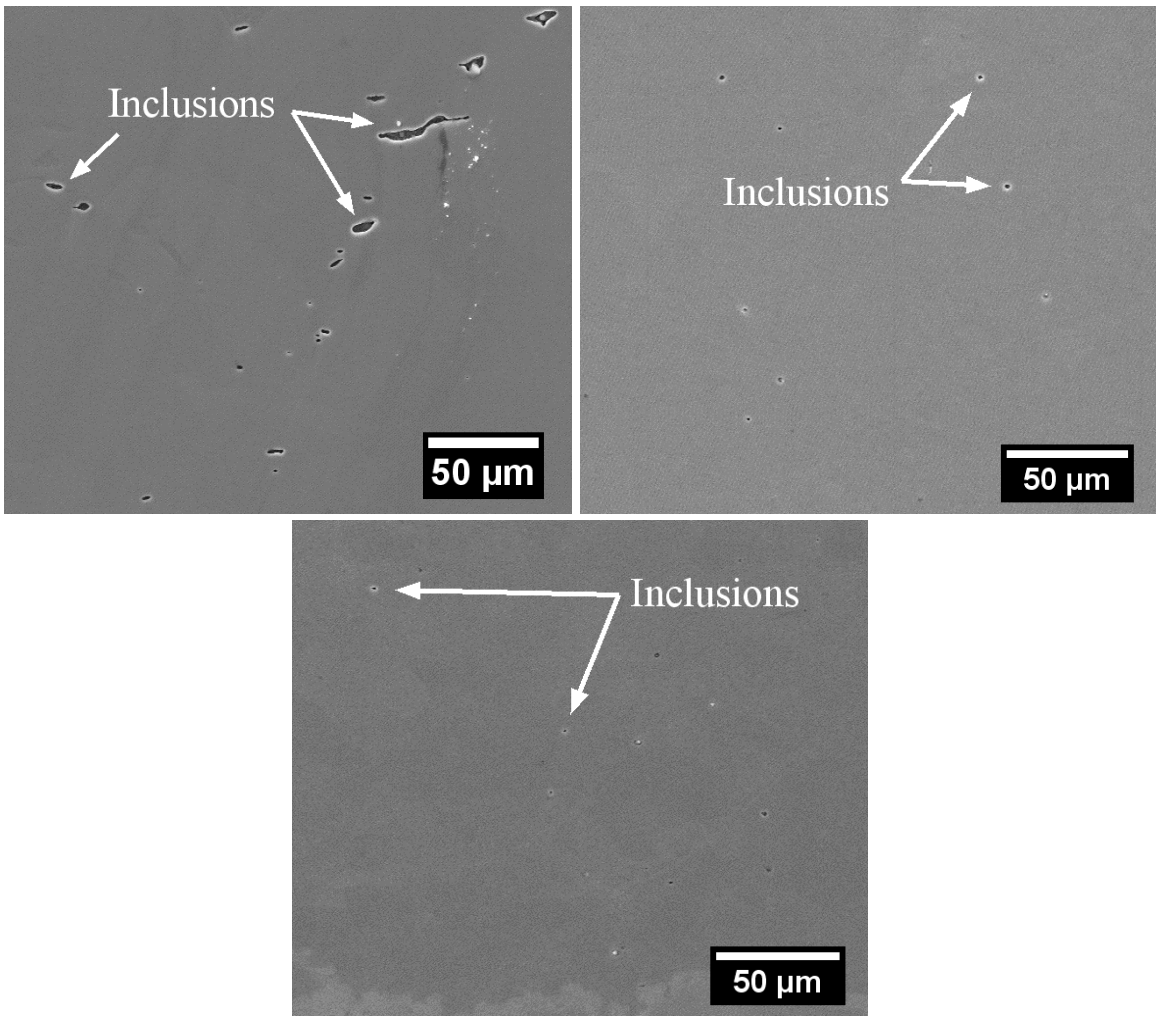

Figure 3.2. Representative images of inclusions in a) alloy AS (CP 304L), b) alloy ES (HP 304L), and c) alloy KS (HP 304L+Ni).

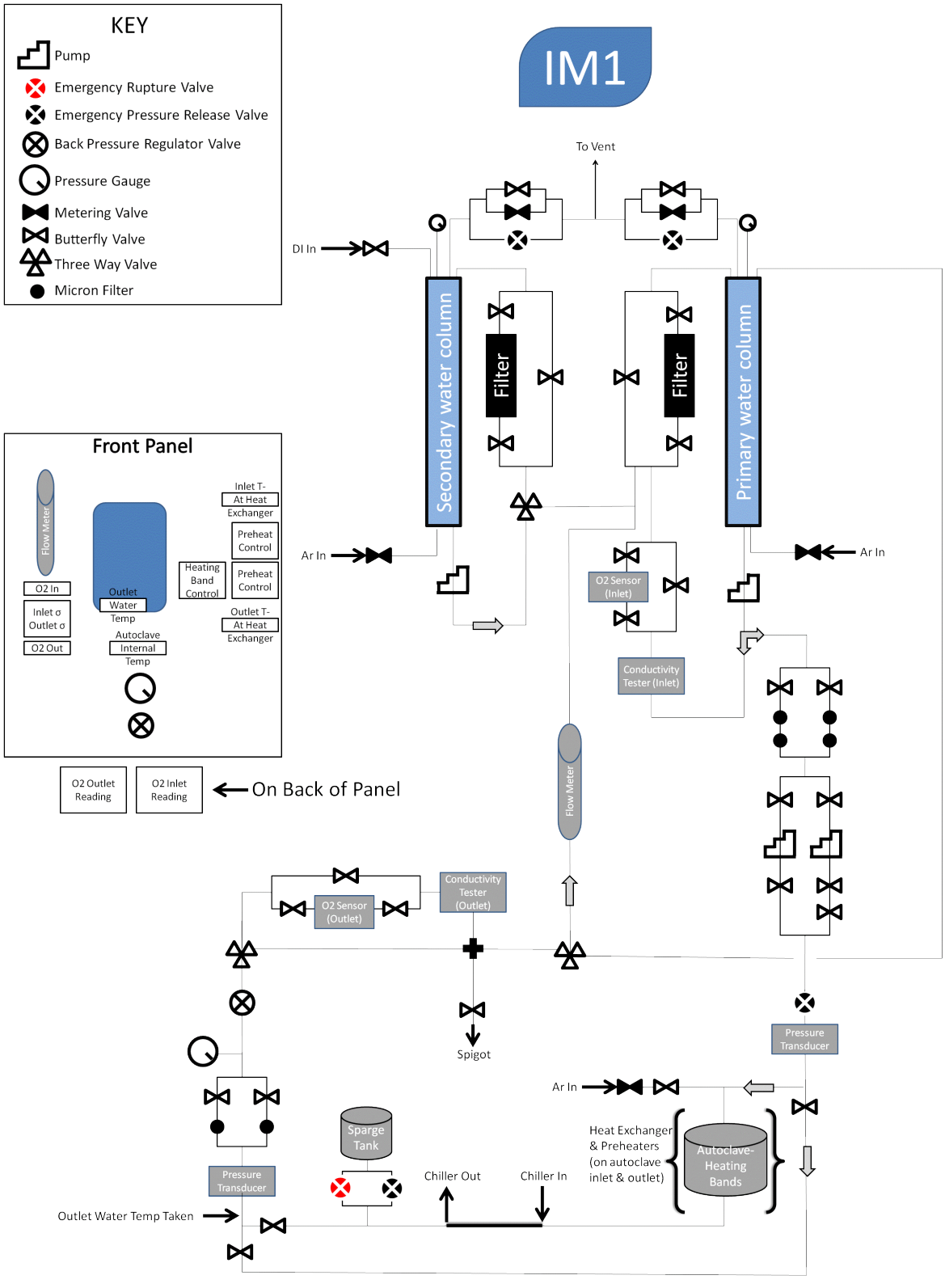

Figure 3.3. Schematic of the IM1 closed water loop and autoclave system.

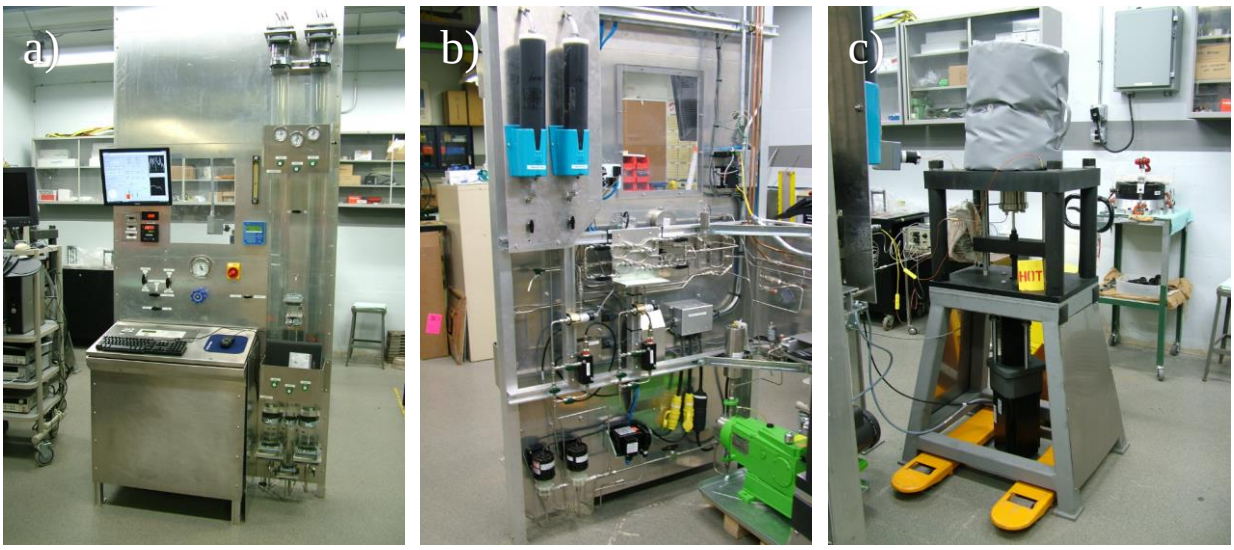

Figure 3.4. Images of the autoclave test system and water loop. a) Control panel front, b) control panel back with plumbing and sensors, and c) load frame, motor and autoclave.

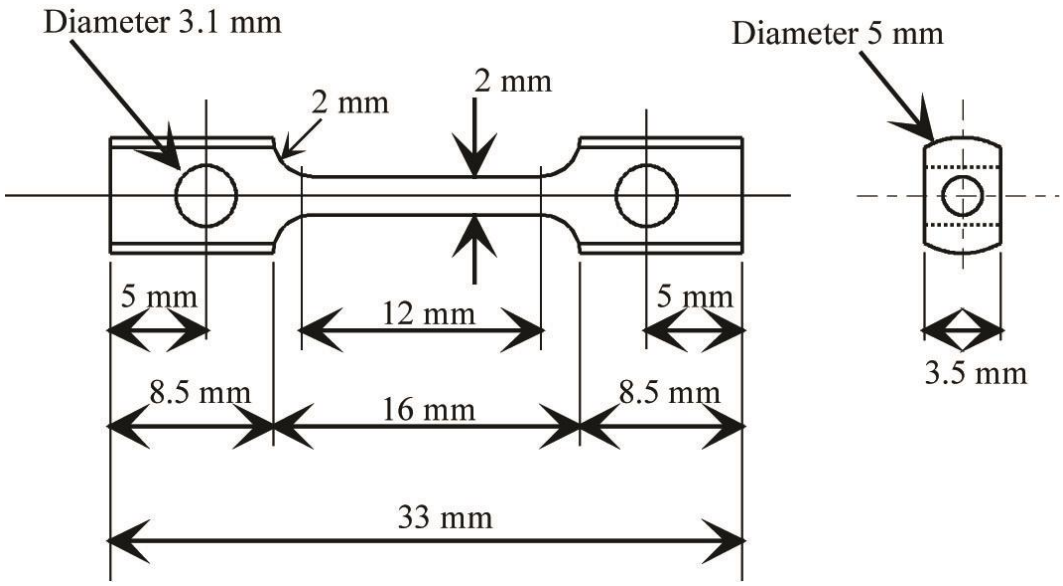

Figure 3.5. Tensile bar sample geometry and dimensions.

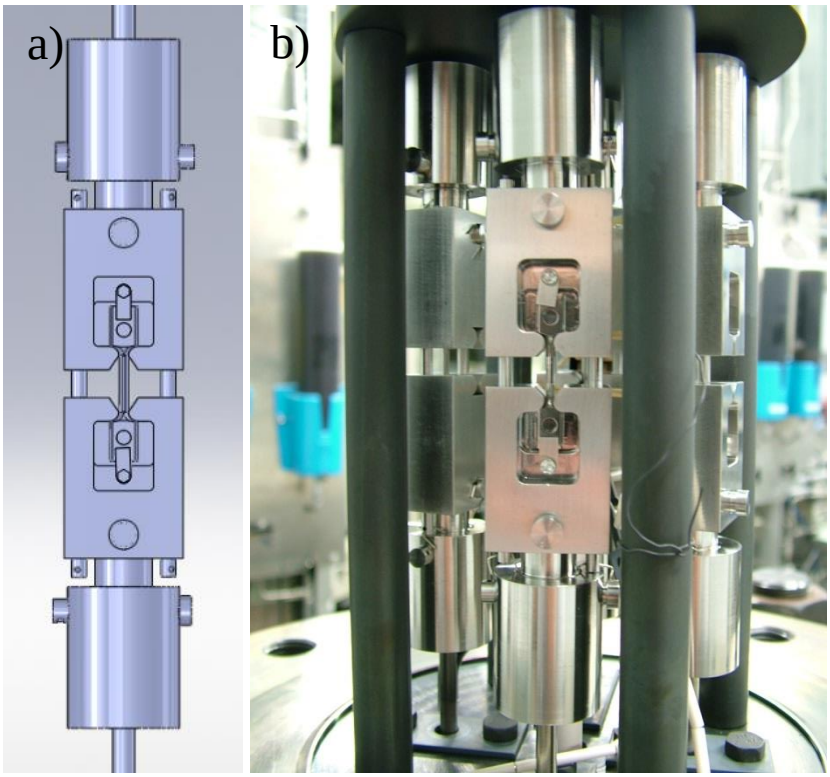

Figure 3.6. a) CERT test loading fixture schematic and b) loading fixture installed in the IM1 autoclave system.

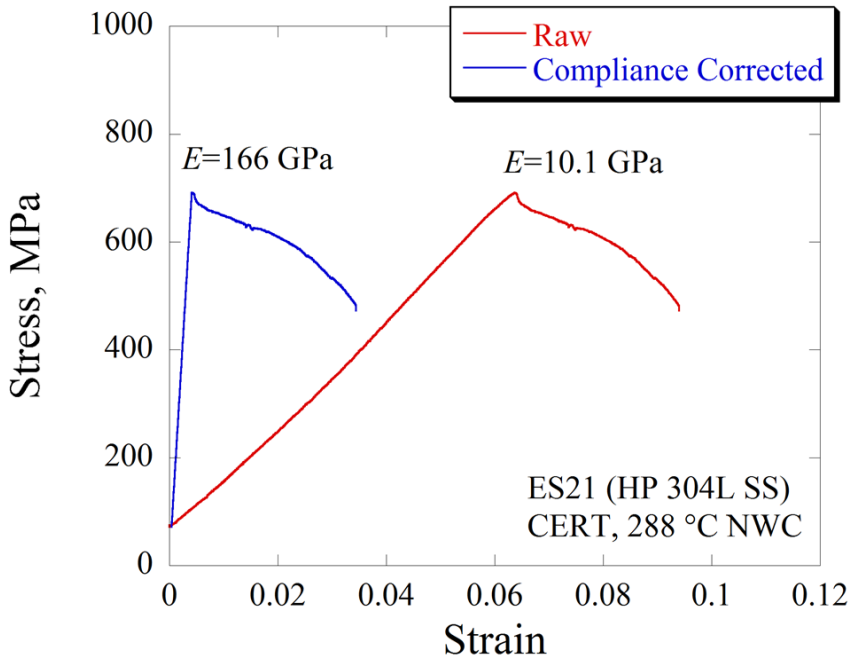

Figure 3.7. Raw and compliance-corrected stress strain curves determined from the CERT test in NWC on 10.7 dpa sample ES21.

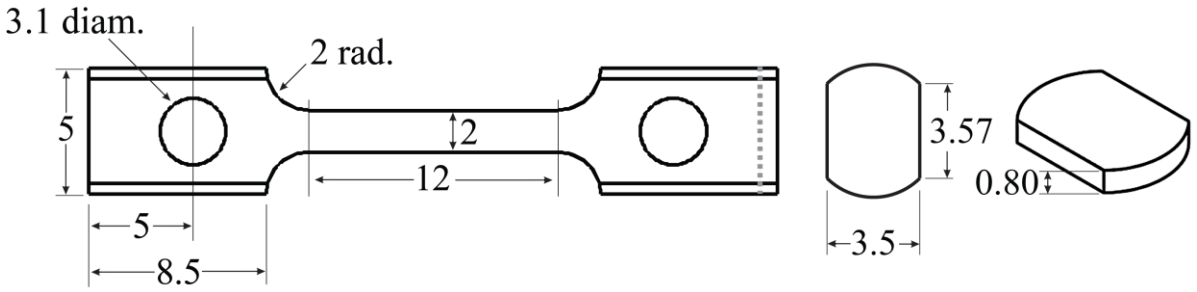

Figure 3.8. Tensile bar geometry and approximate location of the cut made to create bend samples, whose final geometry is shown. Dimensions in mm

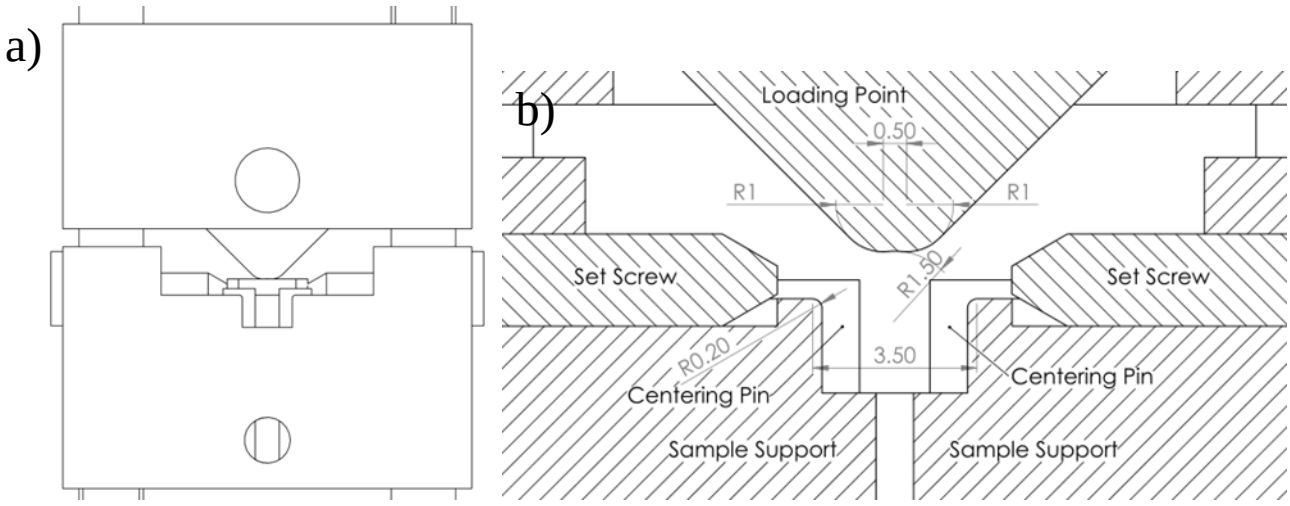

Figure 3.9. a) Schematic of the four-point bend loading fixture including the bend sample and b) cross sectional view excluding the bend sample. Dimensions in mm.

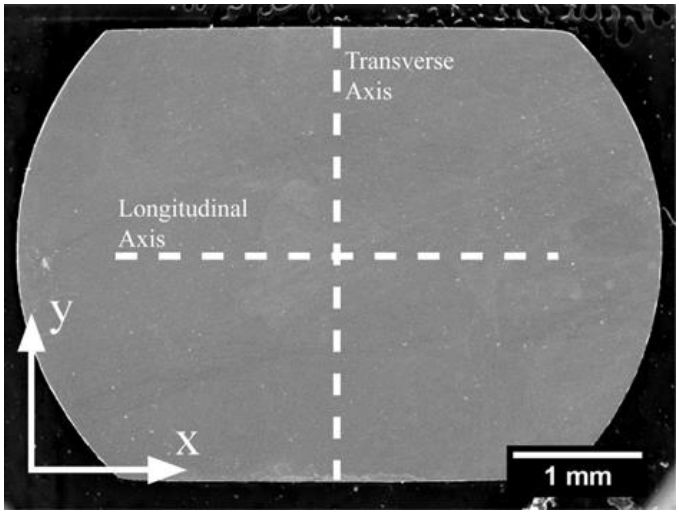

Figure 3.10. Sample orientation and coordinate system. Dashed lines indicate axes for strain profiles.

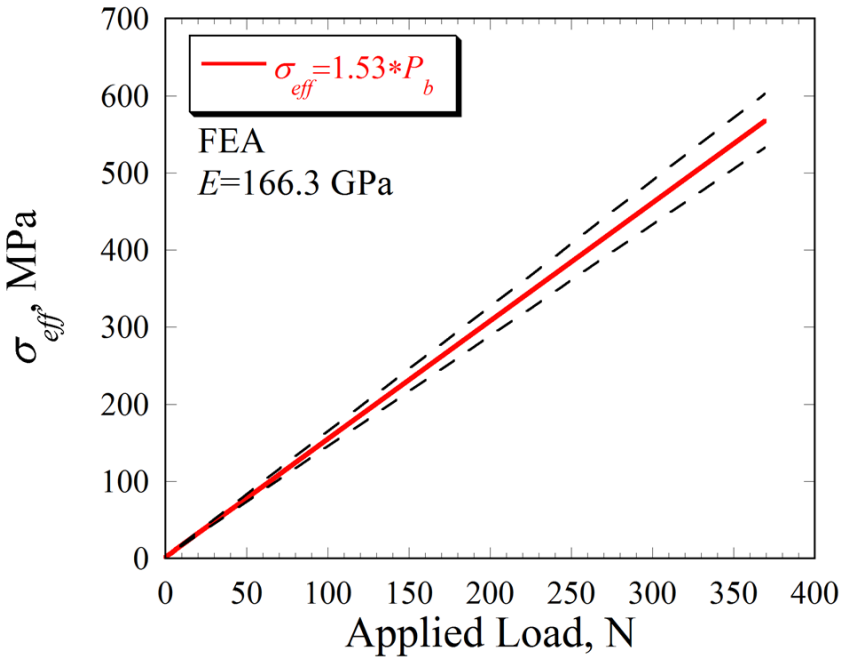

Figure 3.11. The correlation used to determine the effective stress on the four-point bend sample surface during elastic deformation based on the amount of applied load.

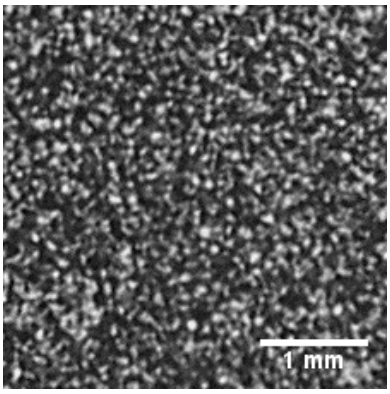

Figure 3.12. DIC speckle pattern applied with Rustoleum spray paint. Particle size ranges between 50 and 100 μm.

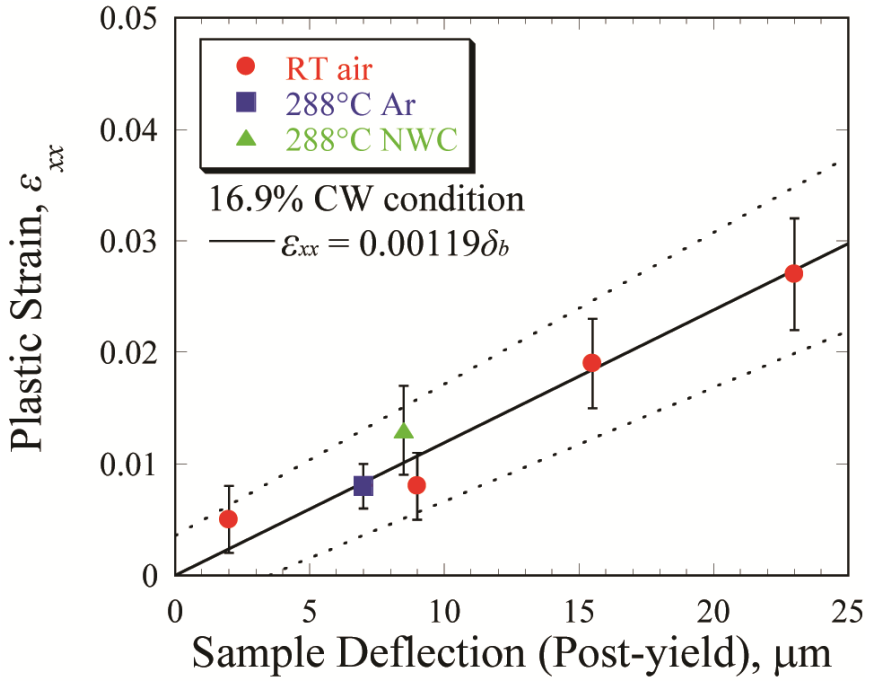

Figure 3.13. Fit and confidence interval for the relationship between bend sample surface strain and deflection.

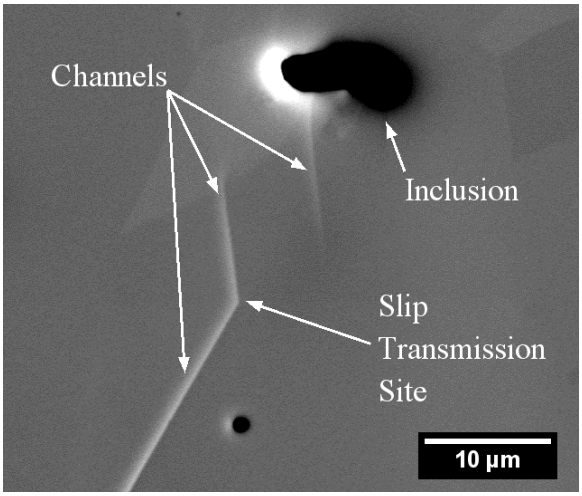

Figure 3.14. Example of a BSE image showing DCs (3) and a slip transmission site.

CHAPTER 4 - RESULTS

This chapter first summarizes results of CERT experiments on neutron irradiated alloys in the 288 °C NWC environment and DC analysis near IGSCC initiation sites. Four-point bend test results are then presented, beginning with FEA results and practice test results which validate the use of the four-point bend test for creating IASCC initiation sites in the irradiated conditions. Finally, results of four-point bend tests on neutron irradiated samples will detail observations of crack initiation sites and analysis of dislocation channeling.

4.1 CERT tests on irradiated materials

CERT tests were performed in 288 °C NWC to compare relative IASCC susceptibility of the irradiated alloys. Mechanical behaviors determined from the CERT tests are summarized in Table 4.1. Dislocation channeling was characterized after sample failure at the IGSCC fracture edge on each sample, where cracking is believed to have initiated.

4.1.1 Stress-strain behavior

Stress-strain curves for each of the irradiated conditions are shown in Figure 4.1. All samples strain softened after yielding, therefore, the yield stress was equal to the maximum stress and uniform elongation values only represent elastic deformation.

Alloy AS at 10.2 and 47.5 dpa were highly susceptible to IASCC, and failed in the elastic regime. Comparing the yield stress measured in the CERT test with that from conventional tensile tests in 330 °C air revealed that these two conditions failed before achieving their full expected yield strength. Less than 0.5% plastic strain was exhibited by each of these samples.

Alloys AS at 5.5 dpa, ES at 10.2 dpa, and KS at 9.6 dpa exhibited a drop in stress at the yield point. This occurrence is common in irradiated materials deformed at a slow strain rate. Alloy AS at 5.5 dpa had limited ductility, similar to the higher dose conditions of this alloy. Alloys ES and KS were significantly more ductile than the alloy AS samples, with total elongation values of 3.45% and 5.14%, respectively.

4.1.2 Fractography

Fracture surfaces of irradiated tensile bar samples after failure in the CERT test are shown in Figure 4.2 and the results of fracture surface analysis are summarized in Table 4.1. The amount of IGSCC varied among the tested conditions, accounting for between 0% and 57.5% of the fracture surface. Alloy AS had a large amount of IGSCC at all irradiation dose conditions, consistent with elongation measurements indicating the high IASCC susceptibility of this alloy. Failure occurred near the tensile bar shoulder on the highest dose sample AS22. HP 304L alloy ES was less susceptible to cracking than CP alloy AS, with only 16.9 %IG on the fracture surface. A small region of mixed mode cracking was observed at the outer edge of the IG region, likely formed as the IG crack transitioned from IG to ductile overload failure. Alloy KS was not susceptible to IASCC under these test conditions, and only ductile failure was observed on the fracture surface of this sample after the CERT test.

4.1.3 Dislocation channeling near IGSCC initiation sites

DC step heights were characterized on the gage surfaces of each sample near the IGSCC fracture edge, where cracking was believed to have initiated. Randomly selected grains near the IG fracture edge were measured, excluding those with multiple active slip systems. In the case of alloy KS with no IGSCC, DC height measurements were recorded in grains near the edge of the necked area in the region of approximate uniform elongation. Alloy AS at 10.2 and 47.5 dpa had the lowest number density of DCs near the fracture edge. The variation in DC density among 5.5 dpa and 47.5 dpa alloy AS samples is exemplified in Figure 4.3, and DC height measurements for all irradiated samples are summarized in Table 4.2. Weighted average channel height decreased in the order: KS13, AS22, AS17, AS13, ES21.

4.2 Development of the four-point bend test

Prior to four-point bend testing neutron irradiated samples, FEA modeling and practice bend tests were used to determine the stress-strain state created on the bend sample surface. FEA was used to analyze the strain distribution as a function of sample deflection and the effects of several hypothetical experimental errors. Practice experiments were then performed on unirradiated SS with different levels of cold work (intended to simulate the yield strength of the irradiated conditions) to confirm the results of the FEA simulation.

4.2.1 Finite element analysis

Alloy 304SS in the cold worked (16.9%) condition was used to calibrate the four-point bend test results against FEA results. A full description of the in-plane surface strain for the 16.9% CW condition at a sample deflection of 58.3 μm is shown in Figure 4.4. This amount of deflection is

shown as it gives a description of the strain state after a small amount of plastic deformation representative of that expected to cause failure in irradiated materials. Figure 4.5 presents a quantitative view of surface strain components for the 16.9% CW condition as a function of bend deflection. Strain was primarily concentrated along the longitudinal axis (ε_{xx}), and the values of both shear and transverse strains (ε_{xy} and ε_{yy}, respectively) in the center 1 mm x 1 mm area of the sample were less than 3% of the applied ε_{xx}, for values of ε_{xx} less than 3%. Transverse (ε_{yy}) strain near the sample edges on the transverse axis approached -40% of the applied ε_{xx}.

The xx component of strain for the same alloy in the as-received condition (no added cold work) is shown in Figure 4.6 at varying amounts of sample deflection. Strain peaks are observed at the locations under loading points after sufficient bend deflection. These formations were a result of the lower yield stress of this material condition. Simulations performed with an increased coefficient of friction between the sample and supports also showed similar strain peak formation. It is apparent that these peaks form due to frictional constraint between the sample and supports. These peaks appear after smaller amounts of bend deflection in softer materials or when the coefficient of friction is increased between the sample and the loading fixture.

4.2.2 Experimental error determination

The FEA model was performed with several geometrical modifications to determine the effect of errors that could possibly occur during four-point bend experiments. Figure 4.7 compares the effect of off-centering the sample by 25 μm and 50 μm. These levels of off-centering could be expected during bend experiments, especially if multiple bend tests are performed on the same sample where the sample must be removed from the fixture and re-loaded. The sample ideally would be placed in the same position in each experiment, but a ~50 μm variation was considered

a reasonable amount of error in sample placement, as this is the upper limit for dimensional tolerance that can be expected due to the electric discharge machining technique used when fabricating the loading fixture. Model results showed that sample off-centering had little effect on the strain profile created during the bend test.

Figure 4.8 compares the effect of laterally off-centering the top loading points. Similar levels of off-centering were analyzed as in the previous analysis, 25 μm and 50 μm. The loading fixture design was expected to prevent this error, although off-centering could be caused by dimensional tolerances in the loading fixture design. Load point off centering had little effect on the strain profile.

Figure 4.9 compares the effect of a variation in sample thickness along the longitudinal direction. Bend samples had known variations in thickness due to sample fabrication, which were confirmed by taking measurements with a micrometer at each of the sample corners. Bend sample thickness variations were no greater than 10 μm, hence the values compared in Figure 4.9 (5 μm and 10 μm). Variation in sample thickness had a small effect on the strain profile.

4.2.3 Four point bend tests on unirradiated materials

To confirm that FEA model results represented experimental results, a series of bend tests were performed on unirradiated 304L SS in as-received and 16.9% cold-worked conditions, which had yield strengths similar to the neutron irradiated conditions. Practice bend tests were conducted in air to relate load cell measurements and DIC surface strain measurements to directly measured sample bend deflection. Four-point bend tests were performed in room temperature (RT) air on a sample of each unirradiated condition (AR and after 16.9% cold work), and interrupted at pre-determined amounts of bend deflection. Larger increments were used on the 16.9% CW

condition due to its higher yield strength. Three additional tests on previously undeformed samples of the 16.9% CW condition were then performed in RT air, 288 °C Ar and NWC conditions. Each of these experiments was performed in a single step to ~40 µm bend deflection to determine whether incremented tests or test environment affected strain. Table 4.3 summarizes the results of all practice bend tests on the unirradiated material conditions.

Figure 4.10 presents load vs. bend deflection curves after the tests in RT air which were performed in increments of bend deflection. The bend load at macroscopic yield increased after each test due to strain hardening. The theoretical elastic slope is also shown in Figure 4.10, calculated using the following static beam-bending equations:

$$\delta(x) = \frac{P_1 b_1 x(L^2 - b_1^2 - x^2)}{6LEI} + \frac{P_2 b_2 x(L^2 - b_2^2 - x^2)}{6LEI} \quad \text{for } 0 \le x \le a_1, \qquad (4.1)$$

$$\delta(x) = \frac{P_1 b_1 x(L^2 - b_1^2 - x^2)}{6LEI} + \frac{P_2 b_2 x(L^2 - b_2^2 - x^2)}{6LEI} + \frac{P_2 (x - a_2)^3}{6EI} \quad \text{for } a_1 \le x \le a_2, \qquad (4.2)$$

$$\delta(x) = \frac{P_1 b_1 x(L^2 - b_1^2 - x^2)}{6LEI} + \frac{P_1 (x - a_1)^3}{6EI} + \frac{P_2 b_2 x(L^2 - b_2^2 - x^2)}{6LEI} + \frac{P_2 (x - a_2)^3}{6EI} \quad \text{for } a_2 \le x \le L, \qquad (4.3)$$

where δ is the beam deflection at any point x along a beam of length L. a_1 and a_2 are the distances from the beginning of the beam (at x=0) to the top loading points 1 and 2 where loads P_1 and P_2 are applied, respectively. Similarly b_1 and b_2 are distances to the loading points from the opposite end of the beam (where x=L). In the case of the symmetric four-point bend test, P_1= P_2, a_1= b_1, and a_2= b_2.

Figure 4.11 shows the average surface strain (measured by DIC) measured in these experiments along with FEA model results. Small differences between the measured and FEA model strains

were likely due to elastic spring-back between increments, which was not accounted for in the measurements.

Figure 4.12 presents the load vs. bend deflection curves of four-point bend tests performed in RT air, 288 °C Ar, and 288 °C NWC environments. Due to the high temperature in 288 °C Ar and NWC environments, sample deflection was not directly measured and the compliance correction technique was used to determine sample deflection. This technique added noise in the deflection measurement because of natural fluctuations in the load cell reading. Speckle pattern DIC was used to measure strain for experiments in RT air and 288 °C Ar, while the indent DIC technique was used in NWC. Figure 4.13 shows good agreement among the strain distributions along the longitudinal axis after these bend tests despite differences in test environment, deflection measurement technique, and strain measurement technique. Average strain measurements from all bend tests on the 16.9% CW condition are compared in Figure 4.14, showing that results in high temperature environments agree well with those in room temperature, and that incremented tests cause negligible differences in strain.

4.3 Four-point bend tests on irradiated materials

Major results and observations from four-point bend tests on irradiated samples are presented in this section, while a more detailed summary for each sample is provided in Appendix B. Cracking and localized deformation results in the NWC environment are presented first, followed by localized deformation results from bend tests in 288 °C Ar.

To establish the response of irradiated material in the four-point bend test, an initial experiment was performed on 10.2 dpa sample AS05 until an observable variation in stress-strain behavior

occurred. Figure 4.15 presents the bend load vs. LVDT (crosshead) deflection curve and the bend sample surface after the test had completed. A rapid transition in load-bearing capacity and a large, singular IG crack on the sample surface were observed. Because it was likely that the initial crack would cause sample failure in all samples similar to the behavior of this sample, subsequent experiments were performed in small stress or strain increments to limit crack growth.

Because experiments on neutron irradiated samples were conducted in an incremented manner, it was necessary to quantify the magnitude of stress and strain applied during each test for comparison of dislocation channeling and cracking among the irradiated conditions. During irradiated four-point bend tests, load vs. deflection behavior (exemplified in Figure 4.16) was linear during elastic deformation, yet differences were observed in comparison to the uniaxial CERT results after the occurrence of yielding: stress did not drop sharply upon yielding and load continued to increase after this point (strain softening was observed in CERT tests). As a result, four-point bend tests interrupted prior to macroscopic yielding are represented in a different manner than those where macroscopic yield was achieved and plastic deformation applied.

Irradiated bend tests stopped prior to macroscopic yield were quantified in terms of the stress applied to the bend sample surface based on the correlation in Figure 3.11. Load rather than deflection was used in this correlation because direct sample deflection measurements were not made on irradiated samples, and compliance affected the deflection measurement recorded at the crosshead. This was inconsequential to the stress determination, because load and deflection were linearly related during elastic deformation, as shown both experimentally and theoretically in Figure 4.10.

Irradiated bend tests stopped after macroscopic yield were quantified in terms of the permanent plastic xx component of strain applied to the bend sample surface based on the correlation in Figure 3.13. Applied stress was unable to be accurately determined from FEA during this regime, due to the lack of knowledge regarding the true stress-true strain behavior of irradiated material.

4.3.1 Stress corrosion cracking and localized deformation in 288 °C NWC

4.3.1.1 Stress corrosion cracking

Results of four-point bend tests on CP 304L alloy AS samples in 288 °C NWC are summarized in Table 4.4. All increments were stopped before macroscopic yield, therefore the effective stress (σ_{eff}, determined from the correlation in Figure 3.11) and stress relative to the tensile yield stress (σ_{eff}/σ_y) are presented. Relative stress was based on yield stress values measured during previous tensile tests in 330 °C air, from ref. [28]. Annotations in Table 4.4 indicate when dislocation channeling was observed (if prior to crack initiation, as channeling was always observed extending from crack tips due to stress concentration), when IGSCC was observed, and when a second crack was observed if multiple cracking sites formed.

Alloy AS samples were highly susceptible to IASCC, and cracking initiated before macroscopic yield at all irradiation dose conditions. The average stress for IASCC initiation at each irradiation damage level is summarized in Table 4.5 and plotted in Figure 4.17, showing that its value decreases with irradiation dose.

Table 4.6 presents the results of four-point bend tests on HP model 304L alloys ES and KS. Plastic strain (ε_{xx}) values are given for tests where macroscopic yield was achieved and plastic

deformation was applied, based on the relationship between plastic ε_{xx} and sample deflection in Figure 3.13. Alloy ES was much less susceptible to IASCC than alloy AS, as crack initiation on sample ES01 was not observed until after macroscopic yield. Crack initiation occurred between bend tests ended at 0.98 σ_y and 1% plastic strain, therefore the crack likely did not form until after macroscopic yield had occurred. This first crack, shown in Figure 4.18a, likely originated at the sample edge. Additional strain was applied after the observation of this crack in an attempt to create a crack within the sample surface. The first crack did not propagate after an additional 0.8% plastic strain, however, in the 8th test, a second IGSCC crack formed. The second crack, shown in Figure 4.18b, also likely originated at the sample edge based on the observation of its width. This second crack propagated rapidly, shown in the low magnification image in Figure 4.19. A reduction in load bearing capacity observed during this test was indicative of sample failure, and no strain measurement was possible due to the large size of the crack. The initial crack did not propagate after formation of the second crack. Alloy KS exhibited no IG cracking in NWC, even after the application of ~10% strain.

Figure 4.20 summarizes all cracking observations in NWC in terms of applied strain. Alloy KS did not form a crack, therefore no data points are shown. The 5.5 dpa sample AS04 formed a crack on the first increment, and two cracks formed during the same increment on 5.5 dpa sample AS02 and 47.5 dpa sample AS10.

4.3.1.2 Influence of surface inclusions

All 10 of 10 intergranular cracks in alloy AS samples emanated from surface inclusions, as shown in Figure 4.21. Table 4.7 further indicates the interaction of IGSCC with surface inclusions in this alloy. The crack on sample AS08 was within 10 μm of a surface inclusion,

shown in Figure 4.22, and likely intersected the inclusion beneath the sample surface. Surface inclusions were observed using BSE imaging of the bend sample surfaces, which allowed for their observation due to the high contrast difference with the austenite matrix. The particle analysis feature in the ImageJ™ software was used to quantify the size of inclusions in the center region of each bend sample, resulting in the histograms showing the distribution of inclusion sizes shown in Figure 4.23. An 'oxide cap' was also observed at all IGSCC initiation sites, and in most cases, obscured the inclusion after the crack had initiated.

Not all bend sample surfaces were recorded in detail prior to crack initiation, but oxide cap formation was observed at 4 of 5 crack sites *before* the crack formed, as shown in Figure 4.24. The exception was sample AS08, shown prior to crack initiation in Figure 4.22a. Once crack initiation occurred, crack opening caused the formation of additional corrosion product (growth of the oxide cap), which can be seen by comparing the images from samples shown in both Figure 4.24 and Figure 4.21. The process of oxide cap formation at an inclusion and subsequent crack initiation on 5.5 dpa sample AS02 is further exemplified in Figure 4.25. XEDS of these areas after crack initiation showed that the oxide cap was rich in O and Mn, exemplified in Figure 4.26.

To determine the type of inclusions which formed an oxide cap and whether inclusion corrosion was affected by the application of stress; inclusions on an unirradiated sample of alloy AS were characterized with XEDS before and after 24 hours of exposure to NWC conditions in an un-stressed state. An exposure time of 24 hours was chosen, as this was approximately the time duration of a single four-point bend test. A total of 24 inclusions were characterized: 13 MnS (high concentrations of Mn and S and a small amount of Cr) and 11 oxide inclusions (XEDS

typically showed Mn, Cr, Ti, O and trace amounts of Al). MnS inclusions were typically larger than oxide inclusions, having average surface areas of 66 ± 2 μm and 25 ± 13 μm, respectively. A complete account of the inclusion chemistry analysis for all alloys can be found in Appendix A. Figure 4.27 shows that oxide inclusions did not undergo significant changes in appearance or composition. Most commonly, oxide inclusion composition decreased in O and increased in Fe after NWC exposure, likely due to surface oxide formation. Conversely, MnS inclusions displayed three different types of response to NWC exposure, exemplified in Figure 4.28: a) Mn oxide formation within the inclusion site, b) dissolution of the inclusion resulting in pit formation, or c) Mn oxide cap formation at the inclusion site. XEDS showed that all MnS locations after NWC exposure were absent of S, but had corrosion product enriched in Mn and O.

Only one inclusion on the unirradiated sample surface formed an oxide cap after NWC exposure (Figure 4.28c), which had a similar appearance to crack initiation sites in the irradiated alloy AS samples. The observation of only a single site with this appearance on the unirradiated sample was not surprising, as only a small number of these sites were observed on irradiated samples, quantified in Table 4.7. Figure 4.29 shows XEDS results from this area, indicating that the oxide cap was rich in O and Mn and had no concentration of S or Ti.

Inclusions were not observed to influence cracking in irradiated alloys ES and KS, and no oxide cap formations were observed on sample surfaces after exposure to NWC. The lack of corrosion was likely because of the oxide nature of inclusions in these alloys, consistent with observations from oxide inclusions in alloy AS.

4.3.1.3 Localized deformation

Surface oxidation was removed from several alloy AS samples to more clearly identify whether DCs were present at IASCC initiation sites. 5 of 6 IGSCC initiation sites observed after oxide removal had a DC intersecting the inclusion where an oxide cap had been previously present, as shown in Figure 4.30. The DCs at IGSCC initiation sites were always discontinuous where they intersected the inclusion. The only crack initiation site without an adjacent DC was the second crack which formed on 10.2 dpa sample AS06 (Figure 4.30d), although a sharp corner was observed in the grain boundary at the location where it intersected the inclusion.

Channel formation was not always observed prior to IGSCC, therefore, the DCs at crack initiation sites may have formed during the stress increment that induced cracking. Channeling *was* observed before crack initiation on several alloy AS samples: AS02 (18 channels), AS08 (72 channels), and AS09 (4 channels); providing further evidence that DCs at IGSCC sites likely formed during the stress increment that led to cracking. Contrary to observations at IGSCC initiation sites, all inclusions with an oxide cap where no IGSCC initiated (7 of 7 sites) had no intersecting channels, as shown in Figure 4.31.

DC measurements on alloys ES and KS were made after similar levels of applied strain in NWC. The results of this analysis are summarized in Table 4.8 and plotted in Figure 4.32. Similar to alloy AS samples, dislocation channeling was observed in these alloys prior to macroscopic yield. The number density of DCs and slip transmission sites increased rapidly until macroscopic yield occurred, where the rate (as a function of strain) of channel and transmission site formation decreased. Channel density was similar for both HP alloys, but the density of slip transmission sites was greater in alloy KS than alloy ES at all strain values.

4.3.2 Localized deformation in 288 °C Ar

Table 4.9 summarizes the results of bend tests in 288 °C Ar. No cracking occurred as a result of bend tests in the high temperature inert environment, even on samples of alloy AS, although a similar or greater amount of strain was applied than that required to cause crack initiation in the NWC environment. The lack of surface oxidation caused by exposure to the 288 °C Ar environment allowed for more accurate measurement of DC formation on bend sample surfaces. Bend tests on each alloy were interrupted at similar levels of relative stress and strain to allow for comparison of DC characteristics. All bend tests in 288 °C Ar were interrupted before macroscopic yield occurred.

Table 4.10 summarizes DC observations after straining in 288 °C Ar, also including the number of DCs intersecting surface inclusions and channel height. The number density of DCs and slip transmission sites are compared in Figure 4.33. After ~680 MPa, DC density was similar in both HP alloys, lower in alloy AS at 10.2 dpa, and lowest in alloy AS at 5.5 dpa. Alloy KS had the highest density of slip transmission sites among all alloys. The number of DC-inclusion intersections in alloy AS was low and did not scale with DC density. DC height measurements were recorded on each sample after ~0.4% strain. The weighted average DC height was relatively similar on each sample, although slightly larger on the two HP alloys, despite the presence of a higher density of DCs than the two alloy AS samples.

After DC characterization, alloy AS samples that were strained in 288 °C Ar (samples AS03 and AS07) were exposed to NWC in an un-stressed condition for 24 hours to determine whether inclusion corrosion was dependent upon prior deformation or DC formation. The number of surface inclusions which formed an oxide cap (summarized in Table 4.7) was similar to those

strained in NWC without pre-straining in Ar. Less than 2% of inclusions formed an oxide cap after NWC exposure, regardless of irradiation dose or straining history.

Table 4.1. CERT test results including both mechanical properties and fractography results. Yield stress values from conventional tensile tests in 330 °C air are also included for reference (from [24], conventional tensile tests conducted at a strain rate $3x10^{-4}$ s^{-1}).

Sample ID	Alloy	Dose, dpa	YS (MPa)	YS in air (MPa)	Max Stress (MPa)	UE (%)	TE (%)	% IG	% Mixed IG/TG	% Ductile
AS13	CP 304L	5.5	755	783	755	0.45	1.04	40.7	0.0	59.3
AS17	CP 304L	10.2	616	824	616	0.37	0.72	55.9	0.0	44.1
AS22	CP 304L	47.5	608	906	608	0.37	0.54	57.5	0.0	42.5
ES21	HP 304L	10.7	691	711	691	0.42	3.45	16.8	7.4	75.8
KS13	HP 304L +Ni	9.6	574	606	574	0.35	5.14	0.0	0.0	100.0

Table 4.2. Summary of DC height analysis from sample replicas after failure during CERT tests in 288 °C NWC.

Specimen	Dose, dpa	TE, %	%IG	Grains Analyzed	Channels Analyzed	Weighted Channel Height, nm
AS13	5.5	1.04	40.7	16	130	291 $^{+58}_{-52}$
AS17	10.2	0.72	55.9	9	82	364 $^{+98}_{-87}$
AS22	47.5	0.54	57.5	7	25	1342 $^{+764}_{-537}$
ES21	10.7	3.45	16.8	10	136	265 $^{+10}_{-10}$
KS13*	9.6	5.14	0.0	11	146	2066 $^{+263}_{-242}$

*Step height measurements taken outside necked region, not near fracture edge.

Table 4.3. Results of practice four-point bend tests on unirradiated 304L SS.

Environment	Sample Condition and ID	Sample Thickness, µm	Increment No.	Yield Load, N	Sample Deflection, µm	Deflection Measurement Technique	Sample Center Strain	Strain Standard Deviation	Strain Measurement Technique
RT Air	AR #1	810	1	449	21.3	Direct	0.004	0.002	DIC
			2	498	29.2	Direct	0.007	0.003	DIC
			3	592	39.0	Direct	0.014	0.004	DIC
			4	672	49.6	Direct	0.020	0.006	DIC
RT Air	16.9% CW #1	817	1	618	30.0	Direct	0.005	0.003	DIC
			2	703	40.1	Direct	0.008	0.003	DIC
			3	841	49.9	Direct	0.019	0.004	DIC
			4	934	59.7	Direct	0.027	0.005	DIC
RT Air	16.9% CW #2	841	1	596	38.4	Direct	0.008	0.002	DIC
288 °C Ar	16.9% CW #3	807	1	654	39.8	Correction Factor	0.008	0.002	DIC, Indent Spacing
288 °C NWC	16.9% CW #4	798	1	698	42.2	Correction Factor	0.013	0.004	Indent Spacing

Table 4.4. Results of four-point bend tests on CP 304L alloy AS samples in 288 °C NWC.

YS in 330°C air, MPa	Bend load at yield, N	Sample ID	Dose, dpa		Four-point bend test no. 1	2	3	4
783 ± 11	NM	AS01	5.5	σ_{eff}, MPa	630 ± 39	824 ± 51[b]		
				σ_{eff}/σ_y	0.80 ± 0.05	1.05 ± 0.07		
		AS02	5.5	σ_{eff}, MPa	545 ± 34	613 ± 38[a]	681 ± 42[c]	
				σ_{eff}/σ_y	0.70 ± 0.04	0.78 ± 0.05	0.87 ± 0.05	
		AS04	5.5	σ_{eff}, MPa	581 ± 36[b]			
				σ_{eff}/σ_y	0.74 ± 0.05			
824 ± 5	NM	AS06	10.2	σ_{eff}, MPa	477 ± 30	545 ± 34	613 ± 38[b]	647 ± 40[c]
				σ_{eff}/σ_y	0.58 ± 0.04	0.66 ± 0.04	0.74 ± 0.05	0.78 ± 0.05
		AS08	10.2	σ_{eff}, MPa	495 ± 31[a]	551 ± 34[a]	585 ± 36[a]	613 ± 38[b]
				σ_{eff}/σ_y	0.60 ± 0.04	0.67 ± 0.04	0.71 ± 0.04	0.74 ± 0.05
906 ± 5	NM	AS09	47.5	σ_{eff}, MPa	441 ± 27[a]	501 ± 31[b]		
				σ_{eff}/σ_y	0.49 ± 0.03	0.55 ± 0.03		
		AS10	47.5	σ_{eff}, MPa	430 ± 27	443 ± 27[c]		
				σ_{eff}/σ_y	0.47 ± 0.03	0.49 ± 0.03		

[a]Dislocation channeling observed with no cracking.

[b]Crack initiation observed.

[c]Second instance of crack initiation observed.

NM indicates that quantity was not measured.

Table 4.5. Average stress for IASCC initiation in alloy AS at each irradiation dose condition, including error sources.

Sample ID	Dose, dpa	Maximum Stress Before IASCC, MPa	Stress After IASCC Observation, MPa	Stress Error due to Increment Size, MPa ($\varphi_{interval}$)	IASCC Initiation Stress, MPa ($\sigma_{CI,sample}$)	Standard Deviation, MPa (φ_{stdev})	Average IASCC Initiation Stress, MPa ($\sigma_{CI,condition}$)
AS01	5.5	630 ± 39	824 ± 51	97	727 ± 102	91	640 ± 99
AS02		613 ± 34	681 ± 38	34	647 ± 43		
AS04		510 ± 32*	581 ± 36	35	546 ± 35		
AS06	10.2	545 ± 34	613 ± 38	34	579 ± 42	14	589 ± 29
AS08		585 ± 36	613 ± 38	14	599 ± 29		
AS09	47.5	441 ± 27	501 ± 31	30	471 ± 30	24	454 ± 32
AS10		430 ± 27	443 ± 27	7	437 ± 27		

*Stress value estimated based on similar crack size in sample AS02

Table 4.6. Results of four-point bend tests on HP 304L alloys ES and KS in 288 °C NWC.

YS in 330°C air, MPa	Bend load at yield, N	Sample ID	Dose, dpa		Four-point bend test no. 1	2	3	4	5	6	7	8	9	10
711 ± 11	529 ± 45	ES01	10.2	σ_{eff}, MPa	552 ± 34[a]	613 ± 38[a]	671 ± 42[a]	722 ± 45[a]	790 ± 49[a]	–[b]	–[b]	–[c]		
				σ_{eff}/σ_y	0.68 ± 0.04	0.76 ± 0.05	0.83 ± 0.05	0.89 ± 0.06	0.98 ± 0.06	–	–	–		
				ε_{xx}	–	–	–	–	–	0.010 ± 0.005	0.008 ± 0.005	–		
606 ± 37	494 ± 45	KS02	9.6	σ_{eff}, MPa	552 ± 34[a]	743 ± 46[a]	–[a]	–[a]	–[a]	–[a]	–[a]	–[a]	–[a]	–[a]
				σ_{eff}/σ_y	0.73 ± 0.05	0.98 ± 0.06	–	–	–	–	–	–	–	–
				ε_{xx}	–	–	0.004 ± 0.004	0.015 ± 0.006	0.014 ± 0.006	0.013 ± 0.006	0.000 ± 0	0.017 ± 0.006	0.014 ± 0.006	0.017 ± 0.006

[a]Dislocation channeling observed with no cracking.

[b]Crack initiation observed.

[c]Second instance of crack initiation observed.

Table 4.7. Inclusions observed on bend sample surfaces, number with corrosion product formation, and whether IGSCC cracks intersected inclusions.

Sample ID	Dose, dpa	Total no. inclusions	No. density inclusions, mm^{-2}	No. inclusions with oxide cap	No. density inclusions with oxide cap, mm^{-2}	IGSCC-inclusion intersections	
						First crack	Second crack
AS-Unirr	0.0	396	82 ± 4	1	0.2 ± 0.2	Not Cracked	
AS01	5.5	646	145 ± 6	3	0.7 ± 0.4	2	N/A
AS02	5.5	614	129 ± 5	4	0.8 ± 0.4	1	1
AS03	5.5	428	129 ± 6	4	1.2 ± 0.6	Not Cracked	
AS04	5.5	650	143 ± 6	4	0.9 ± 0.4	1	N/A
AS06	10.2	422	95 ± 5	3	0.7 ± 0.4	1	2
AS07	10.2	474	107 ± 5	2	0.5 ± 0.3	Not Cracked	
AS08	10.2	412	133 ± 7	3	1.0 ± 0.6	1[a]	N/A
AS09	47.5	699	150 ± 6	4	0.9 ± 0.4	1	N/A
AS10	47.5	660	145 ± 6	7	1.5 ± 0.6	2	3
ES01	10.2	194	111 ± 8	0	0 ± 0	0	NM
ES02	10.7	597	139 ± 6	0	0 ± 0	Not Cracked	
KS01	9.6	512	143 ± 6	0	0 ± 0	Not Cracked	
KS02	9.6	291	167 ± 10	0	0 ± 0	Not Cracked	

[a]Inclusion within 10 μm, possible sub-surface intersection.

N/A indicates that quantity was not available due to the lack of a second crack.

NM indicates that quantity was not measured.

Table 4.8. DC analysis of samples strained in 288 °C NWC. N/A indicates the stress value was not available due to sample yield.

Sample ID	Dose, dpa	σ_{eff}, Mpa	σ_{eff}/σ_y	Strain	Channels, mm^{-2}	Slip transmissions, mm^{-2}	Transmission Sites per Channel
ES01	10.2	552	0.68	0.33%	184 ± 11	40 ± 5	0.22 ± 0.04
		790	0.98	0.47%	788 ± 21	286 ± 13	0.36 ± 0.03
		N/A		2.29%	3262 ± 81	1610 ± 57	0.49 ± 0.03
KS02	9.6	552	0.73	0.33%	132 ± 9	54 ± 6	0.41 ± 0.07
		743	0.98	0.45%	868 ± 31	417 ± 21	0.48 ± 0.04
		N/A		2.35%	3477 ± 107	1980 ± 81	0.57 ± 0.04

Table 4.9. Results of four-point bend tests performed in 288 °C Ar.

YS in 330°C air, MPa	Bend yield load, N	Sample ID	Dose, dpa		Four-point bend test no. 1	2	3	4	5	6
783 ± 11	NM	AS03	5.5	σ_{eff}, MPa	664 ± 41[a]					
				σ_{eff}/σ_y	0.85 ± 0.05					
824 ± 5	747 ± 45	AS07	10.2	σ_{eff}, MPa	509 ± 32	580 ± 36[a]	612 ± 38[a]	647 ± 40[a]	714 ± 44[a]	952 ± 59[a]
				σ_{eff}/σ_y	0.62 ± 0.04	0.70 ± 0.04	0.74 ± 0.05	0.78 ± 0.05	0.87 ± 0.05	1.16 ± 0.07
711 ± 11	529 ± 45	ES02	10.7	σ_{eff}, MPa	523 ± 32[a]	729 ± 45[a]				
				σ_{eff}/σ_y	0.65 ± 0.04	0.90 ± 0.06				
606 ± 37	494 ± 45	KS01	9.6	σ_{eff}, MPa	489 ± 30[a]	680 ± 42[a]				
				σ_{eff}/σ_y	0.65 ± 0.04	0.90 ± 0.06				

[a]Dislocation channeling observed with no cracking.

NM indicates that quantity was not measured.

Table 4.10. DC analysis of samples strained in 288 °C Ar.

Sample ID	Dose, dpa	σ_{eff}, Mpa	σ_{eff}/σ_y	Strain	Channels, mm^{-2}	Slip transmissions, mm^{-2}	Transmission Sites per Channel	Channel-Inclusion Intersections, mm^{-2}	Weighted Average Channel Height, nm
AS03	5.5	664	0.85	0.40%	68 ± 6	16 ± 3	0.24 ± 0.07	5 ± 2	55^{+15}_{-12}
AS07	10.2	714	0.87	0.43%	279 ± 13	81 ± 7	0.29 ± 0.04	11 ± 3	58^{+15}_{-13}
		952	1.16	0.57%	1287 ± 44	478 ± 27	0.37 ± 0.03	21 ± 6	NM
ES02	10.7	523	0.65	0.31%	81 ± 7	19 ± 3	0.23 ± 0.06	2 ± 1	NM
		729	0.90	0.44%	505 ± 17	139 ± 9	0.28 ± 0.03	12 ± 3	70^{+13}_{-12}
KS01	9.6	489	0.65	0.29%	48 ± 6	23 ± 4	0.47 ± 0.13	3 ± 1	NM
		680	0.90	0.41%	564 ± 31	243 ± 20	0.43 ± 0.06	8 ± 3	88^{+17}_{-15}

NM indicates that quantity was not measured.

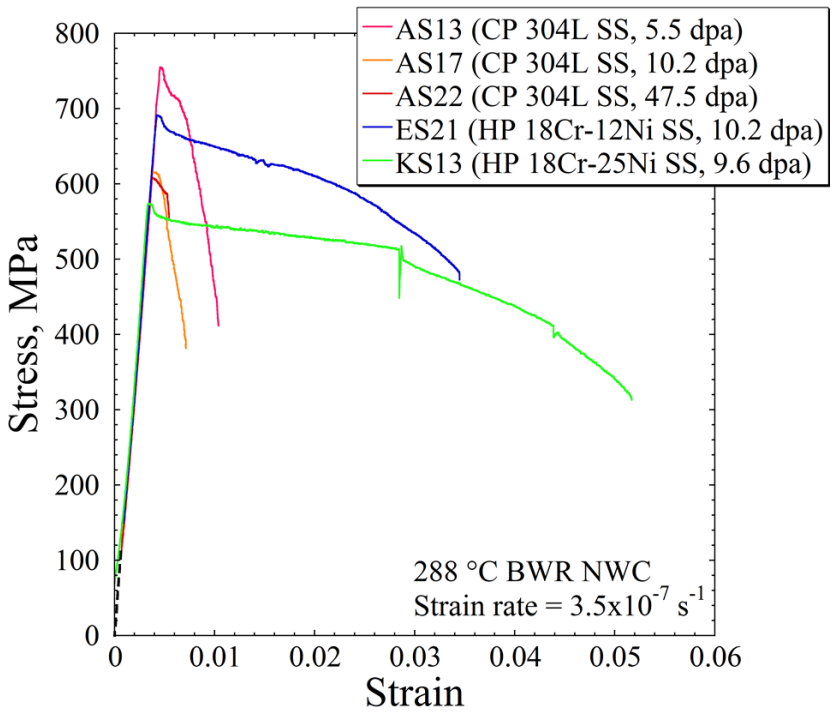

Figure 4.1. Stress-strain curves for irradiated tensile bar samples after CERT testing in NWC.

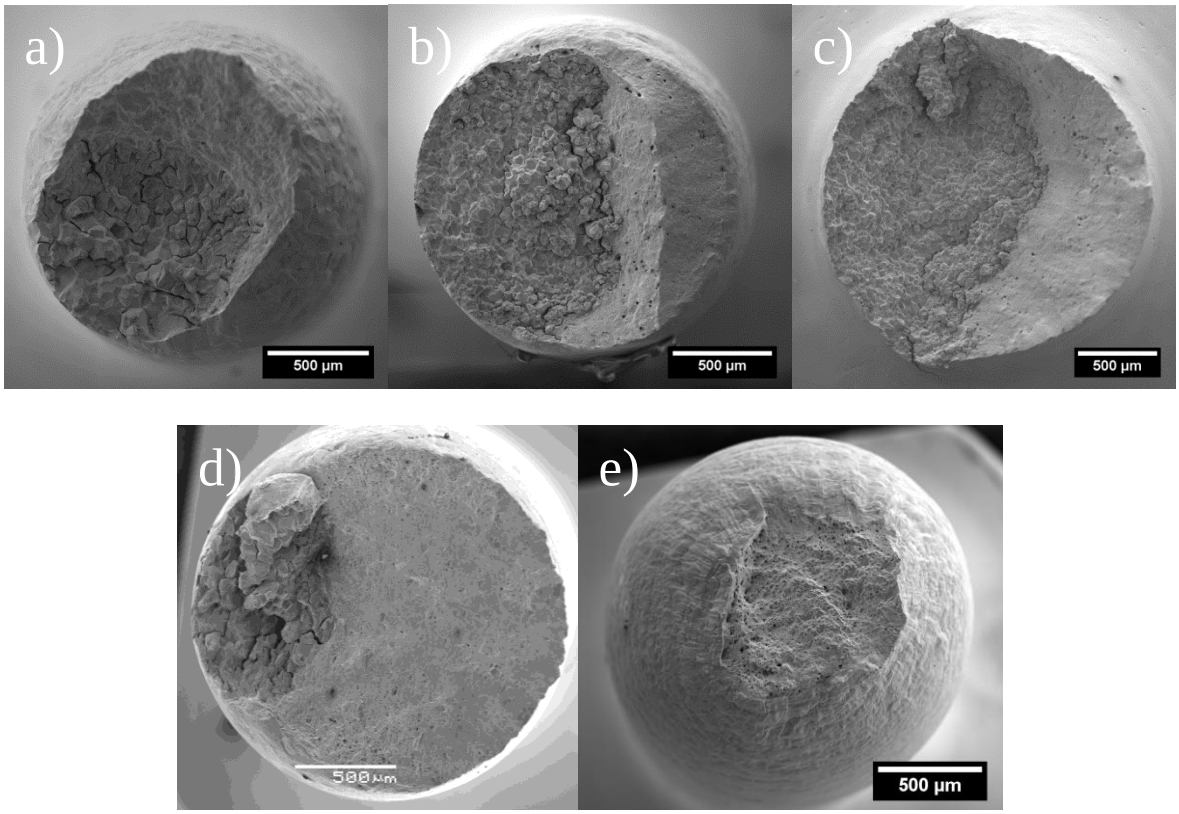

Figure 4.2. Fracture surfaces of samples a) AS13, b) AS17, c) AS22, d) ES21, and e) KS13, strained to failure by CERT in 288 °C NWC.

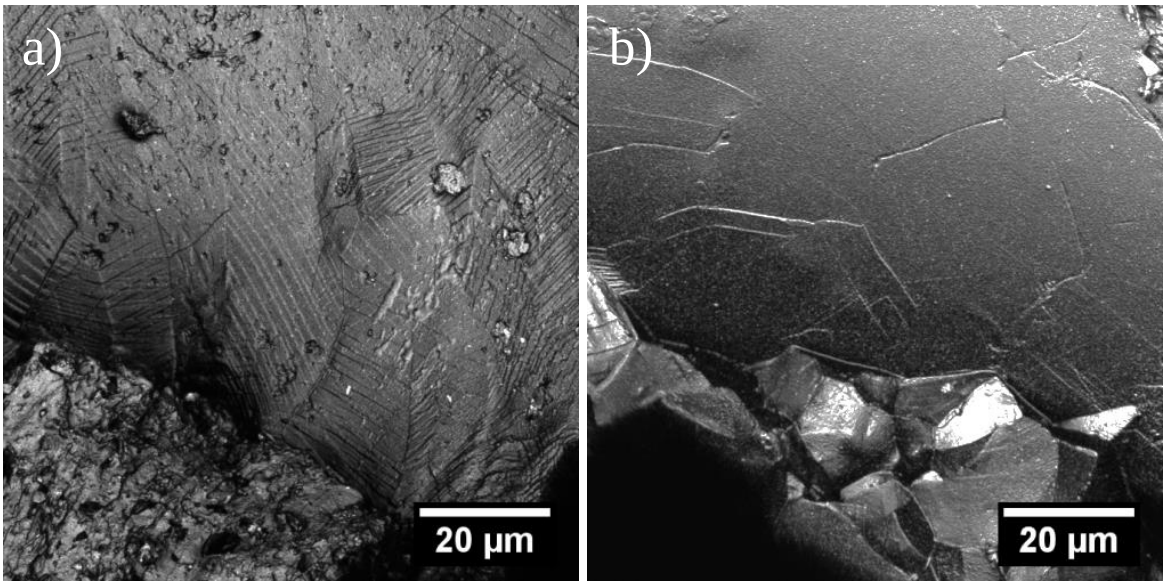

Figure 4.3. Surface topography of the gage surfaces of a) AS13 and b) AS22 near the IG fracture edge after CERT in NWC.

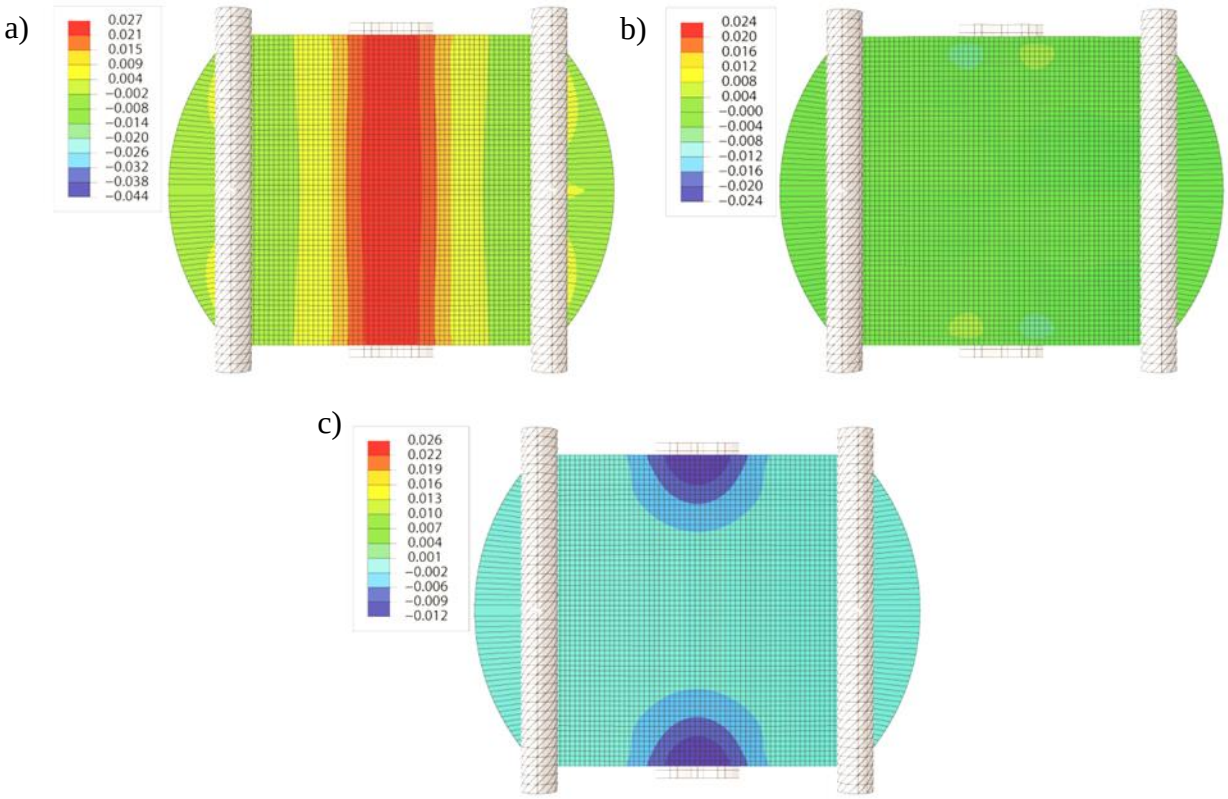

Figure 4.4. Color representations of total strain components: a) xx, b) xy, c) yy, determined from the FEA simulation on the 16.9% CW condition after a bend deflection of 58.3 µm.

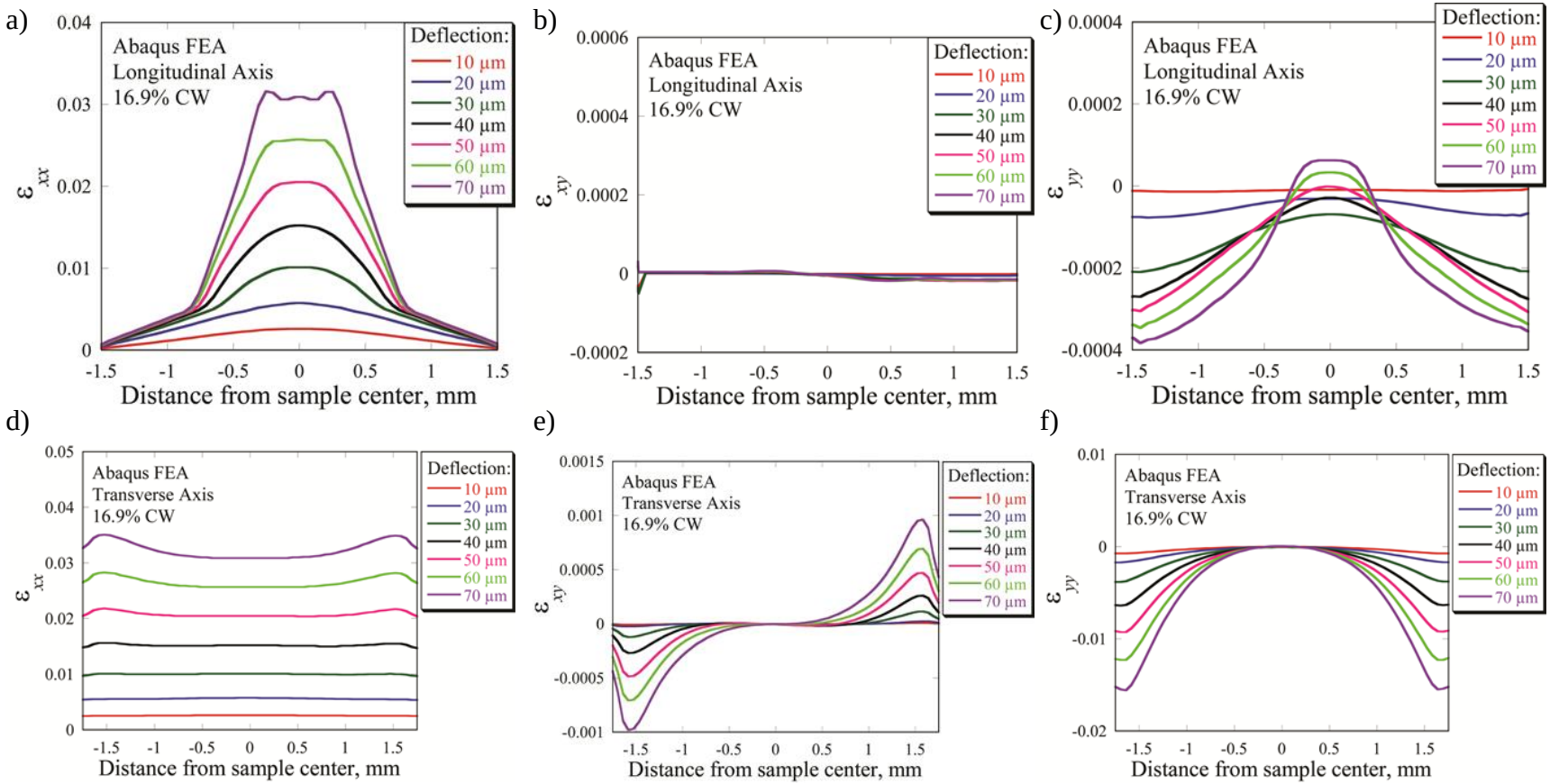

Figure 4.5. FEA results from the 16.9% CW condition at varying sample deflections. a) xx, b) xy and c) yy, components of total strain along the longitudinal axis, d) xx, e) xy, and f) yy components of total strain along the transverse axis of the bend sample.

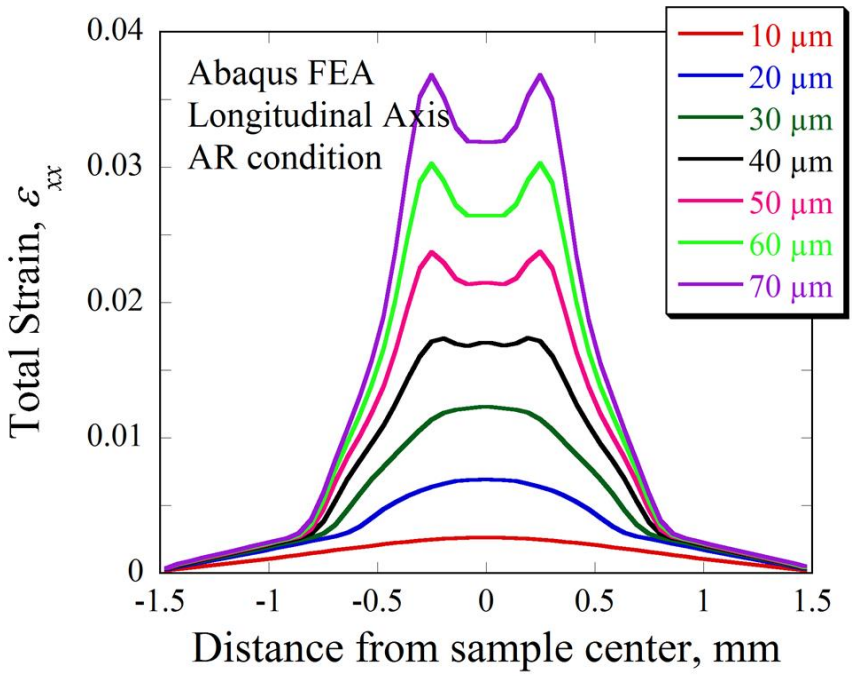

Figure 4.6. Quantitative strain profiles (xx component) at various sample deflections for the AR condition as predicted by FEA model.

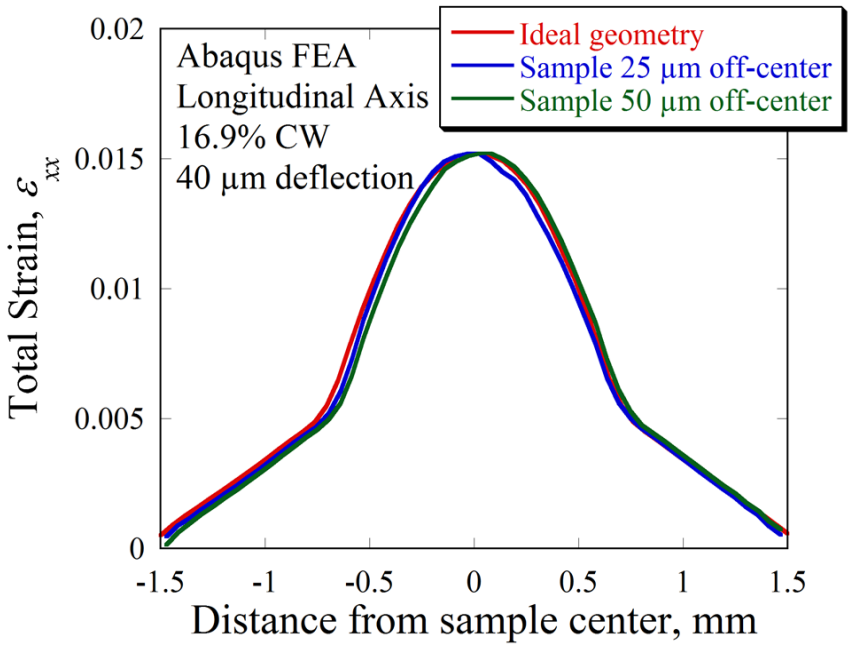

Figure 4.7. The effect of sample lateral off-centering on the profile of the xx component of strain for the 16.9% CW condition at 40 µm deflection.

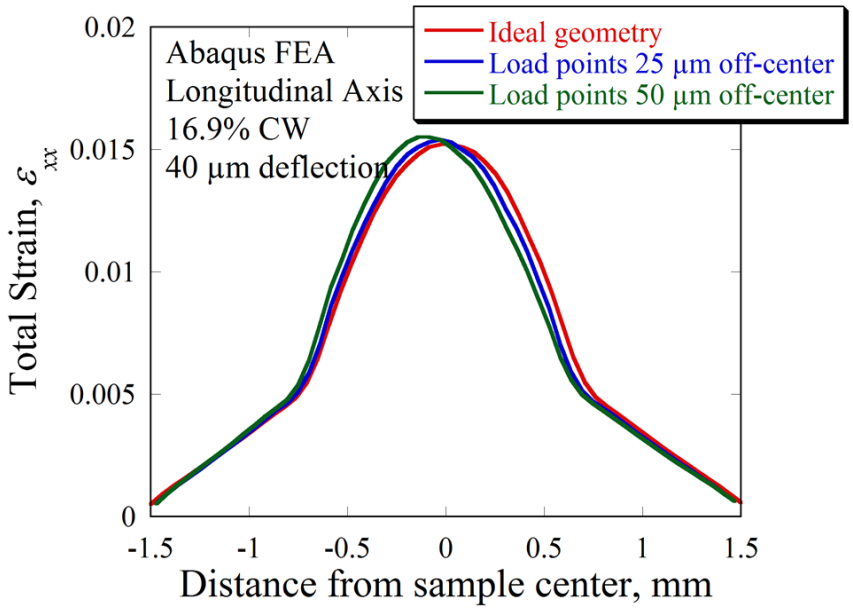

Figure 4.8. The effect of load point lateral off-centering on the profile of the xx component of strain for the 16.9% CW condition at 40 µm deflection.

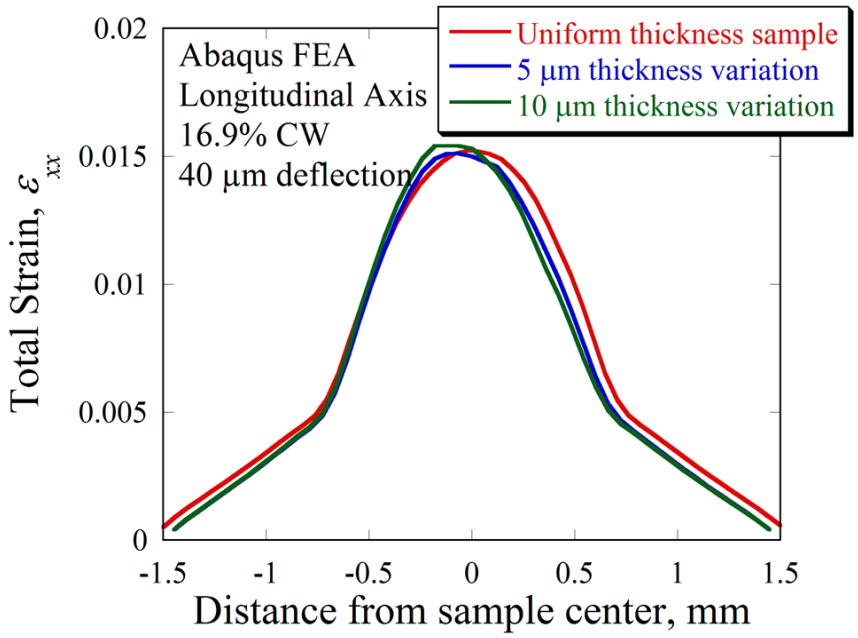

Figure 4.9. The effect of sample thickness variation on the ε_{xx} strain profile determined from FEA simulations on the 16.9% CW condition after 40 µm deflection.

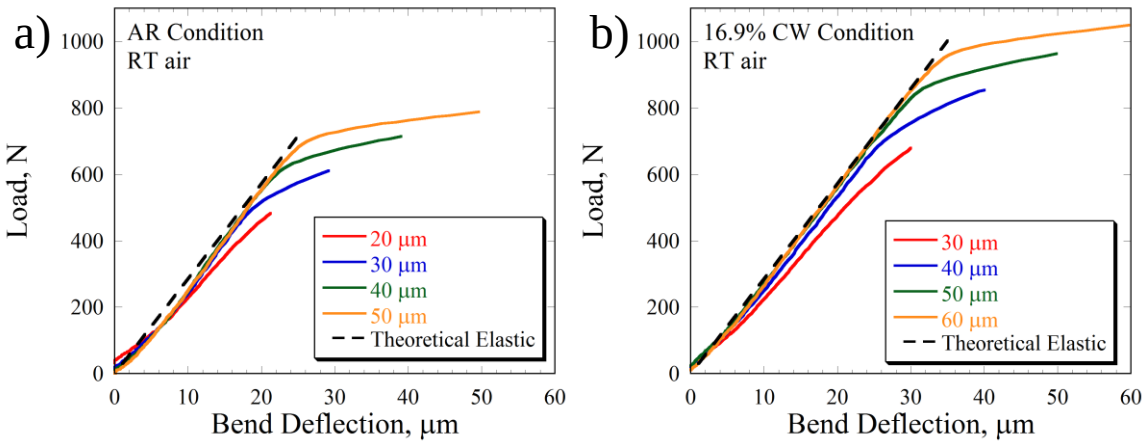

Figure 4.10. Load vs. bend deflection curves from incremented four-point bend tests in RT air on the a) AR condition and b) 16.9% CW condition.

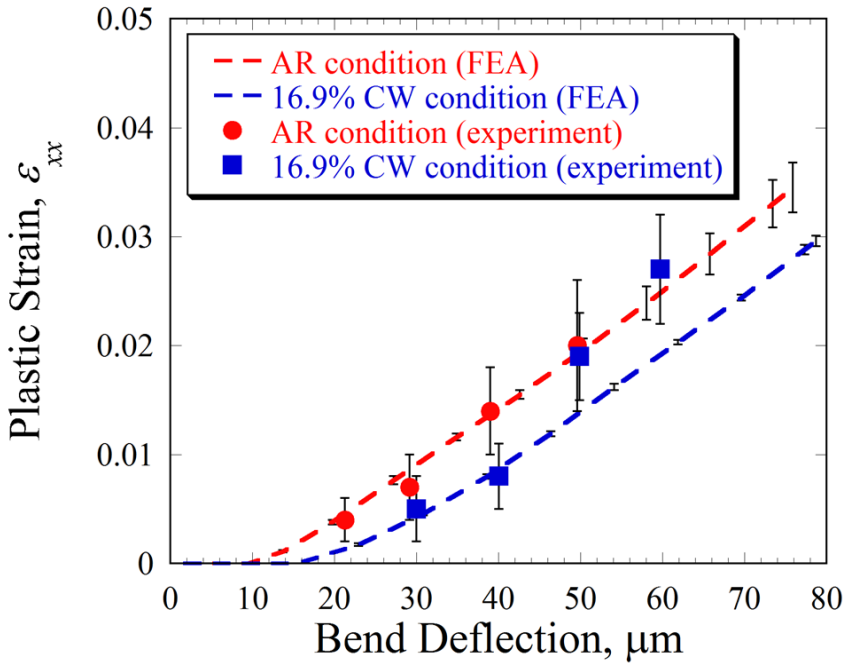

Figure 4.11. Average strain after incremented four-point bend experiments and FEA simulation on unirradiated AR and 16.9% CW samples in RT air.

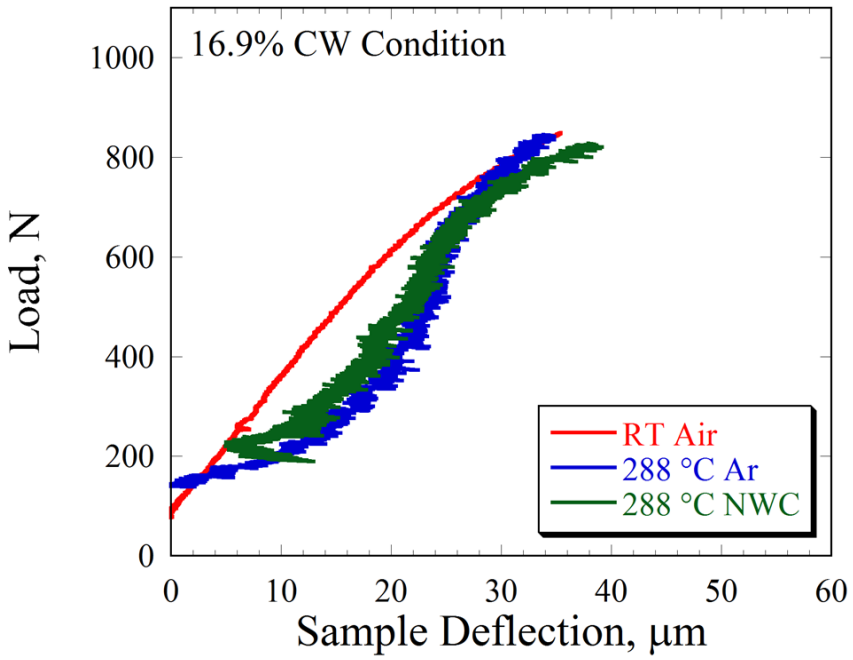

Figure 4.12. Load vs. bend deflection curves after four-point bend tests on unirradiated 16.9% CW samples in RT air, 288 °C Ar, and 288 °C NWC. Deflection in high temperature environments was measured using the compliance correction technique.

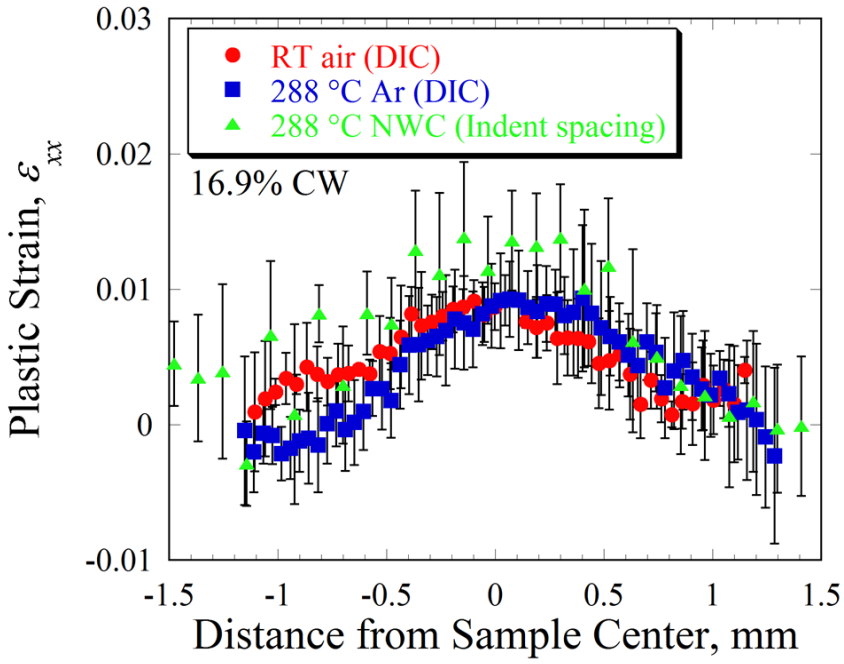

Figure 4.13. Plastic strain along the longitudinal axis of 16.9% CW samples after four-point bend tests to a nominal 40 µm bend deflection in each test environment. Strain in NWC was measured via indent spacing.

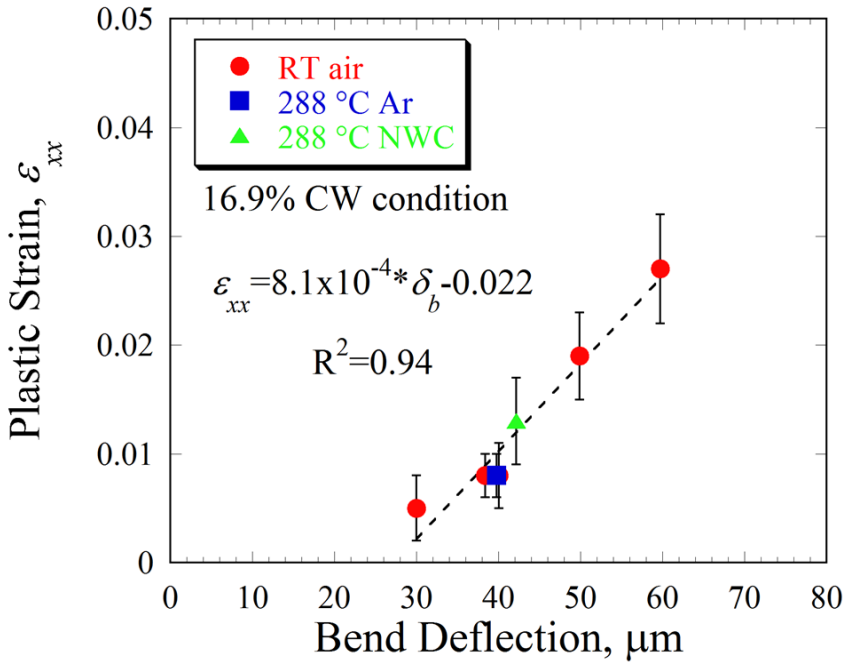

Figure 4.14. Average strain after four-point bend tests on unirradiated 16.9% CW samples in various environments.

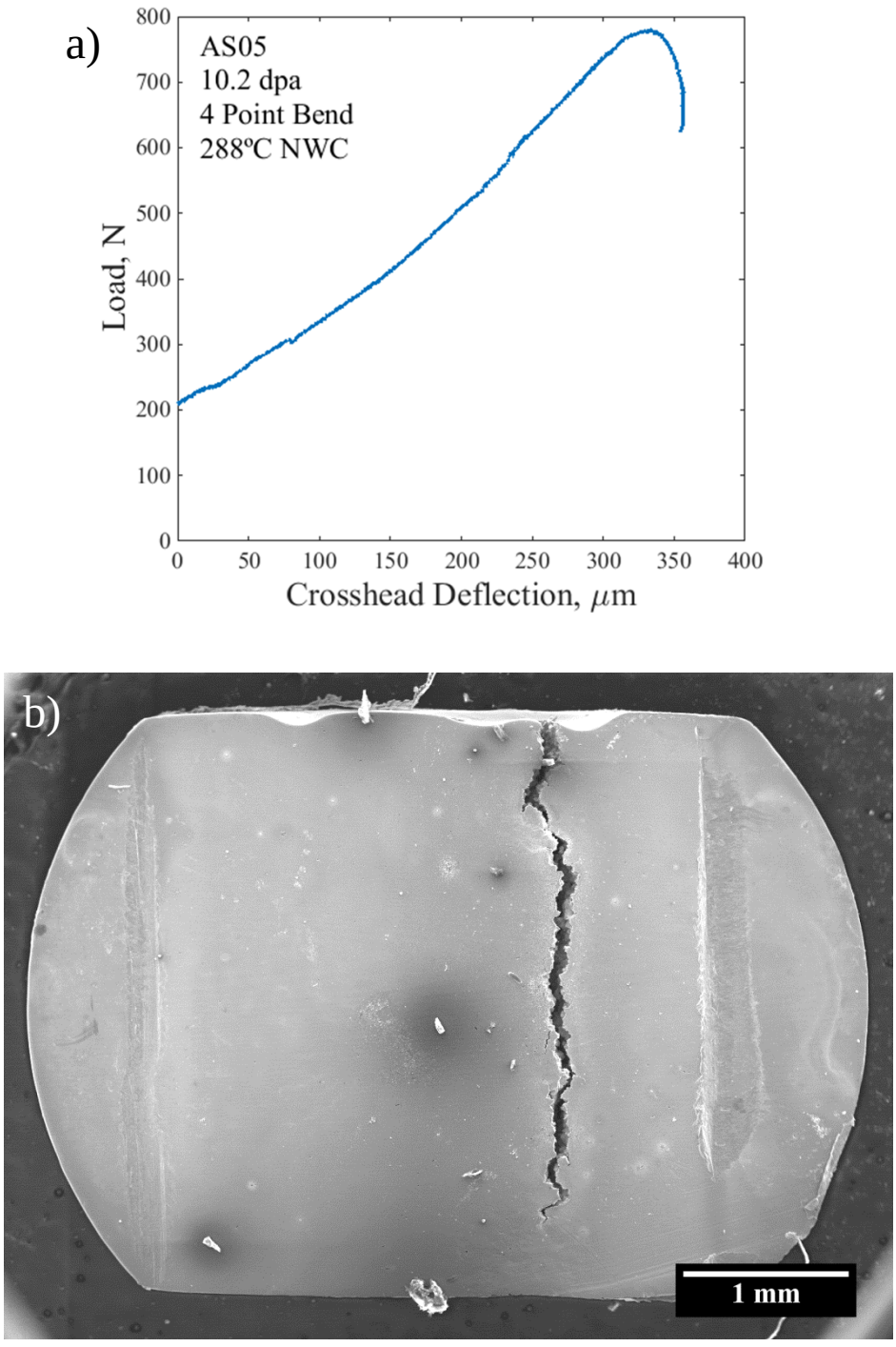

Figure 4.15. a) Load vs. crosshead (LVDT) deflection curve and b) sample surface after the four-bend test on irradiated sample AS05 performed in 288 °C NWC.

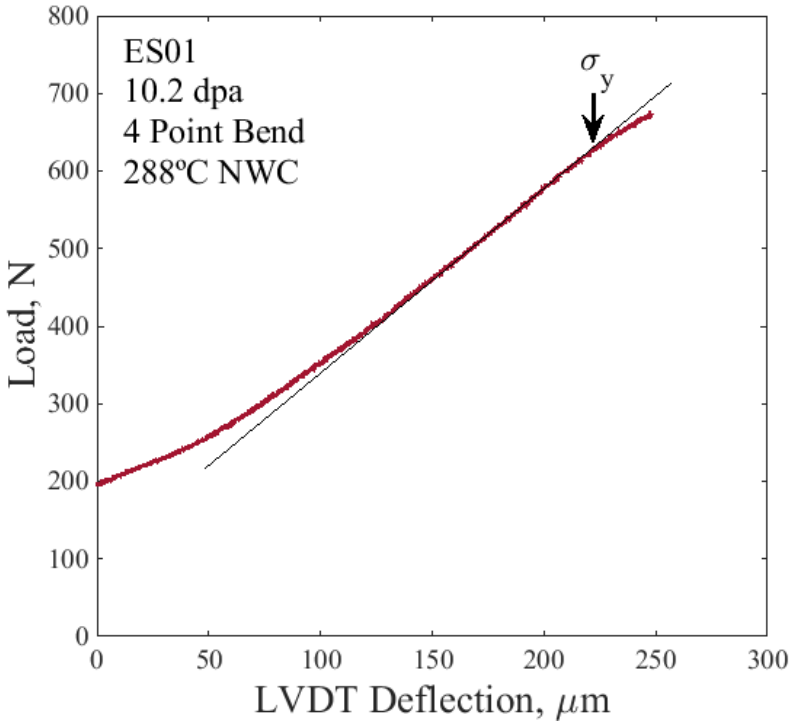

Figure 4.16. Load vs. crosshead (LVDT) deflection during the 7th four-point bend test on sample ES01. A line has been added to indicate linearity of the load vs. deflection behavior during elastic deformation. Differences are also observed in comparison to tensile stress-strain behavior after the occurrence of macroscopic yield: no drop in stress and strain hardening.

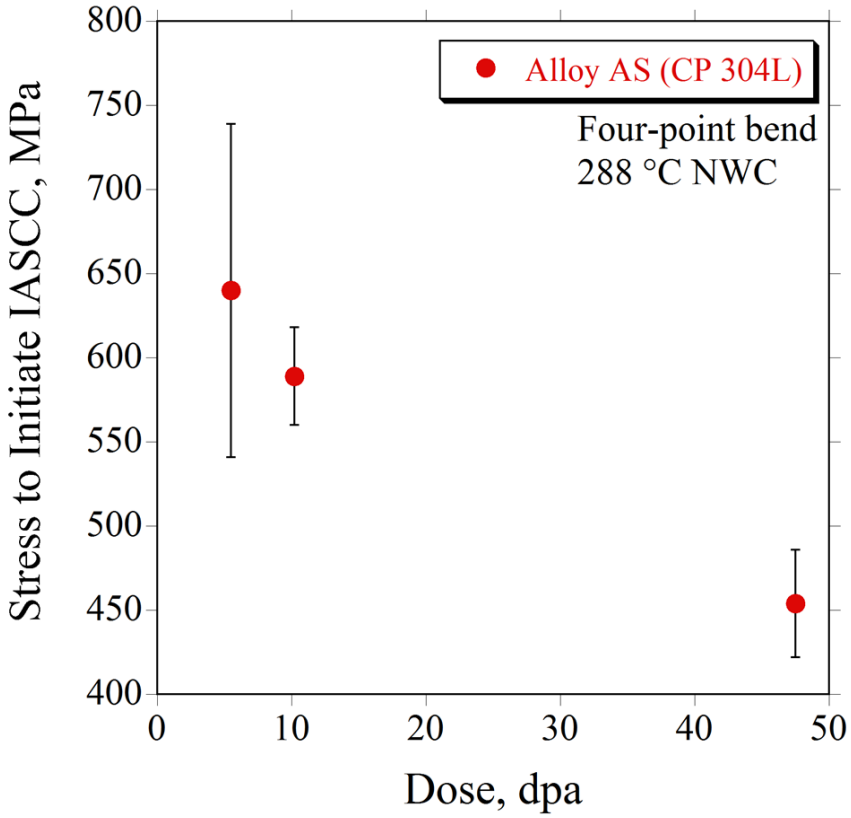

Figure 4.17. Average stress required for IASCC initiation determined from four-point bend tests in NWC on CP 304L alloy AS at irradiation doses 5.5, 10.2 and 47.5 dpa.

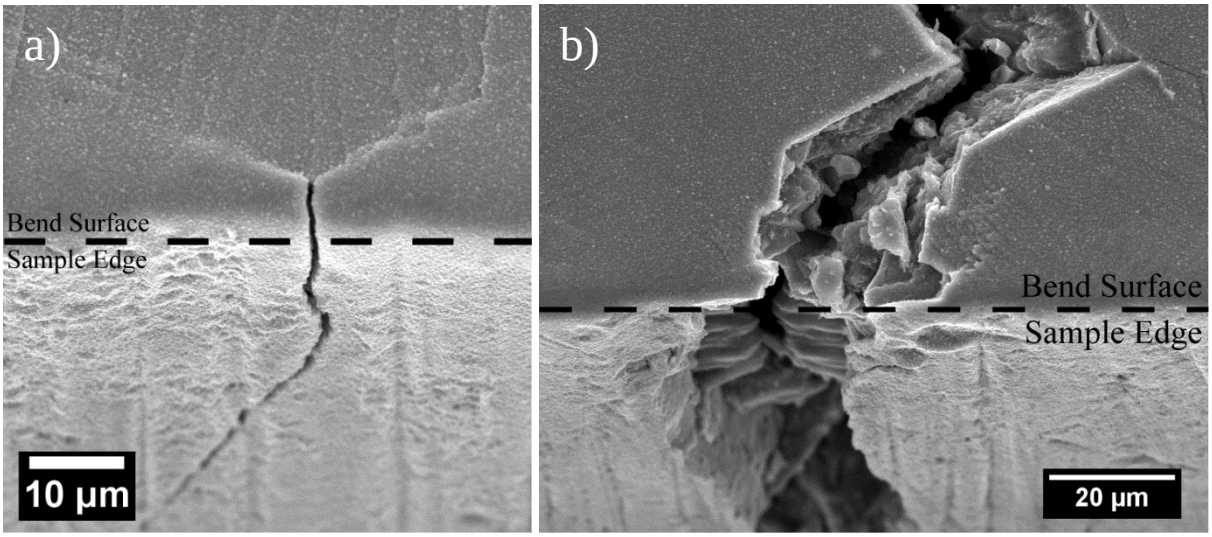

Figure 4.18. IGSCC initiation sites viewed from a ~45° angle of the sample edge on 10.7 dpa sample ES01 after four-point bend tests in NWC. Images were recorded a) after 1% plastic strain and b) after greater than 1.8% plastic strain.

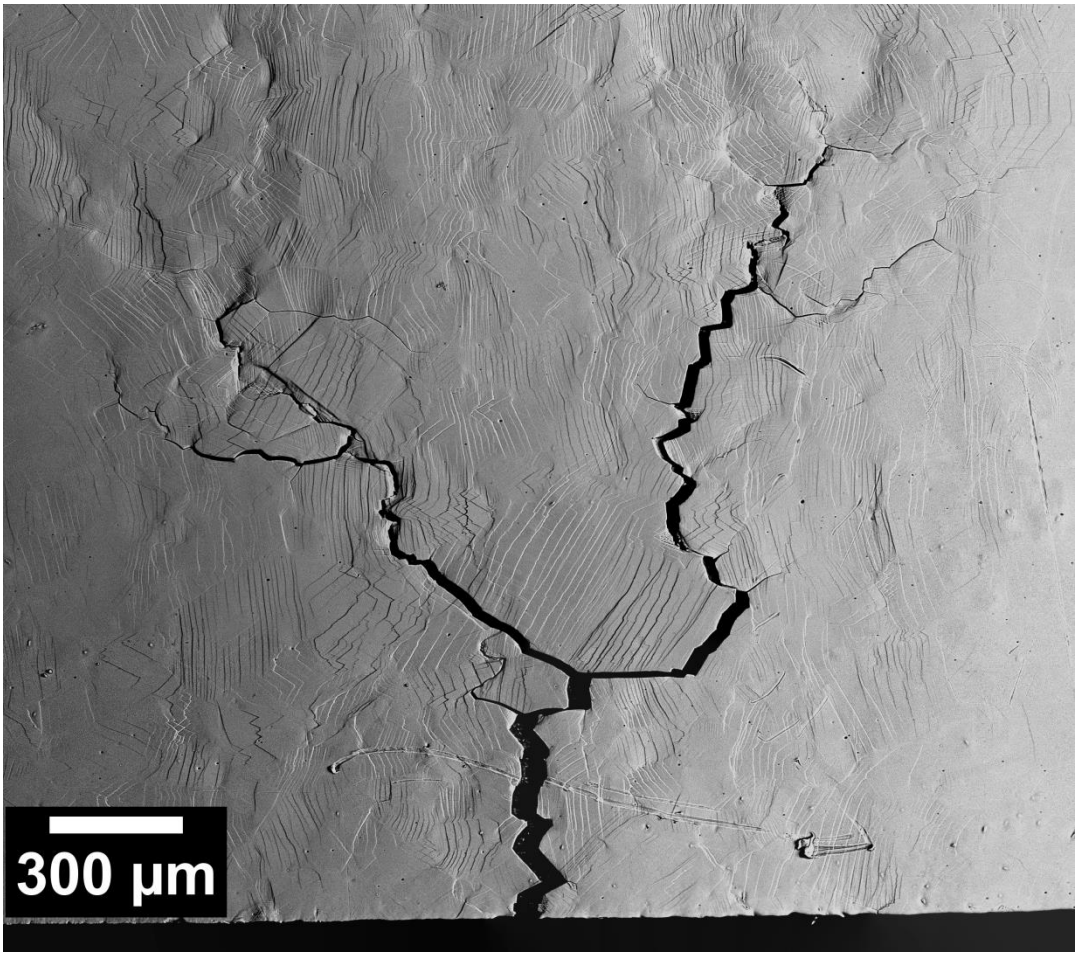

Figure 4.19. Overall view of the second IGSCC crack on 10.7 dpa sample ES01 after greater than 1.8% plastic strain in NWC.

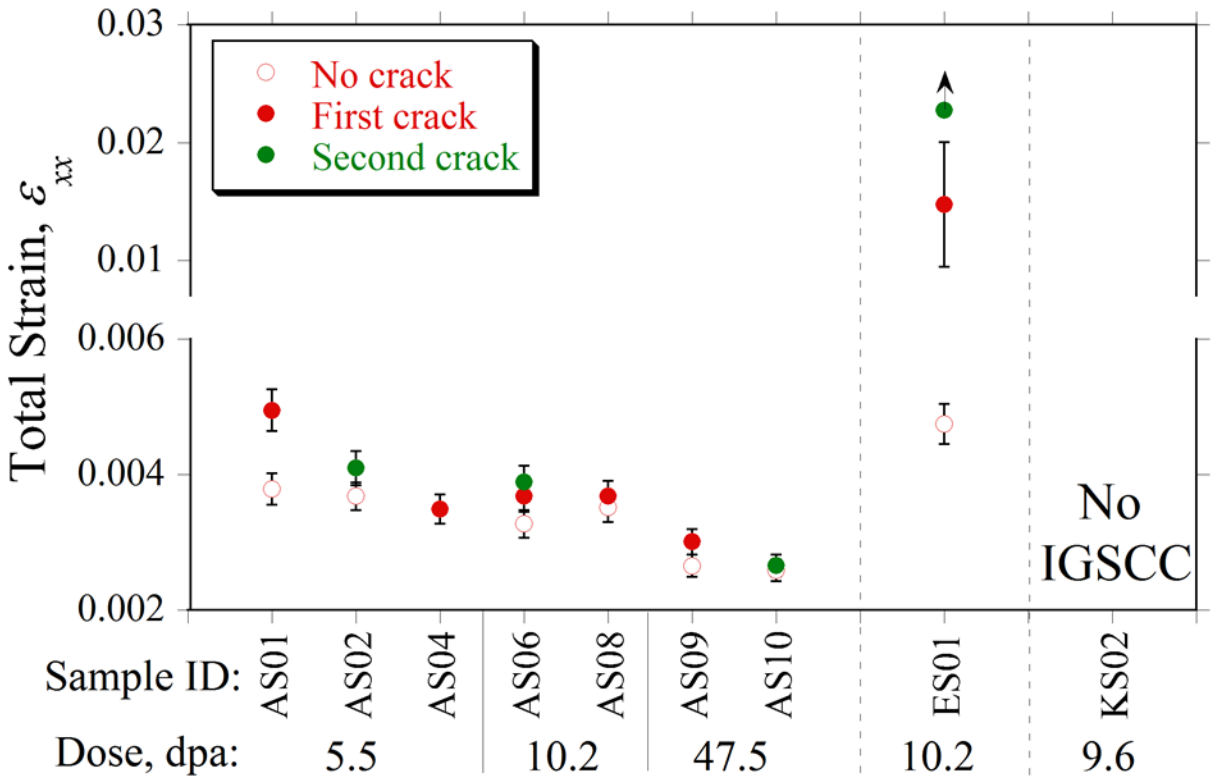

Figure 4.20. The maximum strain at which crack initiation was not observed, the minimum strain at which cracking was observed, and the minimum strain at which a second crack was observed for each four-point bend sample tested in NWC.

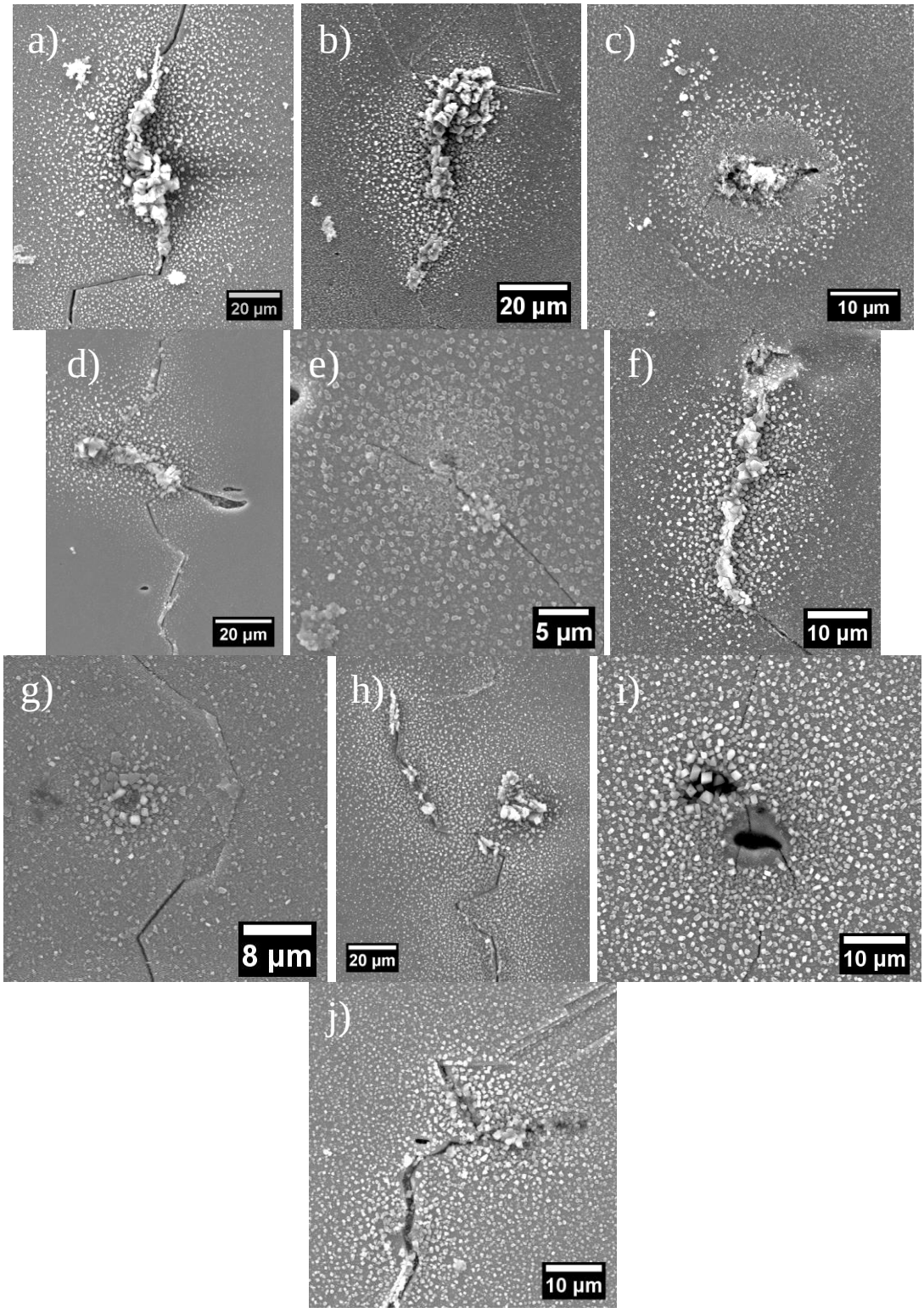

Figure 4.21. Inclusions at the site of crack initiation after four-point bend tests in NWC on 5.5 dpa samples a) AS01, b) AS02, c) AS02 (second crack), and d) AS04, 10.2 dpa samples e) AS06 f) AS06 (second crack) and g) AS08, and 47.5 dpa samples h) AS09, i) AS10 and j) AS10 (second crack).

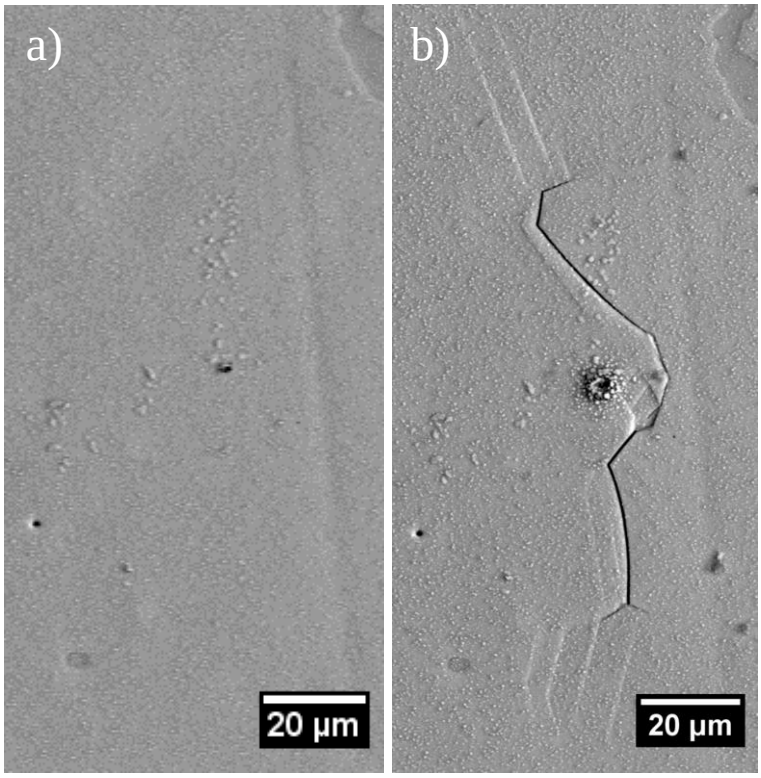

Figure 4.22. The 10.2 dpa sample AS08 after four-point bend tests in NWC ended at a) $0.71\sigma_y$ and b) $0.74\sigma_y$. The IGSCC site likely intersected an inclusion beneath the sample surface, and no oxide formation was observed prior to IGSCC initiation.

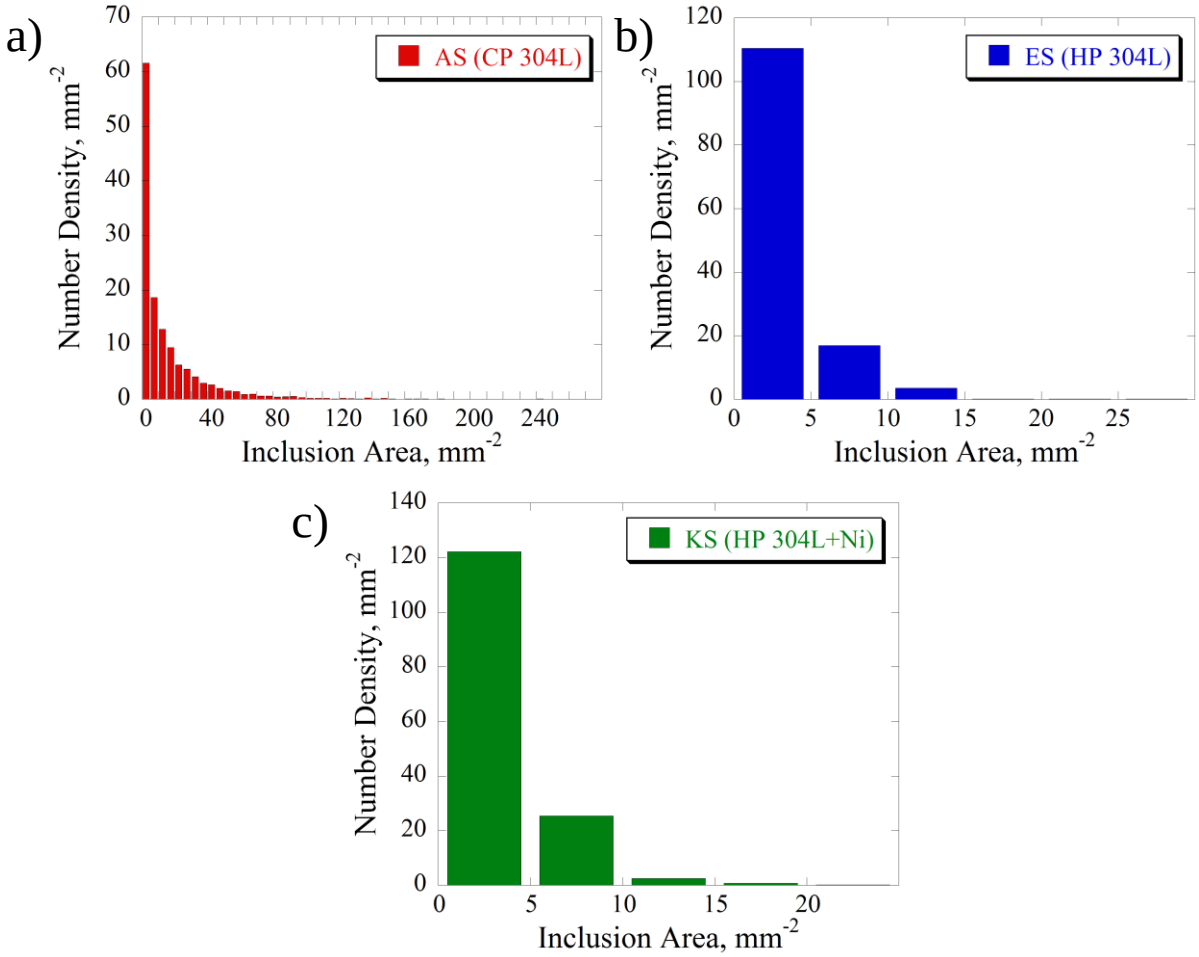

Figure 4.23. Histograms showing the distribution of inclusion size per mm^2 in alloy a) AS, b) ES, and c) KS.

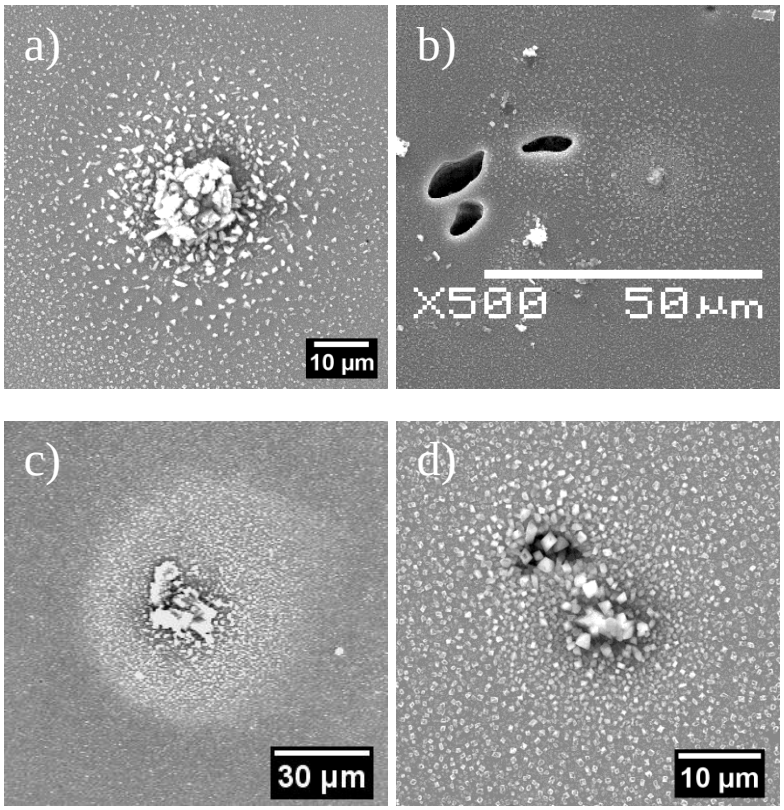

Figure 4.24. Inclusion sites with corrosion product prior to crack initiation during four-point bend tests in NWC on samples a) AS02, b) AS06, c) AS09, and d) AS10.

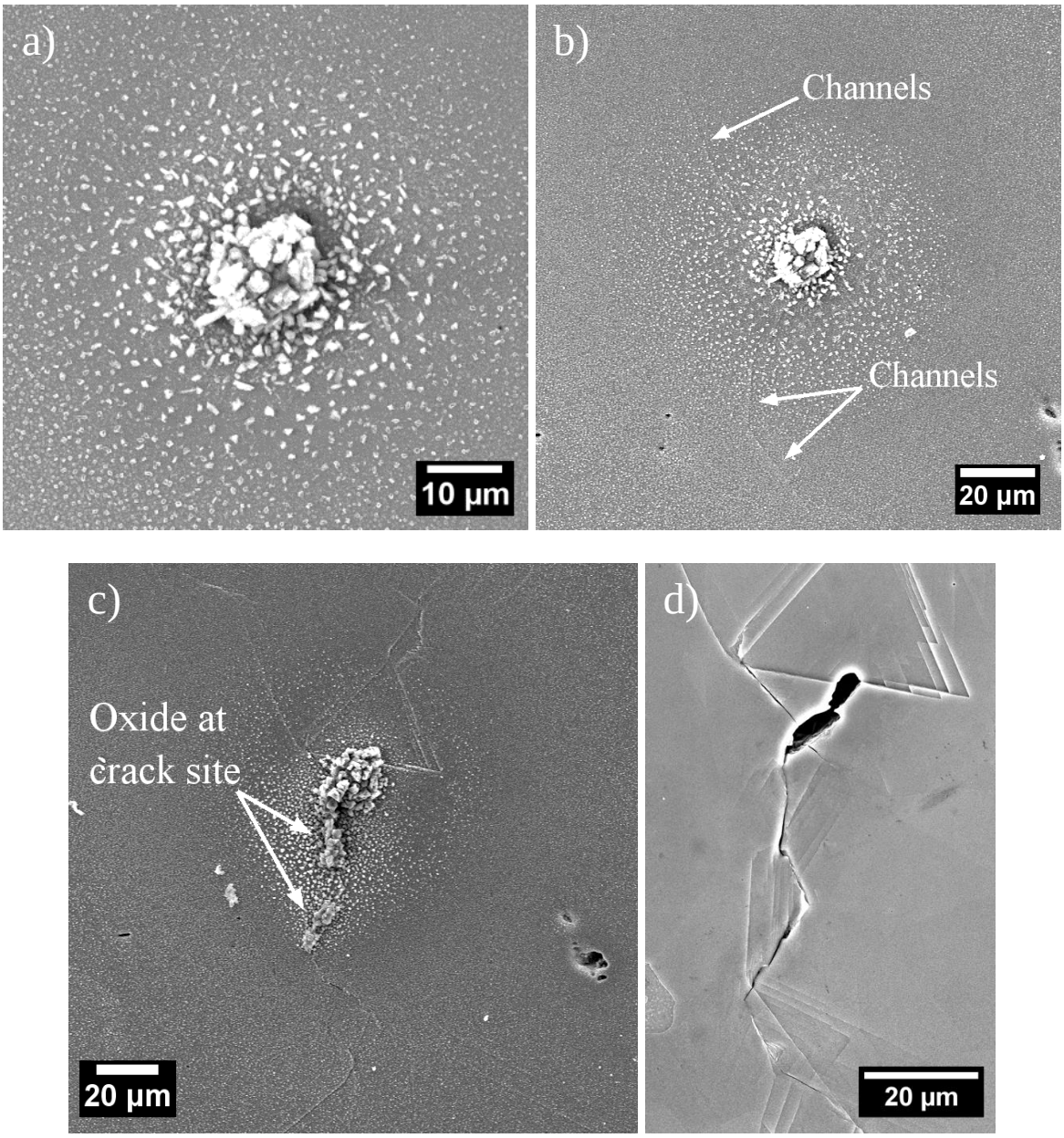

Figure 4.25. The formation of corrosion product at a surface inclusion and subsequent IGSCC initiation. Images taken on 5.5 dpa sample AS02 after four-point bend test increments in NWC ended at a) $0.70\sigma_y$, b) $0.78\sigma_y$, c) $0.87\sigma_y$, and d) $0.87\sigma_y$ post oxide removal.

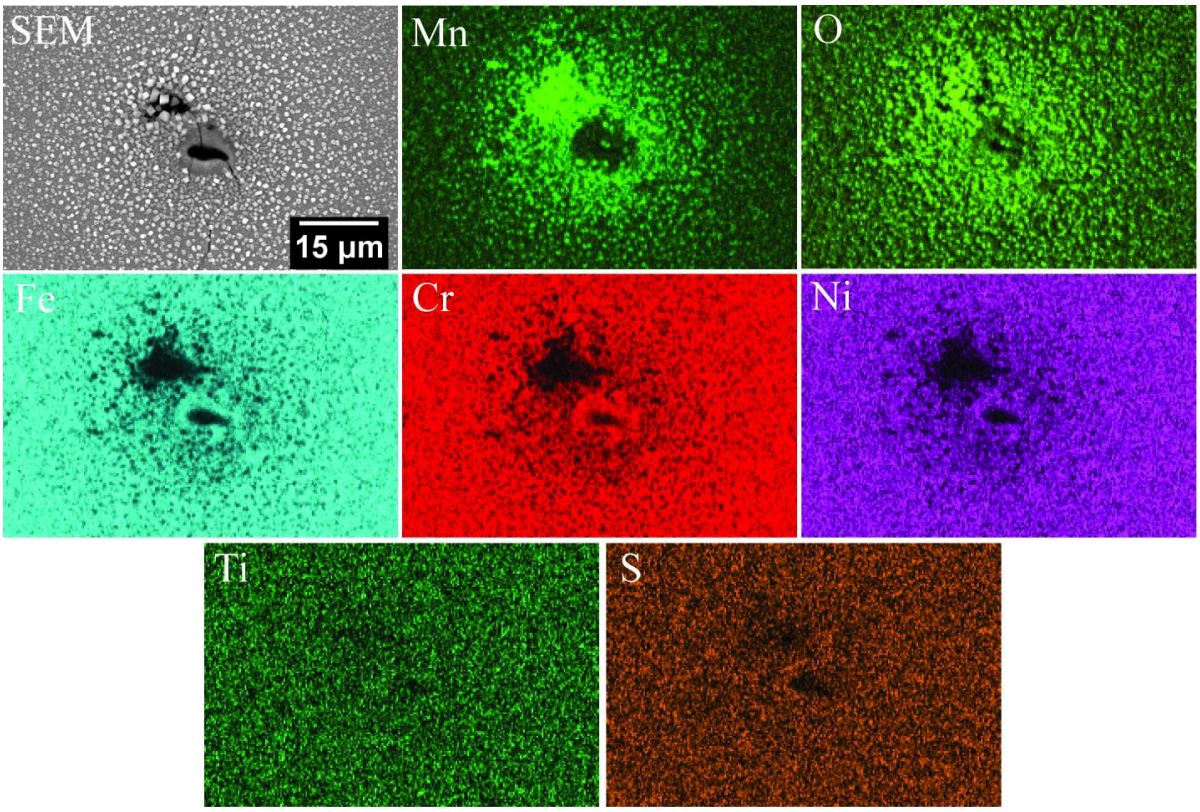

Figure 4.26. Chemical maps near a site of IGSCC initiation after four-point bend testing in NWC on 47.5 dpa sample AS10.

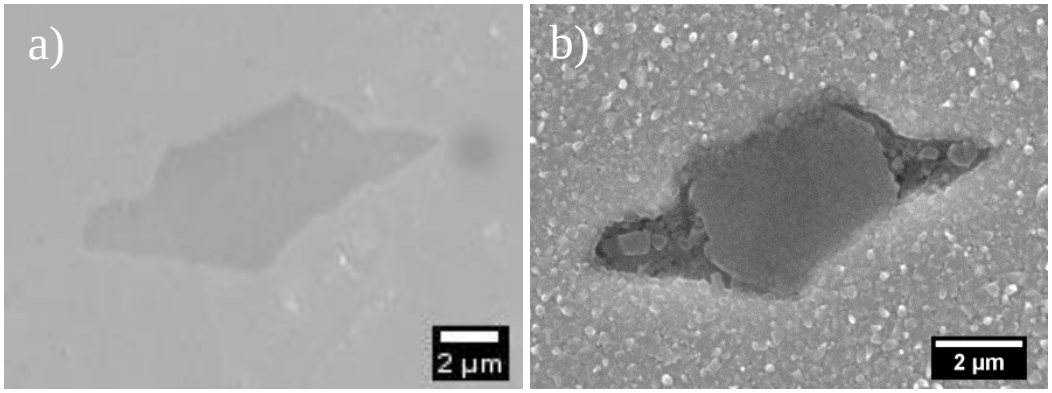

Figure 4.27. Examples of oxide inclusion appearance on an unirradiated sample of alloy AS a) before and b) after 24 hour NWC exposure in an un-stressed condition.

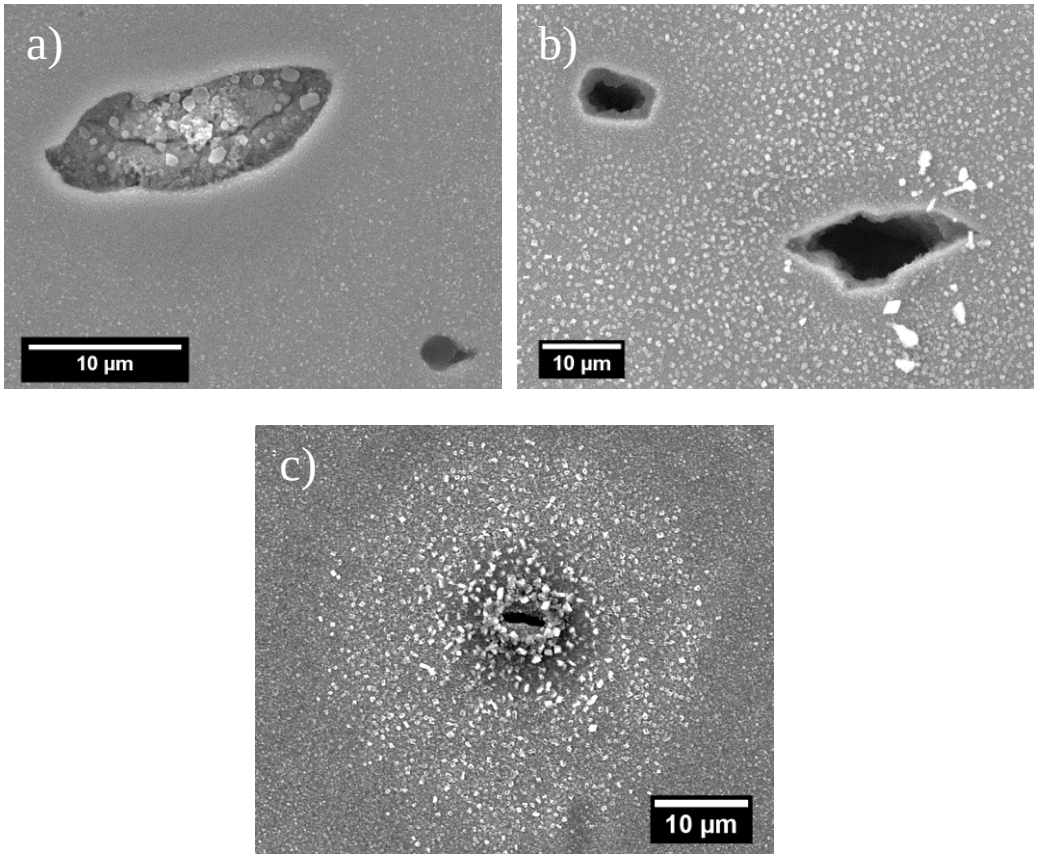

Figure 4.28. MnS inclusions on the surface of the unirradiated alloy AS sample after 24 hours of NWC exposure in an un-stressed condition which a) formed oxide within the inclusion site, b) dissolved completely, and c) formed corrosion product buildup around the inclusion site.

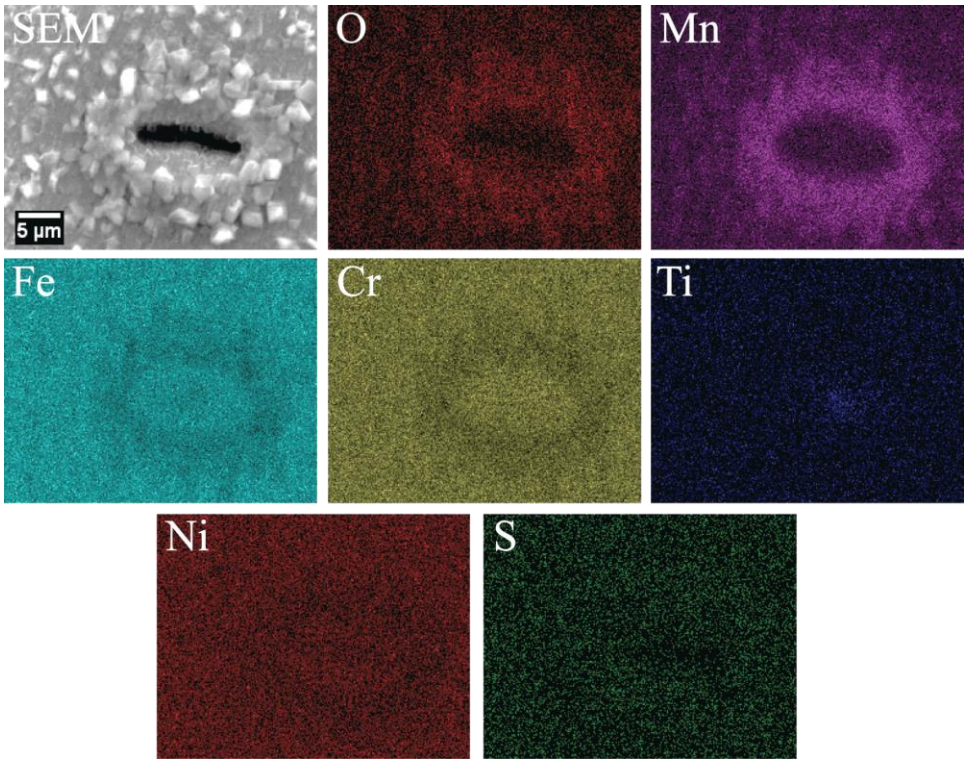

Figure 4.29. XEDS chemical maps at the location of large corrosion product formation on an unirradiated alloy AS sample after NWC exposure in an un-stressed condition.

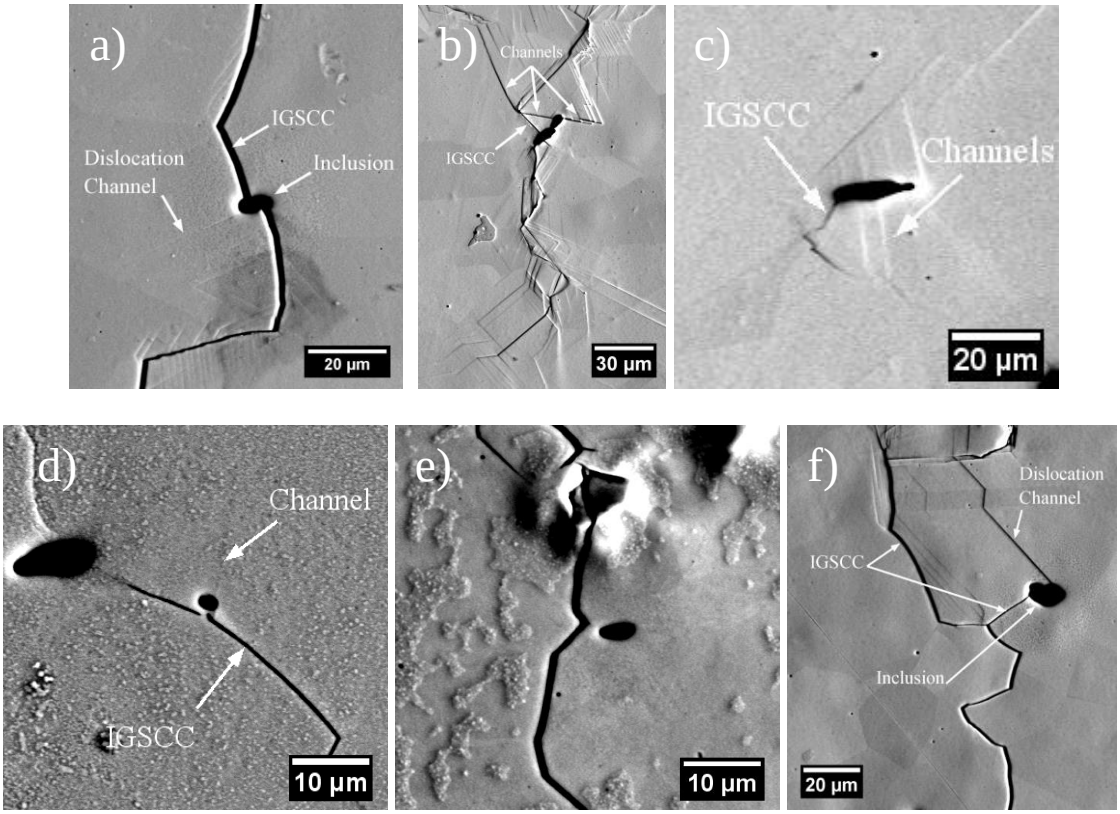

Figure 4.30. DC intersections at surface inclusions where IGSCC initiation occurred after four-point bend testing on 5.5 dpa samples a) AS01, b) AS02, and c) AS02, 10.2 dpa sample d) AS06 and e) AS06 (second crack, no DCs present), and f) 47.5 dpa sample AS09. All images were taken after removal of surface oxidation.

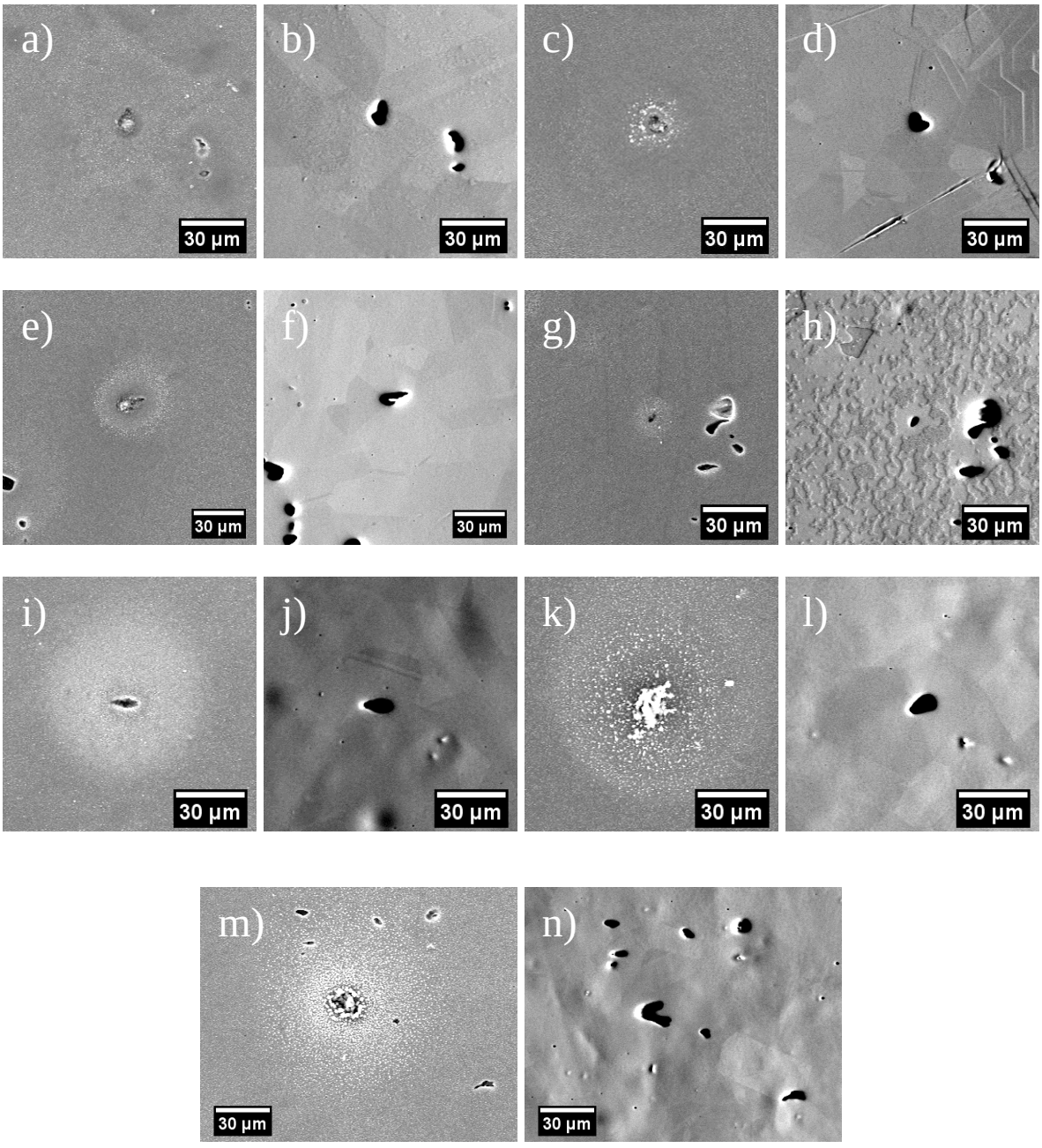

Figure 4.31. Inclusions which formed corrosion product but did not crack after four-point bend testing in NWC. 5.5 dpa samples a) and b) AS01, c) and d) AS02 (channels were near but did not intersect), e) and f) AS02, g) and h) 10.2 dpa sample AS06, and i) through n) 47.5 dpa sample AS09. The first image from each sample shows an inclusion before oxide removal, and second images are the same inclusion with oxide removed.

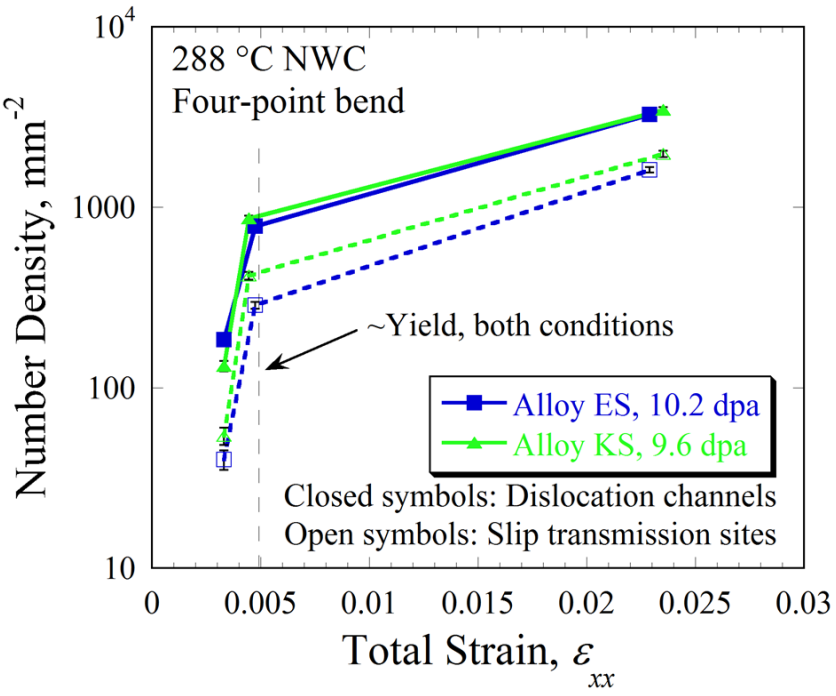

Figure 4.32. Channel and slip transmission site density for alloys ES and KS after four-point bend tests in NWC.

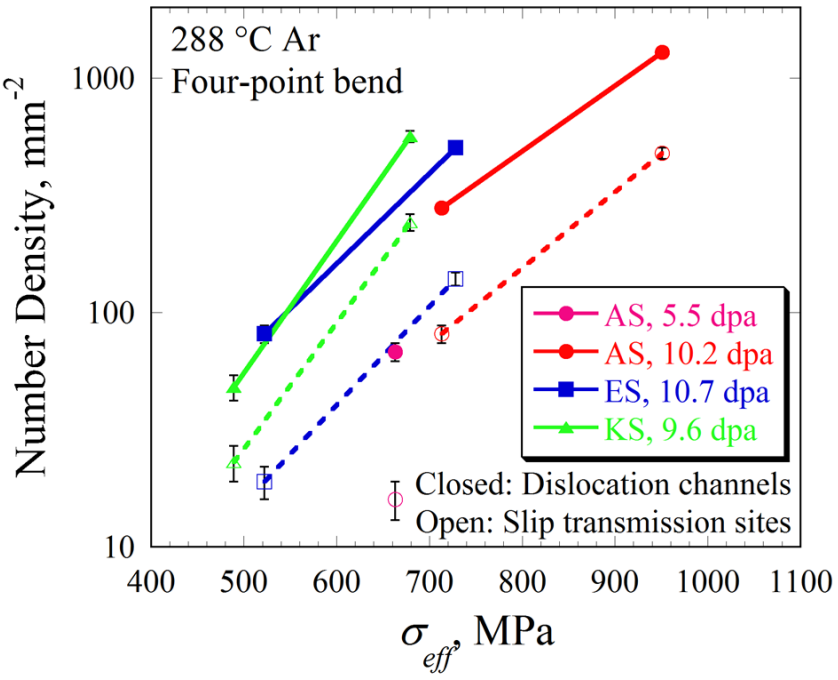

Figure 4.33. Channel and slip transmission site density for alloys AS, ES, and KS after four-point bend tests in 288 °C Ar. All measurements were taken before visible macroscopic yield.

CHAPTER 5 - DISCUSSION

The discussion first addresses observations determined from CERT tests, a common method used to compare SCC susceptibility among irradiated materials. Dislocation channeling was analyzed on CERT sample surfaces, but limitations led to the development of the four-point bend test. In section 5.2, the novel four-point bend SCC test was validated by comparing its results with CERT test results. Similarity between the two test types allowed a more broad analysis of the environmental dependence of IASCC initiation, discussed in section 5.3. Four-point bend test results revealed a decrease in the stress necessary to initiate IASCC with increasing irradiation dose, and section 5.4 discusses the statistical significance of this observation as well as comparison with available literature. Section 5.5 discusses observations of dislocation channeling at IASCC initiation sites in the CP 304L alloy as well as the stress dependence of channel initiation as an explanation for the stress dependence of IASCC initiation. MnS surface inclusions were also observed to affect IASCC initiation in the CP 304L alloy AS, and their contribution to crack initiation is discussed in section 5.6, followed by a discussion of the IASCC initiation mechanism for this alloy in section 5.7. Finally, section 5.8 discusses differences in cracking and dislocation channeling behavior observed among the HP 304L alloys ES and KS, as well as how the cracking mechanism was different in these alloys versus the CP 304L alloy AS.

5.1 Dependencies of IASCC initiation determined from CERT test results

Differences in mechanical behavior and %IG on CERT sample fracture surfaces revealed varying IASCC susceptibility (or a lack thereof in the case of alloy KS) among the irradiated alloys compared in this study. Because of existing correlations between IASCC and localized deformation [10,106,124,125,145,146], DCs near locations of IG fracture on the gage sections of the failed CERT samples were analyzed in more detail. This section discusses how these observations compared with IASCC behavior, and how findings led to development of the four-point bend test to more effectively analyze crack initiation sites.

Weighted average channel height was analyzed first on CERT sample surfaces and compared with %IG in Figure 5.1, because of the strong correlation with IASCC susceptibility determined on proton irradiated samples [9]. In this comparison, it was necessary to normalize the weighted average channel heights by total elongation because total elongation varied among CERT samples, and channel height is known to increase with strain [9]. It was evident that deformation became more localized in samples with increased IASCC susceptibility, except in the case of alloy KS.

The comparison in Figure 5.1 led to further consideration of how alternate DC characteristics (channel density/spacing, and tendency of channels to transmit across GBs) affect IASCC, but again, the varying ductility observed among CERT samples required that the evolution of each be known as a function of strain. While it is known that the number density of dislocation channels increases with strain, an exact correlation has yet to be established and likely varies depending upon alloy and dose [95]. Intersections of discontinuous DCs with GBs have been shown to be more susceptible to IASCC initiation than GBs which exhibit continuous slip, but

DC intersections at GBs can change classification (discontinuous to continuous) with increased strain [146]. Ultimately, uncertainty regarding how these DC parameters evolve with strain undermined the validity of comparing DCs on CERT samples. As a result, additional measurements of DC characteristics on tensile bar gage sections were not performed, and the four-point bend test was developed to compare DC parameters after similar magnitudes of applied stress and strain. Prior to analyzing DC parameters and IASCC initiation sites created in the four-point bend test, general IASCC behavior observed in the four-point bend test was compared to that determined in the CERT test.

5.2 Comparison of four-point bend test results with CERT test results

The four-point bend test was successful in creating IASCC initiation sites with limited propagation, but the validity of results from this test were carefully examined because of the novelty of the test technique and the lack of comparable literature data. The CERT test is a well-established method for comparing relative crack initiation susceptibility among neutron irradiated materials subjected to similar test conditions, therefore a comparison of cracking susceptibility in the four-point bend test relative to the CERT test was used to establish the validity of the novel SCC test. Recall that the same test environment and strain rate used in CERT tests were used in four-point bend tests.

Strain to initiation from four-point bend tests was compared with strain to failure (total elongation) from CERT tests, an indicator of crack initiation susceptibility [28]. Figure 5.2 compares these two metrics, omitting alloy KS because of its lack of IASCC susceptibility in both test types. Strain to crack initiation in the four-point bend test was conservatively estimated by using the midpoint in strain between bend tests interrupted before and after crack initiation, as

described by equation 3.14. Error on these data points was determined using the formulation of equation 3.15.

The four-point bend test reproduced the same order of susceptibility among irradiated conditions tested in the uniaxial CERT test, which validates its ability to create a similar condition for crack initiation as in the CERT test. In both cases, the highest dose sample of alloy AS (47.5 dpa) had the smallest strain to initiation/failure, followed by the 10.2 dpa condition and then the 5.5 dpa condition. The differences in crack initiation/failure between the three conditions were quite small but captured by both test types. The crack initiation/failure strain of alloy ES was much higher in both tests. Error on the data point for alloy ES was much larger than those for alloy AS samples because of the magnitude of the strain increment applied during which cracking occurred, and also because the sample had entered into the plastic deformation regime which required strain to be estimated using the correlation in Figure 3.13.

The similarity in relative cracking susceptibility among the two tests confirmed that the interrupted test technique used for four-point bend tests did not significantly affect cracking behavior (recall that CERT tests were conducted in an un-interrupted manner to failure). Low cycle fatigue was a minor concern in the interrupted four-point bend tests, however, the similar behavior observed among the CERT and four-point bend results indicates that fatigue cracking was unlikely to have affected the bend test results. Unfortunately, literature regarding the effect of fatigue on IASCC is unavailable, and the only fatigue crack initiation studies on irradiated material have been performed in air and at very low irradiation dose by Nogami et al. [147]. In Nogami's study, irradiation caused an increase in slip step spacing, yet fatigue crack initiation was not observed in the proton irradiated material until ~1000 cycles [147]. Fatigue cracking in 300 °C primary water did not occur in unirradiated 304 SS until approximately 10,000 cycles,

even at strain amplitudes as high as 0.5% [148]. Considering that less than 10 loading cycles were applied to irradiated samples in the four-point bend test, it is unlikely that this test method affected the cracking behavior. Furthermore, the alloy KS sample subjected to the largest number of cycles and the largest magnitude of stress and strain during these cycles did not form any crack initiation sites.

5.3 Environmental dependence of IASCC

Comparison among CERT and four-point bend test results in NWC enables a broader consideration of how the test environment affects IASCC initiation. Comparing cracking behaviors in high temperature inert environments with those from high temperature water environment assists with identifying key factors that affect the crack initiation process.

No cracking was observed in the current study after four-point bend tests in inert 288 °C Ar, even after the application of nearly twice the amount of strain necessary to cause IGSCC initiation in NWC. Kodama et al. [149] also reported a lack of IG cracking after CERT tests in Ar conducted on neutron irradiated SS with known susceptibility in simulated LWR environments, although no fracture images were shown. However, other authors have shown GB separation and IG cracking after CERT tests in high temperature inert gas, but only after significant strain between 5% and 10% [8,14,105,106]. The separated GBs in the study by Fukuya et al. [8] were observed in the highly deformed (necked) region of the sample gage section having at least 2% plastic strain (more strain than was applied in the current four-point bend tests in Ar), at GBs inclined nearly normal to the tensile axis. DCs were also observed impinging on the separated GBs from only one of the two adjacent grains, and the separated GBs terminated at triple points. West et al. [106] also observed that only GBs inclined nearly

perpendicular to the tensile axis cracked after 5% strain in 400 °C Ar. GBs inclined normal to the tensile direction, discontinuous DCs [11], and triple points [56] concentrate local stress at GBs, therefore it is likely that GB separation was caused by stress concentration due to a combination of these factors. It is apparent that GB separation and IG cracking are possible in inert conditions, however, the process of purely mechanical GB separation in inert environments is different from the crack initiation process during IASCC because much higher strain is necessary for this type of cracking to occur.

In water environments, IASCC susceptibility has known dependence on ECP. Reduced ECP caused increased strain to failure in CERT tests conducted on the same alloys used in this study [28]. Alloy ES displayed nearly 100% ductile failure after CERT testing in 320 °C primary water, although short brittle cracks (with mixed IG/TG appearance) were observed around the periphery of the sample fracture surface, and numerous instances of GB separation were observed in the highly deformed region of the sample gage as shown in Figure 5.3. Observations of IG crack initiation sites revealed that most cracked GBs were inclined nearly perpendicular to the tensile direction and many had DCs impinging on one side of the cracked grain boundary (Figure 5.3c and d), similar to observations from experiments performed in inert environments. Reduction in the depth of IG crack penetration was also observed after CERT tests conducted in high temperature water with decreasing levels of DO [150]. These observations show that IG crack initiation in water environments, similar to inert environments, is likely caused by stress concentration at the GB. However, it is apparent that the stress necessary for crack initiation and the propensity for crack propagation are affected by the aggressive nature of the environment.

The differences in cracking and mechanical behaviors under varying environmental conditions imply that the cracking mechanism is affected by the corrosive nature of the environment. This

statement is supported by the fact that the density of cracked GBs is always higher after SCC tests in simulated LWR environments than in tests performed in inert gas environments to a similar level of strain [106,125]. Ductility is enhanced in low potential environments (due to limited crack propagation) relative to high potential environments, therefore more GBs achieve the threshold stress or strain required for cracking to initiate. As the high temperature water environment has an evident effect on IASCC susceptibility, the stress-strain condition necessary for crack initiation must be analyzed to understand the mechanism.

5.4 Stress dependence of IASCC initiation

Figure 4.17 showed that the stress required for IASCC initiation decreased in alloy AS with irradiation dose. This observation was unexpected, considering that the hardness of the alloy increased over the same dose range. To improve confidence in the observed results, interval censored data analysis [151,152] was applied to determine whether the differences in the stress required to initiate IASCC among dose conditions were statistically significant.

Using the interval package available in the statistical computing environment, *R* [153], stress intervals during which IASCC initiation occurred were compared considering all samples of alloy AS tested in NWC. Bounds on stress were selected as the maximum value of stress where no cracking was observed and the value of stress applied after a crack had formed, as summarized in Table 5.1. Because crack initiation was observed after the first stress increment applied to sample AS04, the lower stress bound was estimated by comparison with the stress interval applied to sample AS02, which was the same sample condition and had a similar crack length.

The survival curves shown in Figure 5.4 resulted from interval censored analysis comparing 5.5 and 10.2 dpa alloy AS conditions. Survival curves represent the probability of IASCC initiation over certain stress intervals, which are compared to determine the p-value associated with the null hypothesis: that there is no significant difference between the compared curves. The associated p-value for this instance was 0.55, indicating a relatively low (45%) probability that a significant difference existed in the stress required for IASCC initiation. The low confidence in this case was likely due to a combination of the limited dataset and the small difference in irradiation exposure.

Because of their similarity, 5.5 and 10.2 dpa conditions were compared together against the 47.5 dpa condition, resulting in the survival curves shown in Figure 5.5. The p-value for this instance was 0.098, indicating that the stress required for IASCC initiation was lower in the 47.5 dpa condition, with greater than 90% confidence. The comparison drawn from the large interval in irradiation exposure shows strong likelihood that lower stress is able to initiate IASCC at higher levels of radiation damage.

Constant load tests (CLT) are also commonly used to determine SCC initiation susceptibility in neutron irradiated materials, due to simplicity in sample design and experimental setup. In the CLT, several O-ring type samples are typically loaded in series and held at a constant load during exposure to a LWR environment. Time to failure is then recorded and databases have been formed based upon the amount of applied stress, which is varied depending upon the length of the sample or the applied load. Applied stress on the CLT O-ring samples is calculated using the von Mises effective stress, similar to the technique used in the four-point bend tests in this study. Neutron irradiated CLT databases have been accumulated by authors such as Chopra [154] and Bosch [13].

Figure 5.6 shows that a reduction in the stress to initiate IASCC with dose was observed in CLTs, overlapping the stress dependence of IASCC initiation determined from four-point bend tests. Both the magnitude of the stress required for IASCC initiation (~50% of the irradiated yield strength at irradiation dose greater than ~20 dpa) and the trend with dose were similar in CLTs and four-point bend tests, despite several experimental differences:

- Static (constant load) vs. dynamic (four-point bend test) loading
- Low potential, 320 °C primary water environment (constant load) vs. high potential, 288°C NWC (four-point bend test)
- Cold-worked (constant load) vs. solution annealed (four-point bend test) starting material state

Authors that conducted CLTs have been unable to provide a reason for IASCC initiation at applied stress below the yield stress, primarily because of limitations in the observation of crack initiation sites, as CLTs cause significant crack propagation after initiation. Furthermore, it remains unknown why the stress to initiate cracking apparently saturates at ~20 dpa, when irradiated microstructure and hardening saturate at ~5 dpa.

The agreement between CLT and four-point bend test results indicates that the dose dependence of cracking is similar in high temperature water despite differences in sample design, loading geometry, sample condition and corrosion potential. However, the four-point bend test provides an important advantage over CLT tests – the opportunity to observe IASCC initiation sites in detail. Analysis of the features at crack initiation sites has the potential to provide insight as to the underlying mechanisms affecting the crack initiation process, and creates a response to some of the remaining questions such as why the decreasing stress for crack initiation is observed. The

following sections will introduce key features observed at crack initiation sites in each of the tested alloys, and comparisons to relevant literature data.

5.5 Dislocation channeling and IASCC in CP 304L alloy AS

Dislocation channels were observed on all irradiated samples and conditions in the four-point bend test after the application of unexpectedly small stress magnitudes. In several cases, DCs were observed after the application of stress as low as ~50% the macroscopic yield strength, σ_y. Despite the fact that theoretically, all deformation is elastic and fully recoverable prior to reaching σ_y, the observation of DCs indicates that some locations in the microstructure achieved the stress necessary to cause local yielding at applied stress below σ_y. DC formation prior to macroscopic yield has been observed in the literature [88]. However, details regarding how these channels affect SCC initiation, especially in neutron irradiated materials, are limited. In this section, crack initiation behavior and observations of dislocation channeling are compared to establish whether DCs are the cause of IASCC initiation.

Recent work analyzing channeling and cracking behavior in proton-irradiated SS has shown a strong dependence on the interaction between DCs and GBs. DCs which intersect GBs but *do not* transmit strain (via formation of another DC) into the adjacent grain are referred to as discontinuous DCs, and are significantly more likely to result in crack initiation than sites where DCs transmit across the GB (continuous DCs) [11,146]. Stress concentrations are high at discontinuous DC-GB sites, while channels that transmit do not form significant stress concentration, as shown in Figure 5.7. Alternatively, the strain imposed at the GB is small at discontinuous DC-GB intersections, but much higher at sites of slip transmission [146]. Thus, it has been concluded that stress, not strain, is the main factor affecting crack initiation at a GB

[146]. It is not slip at a GB below the oxide layer which causes it to rupture, but local stress that overcomes the cohesive strength of the oxide layer at the GB [146]. These observations are supported by evidence of SCC initiation at GBs with an inclination nearly normal to the tensile axis, which also form a high local stress condition [140].

In alloy AS, removal of surface oxidation after NWC exposure revealed the presence of discontinuous DCs at 5 of 6 crack initiation sites, as shown in Figure 4.30. In most cases, only a few DCs were present at crack initiation sites, and these DCs adjacent to the crack were the only DCs observed in the same longitudinal plane of the sample surface. DCs were only observed on 3 of 7 alloy AS samples prior to crack initiation (as indicated in Table 4.4), but this was likely a result of the discrete nature of surface observations made during the four-point bend test procedure as well as a lack of thorough surface imaging on samples tested early in the campaign.

The limited number of DCs observed on alloy AS sample surfaces prior to crack initiation was different from observations on proton irradiated SS, as dislocation channeling becomes quite developed before crack initiation is observed to occur [9,10,106,125,146]. When DCs first form, they typically are confined to a single grain because the magnitude of the stress induced by the dislocation pileup within the initial DC is insufficient for transmission to occur. As a result, these DCs form stress concentration at the GBs where they terminate. Based on observations from alloy AS and proton irradiated SS, it stands to reason that for IGSCC to occur, a discontinuous DC must either: 1) contain enough dislocations for the stress at the GB to exceed the cohesive strength of the oxide layer at the GB, or 2) form at a location that is favorable for crack initiation to occur. The latter appears to be the case in alloy AS, as surface inclusions were also present at locations of crack initiation (Figure 4.30), and are assumed to have created a favorable location for crack initiation. Despite their presence, the inclusions common to these cracking sites are not

responsible for the observed decrease in stress to initiate IASCC with irradiation dose because they were present in all alloy AS samples regardless of irradiation dose and test environment (NWC or 288 °C Ar). Therefore, the stress dependence of DC formation in alloy AS was analyzed in more detail.

5.5.1 Stress dependence of dislocation channeling in alloy AS

The observation of discontinuous DCs intersecting crack initiation sites, but the limited observations of DCs prior to crack initiation led to an analysis of the stress dependence of dislocation channeling. If the average stress to initiate DCs was less than that to initiate cracking for a particular irradiated condition, it would provide additional evidence that DCs were a causative factor in the crack initiation process, thus causing the decrease in stress required for IASCC initiation with increasing irradiation dose.

DCs form with increasing stress, making possible an estimate of the stress to initiate channeling in alloy AS samples. It was found that the channel density increased linearly with stress for samples at ~10 dpa in the elastic strain region, as shown in Figure 5.8. This correlation was used to back extrapolate to the stress at which DCs began to form on each alloy AS sample, $\sigma_{DC,sample}$, by using the formula:

$$\sigma_{DC,sample} = \sigma_{initial-DC} - \frac{\rho_{channels}}{\beta_{DC-\sigma}} \quad , \qquad (5.1)$$

where $\sigma_{initial\text{-}DC}$ is the stress applied after channels were first observed, $\beta_{DC\text{-}\sigma}$ is the slope of the correlation between channel density and stress, 2.67 channels per mm^2 per MPa, and $\rho_{channels}$ is the density of channels observed. Error on $\sigma_{DC,sample}$ ($\varphi_{DC,sample}$) was calculated using the error propagation technique:

$$\varphi_{DC,sample} = \sqrt{\varphi_{\sigma}^2 + \frac{1}{\beta_{DC-\sigma}^2} \cdot \varphi_{\rho}^2 + \rho_{channels}^2 \cdot \varphi_{\beta}^2}\,, \qquad (5.2)$$

where φ_{σ} is the error on the stress when channels were first observed (based on the correlation in Figure 3.11), φ_{ρ} is the error on the measured channel density (estimated by taking the square root of the number of channels observed, as only one measurement was made per sample), and φ_{β} is the error on the slope of the correlation in Figure 5.8 (±0.77 channels per mm^2 per MPa, determined by calculating the 95% confidence interval on the slope of the correlation using Microsoft Excel).

The average DC initiation stress for each alloy AS dose condition ($\sigma_{DC,condition}$) was then calculated by averaging $\sigma_{DC,sample}$ values if multiple measurements were available:

$$\sigma_{DC,condition} = \frac{1}{N}\sum_{i=1}^{N}\left(\sigma_{DC,sample}\right)_i\,. \qquad (5.3)$$

Error on $\sigma_{DC,condition}$ was calculated using the error propagation technique, also considering the standard deviation among $\sigma_{CI,sample}$ for each condition:

$$\varphi_{DC,condition} = \sqrt{\frac{1}{N^2}\sum_{i=1}^{N}\left(\varphi_{DC,sample}\right)_i^2 + \varphi_{stdev}^2}\,. \qquad (5.4)$$

Results of this analysis are summarized in Table 5.2, showing $\sigma_{DC,sample}$ for each alloy AS sample and $\sigma_{DC,condition}$ for each dose condition. Figure 5.9 shows that at each irradiation dose condition in alloy AS, the average stress to initiate dislocation channeling was less than the stress for IASCC initiation. This result, together with the observation of discontinuous DCs at IGSCC initiation sites, provides evidence that discontinuous DCs cause IASCC initiation and thus the decrease in stress to initiate IASCC with increasing irradiation dose.

The assumption that discontinuous DCs cause high stress concentration at the GB where they terminate and lead to crack initiation fits well with the mechanism described by McMurtrey et al. [146]. However, observational limitations during four-point bend tests prevent this conclusion from being made with certainty, as these channels could possibly have formed after crack initiation. The limited number of channels and their coincidence with surface inclusions at crack initiation sites in alloy AS would indicate that the inclusions possibly played a role in their formation. However, if it is assumed that channels formed at random, analysis of the irradiated microstructure in alloy AS at each dose condition will provide insight as to whether channeling would be expected at varying magnitudes of applied stress, because the irradiated microstructure controls irradiation hardening and thus DC formation.

5.5.2 Microstructure dependence of dislocation channeling

Although it is generally accepted that irradiated microstructure evolution typically saturates by approximately 5 dpa, the availability of microstructural data from alloy AS samples at each irradiation dose allowed microstructural features to be considered as a potential cause for the observed decrease in stress necessary to initiate DCs. Dislocation loop and precipitate microstructure characterization was performed in the previous CIR program by Edwards [23,27] and more recently by Tan [155] to analyze the presence of various irradiation-induced defects, their size, and their number density. Characterization by Edwards was performed on TEM samples of alloy AS at 5.4, 10.3 and 46 dpa, while the characterization by Tan was performed directly on samples removed from the heads of the same tensile bars used in this study: 5.5 dpa sample AS13 and 10.2 dpa sample AS18. Because characterization performed by Tan was conducted on the same materials used in the SCC tests this study, the results of his analysis are considered to more accurately represent the observed behavior.

A summary of the average size and density of irradiation induced defects observed in alloys AS, ES and KS are reproduced from Edwards [23,27] and Tan [155] in Figure 5.10. Edwards showed that the average size of dislocation loops and irradiation-induced precipitates does not change drastically between 5.4 and 46 dpa, although Tan reported loop size to increase between 5.5 and 10.2 dpa as the loop size distribution shifted to larger loop sizes [155]. After 46 dpa, Edwards reported a small density of SFT as well as a small fraction of partially-dissociated dislocation loops [27], indicating that dislocation loops began transforming to SFT [156]. No unfaulted loops or line dislocations were observed at this dose [27]. Despite the discrepancy among the dose dependence of defect size, both authors reported dislocation loop density to decrease with dose, even though the density of loops reported by Tan was less that that reported by Edwards at both ~5 and ~10 dpa. The discrepancy among dislocation loop size and density in these reports would suggest that the tensile bar samples experienced a slightly higher irradiation temperature than the TEM disks, likely as a result of their locations in the BOR-60 reactor during irradiation.

Edwards reported a lack of precipitation after 5.4 dpa, but a density of precipitates had formed after 10.3 dpa [23]. Strongly diffracting second phase particles were observed after both 5.5 and 10.2 dpa by Tan [155]. On account of the small size of these precipitates, neither author observed well-defined diffraction patterns from these precipitates after ~5 or ~10 dpa. Tan observed a weak diffraction spot that indicated these precipitates were either G-phase or $M_{23}C_6$, although these phases could not be conclusively distinguished because both produce a similar diffraction pattern relative to the austenitic matrix, as they have similar crystal structure and lattice constants [155]. After 46 dpa, precipitation was more extensive, and confirmed to be cube-on-cube oriented G-phase (a Ni-Si rich FCC phase) [27]. Based on these observations, it can be assumed that the indistinguishable precipitation observed after ~5 and ~10 dpa was likely a precursor to

the fully developed G-phase, although the strongly diffracting particles reported by each author indicate that these phases at ~5 and ~10 dpa were more developed than simple solute atoms clusters, as shown in Figure 5.11. Both Edwards and Tan reported the density of irradiation-induced precipitates to increase with dose. The apparent temperature difference among samples characterized in these studies based on the dislocation loop observations evidently had little effect on irradiation induced precipitation after ~10 dpa, however, this may have been the cause for the observation of precipitates at 5.5 dpa in the characterization performed by Tan [155].

Although the microstructure characterization at 46 dpa provided by Edwards [27] is likely an inaccurate representation of the microstructure in the 47.5 dpa samples used for CERT and four-point bend tests in this study (due to the observed differences at ~5 and ~10 dpa), the consistency in the observed trends among the datasets is noteworthy. From the available microstructure data, it can be concluded that the size distribution of dislocation loops shifts slightly to larger sizes as dose increases, with a subsequent decrease in dislocation loop density. As irradiation dose progresses past ~10 dpa, it is apparent that these dislocation loops begin to dissociate and form SFT. Irradiation-induced formation of G-phase precipitates is apparent at ~5 dpa, and the number density of precipitates increases with irradiation dose.

The results of these analyses provide an explanation for the increase in hardness as a function of dose in alloy AS, because irradiation induced precipitates are generally considered stronger obstacles to dislocation movement than dislocation loops [62,87]. Although the number density of dislocation loops decreased slightly in alloy AS with dose, it is apparent that this factor was outweighed by the precipitate evolution. Applying the dispersed barrier hardening model described in equations 1.2 and 1.3 to the microstructural analysis performed by Tan [155], the expected change in yield strength can be calculated and compared with the actual change in yield

strength. Using α values of 0.4 and 0.8 for dislocation loops and precipitates, respectively (Frank loops commonly have α values between 0.33 and 0.45 while precipitates have α values of ~1 in austenitic systems [62]), the calculated $\Delta\sigma_y$ for alloy AS samples at 5.5 and 10.2 dpa were 572 and 637 MPa, respectively. Comparing these values to the $\Delta\sigma_y$ measured during conventional tensile tests on alloy AS tensile samples at 5.5 and 10.2 dpa [28], it is observed that these calculated values are very comparable to those that were measured. At 5.5 dpa, alloy AS had a $\Delta\sigma_y$ of 570 ± 18 MPa (a difference of 0.4% from the calculated value) and at 10.2 dpa, the $\Delta\sigma_y$ was 611 ± 13 MPa (a difference of 4.3% from the calculated value). No attempt was made to compare irradiation hardening and microstructure at 47.5 dpa due to the observed differences in microstructure among TEM samples and measurements made from the tensile bars.

Despite the agreement between the characterized microstructure and the observed hardening, an understanding of why the stress to initiate dislocation channels decreased with dose remains unknown. It is possible that dislocation channels are affected by the decreasing loop density as a function of dose, yet considering the increase in hardening, it is not expected that localized deformation would occur under the application of less stress. Jiao and Was [95] provided convincing analysis that an increase in dislocation loop density correlated with weighted average channel height. This result is consistent with the idea that deformation becomes more localized as irradiation-induced defect densities increase, yet it provides no insight into the understanding of how channels form as a function of applied stress.

The observed decrease in loop density must also be interpreted with caution, as TEM analyses of irradiated microstructures only consider very small volumes of material and may not be accurate representations of the bulk microstructure. Fukuya et al. [157] reports that defect diameter and density variations less than a factor of 2 are within experimental error in this type of analysis.

Therefore, the results presented by Tan [155], despite their agreement with the measured hardening, are likely not statistically different. Considering this, it provides an alternate explanation for the low confidence that a statistically significant difference existed in the stress to initiate IASCC among the 5.5 and 10.2 dpa conditions. Additional characterization is necessary to accurately determine the characteristics of the irradiated microstructure on 47.5 dpa alloy AS condition used for CERT and four-point bend tests to confirm whether the dislocation loop density decreases significantly. Furthermore, systematic studies are necessary to understand how the irradiated microstructure affects DC formation.

In addition to the discontinuous DCs at crack initiation sites in alloy AS, inclusions also appeared to play a role in the crack initiation process. The following section addresses these inclusions and how they affected the crack initiation process.

5.6 The role of MnS inclusions in IASCC initiation of CP 304L alloy AS

All IG cracks in alloy AS intersected surface inclusions; indicating that they participated in the IASCC initiation process. As a result, this section addresses potential mechanisms by which these inclusions caused crack initiation, including: local stress concentration, how inclusions affected DC formation, and inclusion dissolution during high temperature water exposure. Inclusions often affect crack initiation in stainless steels (both irradiated and not), therefore a review of the literature is also provided to determine whether similar effects of inclusions have been previously observed.

Inclusions at IASCC initiation sites in alloy AS were confirmed to be MnS, based on observations in this alloy pre-irradiation and the composition of corrosion products at IASCC initiation sites. Exposure of the unirradiated alloy AS sample to NWC conditions showed that

only MnS inclusions were unstable in this environment, as a lack of Ti observed at these sites confirmed that they were not of the oxide variety (the only other inclusion type observed in this alloy). Furthermore, corrosion product near MnS inclusions on the unirradiated alloy AS sample after NWC exposure was enriched in Mn, similar to the corrosion product that had formed near inclusions at IASCC initiation sites.

MnS inclusions have specifically been observed to cause crack initiation in unirradiated pressure vessel steels [158,159], however, cracking after SSRT tests on unirradiated steels was transgranular in nature and required much more strain to cause failure than CERT tests on irradiated materials. Proton-irradiated versions of alloy AS were CERT tested in NWC by Busby [20], and although a high degree of cracking was observed in the irradiated region, no cracks were reported outside the irradiated area. Therefore, irradiation enables IG cracking susceptibility in SS alloys with MnS inclusions, and crack initiation in these irradiated alloys is likely caused by a different mechanism than in unirradiated steels.

Similar to Cookson's [160] observations of inert oxide particles influencing IASCC initiation, inclusions were typically observed at the center of the IG cracks in alloy AS, near the location where the crack had the widest opening. Cracking in alloy AS was obviously initiation controlled, as once a crack had initiated, it would more than likely propagate until failure (as was the case in the CERT samples as well as sample AS06 tested in the four-point bend test). Consequently, it is of great importance to identify how these particular inclusions affected crack initiation.

Prior to analyzing the details of how inclusions affect crack initiation, it must first be established that these inclusions undoubtedly affected crack initiation, and were not intersected by cracks

simply by chance. To do so, the observed frequency of cracks of a certain length that intersected inclusions is compared to a calculated probability that a randomly formed crack (of a certain length) would intersect a MnS inclusion assuming they were randomly distributed on the sample surface. 7 of 10 cracks in the alloy AS four-point bend samples were less than 250 μm long and spanned less than 15 GBs. The other 3 cracks were longer, having lengths of ~720 μm, ~730 μm, and ~1030 μm, spanning 49, 49, and 52 GBs, respectively. By omitting the large cracks, the most conservative evaluation of the frequency of cracks (less than 250 μm or 15 GBs long) observed intersecting MnS inclusions is then 7/10 or 70%. Considering this information, the probability of a randomly generated crack intersecting an inclusion can be calculated and compared with this observed frequency.

To calculate the probability of an IG crack intersecting a surface inclusion, it is first necessary to estimate the number of GBs and the number of inclusions located on GBs. Using the average grain size for alloy AS, 32 ± 5 μm, the area occupied by a single grain (A_g) can be determined assuming hexagonal grains that occupy an area approximately equivalent to a circle with a diameter, d, equal to the average grain size:

$$A_g = \pi\left(\frac{d}{2}\right)^2 = \pi\left(\frac{32\pm5}{2}\right)^2 = 804\pm79\mu m^2 \qquad (5.5)$$

The number of grains in the uniform stress-strain region of the bend sample, N_g, can then be approximated by dividing the sample area S_A (the area of uniform stress and strain across the width of the sample) by the area of the grains:

$$N_g = \frac{S_A}{A_g} = \frac{3500\mu m \cdot 500\mu m}{804\pm79\mu m^2} \approx 2200 grains \qquad (5.6)$$

Each hexagonal grain has 3 associated unique GBs, therefore the total number of available grain boundaries is the number of grains multiplied by 3, or approximately 6,600 GBs.

It is then necessary to determine which surface inclusions to include in the analysis and the density of these inclusions at grain boundaries in alloy AS. As cracking preferentially initiated at MnS inclusions, only these inclusions were included when determining the probability of inclusion occurrence at GBs. Due to the size difference observed among inclusion types determined from the unirradiated alloy AS sample, it was assumed that inclusions with a surface area greater than 45 μm^2 were MnS (halfway between the average surface area of oxide inclusions and MnS inclusions which were measured and chemically analyzed with XEDS on the unirradiated alloy AS sample, shown in Appendix A). The number density of MnS inclusions was then estimated based on the histogram presented in Figure 4.23a, and the uniform stress-strain region of the bend sample would be expected to have ~21 MnS inclusions.

Although MnS inclusions were not all located at GBs on four-point bend sample surfaces, it will be assumed that they were as a conservative estimate when determining the probability for an IG crack to randomly intersect one of these inclusions. Inclusions could either be located at the midpoint of a GB (having only 1 GB intersection) or at a triple point (having 3 GB intersections), but for the most conservative analysis, it is assumed that all inclusions reside at triple points, thus intersecting 3 GBs each. Assuming MnS inclusions are uniformly distributed at GBs on the sample surface, the probability that a MnS inclusion intersects a grain boundary, $P_{GB@MnS}$, is then:

$$P_{GB@MnS} = \frac{3\text{GBs/MnS} \cdot 21\text{MnS}}{6600\text{TotalGBs}} < 0.01 \qquad (5.7)$$

Therefore, the probability that a GB does not intersect a MnS inclusion, $\overline{P}_{GB@MnS}$, is 1-$P_{GB@MnS}$, or 99%.

Assuming that a crack consists of a succession of connected GBs with a random chance of intersecting one of these MnS inclusions and that each successive GB in the crack has an equally random chance of intersecting a MnS inclusion, then the chance of a crack *y* GBs long not intersecting a MnS inclusion, $\overline{P}_{crack@MnS}$ is:

$$\overline{P}_{crack@MnS} = (\overline{P}_{GB@MnS})^{y} \qquad (5.8)$$

and for a crack 15 GBs long, $\overline{P}_{crack@MnS}$ = 0.86. Therefore, it is only 14% likely that an IG crack spanning 15 GBs would intersect a MnS inclusion if the crack formed at a random location on the sample surface. Comparing the 14% probability of a random crack intersection with a MnS inclusion to the 70% observed frequency of IG cracks that intersected MnS inclusions, it can be concluded that MnS inclusions were likely responsible for crack initiation.

5.6.1 Stress concentration at inclusions

The low magnitude of stress required to initiate IASCC in alloy AS led to the expectation that surface inclusions acted as local stress concentrators that caused crack initiation. Early analysis by Goodier [161] quantified stress concentration at surface inclusions in an infinite plate of material under a remotely applied stress, as shown schematically in Figure 5.12a. A similar stress state at surface inclusions on four-point bend sample surfaces was expected, because tensile stress on the bend surface is concentrated at the thin outer layer of the sample and the inclusions are much smaller than the total dimensions of the bend sample.

Assuming that no second phase particle is present within the surface inclusion, stress at any point around the inclusion site is calculated using the formula:

$$\sigma_{\Theta} = \frac{\sigma}{2}\left(1+\frac{a^2}{r^2}-\left(1+\frac{3a^4}{r^4}\right)\cos 2\Theta\right) \qquad (5.9)$$

where σ_θ is the stress at some angle θ about the inclusion, a is the inclusion radius, r is the distance from the center of the inclusion, and σ is the magnitude of the remotely applied stress [162]. The stress distribution extending from the edge of the inclusion (at θ=90°) is plotted in Figure 5.12b, showing that the tensile stress concentration at the inclusion edge is 3 times the applied stress.

The stress concentration at the inclusion site is affected by the presence of a second phase particle. If the particle is stiffer than the matrix (as would be the case for oxide inclusions [163]), the tensile stress concentration forms at θ=0° rather than θ=90°, with a magnitude of ~1.4 times the applied stress [161]. Alternatively, if the particle has a modulus less than that of the austenitic SS (as would be the case for MnS inclusions [163,164]), the tensile stress concentration at θ=90° will be ~20% less than if no particle were present (~2.4 times the magnitude of the applied stress) [161].

This analysis shows that MnS inclusions would be expected to cause a stress concentration equal to σ_y with the application of a stress equal to ~0.42 σ_y. Although this provides an explanation for why IASCC initiation is possible at applied stress less than σ_y (and is similar to the stress threshold for IASCC initiation near 0.50 σ_y at high irradiation dose), stress concentration at inclusion sites cannot be the only factor responsible for IASCC initiation, because it does not explain the observed decrease in stress necessary to initiate cracking with dose. Bulk hardness

increases [28] with irradiation dose in alloy AS, therefore if stress concentration at inclusions controlled IASCC initiation, the stress required for crack initiation would be expected to increase with irradiation dose. This was not the case in alloy AS, because the stress necessary to cause crack initiation *decreased* with irradiation dose, as described previously.

Literature results also show that if stress concentration at inclusions was the controlling factor of IASCC initiation, cracking would have been more likely at oxide inclusions rather than sulfide inclusions. Oxide inclusions initiate cracking during fatigue studies on austenitic spring steel in inert environments, especially those with large sizes [165], and also in martensitic SS [166]. The likely cause for this behavior is that during solidification, sulfide inclusions create a compressive residual stress field in the matrix, while oxides create a tensile stress field due to differences in thermal expansion [167]. Therefore, sulfide inclusions would be expected to retard crack initiation, while oxide inclusions enhance tensile stress in the matrix near the inclusion edge, increasing susceptibility of these sites to crack initiation. Observations of crack initiation sites in alloy AS have confirmed that MnS, not oxide inclusions, are those involved in the crack initiation process, thus eliminating the residual stress field around inclusion sites as a contributing factor in the IASCC initiation process.

This analysis shows that stress concentration at inclusions alone does not control the IASCC initiation process, although the association of DCs at MnS inclusions with adjacent IG cracks implies that stress concentration at inclusions may have still played a role.

5.6.2 Dislocation channeling at MnS inclusions

The majority of crack initiation sites had a discontinuous DC adjacent to the MnS inclusion intersected by the IG crack, however, the limited number of DCs observed at other locations on

the sample surface prior to crack initiation would suggest that these particular DCs had not formed randomly at these sites. A simple analysis is performed in this section to compare the observed frequency of DCs at MnS inclusions with adjacent IG cracks (5 of 6 crack initiation sites had adjacent DCs, or 83%) to the probability that a DC would have formed at this site at random.

Assuming that DC formation occurs randomly on the bend sample surface in the uniform stress region, the probability of a DC intersecting a MnS inclusion can be conservatively estimated by combining the probabilities that: 1) a grain forms a DC and 2) a grain is adjacent to a MnS inclusion. The largest number of DCs observed prior to IASCC initiation was on sample AS08, which displayed a total of 72 DCs prior to the occurrence of IASCC. For a conservative estimate, it is assumed that each of these DCs formed randomly in its own grain, therefore the probability of a grain having a DC is 72 DCs/2200 total grains or ~3%. The probability that a grain is adjacent to a MnS inclusion can be determined using a similar analysis as described previously. Again, a conservative assumption is that each MnS resides at a triple point, therefore each MnS touches three grains, or 63 grains out of the 2200 total grains on the sample. The probability of observing a grain with both an adjacent MnS inclusion and a channel, assuming both MnS inclusions and channels are independently distributed at random locations on the sample surface is then: 72/2200 x 63/2200, or ~0.01%. Obviously, this probability is much lower than the observed frequency (83%), therefore DCs at MnS inclusions intersected by IG cracks formed preferentially.

Although DCs at crack initiation sites formed preferentially, it remains unknown whether these DCs formed prior to crack initiation or after. Observations of DC formation after IG crack initiation show a network of DCs that fan from the ends of IG cracks, indicating that stress

concentration ahead of a crack tip has a definite influence on DC formation. However, comparing the observed frequency of MnS inclusions intersected by both DCs and IG cracks (5 of 6 crack initiation sites had adjacent DCs, or 83%) to the observed frequency that MnS inclusions which did not have adjacent IG cracking *nor* intersecting DCs (7 of 7 sites, or 100%) strongly suggests that the discontinuous DCs at crack initiation sites influenced crack initiation, and therefore, formed prior to the initiation event. It is likely that stress concentration at the MnS inclusion site led to the formation of the discontinuous DC, which increased stress at the intersecting GB past that necessary for crack nucleation to occur.

It must also be noted that the inclusions compared in this analysis, although not confirmed as MnS prior to four-point bend testing, were distinguishable as MnS because of the composition of corrosion product after NWC exposure and the formation of an 'oxide cap' which was unique to MnS inclusions. It was apparent that this oxide cap formed a preferential condition for crack initiation, as all crack initiation sites displayed this formation at the associated MnS inclusion after crack initiation, and it was also observed prior to the observation of crack initiation in 4 of 5 cases. Considering that pitting at sulfide inclusions is known to cause increased SCC susceptibility [168,169], the response of MnS inclusions to NWC exposure was examined more closely.

5.6.3 MnS dissolution in NWC conditions

SCC cracks have been shown to initiate as a result of pitting at MnS inclusions in 403 SS tested in a corrosive medium at temperatures at or below 100 °C [169], therefore, their response to NWC exposure is considered as a factor affecting IASCC initiation in alloy AS. MnS inclusions serve as pit initiation sites in austenitic stainless steel exposed to room temperature aqueous

environments [40–43,170–172], and are more potent pit initiators than oxides [43]. In fact, Szklarska-Smialowska [173] has proposed that pits are nucleated at sulfide inclusions and that oxide inclusions (without a sulfide shell) do not nucleate pits.

Despite the known susceptibility of MnS inclusions to pitting, a different mechanism of MnS inclusion dissolution is likely active during exposure to high temperature water. A Mn/S/H_2O Pourbaix diagram was reported by Zhou et al. [174] at 250 °C, but for accuracy, it is necessary to adjust the stability lines in this diagram to account for the temperature difference between 250 °C and that in the 288 °C NWC condition. Comparing relative locations of stability lines for the Mn/S/H_2O system at room temperature [175] shows that increasing temperature causes the Mn^{2+}/Mn oxide stability line to shift to left, but more accurate determination is accomplished by adjusting for the shift in temperature using the Nernst equation. The equations of interest and their respective standard electrode potentials, E_0, are as follows:

$$S + 4H_2O \rightleftarrows SO_4^{2-} + 8H^+ + 6e^-, \quad E_0 = -0.621V \qquad (5.10)$$

$$Mn^{2+} + 2H_2O \rightleftarrows MnO_2 + 4H^+ + 2e^-, \quad E_0 = -1.224V \qquad (5.11)$$

$$2Mn^{2+} + 3H_2O \rightleftarrows Mn_2O_3 + 6H^+ + 2e^-, \quad E_0 = -1.485V \qquad (5.12)$$

$$3Mn^{2+} + 4H_2O \rightleftarrows Mn_3O_4 + 8H^+ + 2e^-, \quad E_0 = -0.1007V \qquad (5.13)$$

$$Mn_2O_3 + H_2O \rightleftarrows 2MnO_2 + 2H^+ + 2e^-, \quad E_0 = 0.261V \qquad (5.14)$$

$$3Mn_2O_3 + 2H^+ + 2e^- \rightleftarrows 2Mn_3O_4 + H_2O, \quad E_0 = 0.8297V \qquad (5.15)$$

$$MnO_4^- + 4H^+ + 3e^- \rightleftarrows MnO_2 + 2H_2O, \quad E_0 = 1.679V \qquad (5.16)$$

The y-intercept (y, in V) and pH-dependent slope (x) corresponding to each of these equations at 250 °C, were determined from the Pourbaix diagram constructed by Zhou et al. [174], according to the equation:

$$E = y + x(pH)\ . \qquad (5.17)$$

By equating the formula in equation 5.17 for each respective reaction in equations 5.10 through 5.16 to the Nernst equation:

$$E = E_0 + T\left(\frac{R}{F}\right)\left(\frac{1}{n}\log\left(\frac{[A]^a}{[B]^b}\right) - \frac{m}{n}(pH)\right), \qquad (5.18)$$

the constants $\frac{R}{F \cdot n}\log\left(\frac{[A]^a}{[B]^b}\right)$ and $\frac{R \cdot m}{F \cdot n}$ were determined for each reaction as shown in Table 5.3. In the Nernst equation, *T* is the temperature in K, *R* is the gas constant (8.314 C·V/mol·K), and *F* is Faraday's constant (96,500 C/mol). The calculated constants were then input into the Nernst equation at a temperature of 288 °C to determine the corresponding slope and intercept terms in equation 5.17 for each stability line at 288 °C. The reconstructed the Pourbaix diagram at 288 °C is shown in Figure 5.13.

In NWC conditions (at ~200 mV_{SHE} and pH ~5.5), MnS dissolves to form SO_4^{2-} and Mn_2O_3, consistent with current observations of Mn and O enriched corrosion product at all prior MnS inclusions. Similar, heavy surface oxidation has been previously observed at SCC initiation sites adjacent to MnS inclusions in unirradiated pressure vessel steels tested in high temperature water [158]. It is not expected that irradiation would have a significant effect on MnS inclusions or their corrosion behavior, as S segregation has not been readily observed in neutron irradiated SS [176].

MnS inclusions at IASCC initiation sites were unique in that oxide formation occluded these inclusion sites, and only rarely was an 'oxide cap' observed at MnS inclusions. Only one MnS inclusion formed an oxide cap on the unirradiated alloy AS sample exposed to NWC for 24

hours. Considering the previous analysis which determined an average of 21 MnS surface inclusions in the uniform stress-strain region of an alloy AS bend sample, a conservative estimate is that 4 of these 21 inclusions (~19%) form an oxide cap after NWC exposure, yet only one or two sites typically result in IASCC initiation. A possible explanation for the limited number of inclusion sites which form an oxide cap is the presence of inactive inclusions such as those reported in most pitting initiation studies [43,173,177]. Hoar et al. [177] proposed that cathodic polarization in areas surrounding an active pit prevents the breakdown of other inclusions within these polarized areas. In the case of alloy AS, however, this is an unlikely explanation for the infrequent observation of oxide-capped inclusions because no MnS inclusions were completely inactive. On the unirradiated alloy AS sample which was exposed to NWC for 24 hours, *all* MnS inclusions dissolved to form Mn oxide, but only one resulted in oxide cap formation. It is possible that oxide caps form as a result of specific inclusion geometry (opening size and sub-surface shape) and water flow across the sample surface (flow rate and direction), although understanding these effects requires more accurate modeling to understand.

Oxide cap formation was observed prior to the occurrence of crack initiation in all but one case, indicating that it had created a preferential condition for crack initiation. When an actively dissolving MnS inclusion site is occluded by an oxide cap, a crevice condition is formed. Within the crevice, deaeration of water due to oxide formation causes local acidification as well as the formation of a potential gradient between the crevice depth and the crevice mouth [178]. This potential gradient and the presence of a high sulfate (SO_4^{2-}) ion concentration (due to MnS dissolution) attract these anions into the crevice, increasing the local conductivity. This is similar to the process that occurs at a crack tip, shown schematically in Figure 5.14.

It is well established from CGR tests that an increase in conductivity enhances crack growth [179,180], and that chemistry at the crack tip can be fully mature in cracks 20 μm long [181]. MnS inclusions in alloy AS were often observed to have a surface dimension close to or greater than 20 μm, therefore it is very likely that a dissolving MnS inclusion would be capable of forming this type of condition. Furthermore, previous SSRT test results have shown that MnS inclusion dissolution enhances crack initiation susceptibility by shifting the critical crack initiation ECP to less than -200 mV_{SHE} [182]. This ECP shift was attributed to an increase in sulfate concentration, because a similar effect was observed upon direct addition of sulfate ions to the water environment when testing reactor pressure vessel steels [182].

5.6.4 Observations of inclusions affecting IASCC

Tsukada [183] reported that stainless steel with a high S concentration (0.03 wt%, where alloy AS had only 0.015 wt%) exhibited high IASCC susceptibility, although Cookson [160] did not observe a distinct increase in the crack initiation susceptibility of a proton-irradiated high S alloy when compared to its ultra-high purity analog. In Cookson's study [160], sulfide inclusions were observed, but no additional characterization of these inclusions was reported. Furthermore, no indication was made as to whether the sulfide inclusions displayed any particular response to LWR exposure, and samples were strained to failure making it impossible to determine whether sulfide inclusions caused crack initiation at lower applied stress or strain than in HP samples without sulfides. No difference in strain to failure was observed among the high S and HP alloys, as proton irradiated sample ductility is primarily governed by the unirradiated portion of the sample.

Literature regarding the specific effect of MnS inclusions on IASCC in SS is limited, but MnS inclusions have been previously observed at IGSCC initiation sites in proton irradiated SS by Jiao [124]. He found IG cracks adjacent to MnS inclusions intersected by DCs, similar to observations in this study. It has been proposed that internal cracks within inclusions can lead to matrix cracking [160,184–186], and cracks within inclusions intersected by channels were observed both by Jiao [124] and in this study (exemplified in Figure 5.15). However, it is unlikely that internal cracks within MnS inclusions initiated IASCC, as internal inclusion cracks were only observed in the four-point bend test after an applied stress much larger than that required to cause crack initiation in the NWC environment. Furthermore, after exposure to NWC, the sample with cracked inclusions created by Ar straining was no more likely to form oxide-capped inclusions than samples strained in NWC. Because the oxide cap forms a preferential site for IASCC initiation, it is concluded that IASCC was initiated by a process other than internal inclusion cracking.

The results of Cookson [160,186] further indicate that IASCC initiation at MnS inclusions is caused by a different mechanism than IASCC initiation at inert oxide inclusions, as IGSCC at inert oxide inclusions in Cookson's study was only observed after the application of a relatively large amount of plastic strain. No cracks were observed after the application of 1.1% plastic strain in Cookson's study [160,186], while the 5.5 dpa alloy AS condition (with the highest strain to crack initiation of all alloy AS dose conditions) cracked at an average of 0.38% total strain, before the onset of macroscopic yielding. Cookson concluded that the fracture or matrix debonding of inert inclusions in irradiated SS created a crevice condition which leads to crack initiation. Inclusion cracking in four-point bend tests was only observed on the 10.2 dpa sample AS07 after the application of 0.57% strain in 288 °C Ar, significantly more than the strain

necessary to cause IASCC for this condition (~0.35%). Furthermore, neither 5.5 nor 10.2 dpa alloy AS samples displayed internal inclusion cracks after ~0.4% strain (a strain similar to that necessary to initiate IASCC in NWC). These observations show that inert particles require some threshold stress/strain condition for internal cracking or matrix debonding to occur, the magnitude of which is larger than that necessary to cause IASCC initiation in alloy AS. At MnS inclusions in alloy AS, the crevice condition (similar to that at cracked oxide inclusions) is created as a result of NWC exposure without the application of stress, and as a result, the stress-strain condition necessary for crack initiation at MnS inclusions is much lower than in alloys with only inert oxide inclusions.

Although MnS inclusion sites are able to form a crevice condition without the application of stress, the formation of this environmental condition itself is *not* sufficient for IASCC initiation. Crack initiation only occurs after the application stress, and observations of discontinuous DC intersection at 5 of 6 crack sites indicate that stress concentration as a result of these DCs was also a likely factor.

5.7 The IASCC initiation mechanism in CP 304L alloy AS

The stress dependence of IASCC and dislocation channeling, combined with the observations of MnS inclusions at IASCC initiation sites, leads to the following proposed mechanism for IASCC initiation in alloy AS.

A locally aggressive environmental condition, caused by the dissolution of MnS inclusions and the occlusion of these sites by the formation of an oxide cap, greatly enhances susceptibility to IASCC initiation. Similar to the situation illustrated in Figure 5.14, deaeration of the water within the crevice formed by the oxide-capped inclusion site causes local acidification and the

formation of a potential gradient between the tip and the mouth of the crevice [178]. This potential gradient and the presence of a high sulfate (SO_4^{2-}) ion concentration (due to MnS dissolution) causes sulfate anions to be attracted into the crevice, increasing the local conductivity. Enhanced conductivity and sulfate concentration in LWR environments have both been shown to enhance crack growth and initiation.

In addition to the locally aggressive environment, local stress amplification at this site was required for cracking to occur. The observation of DCs at oxide-capped MnS inclusion sites associated with IGSCC (and the lack of DCs at oxide-capped MnS inclusions not associated with IGSCC) strongly suggests that a DC was a *necessary condition* for IGSCC initiation. Therefore, it is probable that the superposition of stresses caused by 1) the dissolved inclusion and 2) a favorably oriented GB led to the formation of the DC, which then further amplified the local stress at the grain boundary intersecting this inclusion site. A schematic of this IASCC initiation process is illustrated in Figure 5.16. There is one exception to this situation, where a DC was not observed intersecting the inclusion where IASCC initiated, shown in Figure 4.30d. In this case, the crack likely initiated from a sharp corner in the GB, which would have served as the stress concentrator. Kamaya et al. [56] have shown that microstructural features such as this cause local stress concentration, so a DC was not necessary to initiate IASCC at this location.

The decrease in stress to initiate IASCC with increasing irradiation dose would suggest that the DCs at the cracking sites were able to form at lower stress in higher dose material. However, irradiated microstructure characterization is at this time unable to fully support this assertion. An alternative explanation for the decrease in stress is proposed by assessing how GB chemistry (RIS) is affected by irradiation dose. GB compositions for the alloys used in this study have been analyzed quantitatively by Field et al. [71,187] using STEM-EDS, and are summarized in Table

5.4. RIS increased with irradiation dose in alloy AS, despite general agreement that RIS typically saturates at ~5 dpa. The decreasing GB Cr concentration in alloy AS was considered as a factor affecting IASCC susceptibility due to the previous observations of Bruemmer et al. [31]. However, GB Cr concentration was likely not a causative factor because alloy KS (which had no cracking susceptibility, discussed in the following section) had the lowest GB Cr concentration of the alloys used in this study.

Alternatively, Si segregation increased in alloy AS with dose, and has been shown to correlate with IG corrosion in irradiated SS by Jacobs et al. [188] and Fukuya et al. [15], as shown in Figure 5.17. The acidic environment formed within a dissolving MnS crevice was likely analogous to the acidic environment used by Fukuya [15] to analyze IG corrosion, therefore exacerbating corrosive attack at the GB intersecting this site. Because Si enrichment increased with irradiation dose, it is possible that this effect decreased the stress threshold for IASCC as the GB became weakened due to corrosion. The influence of RIS on IASCC is consistent with the observation that Σ3 CSL boundaries are less prone to segregation in these alloys than random high angle (RHA) boundaries (Table 5.4), and the observation that cracking at RHA boundaries was more likely than at Σ3 CSL boundaries in proton-irradiated alloys [10].

The decrease in stress necessary to cause IASCC initiation was also observed in the CLT database, described in section 5.4. This consistency with four-point bend test results would imply that a similar mechanism was active in the CW materials tested in low ECP primary water, although consideration of MnS stability under primary water conditions (by viewing the Pourbaix diagram illustrated by Zhou et al. [174]) suggests that MnS dissolution would not be a concern at such low ECP. However, SCC susceptibility was enhanced in SSRT tests performed on unirradiated pressure vessel steels in MnS saturated primary water conditions, and the MnS

saturated water reduced the critical potential for SCC from 0 mV_{SHE} to between -550 to -700 mV_{SHE} [159]. Furthermore, a similar stress threshold for IASCC initiation (at ~40% σ_y) was observed in uniaxial constant load tests performed on irradiated samples tested in a 32 ppm DO, high-ECP environment [189].

Comparing the irradiation dose at which the stress threshold for IASCC initiation was achieved in these three studies (uniaxial constant load tests in high-ECP NWC [189], four-point bend tests in intermediate-ECP NWC, and CLTs in low-ECP primary water [13,154]) indicates that the stress threshold was achieved at a lower irradiation dose with increasing ECP. These observations support the assertion that IG cracking is influenced by a weakening of GBs due to corrosion, since dislocation channeling is not affected by corrosion potential. Despite the inference of MnS-assisted IASCC initiation causing the similarity in the observed stress dependence of IASCC among constant load and four-point bend test results, further analysis is necessary to confirm MnS inclusions were a factor in CLT experiments in a low potential environment.

5.8 Dislocation channeling and IASCC in HP alloys ES and KS

Despite the proposed crack initiation mechanism provided for alloy AS, additional analysis was necessary to explain the reduced IASCC susceptibility in alloy ES and the lack of susceptibility in alloy KS. This section illustrates the observed differences among the three alloys and provides support for how the IASCC mechanism is altered by differences in dislocation channeling behavior, alloy composition, and alloy microstructure.

HP alloy ES contained no MnS inclusions, and the crack initiation susceptibility was significantly less than alloy AS in NWC. After straining to failure in the CERT test, alloy ES had

less %IG and displayed a larger total elongation. In the four-point bend test, strain to crack initiation was larger in alloy ES, and a well-developed DC network (~788 DCs/mm^2) had formed on the bend sample surface prior to crack initiation. This is compared to a maximum of only ~41 DCs/mm^2 prior to crack initiation on alloy AS at a similar irradiation dose. Considering the proposed mechanism of IASCC initiation in alloy AS, the IASCC-enhancing effect of MnS is clear. Only smaller, inert oxide type inclusions were present in alloy ES, which were not a factor affecting IASCC initiation in alloy AS.

Comparing the SCC behavior of alloy ES with alloy KS (which was not susceptible to IASCC) reveals that small oxide inclusions were not responsible for crack initiation, as they were present with similar size and number density in both alloys ES and KS. Therefore, crack initiation in alloy ES must be caused by a mechanism unrelated to inclusions. Due to the dependence of IASCC on dislocation channeling [9,10,106] and the IASCC-enhancing effect of discontinuous DC-GB intersections observed by McMurtrey et al. [146], further analysis of DC parameters was performed. Dislocation channeling observations from four-point bend tests in 288 °C Ar and NWC were combined in this analysis as no distinct difference in DC density or transmission site density was observed in either test environment (Figure 5.18). This result was expected, as the only environmental parameter known to affect dislocation channeling is temperature [126].

To compare the propensity of each alloy to transmit DCs across GBs, a parameter was defined called the ‘channel transmission frequency.’ This parameter is the slip transmission site density normalized by the channel density at a particular strain in the four-point bend test. Recall that slip transmission sites were locations where channels were observed to propagate across a GB into an adjacent grain. Considering the possibility of the formation of long chains of DCs across many grains, the theoretical limit in the channel transmission frequency is 1. Channel

transmission frequency is compared among irradiated alloys in Figure 5.19, showing that alloy KS was the most likely to transmit DCs at all levels of applied strain. Channel transmission frequency was similar in alloys ES and AS, however, the channel transmission frequency in alloy AS was less relevant due to the limited extent of channel formation prior to IASCC initiation and the previously described IASCC initiation mechanism.

Transmission of DCs across GBs likely limited stress accumulation at DC-GB intersections (as shown in Figure 5.7), thus preventing IG crack initiation in alloy KS. This observation agrees with the mechanism of crack initiation determined by McMurtrey et al. [10,11,146], who showed that discontinuous DC-GB intersections were more likely to cause IASCC initiation than intersections where channels transmitted across the GB. It should be noted that only a small fraction of discontinuous DC-GB intersections resulted in IASCC initiation in McMurtrey's study [10,146], therefore only certain sites were able to exceed the stress requirement for IASCC initiation. This was also the case in this study, as numerous discontinuous DC-GB intersections were observed prior to crack initiation in alloy ES. Furthermore, a limited number of DC-transmitting GBs formed crack initiation sites in McMurtrey's study. However, considering the high strain applied (6.5% total strain) at which these cracks were observed, it is not surprising that DC-transmitting GBs had also not yet achieved the stress necessary for crack initiation in alloy ES before the formation of the large crack which led to sample failure.

A direct quantitative comparison of the channel transmission frequency with McMurtrey's data [146] is not possible, as the total number of channels was not reported in his study. However, the density of slip transmission sites in McMurtrey's study (the area density of GBs with continuous slip plus the area density of discontinuous GBs with GB slip, which were indistinguishable in four-point bend surface analysis) can be compared with that observed from four-point bend test

analysis. The area density of slip transmission events observed by McMurtrey after 2.5% strain in Ar was 577 mm^{-2}, much less than the density of slip transmission sites on alloys ES and KS after ~2.3% strain in the four-point bend test (1610 mm^{-2} and 1980 mm^{-2}, respectively). The grain size of the alloy used in McMurtrey's study was nearly 2 times that in the current materials (~50 μm), therefore the number of sites available for slip transmission was less by a factor of ~2. Another factor is that measurements of slip transmission recorded on four-point bend samples were not limited to GBs, therefore channel cross-slip within grains (as has been observed previously by Cui et al. [190]) also likely added to the measured slip transmission site density.

Considering these differences, alloy KS still had the highest density of slip transmission sites, providing comparative evidence to support its lack of cracking susceptibility. The area density of slip transmission events in alloy ES was more similar to that observed by McMurtrey [146], also providing comparative evidence to support the observed IASCC susceptibility of this alloy. Furthermore, locations of secondary cracking on the gage section of the alloy ES sample after CERT testing in the low potential primary water environment (Figure 5.3) [28] were often intersected on one side by discontinuous DCs.

An additional comparison of the effect of dislocation channeling can be made by comparing the cracking behavior of alloys AS and ES after CERT testing in the low-ECP primary water environment, as shown in Figure 5.20 [28]. MnS dissolution is not expected in the low ECP (-860 mV_{SHE}) primary water environment based on the Mn/S/H_2O Pourbaix diagram [174], therefore the effect of MnS in this comparison is expected to be limited. Furthermore, alloys AS and ES had relatively similar base composition (although minor solute elements were more prominent in the CP alloy AS), both experienced similar total elongation after the CERT test in primary water (alloy AS failed after 4.65% strain and alloy ES after 4.60% strain) [28], and the

slip transmission frequency of both alloys was similar (although at low levels of strain). It is therefore somewhat surprising that the surface crack density on alloy AS was noticeably higher than alloy ES. This comparison implies that the cracking susceptibility of GBs in irradiated materials can vary greatly among similar alloys with similar channeling behavior, illuminating another factor which requires additional consideration in the IASCC mechanism.

The difference in GB cracking susceptibility observed among alloys AS and ES strained in primary water provides supportive evidence as to why even DC-transmitting GBs in alloy KS did not crack. In McMurtrey's studies [5,75], crack initiation was infrequently observed at DC-GB intersections that transmitted slip in the 13Ni-15Cr proton irradiated alloy, therefore it must not be assumed that these intersections are immune to crack initiation. However, no cracking even at DC-transmitting boundaries was observed in McMurtrey's high Ni alloy (21Ni-32Cr) [75] nor in alloy KS after ~10% strain in the four-point bend test or after straining to complete failure in the CERT test in NWC. It is apparent that GBs in high Ni alloys are inherently less susceptible to cracking, regardless of local DC behavior.

The IASCC-suppressing effect of Ni has also been observed independently by Cookson [160] in a proton-irradiated 20Cr/24Ni SS, and by Kodama et al. [191], who compared several neutron irradiated SS. As Ni concentration has a strong effect on SFE in SS, cross-slip is considered to enhance the propensity for slip transmission in irradiated alloys, thus improving IASCC resistance. Cross-slip of channels within grains has been observed by Cui [190] and channel widening has been observed in locations where channels intersect boundaries [99], indicating that cross slip becomes more prevalent as a result of stress accumulation during dislocation pileup within a channel. It is presently unknown whether DC transmission at GBs is caused by the formation of a new dislocation source in the adjacent grain or by direct transmission of

dislocations across the boundary [146]. Therefore, two possibilities are considered as to how SFE affects DC transmission at GBs. First, as DCs cross-slip in a single grain (either altering the direction of the channel or by widening the channel at the GB intersection), the stress vector associated with the dislocation pileup is altered such that activation of a dislocation source in the adjacent grain is more favorable. Alternatively, TEM studies on Ni alloys have shown that alloy composition can affect direct transmission of dislocations at GBs [192], therefore composition could also possibly have affected direct transmission. Additional work is necessary to understand these interactions in irradiated materials.

Channel transmission frequency was also potentially affected by dislocation barriers in the alloy microstructure. Alloy ES had a moderate density of deformation twins and lattice distortion prior to deformation, due to insufficient solution annealing after alloy fabrication. The effect of the compositional difference between alloys ES and KS was obscured by this microstructural difference, thus preventing the conclusive attribution of either factor to the channel transmission propensity. Large inclusions and pockets of δ ferrite (a harder phase than the austenitic matrix [193]) were present in alloy AS, but not in alloys ES or KS. Microstructural barriers have a known influence on material hardness, but in irradiated materials, these barriers also possibly affect DC transmission at GBs.

The comparison of cracking with channel transmission frequency emphasizes the importance of DC-induced stress concentration at GBs in the IASCC initiation process. Consistent with the suggested mechanism of crack initiation in proton irradiated SS [146], crack initiation in neutron irradiated alloys is affected by stress accumulation at GBs due to discontinuous DC-GB intersections. This was a notable difference among alloys ES and KS, and likely caused the

IASCC susceptibility observed in alloy ES. SFE and microstructure are likely contributors to slip transmission propensity in an irradiated alloy.

Dislocation channeling is a critical factor in the IASCC initiation process, regardless of alloy or IASCC susceptibility. In alloy ES, DCs cause stress concentration when they form discontinuous intersections at GBs, leading to crack initiation once the stress concentration exceeds a critical value necessary to rupture the surface oxide at the GB. This stress concentration is also an important factor affecting crack initiation in alloy AS, but IASCC susceptibility is enhanced by the presence of MnS inclusions which create preferential sites for crack initiation. Alloy KS was not susceptible to IG crack initiation because, similar to alloy ES, it contained no MnS inclusions, but also because the propensity to transmit DCs across grain boundaries was greater than alloys ES and AS. A higher propensity for DC transmission limits the stress concentration which can be achieved at DC-GB intersections. However, the complete lack of crack initiation at DC-transmitting GBs in alloy KS after the application of large amounts of strain indicates that GB susceptibility is also controlled by other factors. Additional work is necessary to determine why GBs display varying susceptibility to IASCC initiation, especially in high Ni stainless steels, which are not susceptible to IASCC.

Table 5.1. Stress values input into the interval censored data analysis technique for alloy AS. Lower bounds represent the maximum stress at which cracking was not observed and upper bounds represent the stress where crack initiation was observed.

Sample ID	Dose, dpa	Lower Bound, MPa	Upper Bound, MPa
AS01	5.5	630	824
AS02		613	681
AS04		510*	581
AS06	10.2	545	613
AS08		585	613
AS09	47.5	441	501
AS10		430	443

*Stress value estimated based on similar crack size in sample AS02

Table 5.2. Calculated stress required to initiate dislocation channels for all irradiated conditions.

Sample ID	Dose, dpa	Initial Channel Observation		Stress to initiate channeling, MPa ($\sigma_{DC,sample}$)	Standard Deviation, MPa (φ_{stdev})	Stress to initiate channeling, per condition MPa ($\sigma_{DC,condition}$)
		Stress, MPa	Channel Density, mm^{-2}			
AS02	5.5	613 ± 38	10.3 ± 2.4	609 ± 39	21	624 ± 44
AS03		664 ± 41	67.7 ± 6.1	639 ± 66		
AS07	10.2	580 ± 36	8.0 ± 2.1	577 ± 37	66	530 ± 72
AS08		495 ± 31	31.4 ± 4.2	483 ± 39		
AS09	47.5	441 ± 27	2.3 ± 1.1	440 ± 27	21*	440 ± 34

*Standard deviation calculated by taking the square root of the stress value, as only one measurement was available

Table 5.3. pH dependent slope (*x*) and y-intercept (*y*) determined for each relevant chemical equation (equations 5.10 through 5.16) at 250 °C (from Zhou [174]), constants E_0, $\frac{R}{F \cdot n}\log\left(\frac{[A]^a}{[B]^b}\right)$, and $\frac{R \cdot m}{F \cdot n}$ determined from the Nernst equation, and corresponding pH dependent slope (*x*) and y-intercept (*y*) for each equation at 288 °C.

	Equation	Constants from Zhou		Nernst Equation Constants			Constants at 288 °C	
Chemical Reaction	No.	x	y	E_0	$(R/F \cdot n)\log([A]^a/[B]^b)$	$(R \cdot m)/(F \cdot n)$	x	y
$S \leftrightarrow SO_4^{2-}$	5.10	-0.14	0.36	-0.62	9.44	-1.34	-0.15	0.43
$Mn^{2+} \leftrightarrow MnO_2$	5.11	-0.20	1.14	-1.22	22.71	-1.96	-0.22	1.30
$2Mn^{2+} \leftrightarrow Mn_2O_3$	5.12	-0.20	1.17	-1.49	25.48	-1.95	-0.22	1.34
$3Mn^{2+} \leftrightarrow Mn_3O_4$	5.13	-0.24	1.29	-0.10	13.40	-2.30	-0.25	1.39
$Mn_2O_3 \leftrightarrow 2MnO_2$	5.14	-0.10	0.93	0.26	6.40	-1.01	-0.11	0.97
$3Mn_2O_3 \leftrightarrow 2Mn_3O_4$	5.15	-0.11	0.81	0.83	-0.15	-1.02	-0.11	0.81
$MnO_4^- \leftrightarrow MnO_2$	5.16	-0.14	1.62	1.68	-0.54	-1.36	-0.15	1.62

Table 5.4. Grain boundary composition measurements made by Field et al. [71,187] using STEM-EDS. All values in wt. %.

			Fe		Cr		Ni		Si	
Alloy	**Dose**	**Boundary Type**	**Boundary Concentration**	**Diff. from Bulk**	**Boundary Concentration**	**Diff. from Bulk**	**Boundary Concentration**	**Diff. from Bulk**	**Boundary Concentration**	**Diff. from Bulk**
AS	5.5	RHA	64.1 ± 2.2	-1.6	17.6 ± 1.5	-2.4	15.5 ± 1.9	4.7	1.2 ± 0.3	0.6
		Σ3	66.4 ± 2.0	0.8	20.0 ± 1.9	0.0	11.2 ± 1.7	0.4	0.6 ± 0.2	0.0
	10.2	RHA	62.7 ± 2.3	-3.0	16.3 ± 1.8	-3.7	17.8 ± 2.2	7.0	1.3 ± 0.3	0.7
		Σ3	65.2 ± 1.5	-0.5	19.4 ± 1.3	-0.6	12.6 ± 1.6	1.8	0.8 ± 0.2	0.2
	47.5	RHA	58.8 ± 2.9	-6.8	15.1 ± 1.9	-4.8	22.4 ± 2.8	11.6	1.6 ± 0.4	1.1
		Σ3	66.3 ± 3.0	0.6	20.3 ± 2.1	0.3	11.0 ± 2.7	0.2	0.5 ± 0.2	0.0
ES	11.8	RHA	64.8 ± 1.8	-3.0	16.2 ± 1.3	-2.6	18.6 ± 1.6	6.3	NM	
		Σ3	63.7 ± 1.3	-4.1	19.3 ± 0.8	0.6	15.7 ± 1.3	3.4	NM	
KS	9.6	RHA	50.3 ± 2.2	-8.5	14.9 ± 1.2	-3.3	36.8 ± 1.8	11.8	NM	
		Σ3	47.1 ± 1.9	-5.3	16.5 ± 1.2	-1.7	32.0 ± 2.6	6.9	NM	

NM indicates that value was not measured

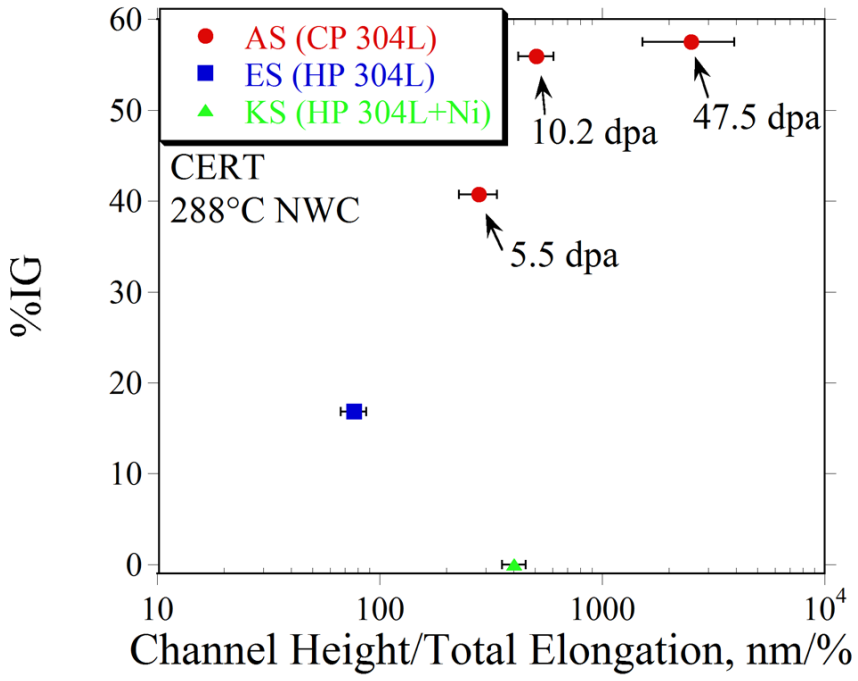

Figure 5.1. %IG plotted as a function of the weighted average channel height normalized by total elongation.

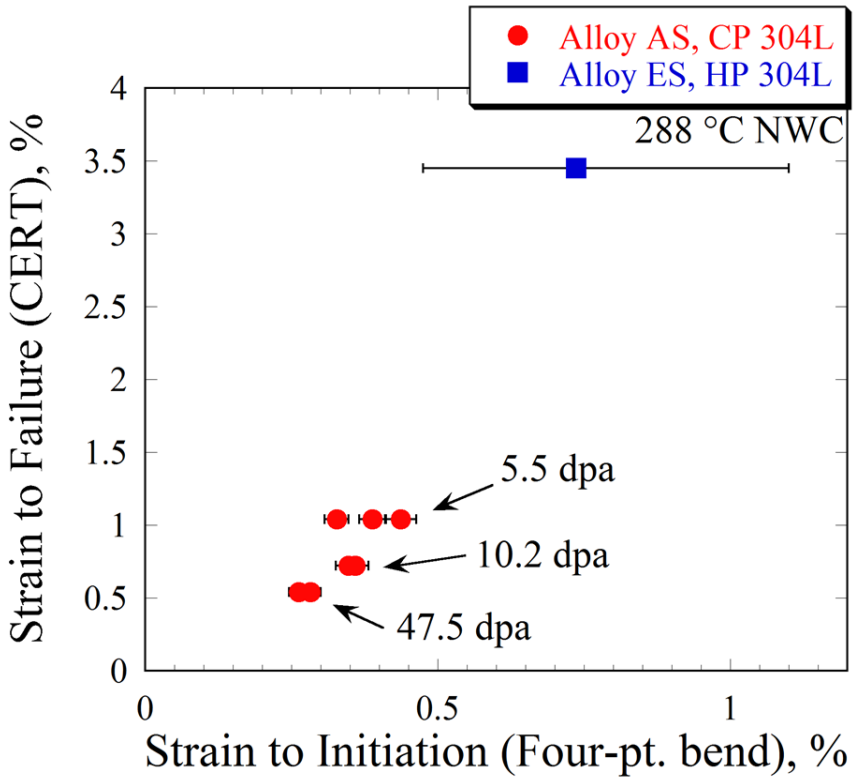

Figure 5.2. Strain to failure from CERT experiments plotted versus strain to initiate cracking in the 4-point bend experiment.

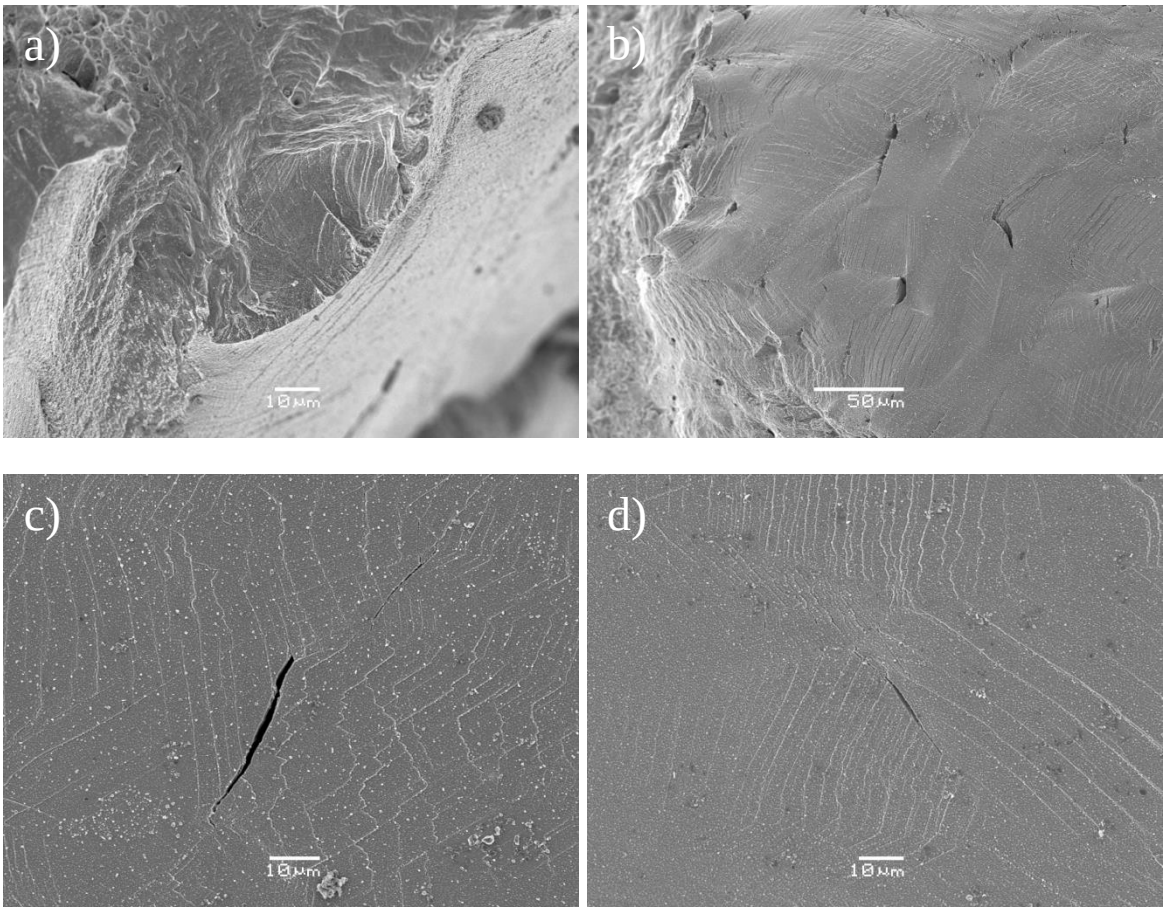

Figure 5.3. The ~10 dpa alloy ES tensile bar sample after straining to failure in the CERT test in 320 °C primary water showing a) mixed mode IG/TG brittle cracking at the periphery of the fracture surface, and b-d) GB separation observed within the necked region of the gage section.

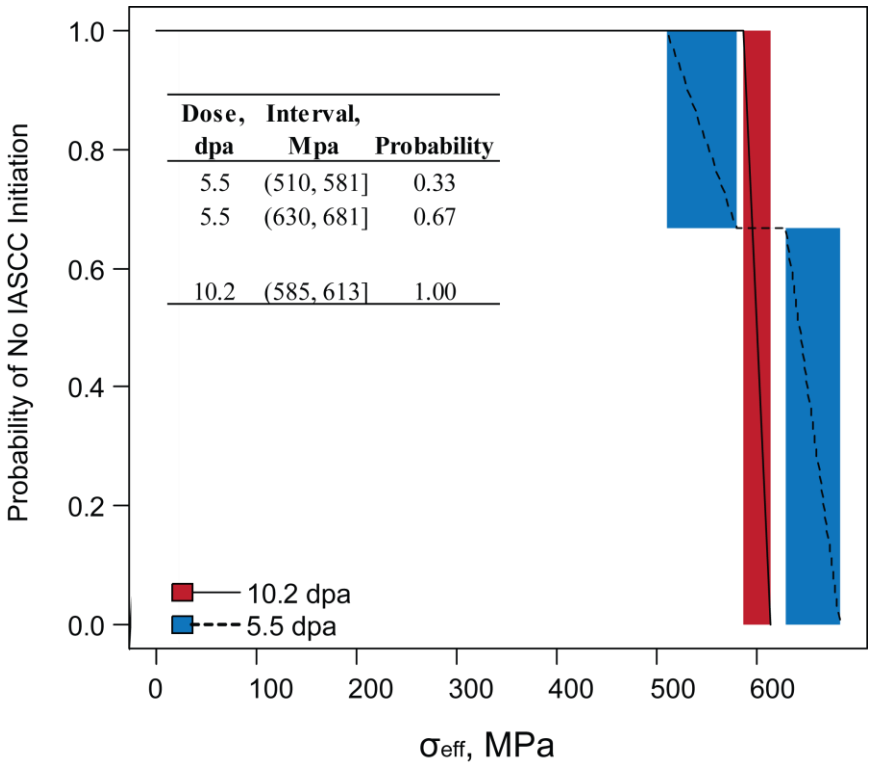

Figure 5.4. Survival curves determined from interval analysis of alloy AS bend test samples at 5.5 and 10.2 dpa.

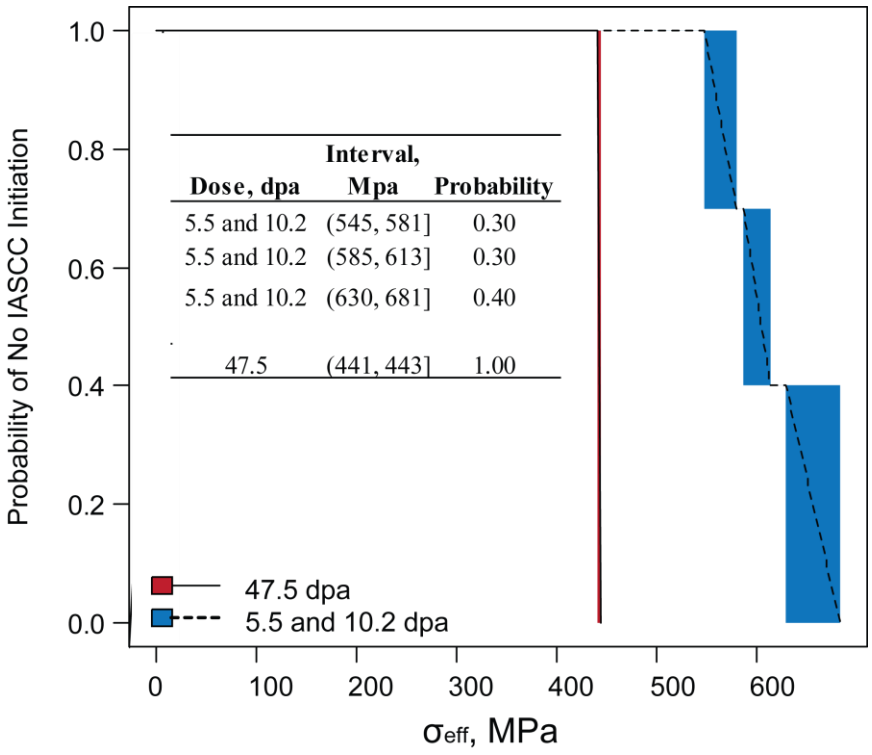

Dose, dpa	Interval, Mpa	Probability
5.5 and 10.2	(545, 581]	0.30
5.5 and 10.2	(585, 613]	0.30
5.5 and 10.2	(630, 681]	0.40
47.5	(441, 443]	1.00

Figure 5.5. Survival curves determined from interval analysis of alloy AS bend test samples at low dose (5.5 and 10.2 dpa) and high dose (47.5 dpa).

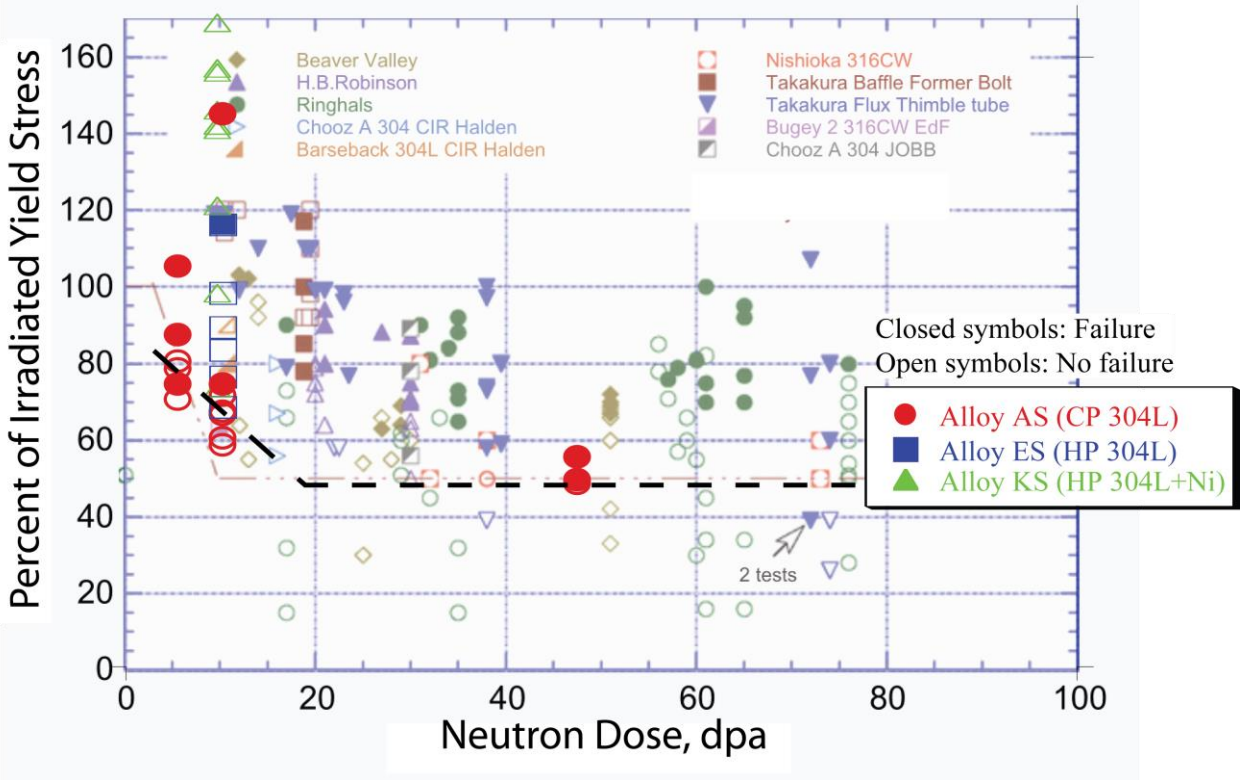

Figure 5.6. Stress (relative to the irradiated yield strength) required to cause failure as a function of dose. 4-point bend test data is overlaid on the constant load database, from [154]. The dashed black line represents an approximate lower threshold for failure determined from bend test experiments.

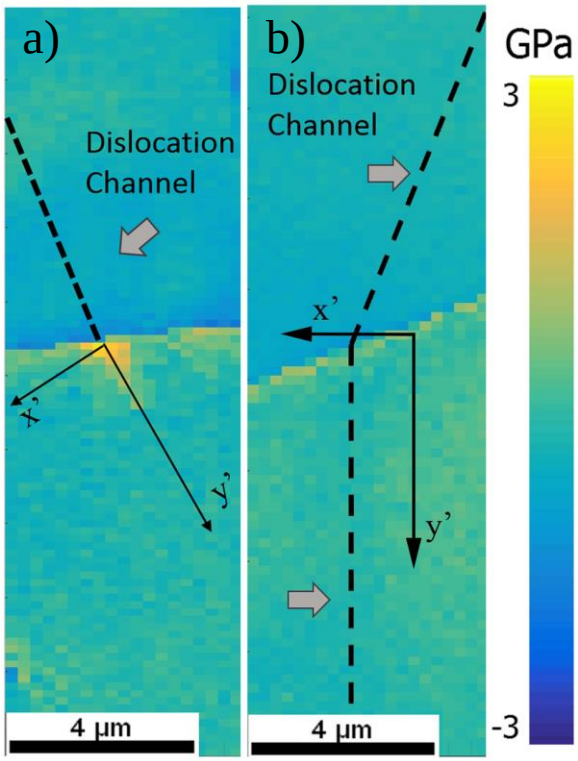

Figure 5.7. High-resolution EBSD stress measurements at a) a discontinuous DC (dashed line) intersecting a GB, showing high stress concentration at the intersection site and b) a DC that transmits through a GB, without any stress concentration at the intersection. Measurements taken on a 5 dpa proton irradiated 13Cr-15Ni austenitic SS after 3% plastic strain in 288 °C Ar at a rate of $3x10^{-7}$ s^{-1}, courtesy of Drew Johnson at the University of Michigan.

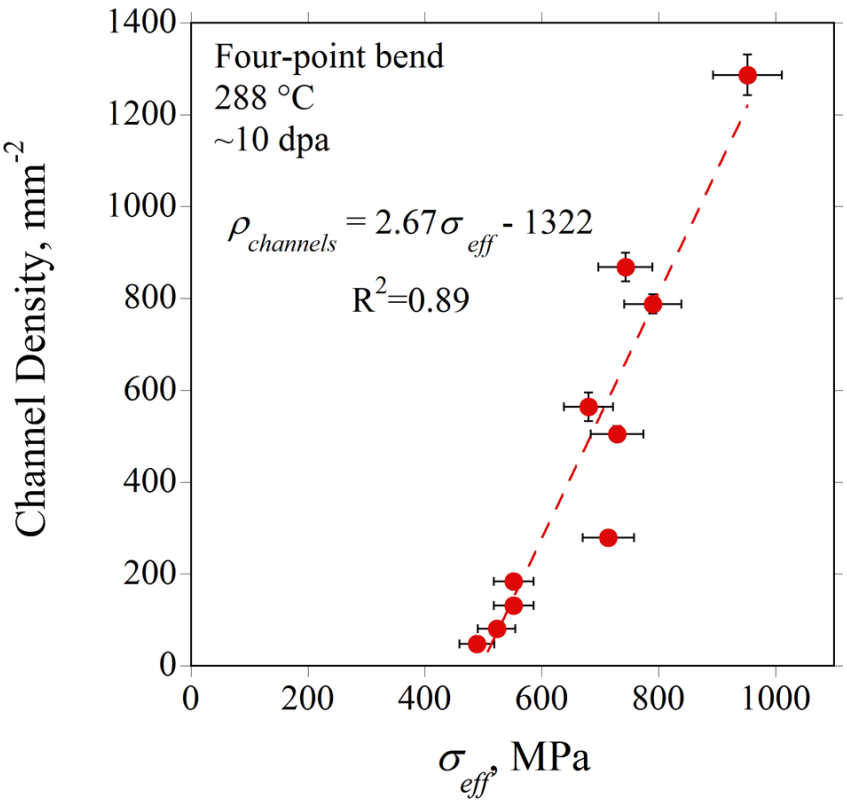

Figure 5.8. Stress dependence of channel density for ~10 dpa irradiated conditions during elastic deformation at 288 °C.

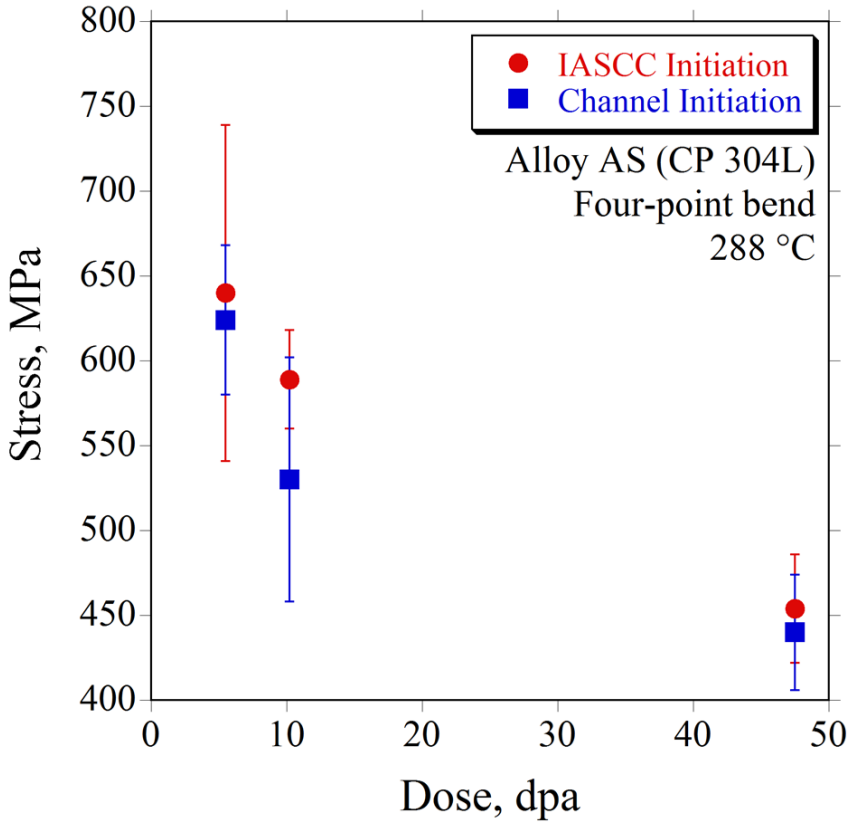

Figure 5.9. Average stress for initiation of DCs and IASCC in alloy AS as a function of irradiation dose.

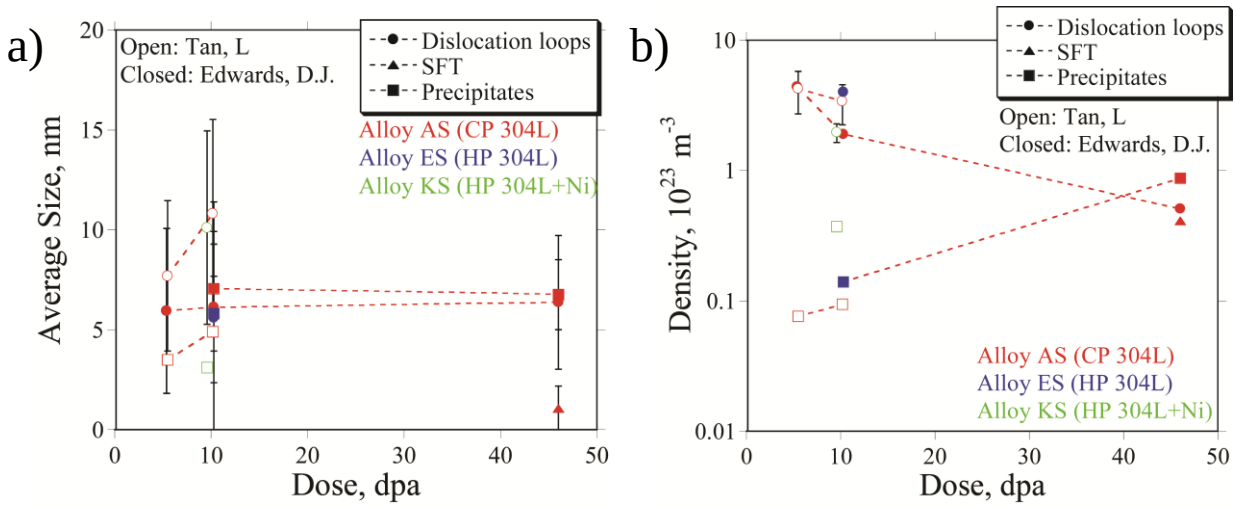

Figure 5.10. Average a) size and b) density of irradiation induced defects observed in the irradiated alloys AS, ES, and KS. Data reproduced from Edwards et al. [23,27] and Tan et al. [155].

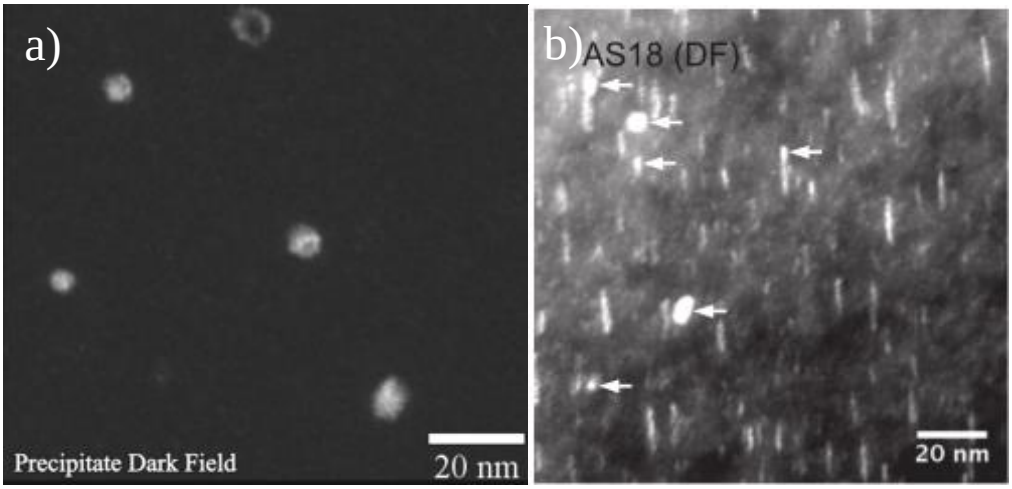

Figure 5.11. Dark field images of strongly diffracting irradiation-induced precipitates in a) 10.3 dpa alloy AS (from [23]) and b) 10.2 dpa sample AS18 (from [155]).

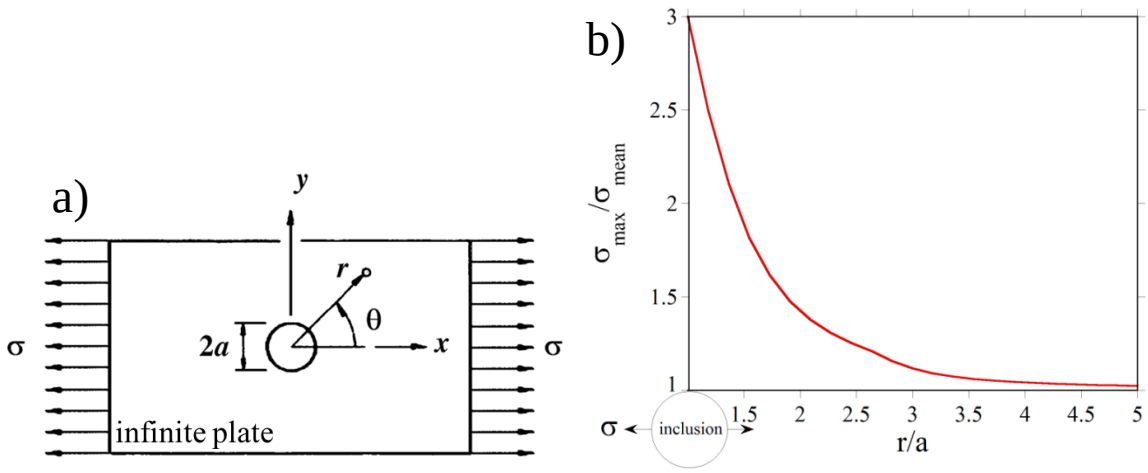

Figure 5.12. a) Illustration showing an inclusion (in this case, a void) located in an infinite plate under a remotely applied tensile stress, from [162]. b) Resulting stress concentration as a function of distance from the edge of the void (at θ = 90°).

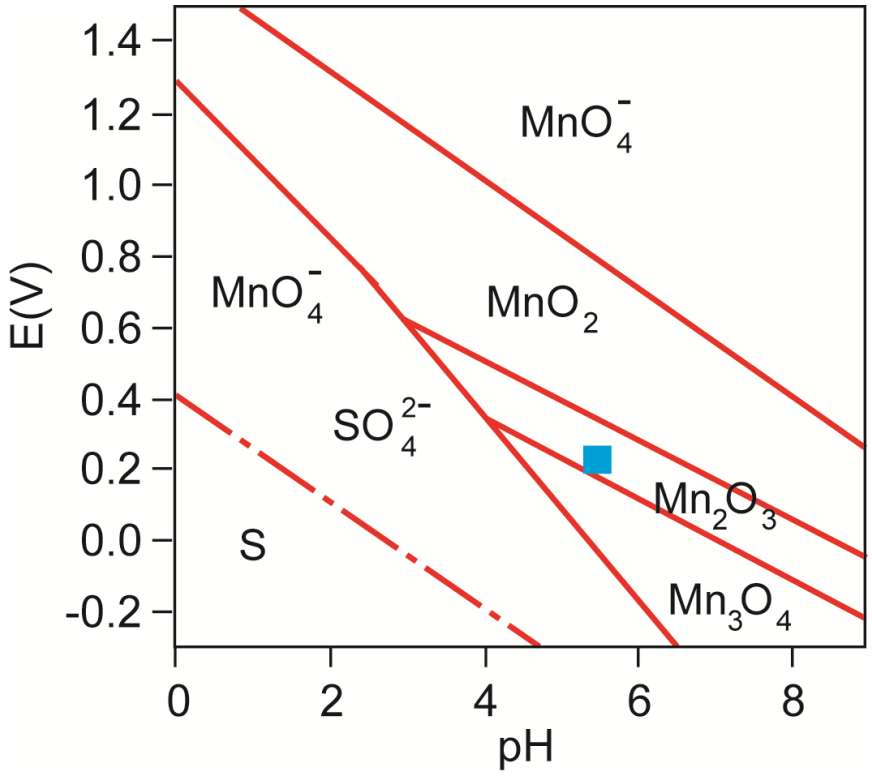

Figure 5.13. Mn/S/H_2O Pourbaix diagram at 288 °C showing the location of stability in NWC conditions indicated by the blue square. Stability lines in this diagram were adapted from the Mn/S/H_2O Pourbaix diagram at 250 °C reported by Zhou et al. [174]. Dot-dashed lines represent S containing species and solid lines represent Mn containing species.

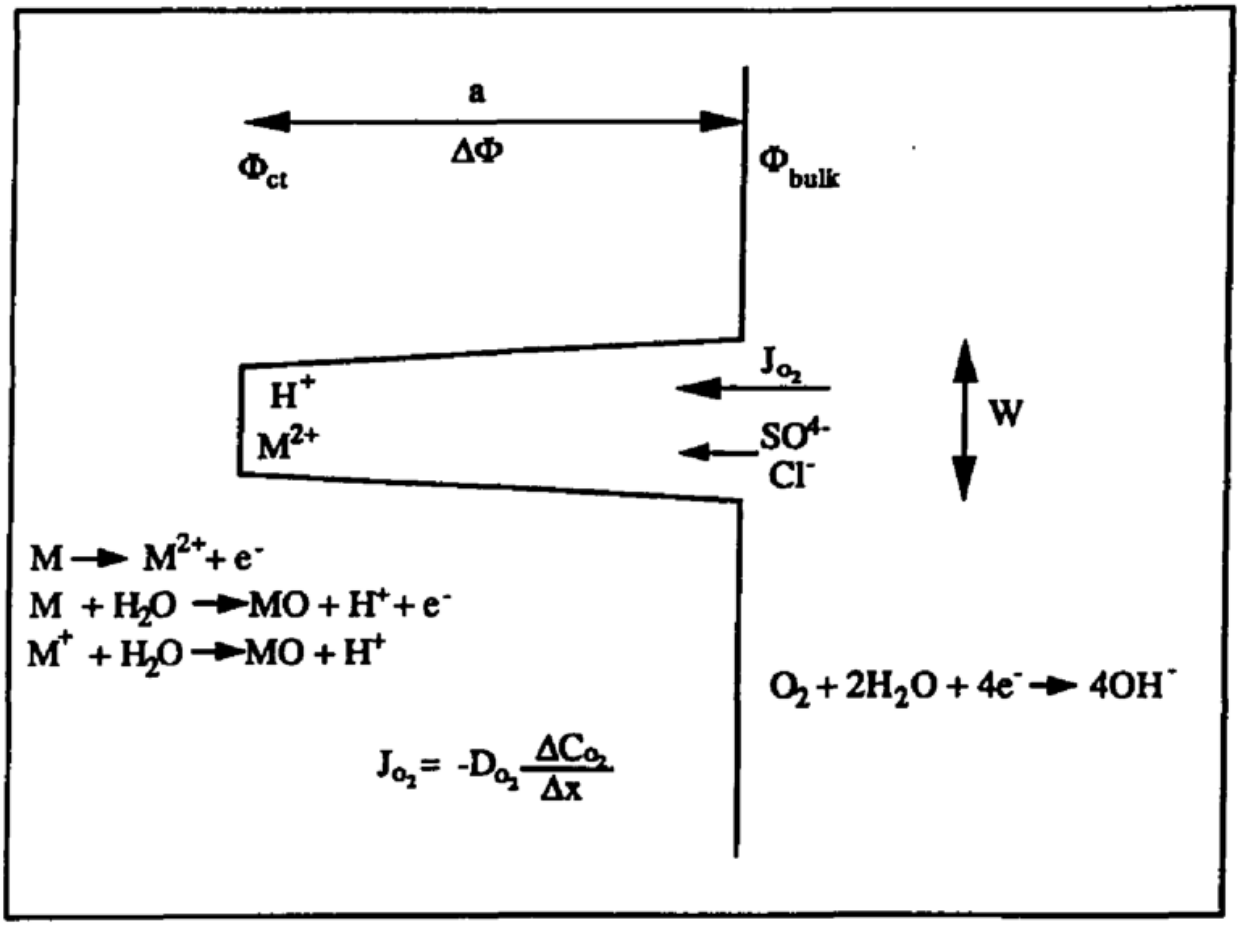

Figure 5.14. Schematic of electrochemical reactions which occur at various locations of a crack, analogous to the reactions which occur during crevice formation during MnS dissolution. From [160] but adapted from [181].

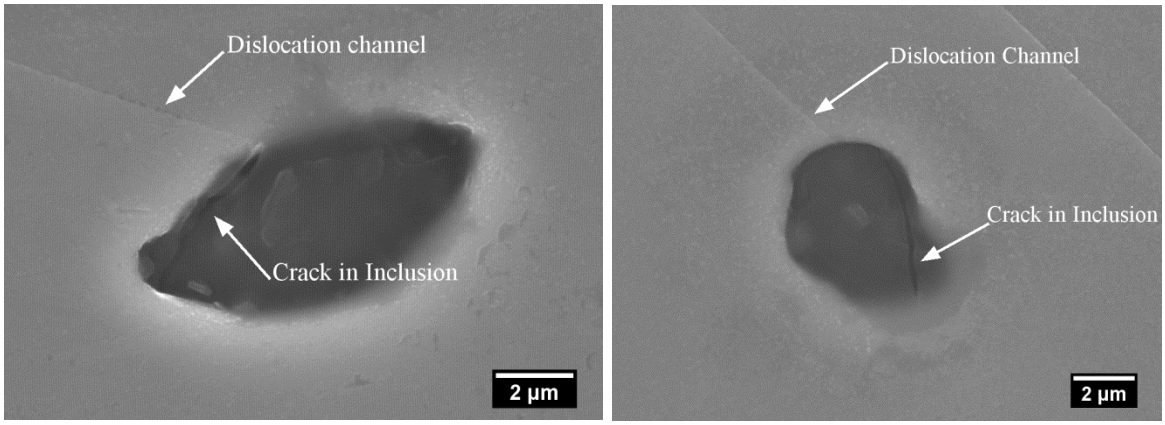

Figure 5.15. Cracking within inclusions caused by DC intersection on the surface of sample AS07 after the four-point bend test increment in 288 °C Ar ended at $1.16\sigma_y$.

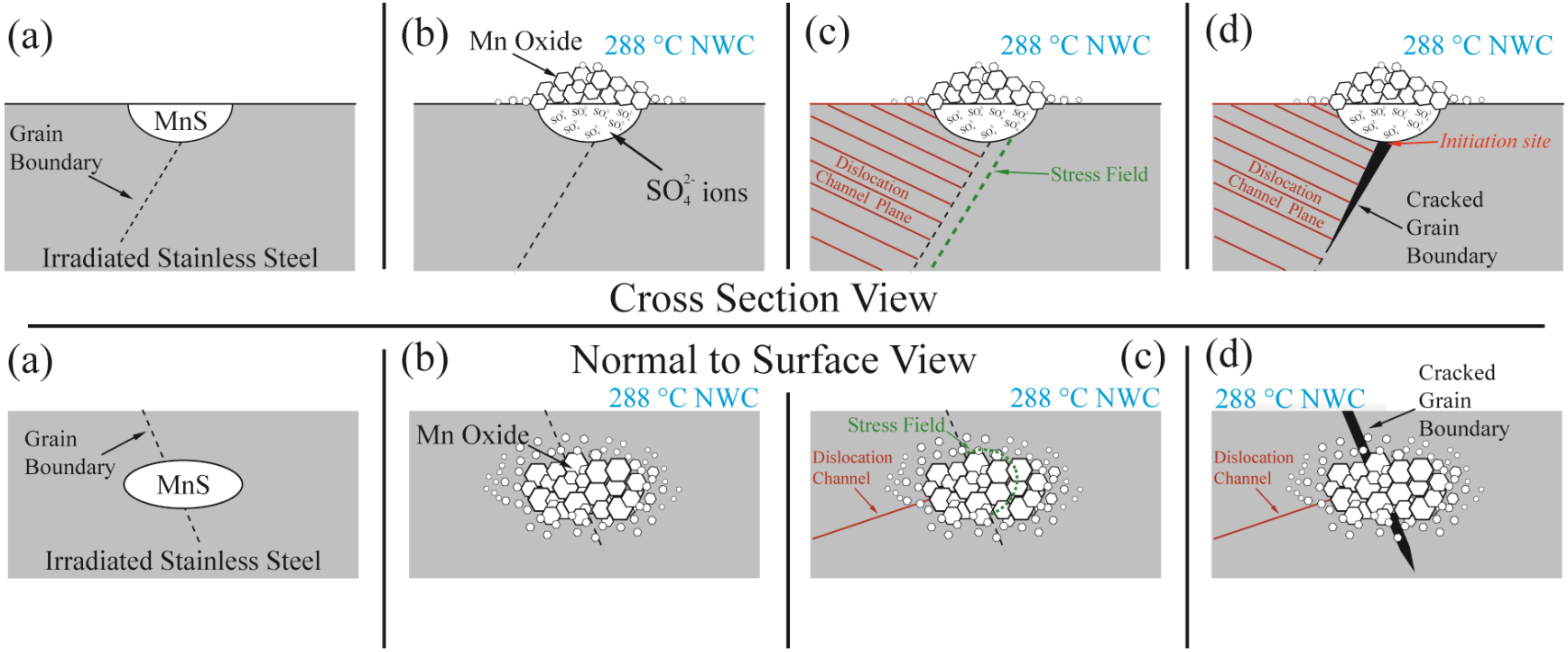

Figure 5.16. A schematic of the IASCC initiation mechanism in alloy AS caused by a dissolving MnS inclusion and a stress field formed by a discontinuous DC intersecting the incident GB. a) A MnS inclusion at a grain boundary prior to exposure, b) after exposure to NWC, the MnS oxide dissolves to form Mn oxide which occludes the inclusion site and accumulates SO_4^{2-} within the occluded crevice, c) a discontinuous dislocation channel intersects the grain boundary at the inclusion site, creating a field of high stress, and d) IGSCC initiates at this site.

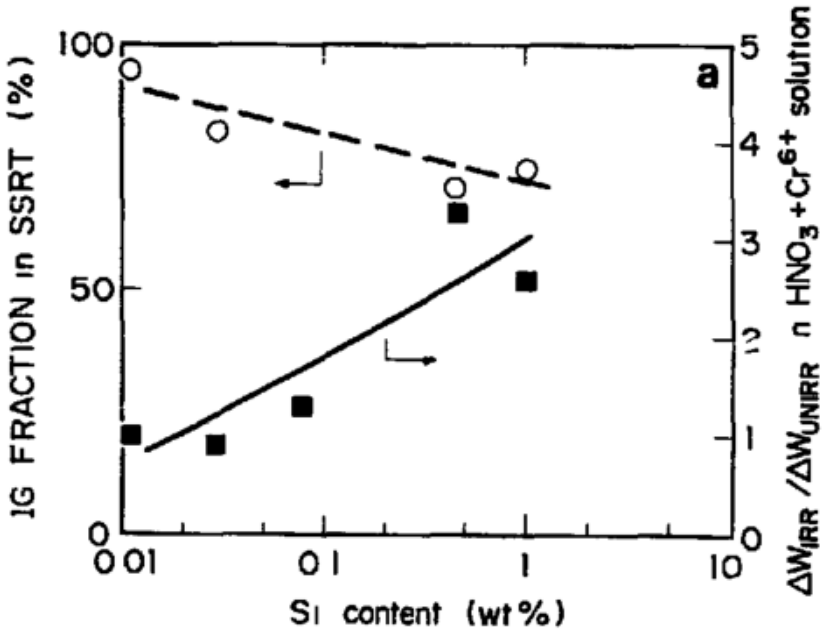

Figure 5.17. Weight loss due to IG corrosion as a function of Si segregation caused by RIS in irradiated SS (right axis), from [15].

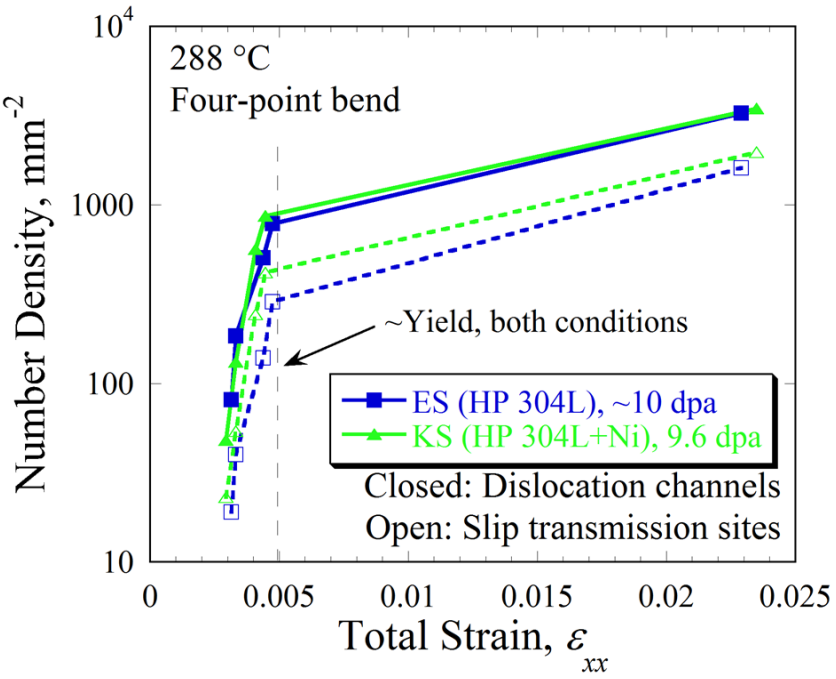

Figure 5.18. DC and slip transmission site density on four-point bend sample surfaces of HP alloys ES and KS deformed at 288 °C, without regard to differences in test environment.

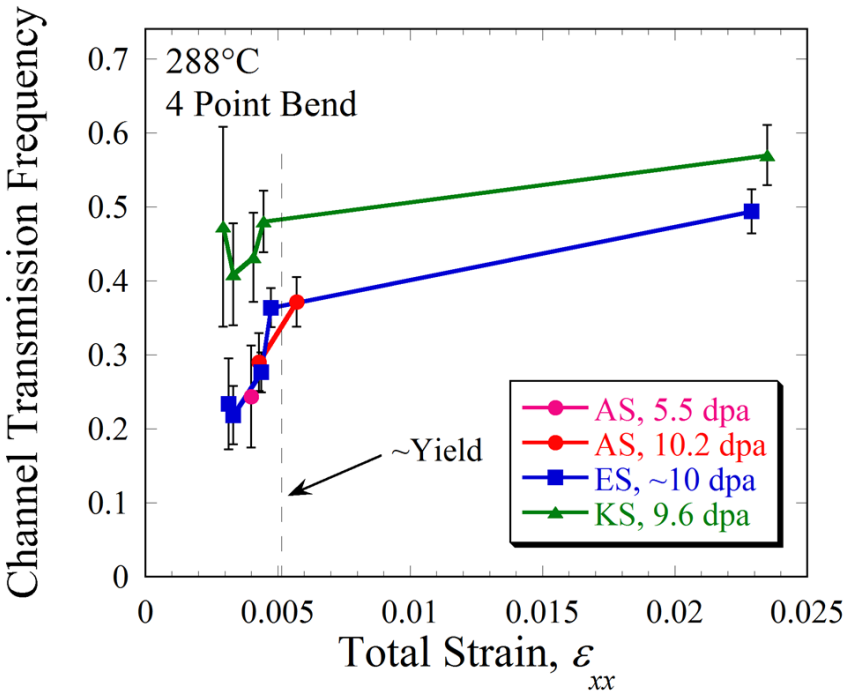

Figure 5.19. Channel transmission frequency (slip transmission site density normalized by total DC density) for each alloy after four-point bend tests in 288 °C Ar or NWC.

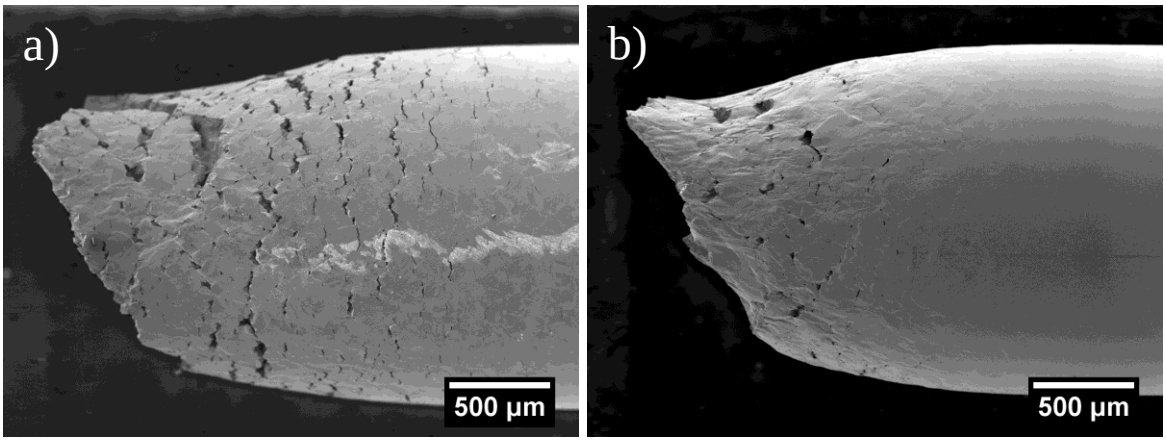

Figure 5.20. Gage surfaces of a) 10.2 dpa alloy AS and b) 11.8 dpa alloy ES after straining to failure in the 320 °C primary water environment at low ECP.

CHAPTER 6 - CONCLUSIONS

CP 304L SS (alloy AS) was highly susceptible to IASCC at irradiation doses between 5.5 and 47.5 dpa, HP 304L (alloy ES) was less susceptible at ~10 dpa, and HP 304L+Ni (alloy KS) was not susceptible at all to IG cracking at 9.6 dpa, based on results of CERT tests in 288 °C NWC. Differences in strain to failure among these conditions prevented a direct comparison of dislocation channeling at intergranular crack initiation sites after CERT tests, therefore a novel four-point bend SCC experiment was developed to more carefully analyze dislocation channeling and sites of crack initiation. The same relative cracking susceptibility among the alloys determined from the CERT test was reproduced in the four-point bend test, indicating that a similar condition for crack initiation had been created in the novel SCC experiment. The four-point bend test was successful in forming IASCC initiation sites and led to the following major conclusions:

- Dislocation channeling was found to be a major factor controlling IASCC crack formation in both alloys AS and ES.
- The stress necessary to initiate IASCC in the CP 304L alloy (alloy AS) decreased with irradiation dose during SCC experiments performed in NWC conditions. Because dislocation channeling preceded IG cracking, the stress at which channels appear decreases with dose and likely controls the cracking.

- MnS surface inclusions greatly enhanced susceptibility to IASCC initiation in CP 304L alloy AS. MnS dissolves during exposure to the NWC environment, forming sulfate ions (SO_4^{2-}) and Mn_2O_3. In all locations where IG cracking was observed to initiate, an oxide cap was formed, occluding the inclusion site and creating a crevice condition with a deaerated and acidified environment within the crevice. Deaeration also forms a potential gradient between the crevice tip and mouth, attracting sulfate ions into the crevice. Increased sulfate concentration increases conductivity, establishing an environmental condition with a high potential for crack initiation and growth. The aggressive environment in conjunction with local stress concentration is responsible for crack initiation in alloy AS. This stress concentration is achieved by a superposition of stresses caused by 1) a favorably oriented grain boundary, 2) the dissolved inclusion site, and 3) a discontinuous dislocation channel intersecting the grain boundary.
- HP 304L stainless steel (alloy ES) was less susceptible to IASCC than CP 304L alloy AS due to a lack of MnS inclusions, but IASCC initiation was still possible in this alloy because stress concentrations at discontinuous dislocation channel – grain boundary intersections were able to rupture the surface oxide and nucleate cracking.
- HP 304L+Ni stainless steel (alloy KS) was not susceptible to IASCC because this alloy had no MnS inclusions and the highest propensity to transmit dislocation channels across grain boundaries, thus relieving stress at the DC-GB site.

CHAPTER 7 - FUTURE WORK

As the four-point bend test is a novel experiment for testing SCC susceptibility, there are many opportunities for future work. The observation of cracking at the sample edge in alloy ES revealed that the sample design may likely be improved to cause cracking within the sample interior when materials have significant ductility. FEA modeling should be revisited to compare the effect of adding a chamfer or round to the sample edges, which may alleviate this issue.

The similar stress dependence for IASCC initiation between the four-point bend test and CLTs is an interesting commonality that should be further investigated. Four-point bend tests should be conducted in 320 °C primary water as well as on materials which were in a cold-worked condition prior to irradiation, to determine whether crack initiation is affected by the mechanism presented in this study. MnS dissolution has been observed in lower potential high temperature environments such as 320 °C primary water [194], therefore it is possible that these types of inclusion and a similar stress dependence of DC formation caused the similarity between test types.

Although current results indicated that inclusions did not concentrate stress and cause adjacent channel formation, these experiments were performed without viewing the effect of inclusion dissolution on stress concentration. It is of interest to determine whether inclusion dissolution affects deformation by performing experiments in Ar *after* exposure to NWC.

Additional work is necessary to understand the fundamental mechanisms affecting why DCs are able to form at lower stress in higher dose material. A systematic study is necessary to perform deformation experiments on alloys with controlled and well-characterized microstructures. It is possible that the critical resolved shear stress is affected by radiation-induced defect characteristics such as type, size, and number density.

The effect of the decreasing stress to initiate channels must also be separated from the possible effect of GB degradation after high temperature water exposure in irradiated materials. The observed correlation between Si segregation and GB corrosion implies that GBs may become weakened, thus explaining the decreasing stress to initiate IASCC. Additional characterization needs to be performed on irradiated alloys after exposure to determine whether GB corrosion is an affecting factor in the GB cohesive strength.

Finally, the current study was unable to isolate the effects of SFE and microstructure on dislocation channel transmission at GBs in irradiated materials. It is necessary to focus on what mechanism causes slip transmission to occur, and why slip transmission is more favorable in certain alloys.

APPENDICES

APPENDIX A - INCLUSION CHEMISTRY ANALYSIS

Chemical analysis of surface inclusions was performed on unirradiated samples of alloy AS (both before and after 24 hour exposure to NWC), alloy ES, and alloy KS using EDX. Inclusion compositions determined from XEDX spectra (in at% and wt%) and images of both the inclusion and resulting EDX spectrum have been provided.

Table A.1. Inclusion and matrix compositions (at%) determined from EDX for the unirradiated sample of alloy AS prior to NWC exposure.

Inclusion No.	Width, µm	Height, µm	O	Al	S	Ti	Cr	Mn	Cu	V	Fe	Ni	Mo	Type
1	23.1	10	–	–	45.5	1.1	4.8	48.6	–	–	–	–	–	MnS
2	5.2	3.5	–	3.0	0.8	31.4	27.9	36.9	–	–	–	–	–	Oxide
3	5.2	1.7	–	0.5	34.5	8.3	10.1	46.7	–	–	–	–	–	MnS
4	27	4.4	–	0.2	41.1	1.6	7.4	49.7	–	–	–	–	–	MnS
5	11.8	6.5	–	2.2	40.1	4.2	8.1	45.4	–	–	–	–	–	MnS
6	11.7	5.6	36.8	0.8	–	23.2	15.9	23.3	–	–	–	–	–	Oxide
7	9.6	5.7	37.2	1.3	1.0	23.2	15.4	22.0	–	–	–	–	–	Oxide
8	7	4.4	37.8	2.4	0.2	20.7	16.5	22.4	–	–	–	–	–	Oxide
9	9.1	6.5	36.6	4.1	0.8	17.7	18.6	22.2	–	–	–	–	–	Oxide
10	11.3	4.9	39.2	2.4	1.1	19.5	15.9	21.9	–	–	–	–	–	Oxide
11	12.2	7.4	–	–	47.0	–	4.2	48.8	–	–	–	–	–	MnS
12	29.2	11.8	–	–	45.0	–	6.4	48.6	–	–	–	–	–	MnS
13	17.4	8.7	–	–	45.4	2.8	–	47.8	3.7	0.3		–	–	MnS
14	50.5	11.3	–	–	40.9	1.0	–	40.1	–	0.4	9.0	–	–	MnS
15	10.9	5.7	–	–	35.7	1.4	–	34.2	–	0.5	15.1	–	–	MnS
16	14.8	5.2	–	–	33.9	1.3	–	31.1	–	0.7	15.7	–	–	MnS
17	20	7.8	–	–	45.0	1.3	5.8	44.8	2.8	0.3	–	–	–	MnS
18	8.3	7.4	–	–	42.9	1.0	10.7	42.5	2.5	0.4	–	–	–	MnS
19	10.9	11.3	–	–	42.8	1.6	7.0	46.4	1.9	0.3	–	–	–	MnS
20	5.2	3.5	–	–	43.7	1.0	–	49.6	5.2	0.5	–	–	–	MnS
21	8.7	4.4	11.2	–	20.7	6.2	13.0	21.7	2.0	–	22.6	2.7	–	MnS
22	15.7	7.4	34.5	3.1	–	16.8	16.8	19.8	–	–	6.9	0.9	–	Oxide
23	13.5	5.7	33.5	3.0	–	14.2	16.4	15.1	–	–	14.8	2.0	–	Oxide
24	10.5	3.5	26.6	0.9	–	8.0	15.5	21.7	–	–	16.3	1.2	9.5	Oxide
Matrix			–	–	–	–	21.9	–	–	–	67.6	10.5	–	–

– indicates that quantity was not measured

Table A.2. Inclusion and matrix compositions (at%) determined from EDX for the unirradiated sample of alloy AS after 24 hours of NWC exposure.

Inclusion No.	Width, µm	Height, µm	C	O	Al	Si	S	Ti	Cr	Mn	Fe	Ni	Type
1	23.1	10	–	26.7	–	1.4	3.8	1.6	6.5	56.1	3.9	–	MnS
2	5.2	3.5	–	15.1	–	0.3	0.2	10.9	21.9	13.3	33.4	4.9	Oxide
3	5.2	1.7	–	13.6	–	0.6	2.8	7.0	18.7	21.0	31.6	4.6	MnS
4	27	4.4	–	9.7	–	0.6	0.8	2.3	16.8	24.0	39.9	5.9	MnS
5	11.8	6.5	–	10.6	–	0.2	13.8	4.8	14.8	30.7	22.0	3.1	MnS
6	11.7	5.6	–	21.0	–	0.5	0.6	18.1	20.2	17.2	19.8	2.5	Oxide
7	9.6	5.7	–	22.2	–	0.5	0.2	21.3	20.4	16.7	16.3	2.7	Oxide
8	7	4.4	–	19.5	1.6	0.4	0.3	18.1	21.9	18.4	17.4	2.5	Oxide
9	9.1	6.5	–	22.8	2.5	0.3	0.4	14.4	20.4	24.5	12.8	1.9	Oxide
10	11.3	4.9	–	20.7	1.8	0.4	0.3	17.1	21.6	15.8	19.4	2.8	Oxide
11	12.2	7.4	–	16.5	0.3	1.5	0.1	2.2	21.3	6.4	44.9	6.7	MnS
12	29.2	11.8	–	34.5	0.3	1.7	0.2	4.5	20.2	9.7	25.0	3.9	MnS
13	17.4	8.7	–	22.4	0.4	1.3	1.2	3.0	10.4	51.2	8.8	1.4	MnS
14	50.5	11.3	–	20.0	0.3	0.6	2.8	1.1	9.2	50.7	13.4	1.9	MnS
15	10.9	5.7	–	12.6	0.0	0.1	9.7	0.9	12.1	35.8	24.9	4.0	MnS
16	14.8	5.2	–	7.8	0.0	0.1	14.2	1.1	14.3	29.0	29.4	4.2	MnS
17	20	7.8	–	28.7	0.3	0.8	1.9	1.3	6.0	57.4	2.8	0.8	MnS
18	8.3	7.4	–	22.3	0.3	0.9	1.0	1.1	9.5	47.8	14.7	2.4	MnS
19	10.9	11.3	–	29.7	0.2	0.9	2.1	3.8	9.1	43.5	9.4	1.4	MnS
20	5.2	3.5	–	8.2	0.2	0.8	0.3	1.8	16.8	32.0	35.1	4.8	MnS
21	8.7	4.4	–	15.2	0.3	0.6	0.2	6.8	12.8	36.8	23.7	3.6	MnS
22	15.7	7.4	–	23.8	2.1	0.3	0.2	20.4	21.1	20.2	10.5	1.5	Oxide
23	13.5	5.7	–	19.2	1.8	0.4	0.2	17.7	22.5	12.2	23.1	3.0	Oxide
24	10.5	3.5	–	18.4	0.9	0.6	0.4	9.1	18.9	27.7	21.9	2.2	Oxide
Matrix - 1			–	6.9		0.7	0.3	0.2	18.7	2.2	60.7	10.4	–
Matrix - 2			–	9.4	0.6	0.8	0.4	0.3	18.2	4.4	55.3	10.6	–
Matrix - 3			–	6.6	0.1	0.6	0.5	0.2	19.4	2.1	59.9	10.8	–
Matrix - 4			–	5.3	0.0	0.5	0.3	0.2	18.9	2.2	61.1	11.5	–
Matrix - 5			–	6.6	0.4	0.6	0.3	0.1	18.3	1.9	61.3	10.5	–

– indicates that quantity was not measured

Table A.3. Inclusion and matrix compositions (at%) determined from EDX for the unirradiated sample of alloy ES.

Inclusion No.	Width, µm	Height, µm	O	Al	Ti	Cr	Mn	Fe	Ni
1	2.0	1.7	14.1	2.4	0.7	22.8	7.9	45.3	6.8
2	1.9	2.3	13.7	2.1	0.5	24.0	8.1	45.4	6.2
3	2.5	2.9	12.9	3.4	0.4	20.1	5.6	50.4	7.3
4	2.5	2.0	15.2	2.2	0.7	25.5	9.4	40.9	6.1
5	2.8	2.9	16.9	3.4	0.7	30.0	14.6	30.4	4.0
6	1.7	1.8	14.9	3.6	0.4	24.1	10.1	41.1	5.8
7	2.2	2.9	17.6	0.2	0.5	33.0	13.3	30.9	4.5
8	3.2	3.1	19.2	3.2	0.7	31.8	16.0	25.6	3.5
9	2.6	2.5	16.8	1.7	0.7	28.4	11.5	35.9	4.9
10	2.8	2.6	12.6	3.6	0.5	24.0	10.2	43.0	6.1
11	2.0	2.5	9.0	0.8	0.8	31.4	12.7	39.1	6.2
Matrix - 1			2.8	0.3	0.2	18.0	1.1	66.3	11.4
Matrix - 2			2.8	0.2	0.2	17.5	1.2	66.6	11.5
Matrix - 3			2.5	0.2	0.3	17.8	1.1	67.0	11.1

Table A.4. Inclusion and matrix compositions (at%) determined from EDX for the unirradiated sample of alloy KS.

Inclusion No.	Width, µm	Height, µm	O	Al	Si	Ti	Cr	Mn	Fe	Ni
1	2.7	1.6	15.8	6.3	–	1.0	25.5	15.3	25.8	10.3
2	2.0	2.0	8.7	3.5	–	0.4	18.1	3.3	45.7	20.4
3	2.3	2.5	27.1	10.3	0.6	1.0	16.0	6.3	28.8	9.9
4	2.2	2.4	29.2	10.4	1.2	0.6	16.3	6.6	25.8	9.9
5	2.1	2.2	29.2	13.6	0.2	0.3	14.7	6.1	26.2	9.7
6	1.2	1.1	25.0	10.1	0.8	0.7	16.8	7.3	29.1	10.2
7	2.6	2.5	28.4	9.2	0.7	1.5	16.7	7.1	26.4	9.9
8	1.8	1.6	24.9	9.0	0.3	0.3	15.4	4.6	33.0	12.5
9	1.8	1.6	24.3	9.7	0.7	0.9	17.2	7.2	29.3	10.7
10	2.2	2.1	29.6	11.7	0.7	0.4	16.0	5.6	26.7	9.4
Matrix - 1			2.6	0.1	–	0.3	18.6	1.3	52.9	24.1
Matrix - 2			7.5	0.5	0.4	0.3	17.5	1.2	50.9	21.8
Matrix - 3			6.7	1.1	0.5	0.2	18.3	0.9	50.6	21.5

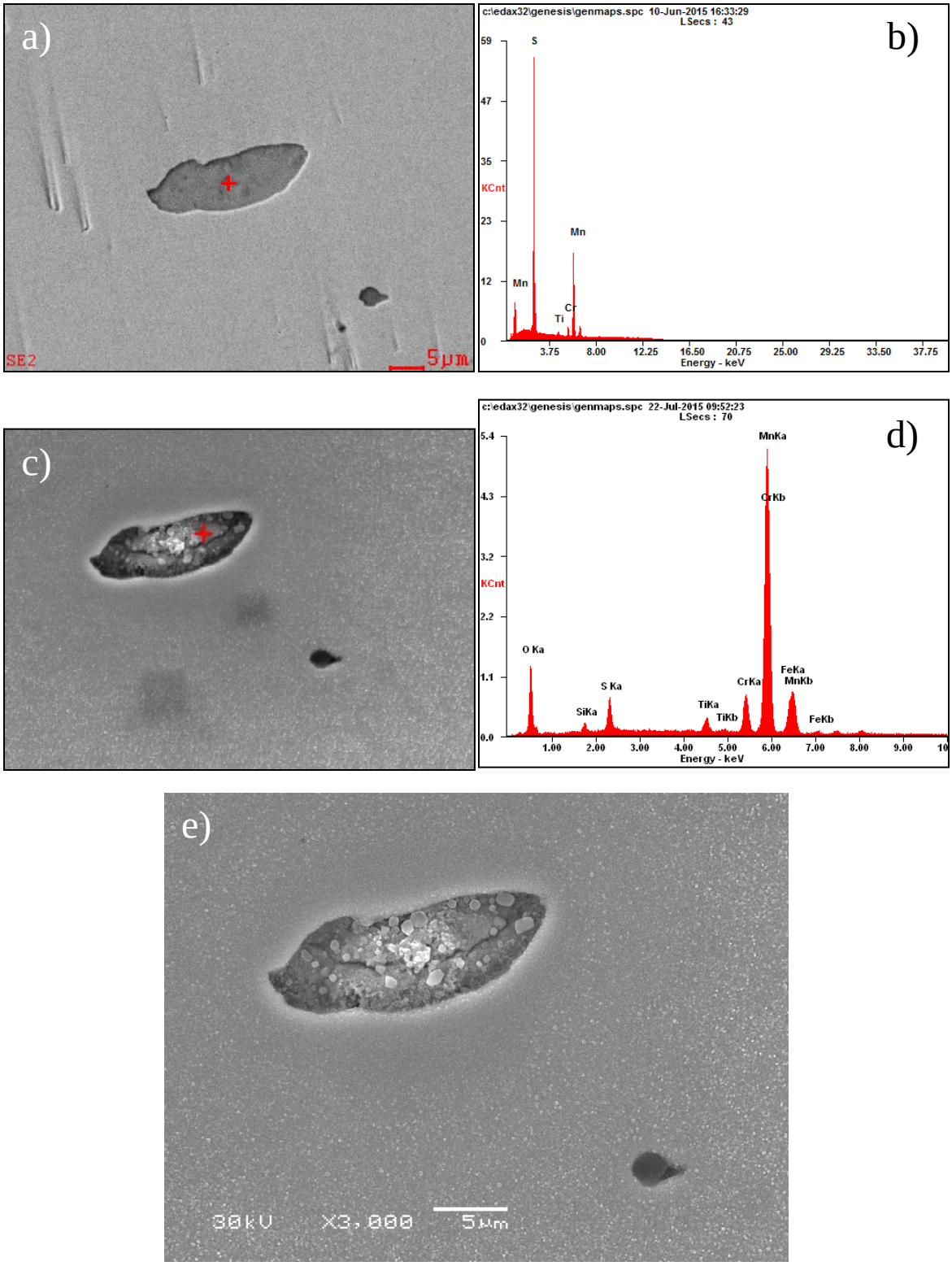

Figure A.1. SEM and corresponding EDX spectra for inclusion 1 on the unirradiated alloy AS specimen. a) and b) pre-exposure, c) through e) after 24 hour exposure to NWC.

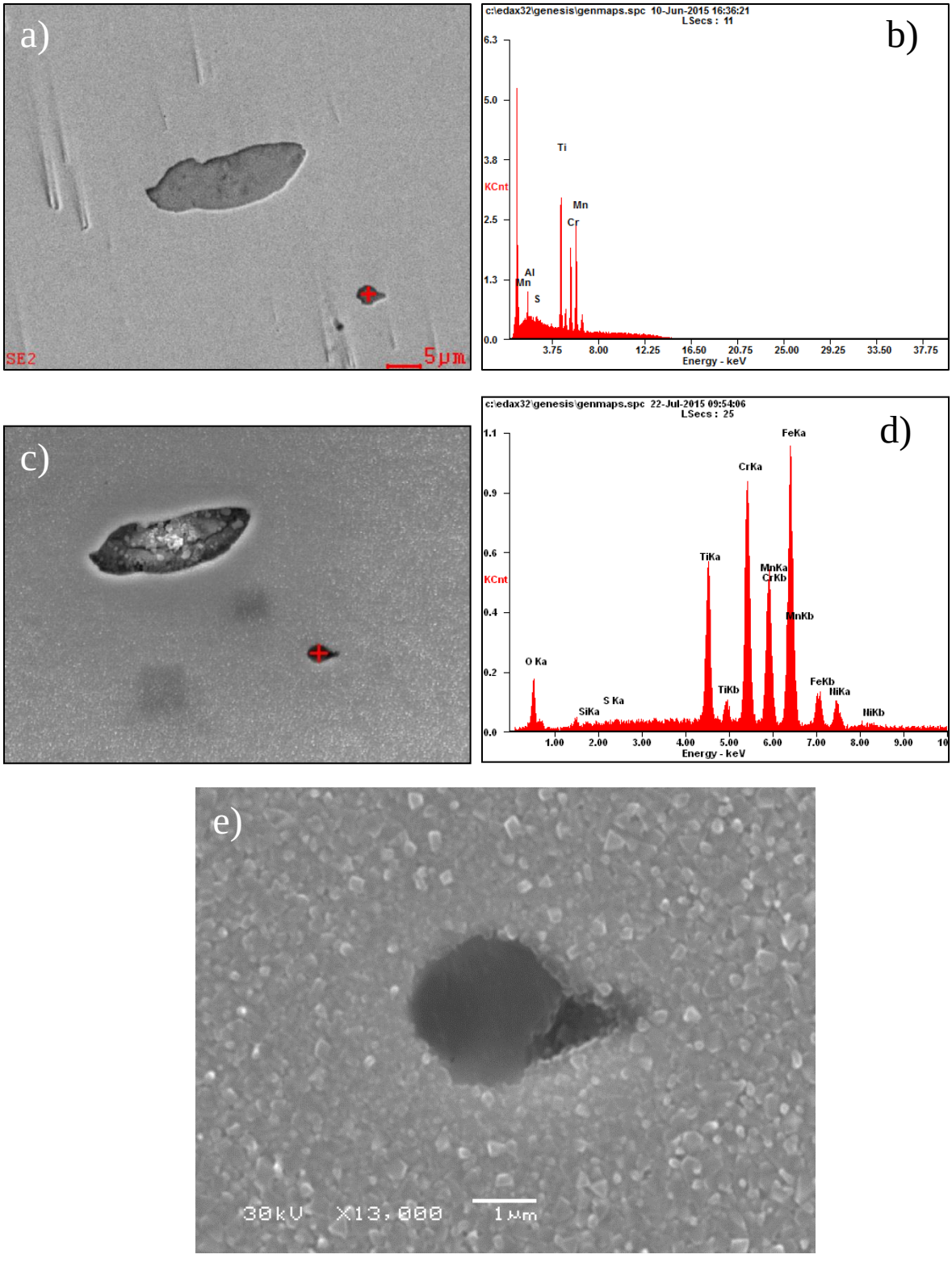

Figure A.2. SEM and corresponding EDX spectra for inclusion 2 on the unirradiated alloy AS specimen. a) and b) pre-exposure, c) through e) after 24 hour exposure to NWC.

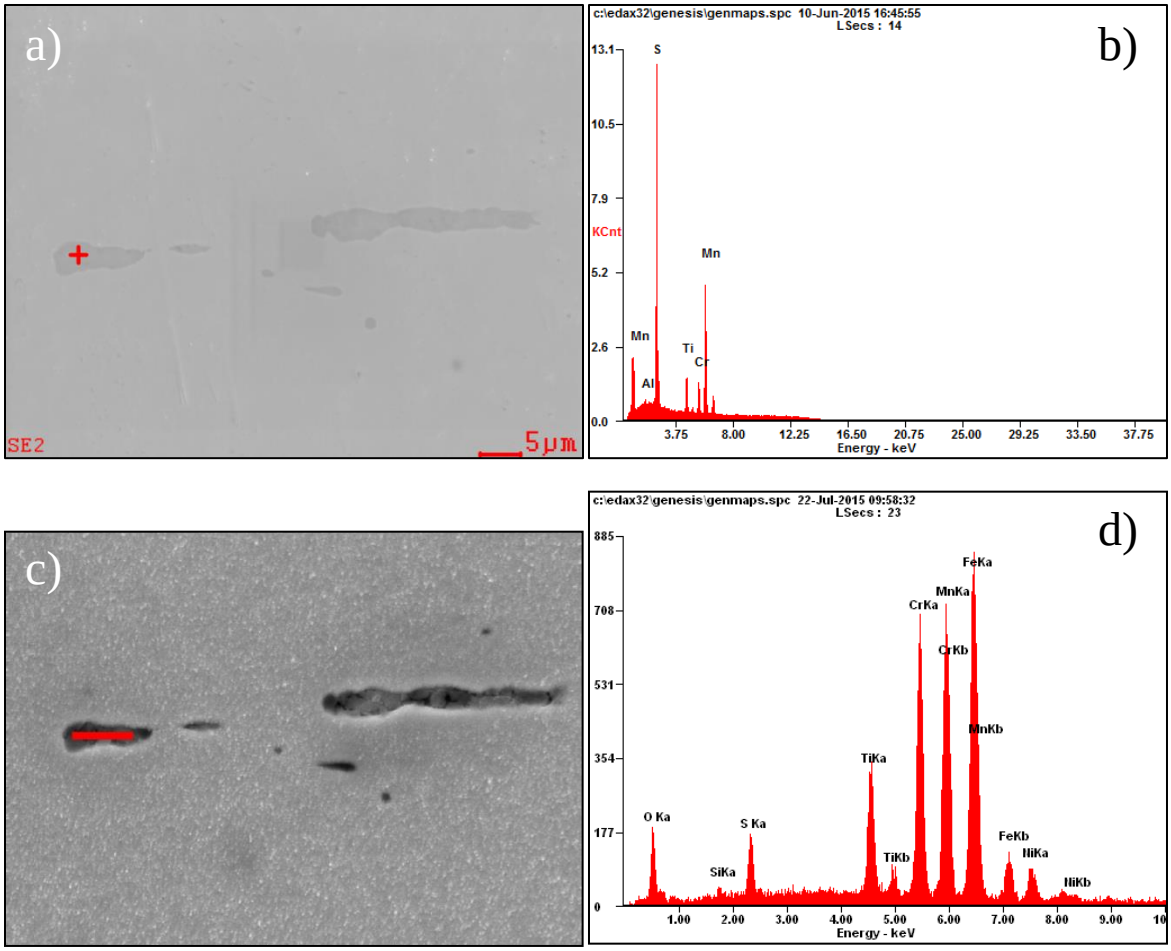

Figure A.3. SEM and corresponding EDX spectra for inclusion 3 on the unirradiated alloy AS specimen. a) and b) pre-exposure, c) and d) after 24 hour exposure to NWC.

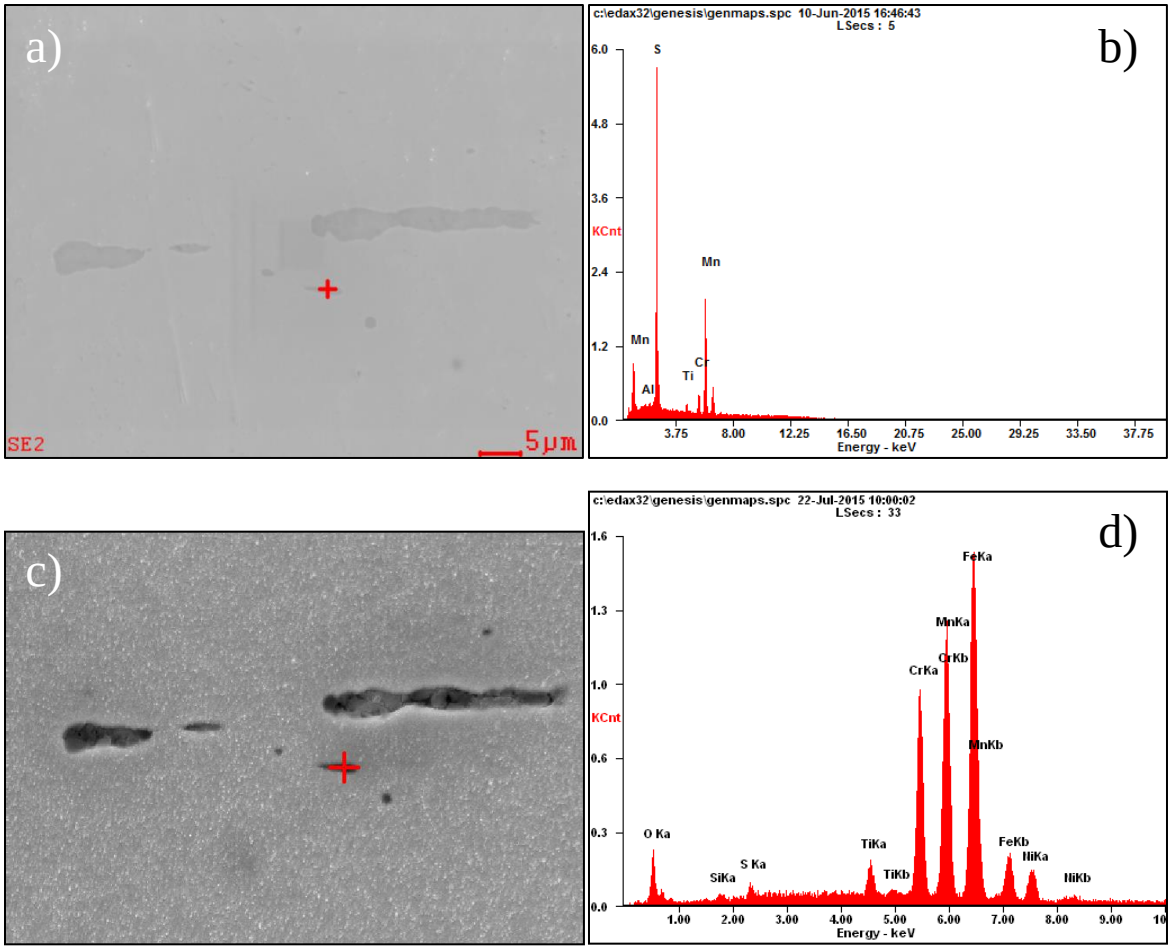

Figure A.4. SEM and corresponding EDX spectra for inclusion 4 on the unirradiated alloy AS specimen. a) and b) pre-exposure, c) and d) after 24 hour exposure to NWC.

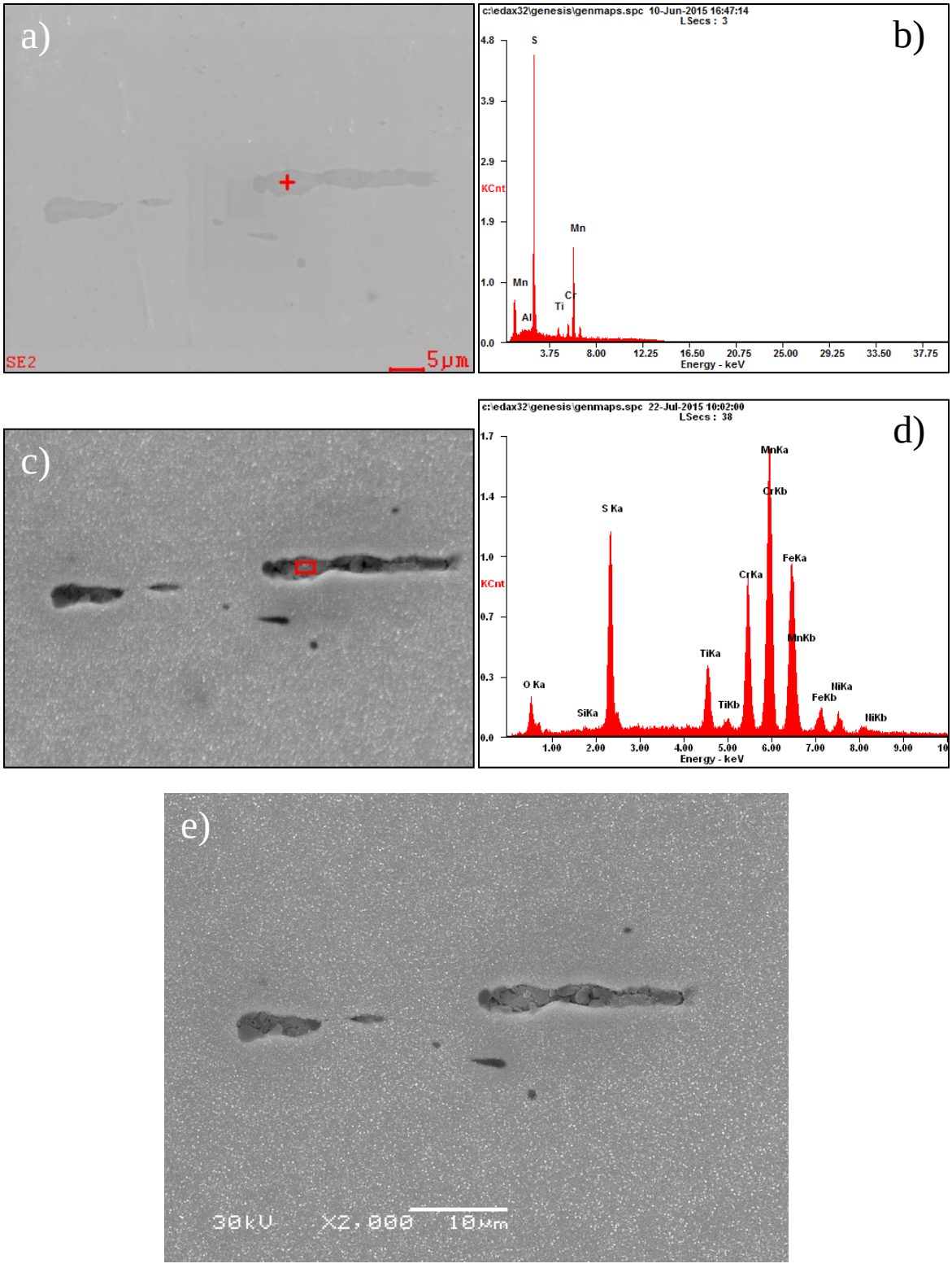

Figure A.5. SEM and corresponding EDX spectra for inclusion 5 on the unirradiated alloy AS specimen. a) and b) pre-exposure, c) through e) after 24 hour exposure to NWC.

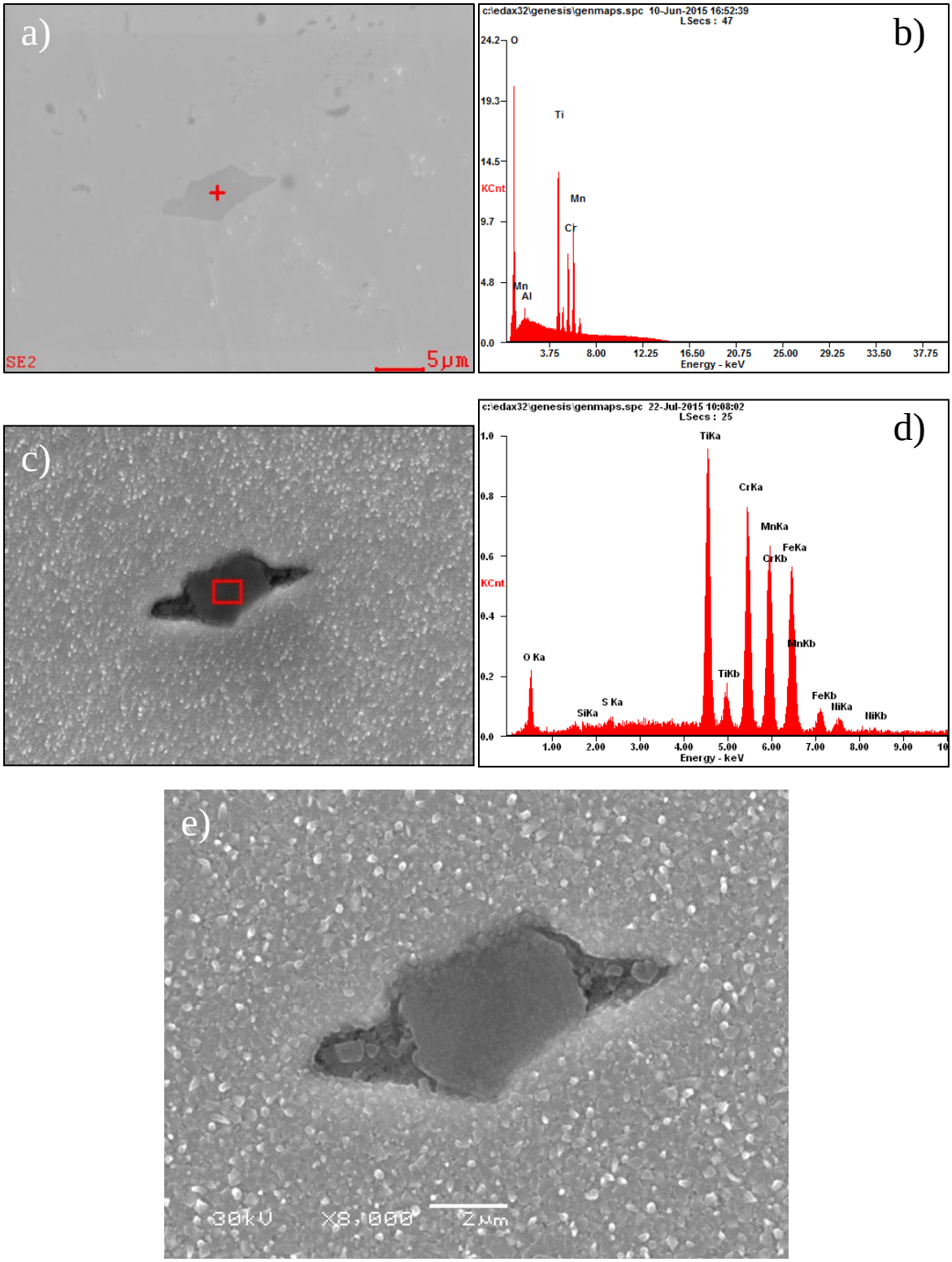

Figure A.6. SEM and corresponding EDX spectra for inclusion 6 on the unirradiated alloy AS specimen. a) and b) pre-exposure, c) through e) after 24 hour exposure to NWC.

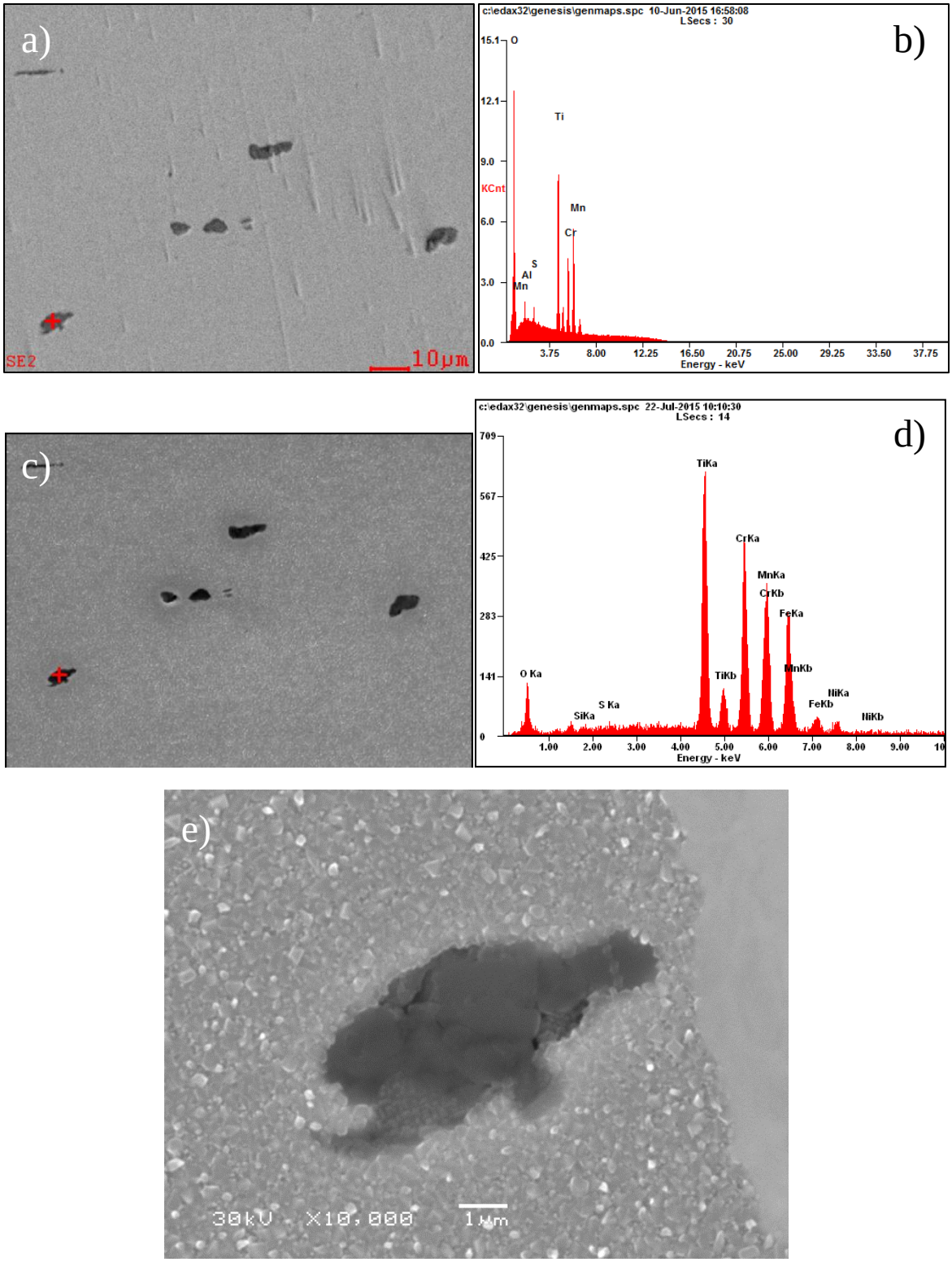

Figure A.7. SEM and corresponding EDX spectra for inclusion 7 on the unirradiated alloy AS specimen. a) and b) pre-exposure, c) through e) after 24 hour exposure to NWC.

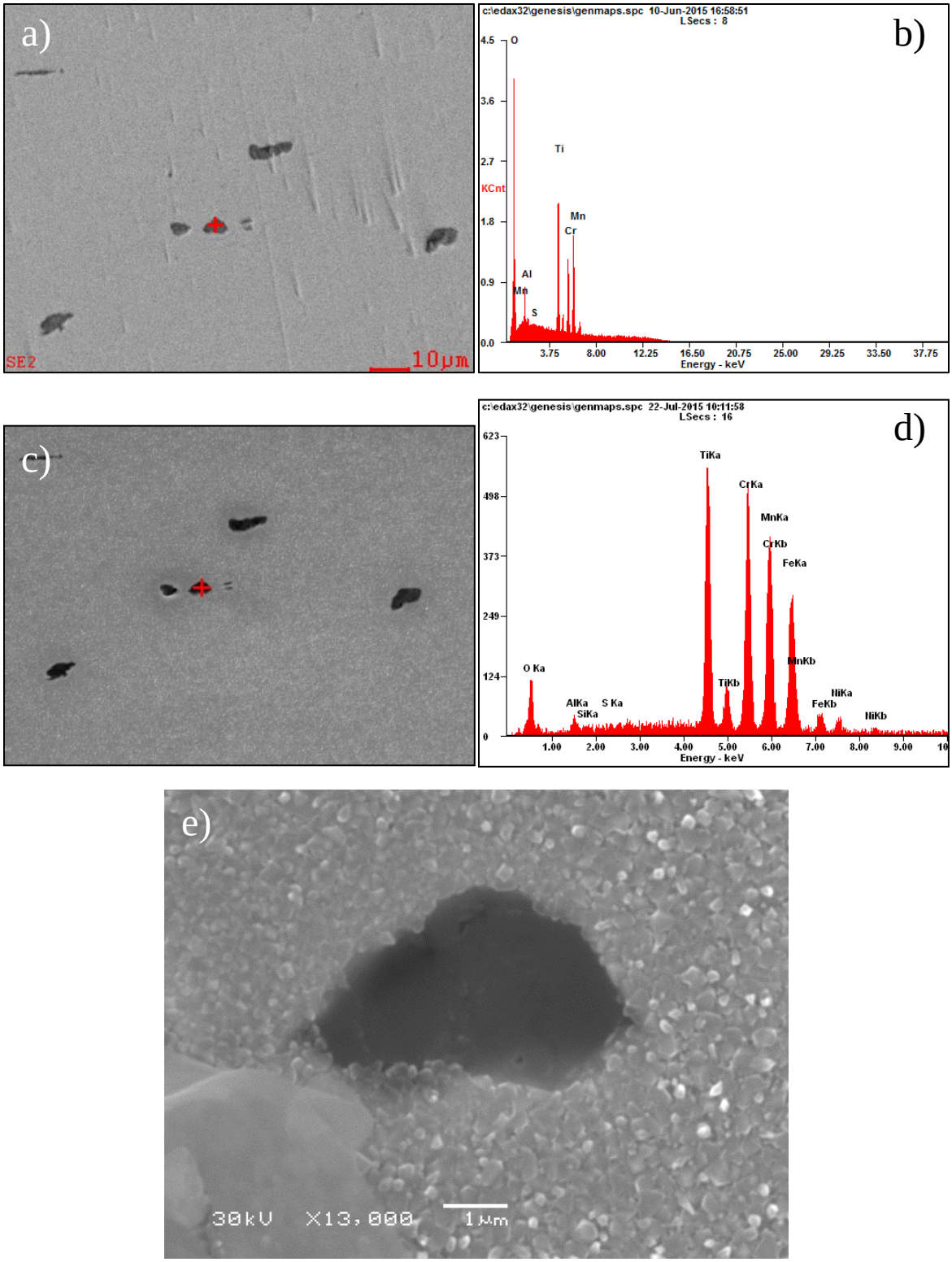

Figure A.8. SEM and corresponding EDX spectra for inclusion 8 on the unirradiated alloy AS specimen. a) and b) pre-exposure, c) through e) after 24 hour exposure to NWC.

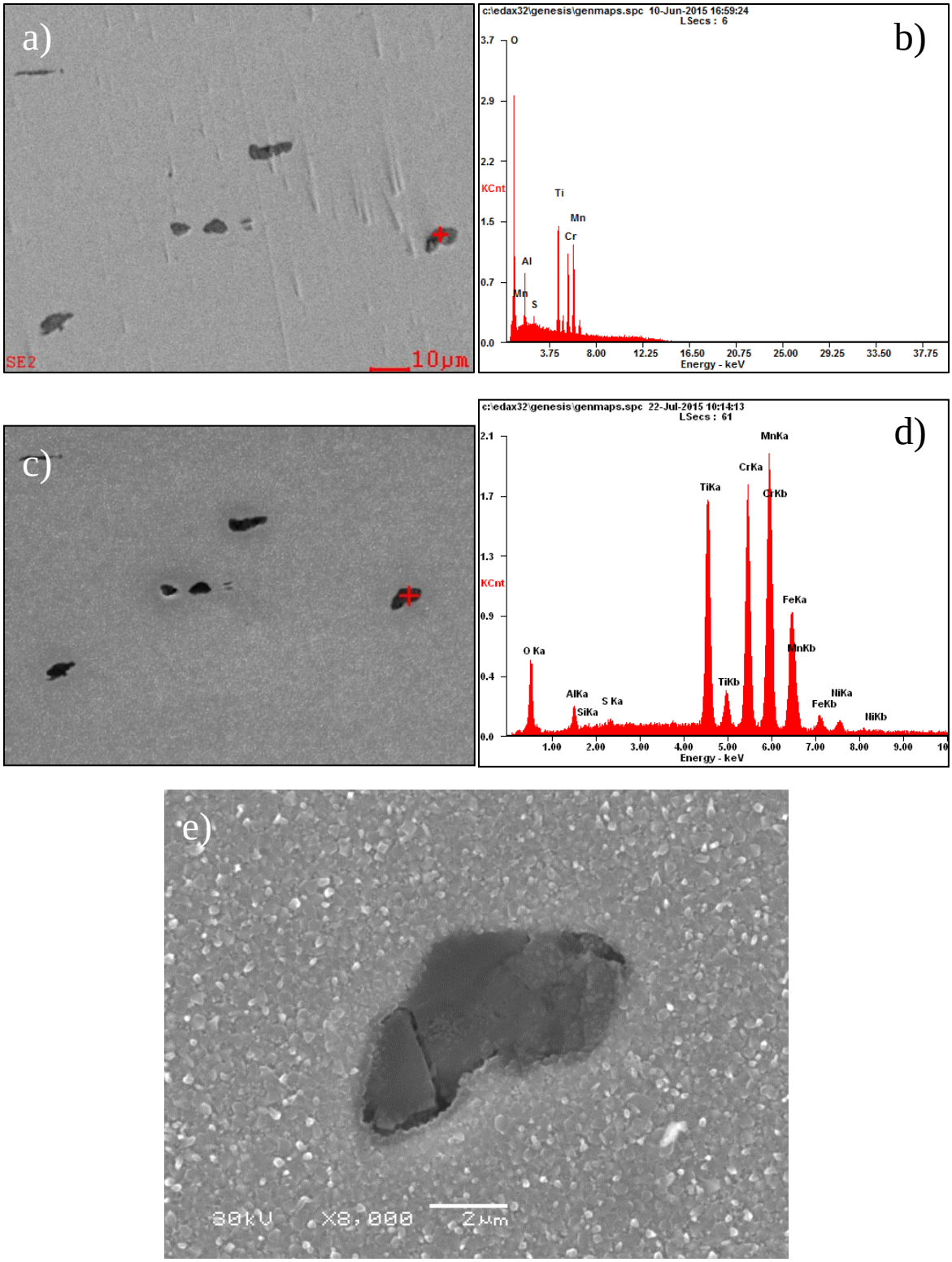

Figure A.9. SEM and corresponding EDX spectra for inclusion 9 on the unirradiated alloy AS specimen. a) and b) pre-exposure, c) through e) after 24 hour exposure to NWC.

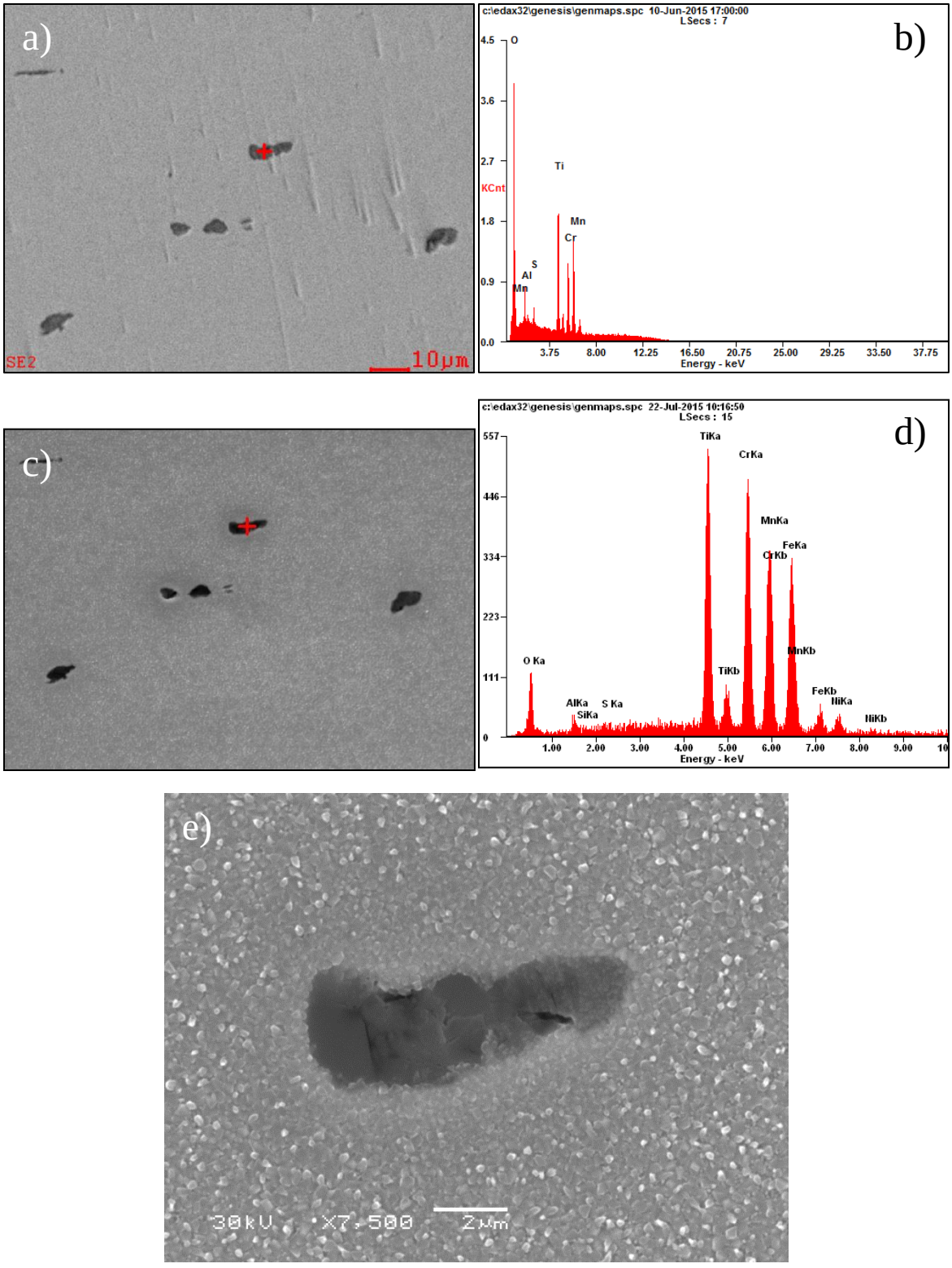

Figure A.10. SEM and corresponding EDX spectra for inclusion 10 on the unirradiated alloy AS specimen. a) and b) pre-exposure, c) through e) after 24 hour exposure to NWC.

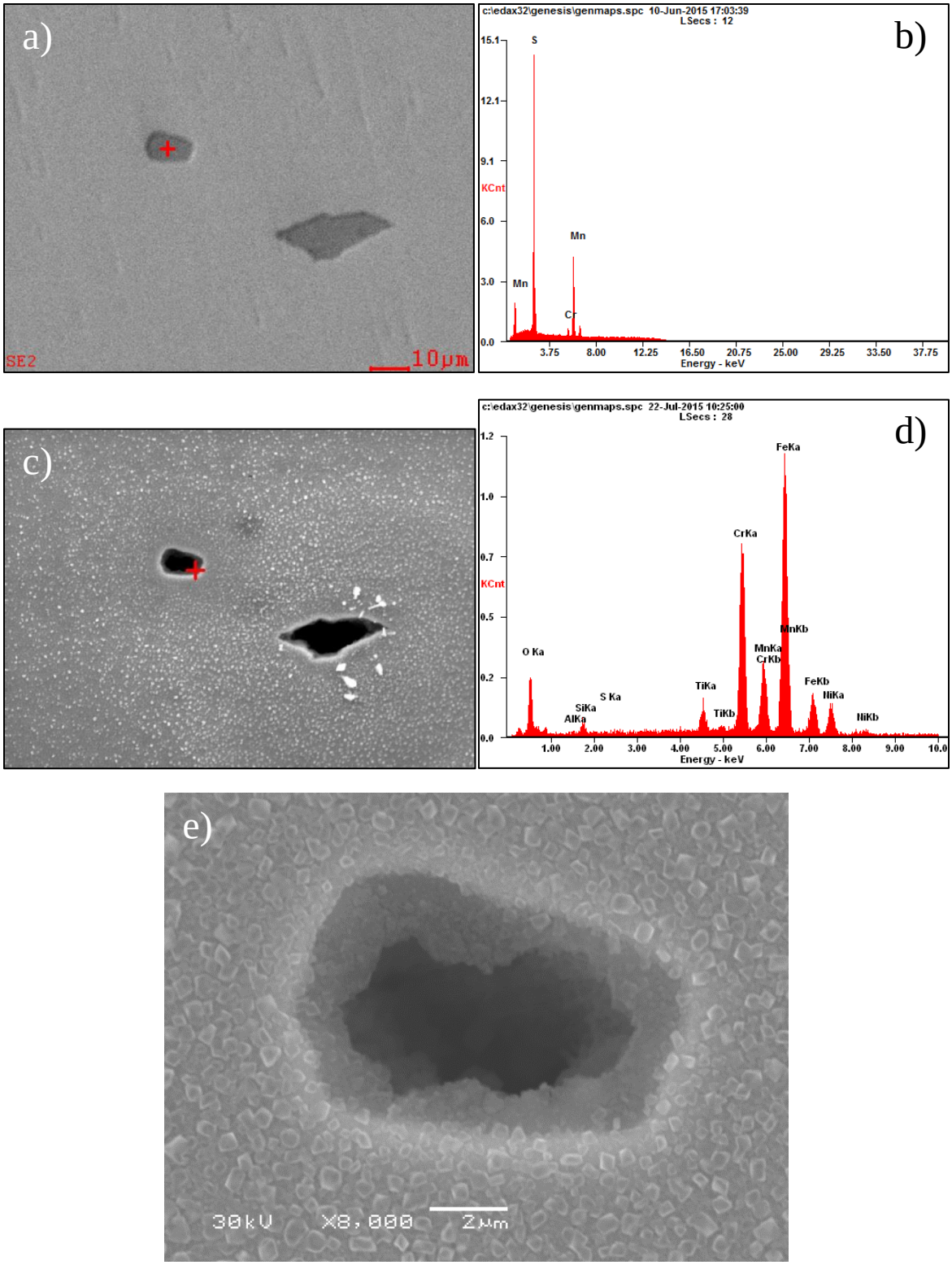

Figure A.11. SEM and corresponding EDX spectra for inclusion 11 on the unirradiated alloy AS specimen. a) and b) pre-exposure, c) through e) after 24 hour exposure to NWC.

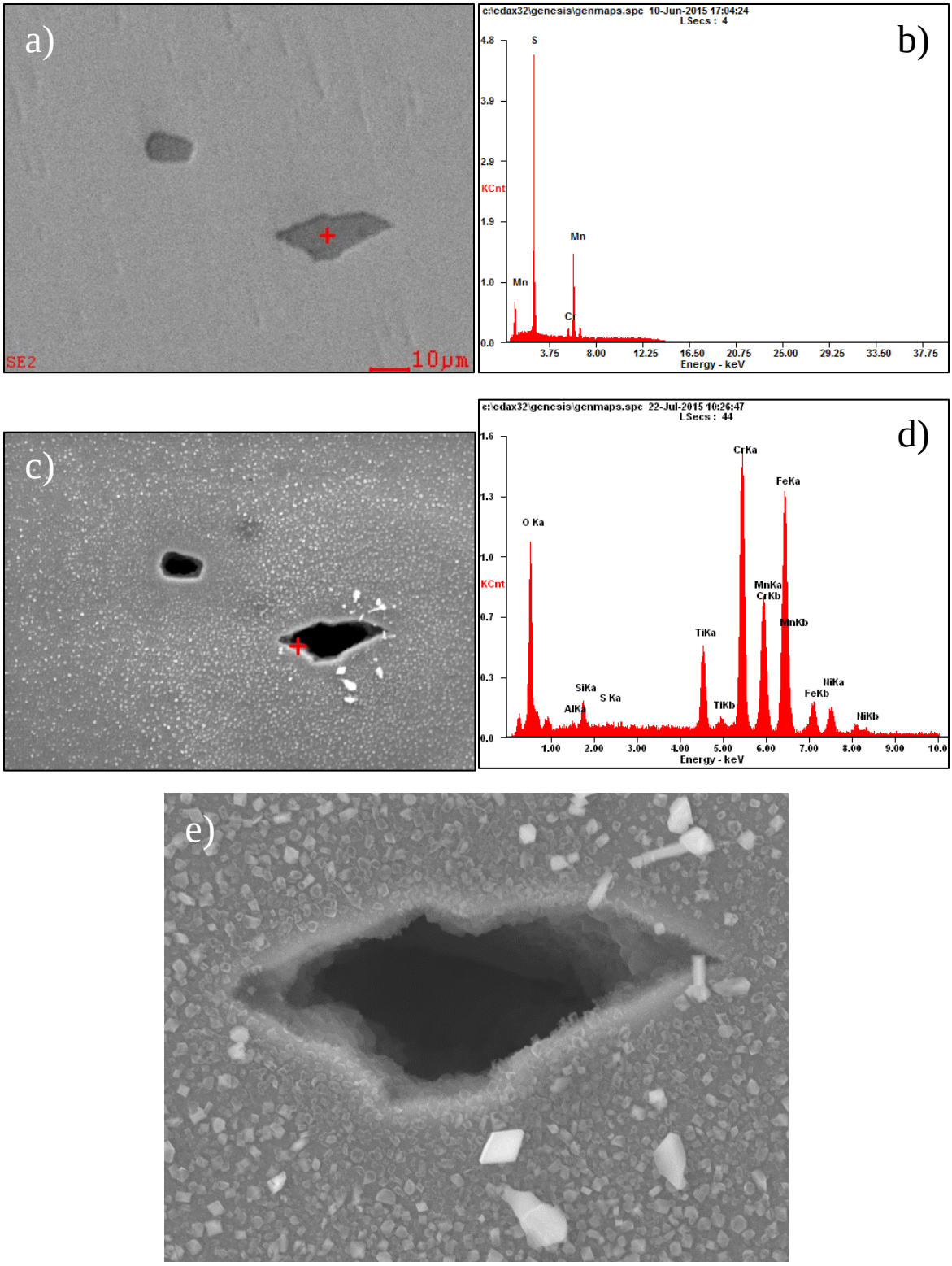

Figure A.12. SEM and corresponding EDX spectra for inclusion 12 on the unirradiated alloy AS specimen. a) and b) pre-exposure, c) through e) after 24 hour exposure to NWC.

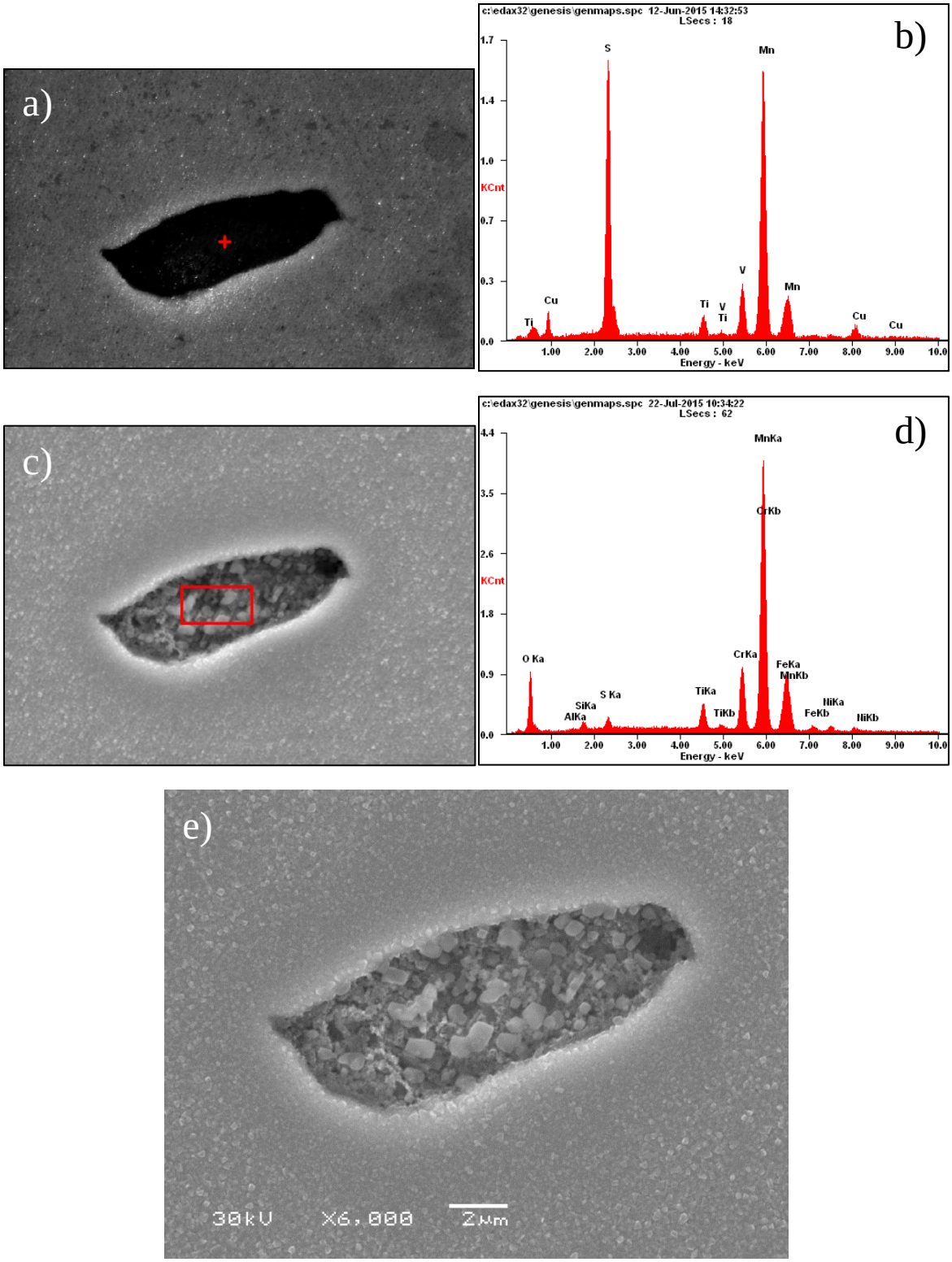

Figure A.13. SEM and corresponding EDX spectra for inclusion 13 on the unirradiated alloy AS specimen. a) and b) pre-exposure, c) through e) after 24 hour exposure to NWC.

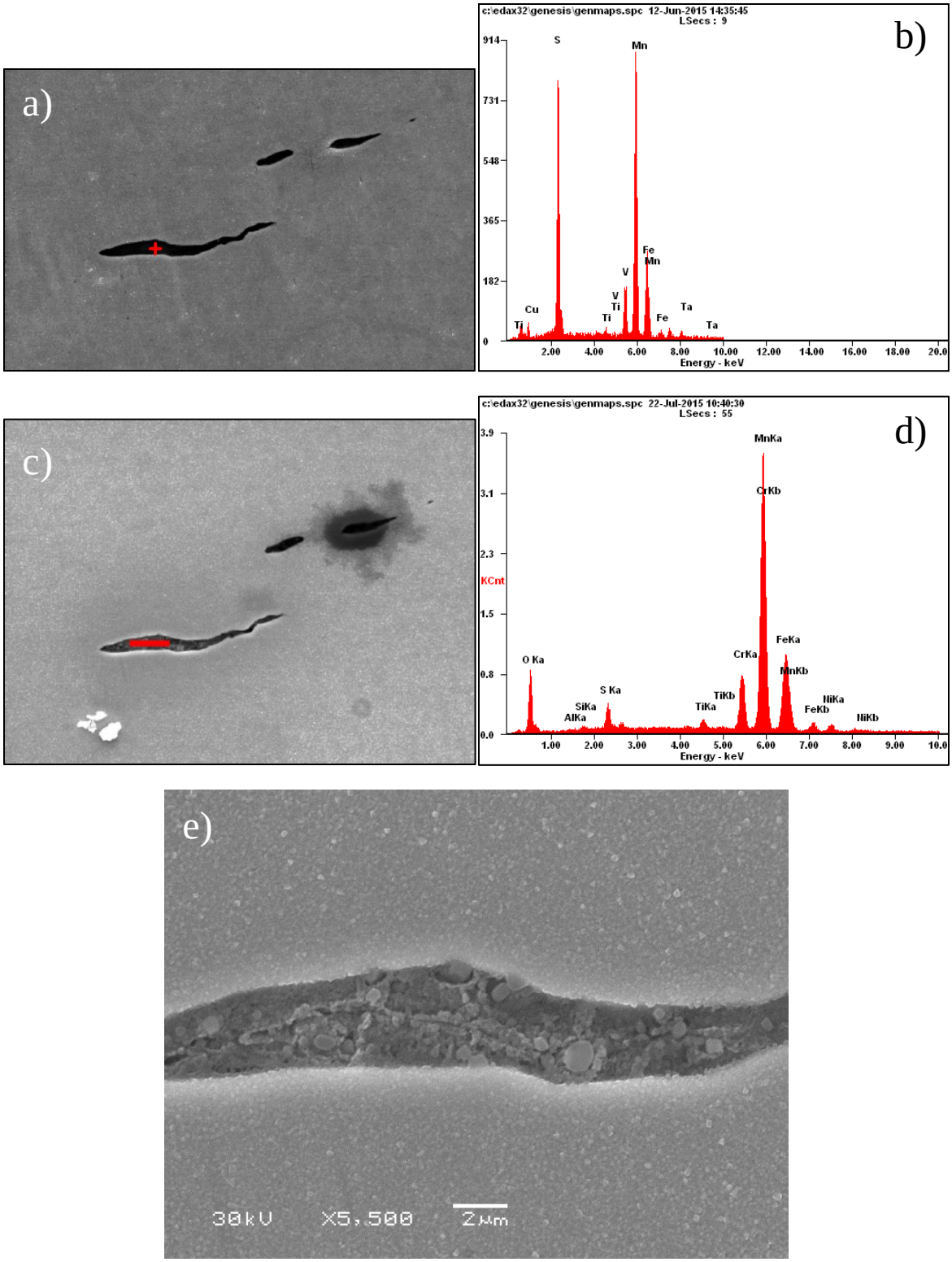

Figure A.14. SEM and corresponding EDX spectra for inclusion 14 on the unirradiated alloy AS specimen. a) and b) pre-exposure, c) through e) after 24 hour exposure to NWC.

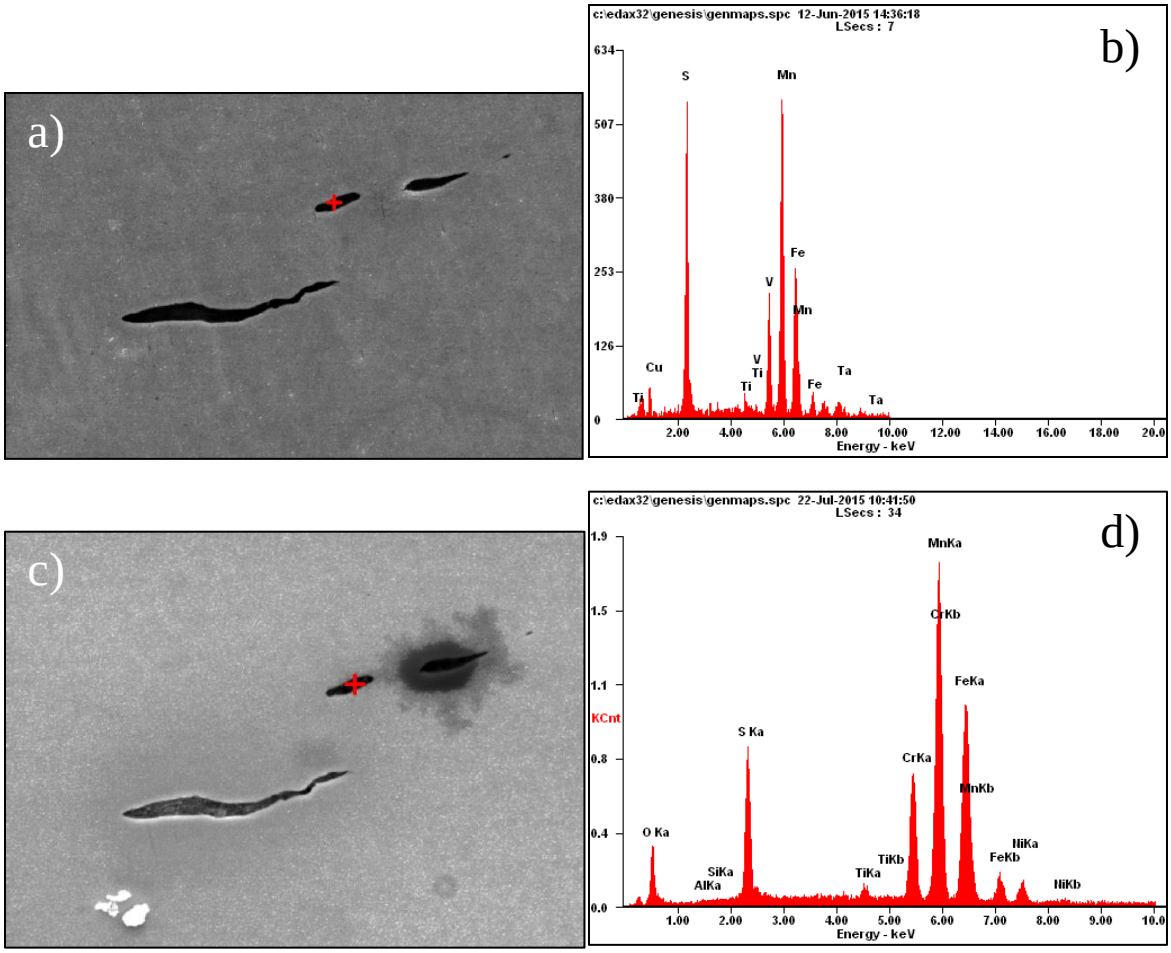

Figure A.15. SEM and corresponding EDX spectra for inclusion 15 on the unirradiated alloy AS specimen. a) and b) pre-exposure, c) through d) after 24 hour exposure to NWC.

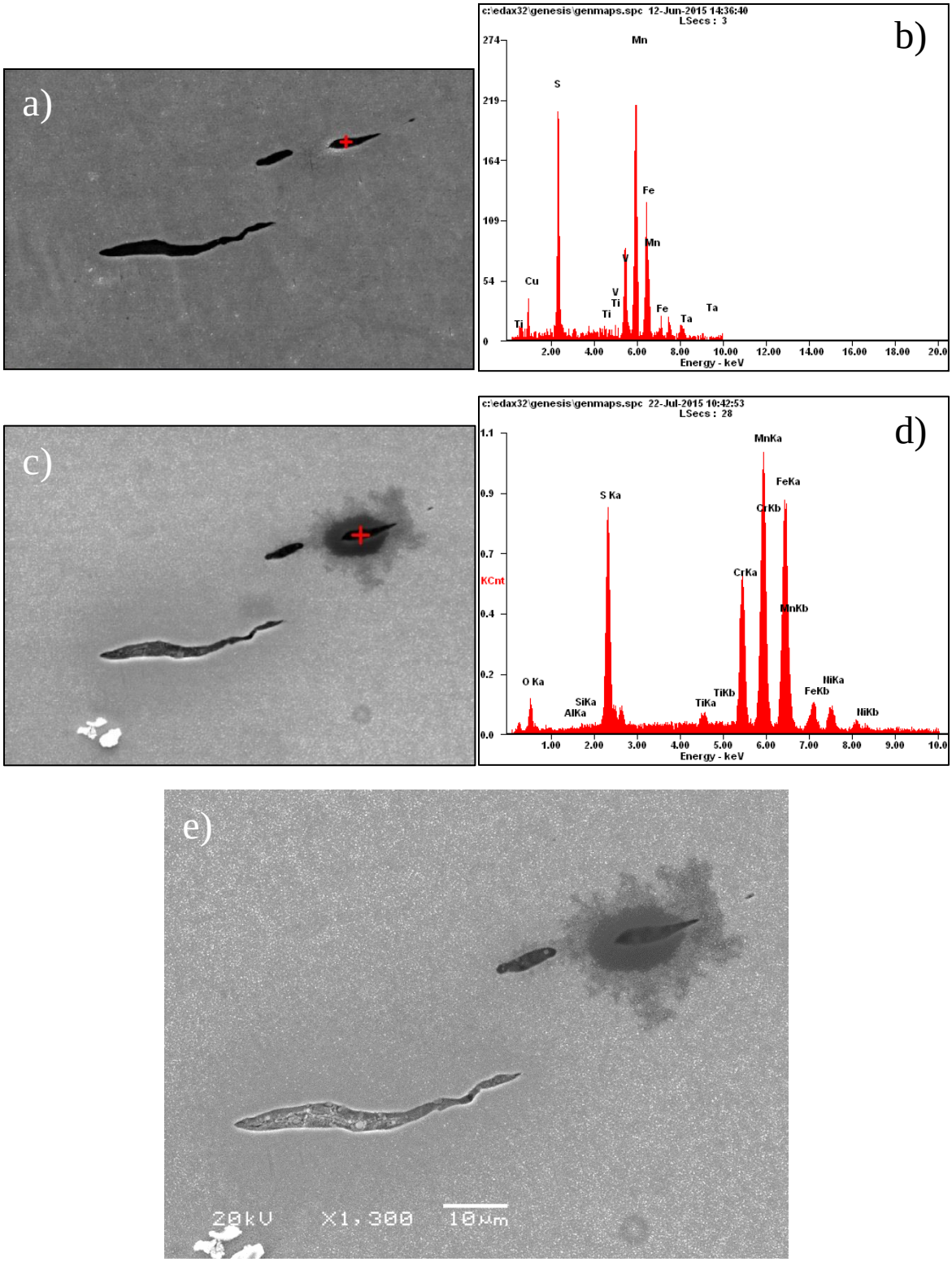

Figure A.16. SEM and corresponding EDX spectra for inclusion 16 on the unirradiated alloy AS specimen. a) and b) pre-exposure, c) through e) after 24 hour exposure to NWC.

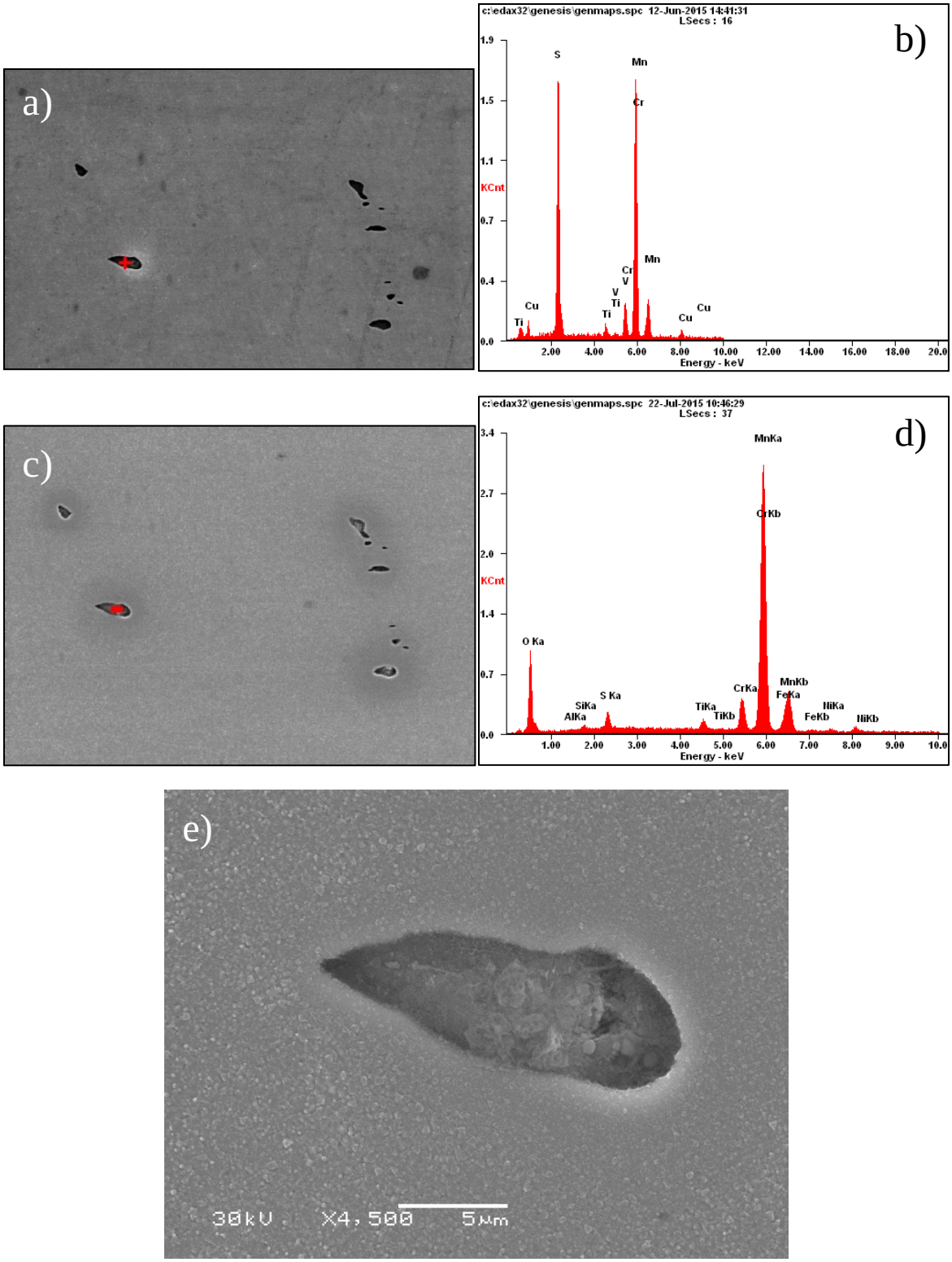

Figure A.17. SEM and corresponding EDX spectra for inclusion 17 on the unirradiated alloy AS specimen. a) and b) pre-exposure, c) through e) after 24 hour exposure to NWC.

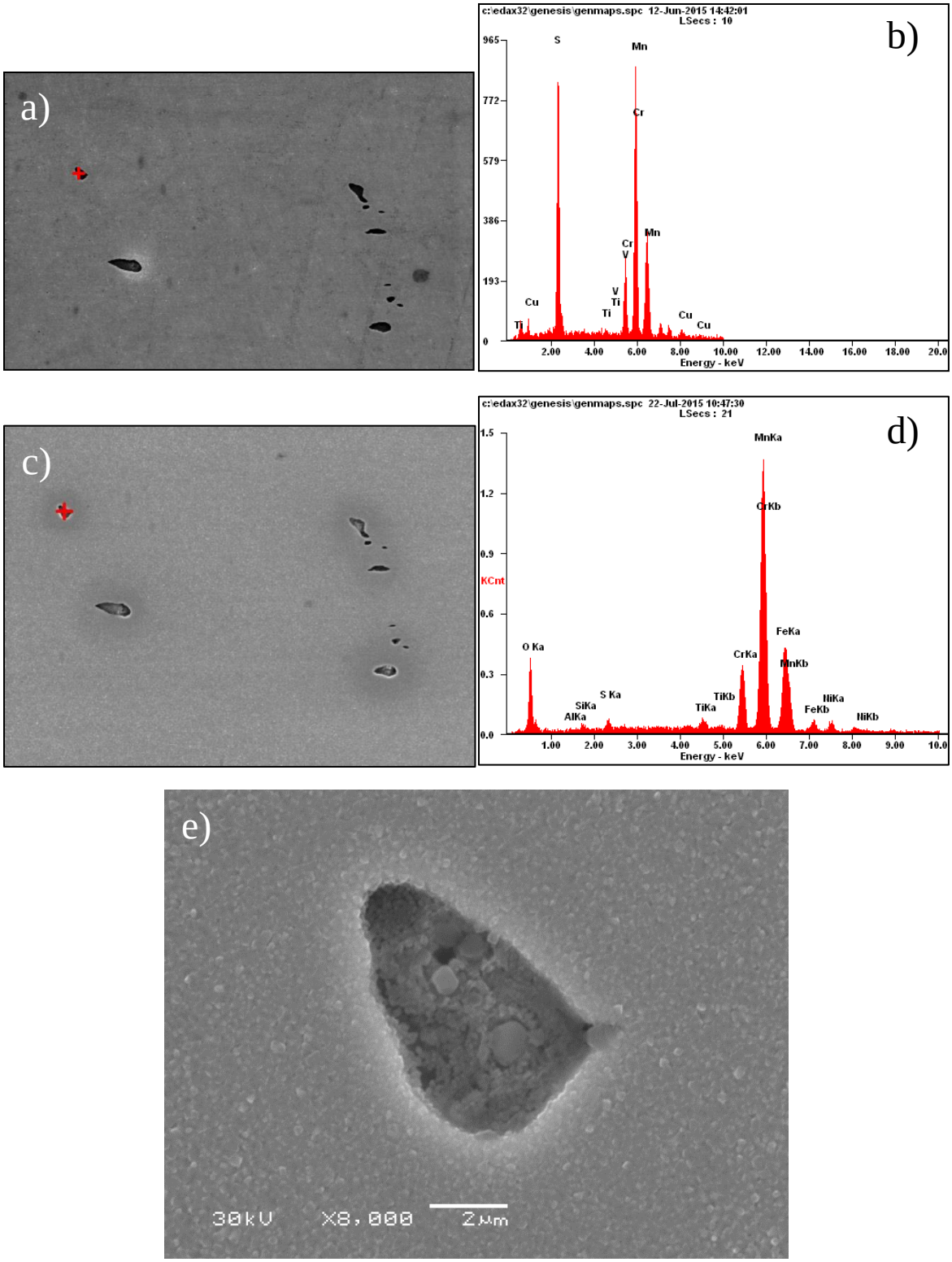

Figure A.18. SEM and corresponding EDX spectra for inclusion 18 on the unirradiated alloy AS specimen. a) and b) pre-exposure, c) through e) after 24 hour exposure to NWC.

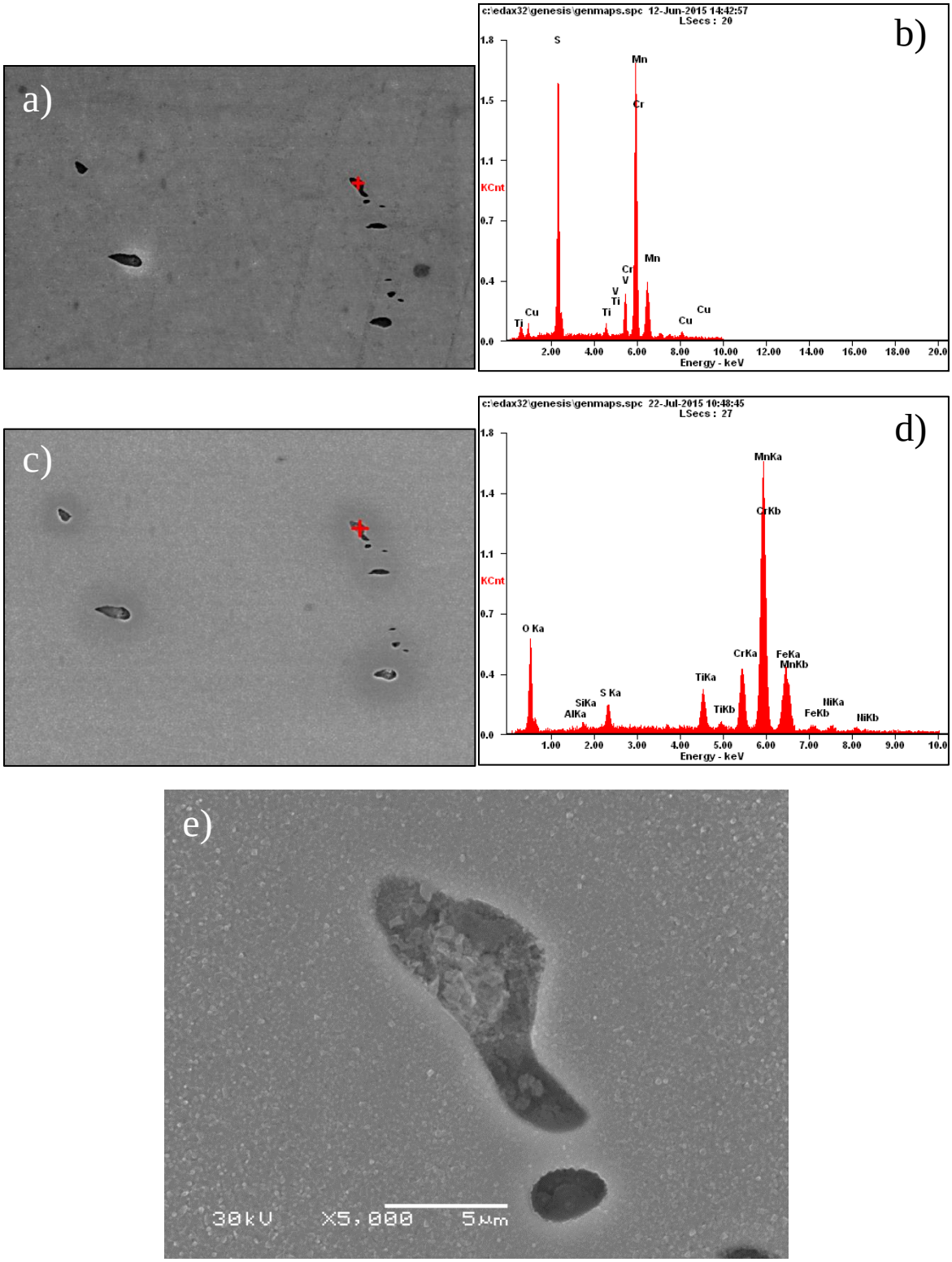

Figure A.19. SEM and corresponding EDX spectra for inclusion 19 on the unirradiated alloy AS specimen. a) and b) pre-exposure, c) through e) after 24 hour exposure to NWC.

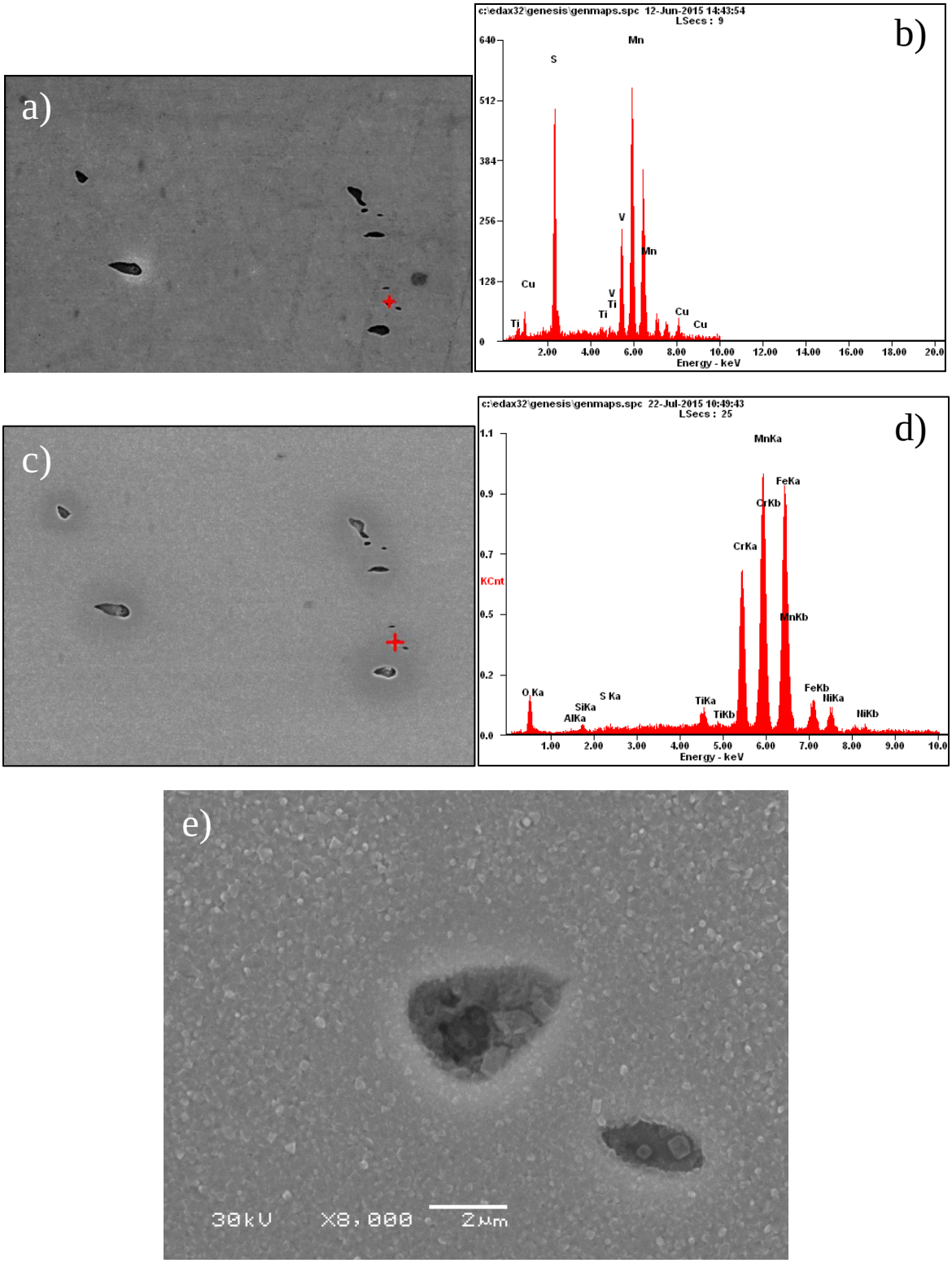

Figure A.20. SEM and corresponding EDX spectra for inclusion 20 on the unirradiated alloy AS specimen. a) and b) pre-exposure, c) through e) after 24 hour exposure to NWC.

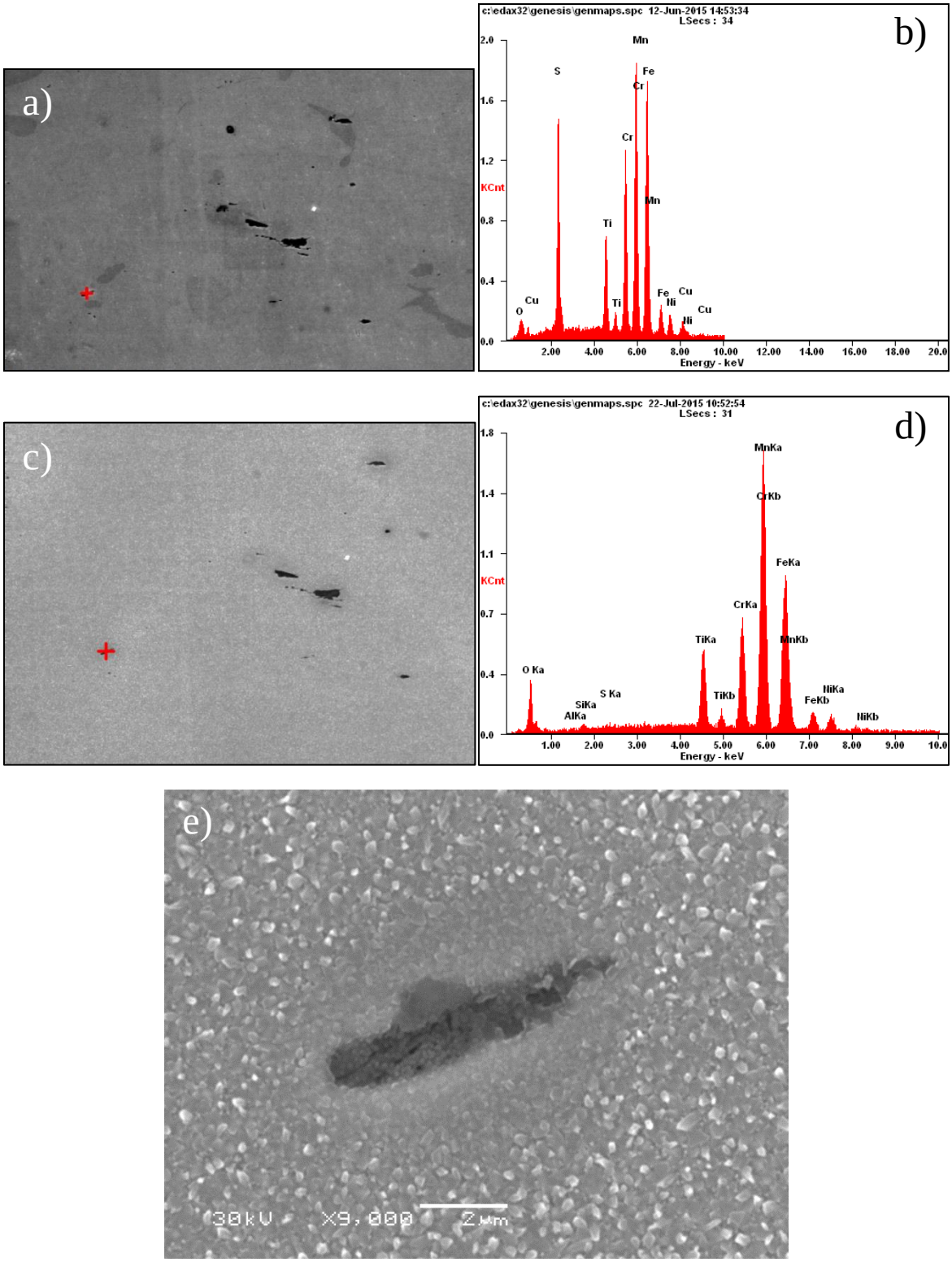

Figure A.21. SEM and corresponding EDX spectra for inclusion 21 on the unirradiated alloy AS specimen. a) and b) pre-exposure, c) through e) after 24 hour exposure to NWC.

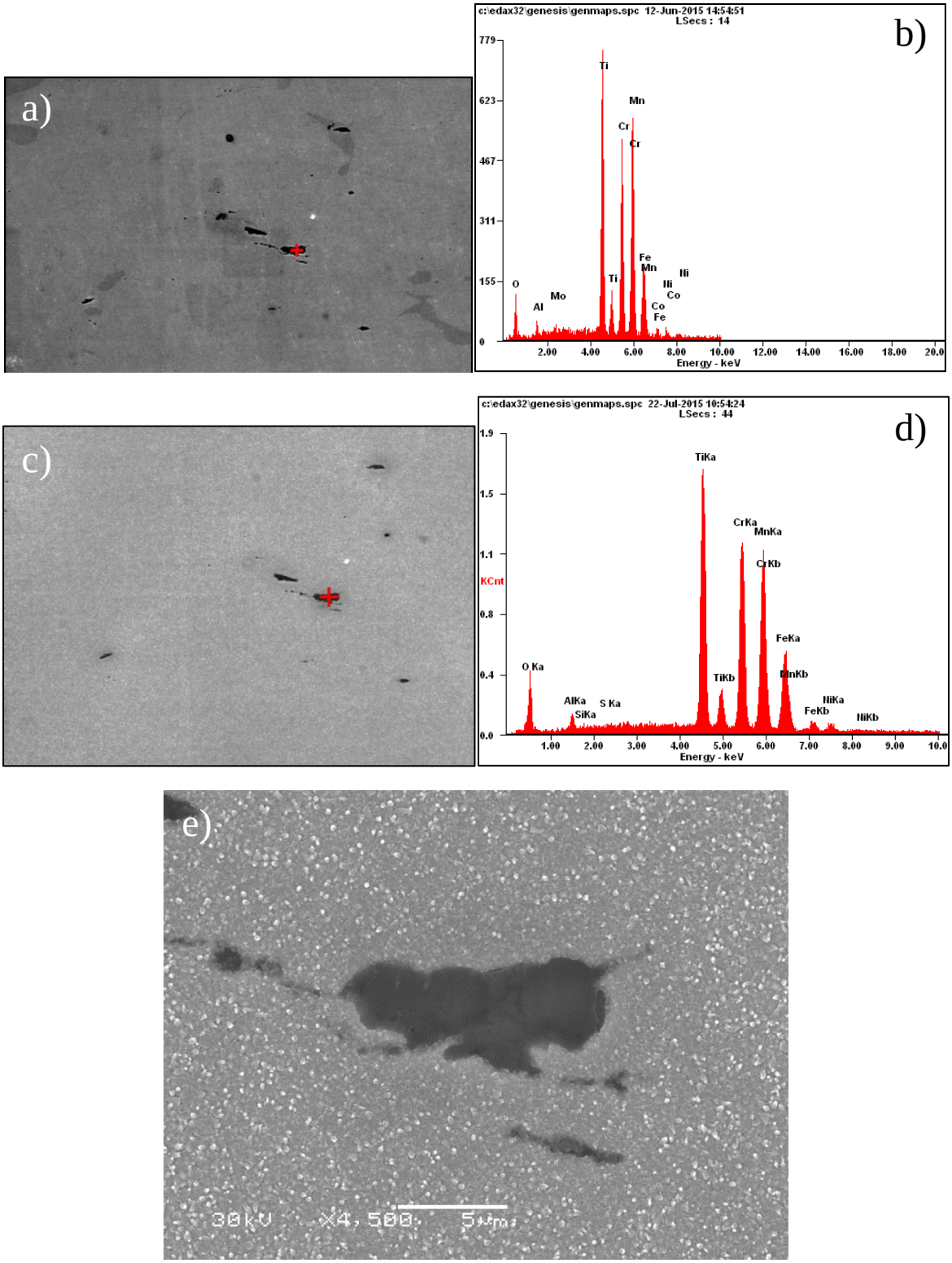

Figure A.22. SEM and corresponding EDX spectra for inclusion 22 on the unirradiated alloy AS specimen. a) and b) pre-exposure, c) through e) after 24 hour exposure to NWC.

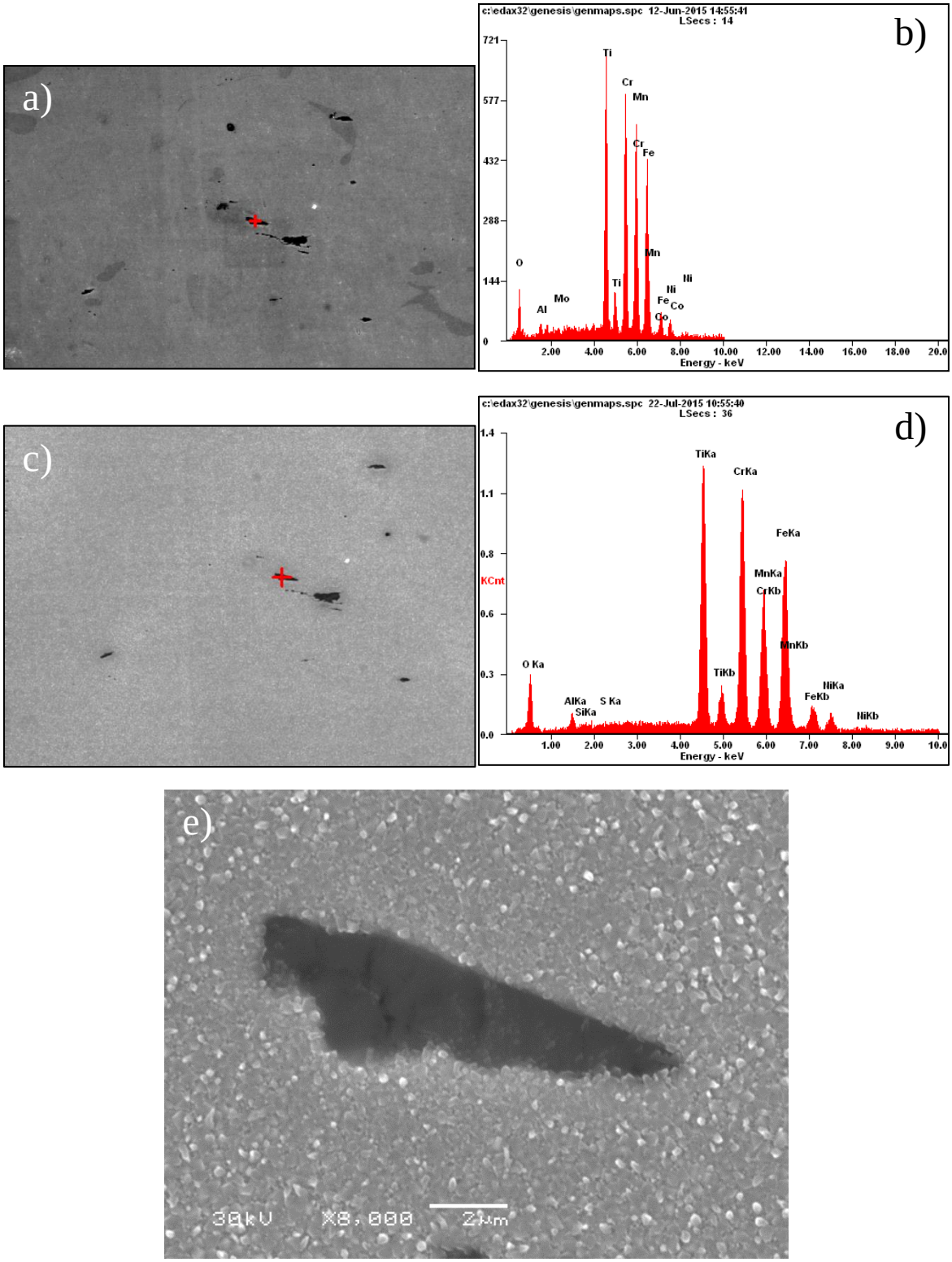

Figure A.23. SEM and corresponding EDX spectra for inclusion 23 on the unirradiated alloy AS specimen. a) and b) pre-exposure, c) through e) after 24 hour exposure to NWC.

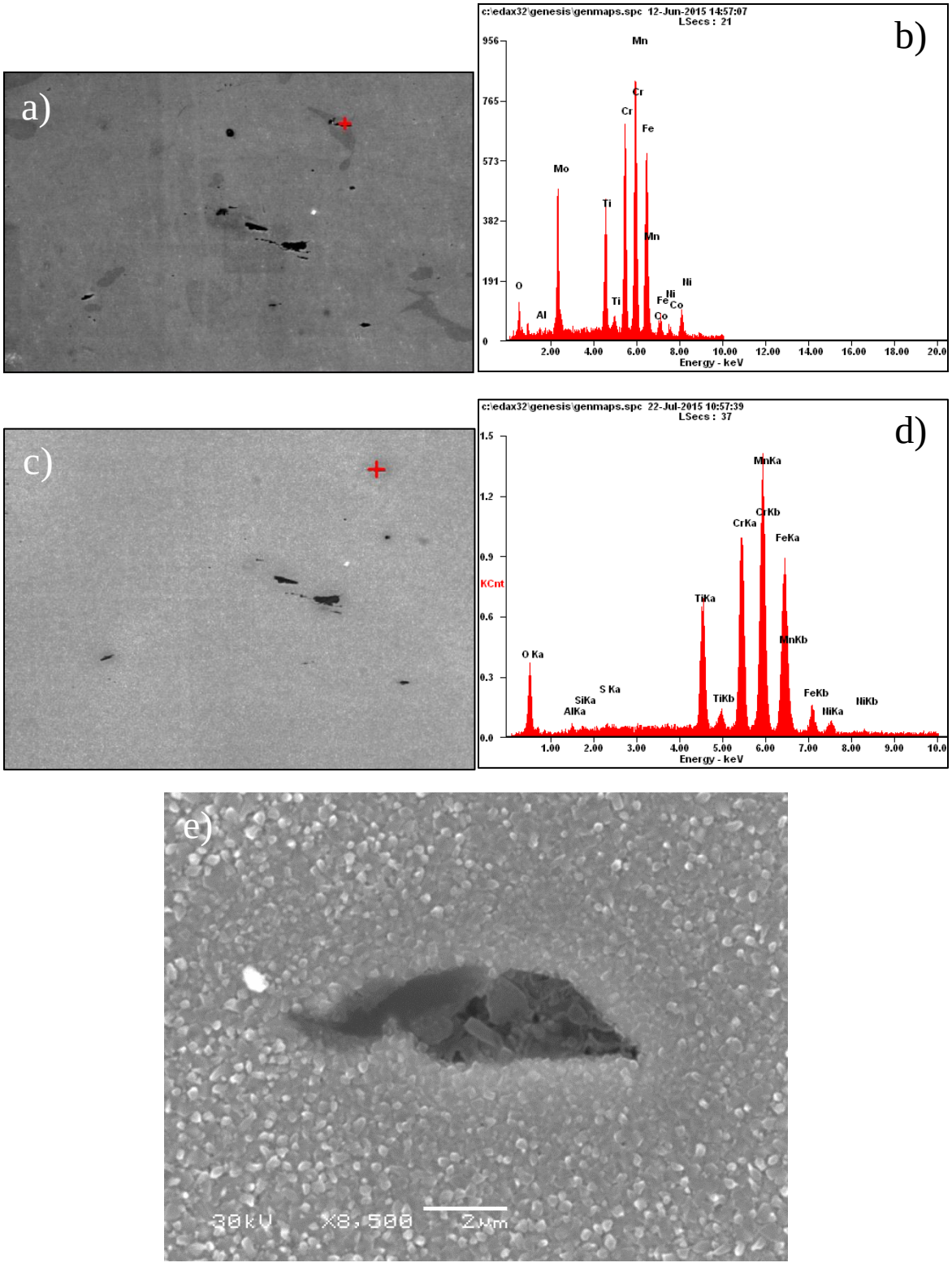

Figure A.24. SEM and corresponding EDX spectra for inclusion 24 on the unirradiated alloy AS specimen. a) and b) pre-exposure, c) through e) after 24 hour exposure to NWC.

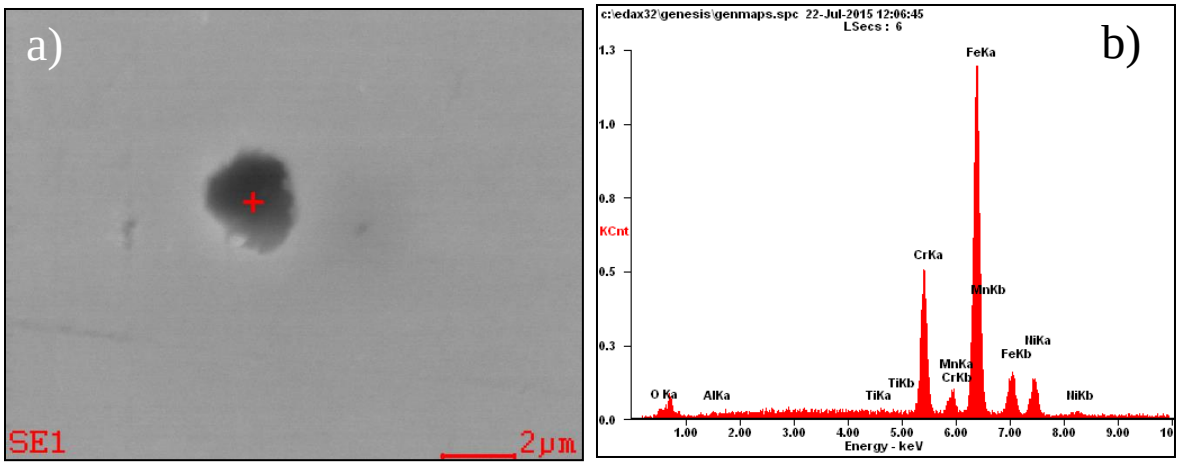

Figure A.25. a) SEM and b) corresponding EDX spectra for inclusion representative of those observed on the unirradiated alloy ES specimen.

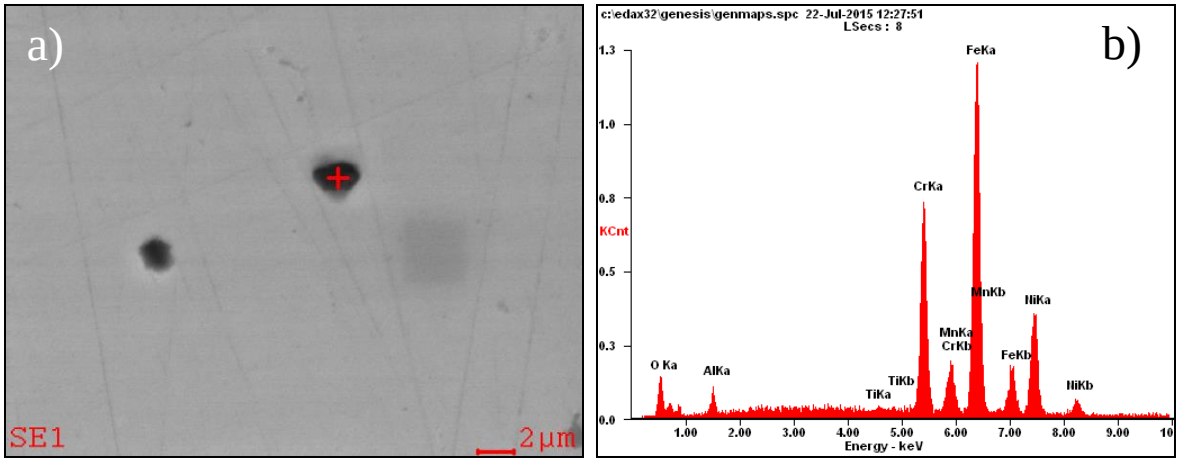

Figure A.26. a) SEM and b) corresponding EDX spectra for inclusion representative of those observed on the unirradiated alloy KS specimen.

APPENDIX B - DETAILED SUMMARY OF FOUR-POINT BEND TESTS

This appendix presents a detailed account and images from each four-point bend test on neutron irradiated samples in the order they were tested. Included are descriptions of the increments and observations made during the experiment, and images of load vs. deflection curves, bend sample surfaces and IASCC initiation sites.

AS05

The first neutron irradiated sample tested was 10.2 dpa AS05. Strain was applied until an observable change in the load vs. deflection curve, shown in Figure B.1. Failure occurred rapidly after the curve initially started to deviate from linearity. A single IG crack was observed, as shown in Figure B.2. The crack extended from one edge of the sample nearly across the full sample width. Large corrosion product was observed at the tip of the crack and on IG facets in the crack opening. A low density of DCs was observed in in the center of the sample and on either side of the crack.

AS01

5.5 dpa sample AS01 was strained in two steps (0.80σ_y and 1.05σ_y), as shown in Figure B.3. Only a limited number of images were recorded after the first increment, but no indications of DCs or cracking were observed. An IG crack was observed after the second increment, shown in Figure B.4. BSE images along the crack length are shown in Figure B.5, indicating DCs near the crack ends. Large corrosion product obscured the crack opening at the center of the crack in

Figure B.5b, and a lack of DCs was observed in this region. After oxide removal, a pit where an inclusion was previously located was observed at the crack initiation site, Figure B.6. One small DC was also visible in this area, intersecting the right side of the inclusion.

The entirety of the sample middle region was imaged after the IGSCC crack had initiated. Slip lines were visible in regions extending from the ends of the IGSCC crack up to a distance of 3 mm away from the crack itself. When looking in the same longitudinal plane as the crack initiation site, however, no other DCs were observed across the width of the sample, Figure B.7.

AS06

10.2 dpa sample AS06 was strained in four steps, shown in Figure B.8, stopped at 0.58σy, 0.66σy, 0.74σy, and 0.78σy. Two IGSCC cracks initiated on this sample surface at locations indicated in Figure B.9. The irregularity in sample shape observed near the bottom edge was due to pre-existing engravings of the sample ID on the tensile bar head.

A small IGSCC crack was observed after straining to 0.74σy, shown in Figure B.10. Prior to the initiation of this crack, a small inclusion with corrosion product formation was observed (Figure B.10a). After the crack initiated (Figure B.10b), corrosion product at this inclusion dissolved and was replaced by corrosion product formation at the mid-point of the crack. Similar to the crack in the 5.5 dpa alloy AS sample tested previously, no DCs were visible on either side of the crack; only extending from the crack tips on either end. After characterizing this location, additional strain was applied in an attempt to create a second crack. The application of additional strain did not cause the original crack to propagate, Figure B.10c. After removing oxidation from the sample surface a very DC was observed adjacent to the small inclusion near the crack initiation site.

A second crack formed after straining to 0.78σy, shown in Figure B.11. This crack formed ~1.2 mm from the initial crack and was assumed to not be caused by DCs formed at the first crack. The appearance of this crack was similar to the crack on sample AS01, with corrosion product formation near the initiation site, a lack of slip lines at the crack center, and slip lines near the ends of the crack. After removing oxidation from the sample surface, it was also evident that an inclusion on the sample surface affected crack initiation, Figure B.11b. A sharp corner in the grain boundary at this inclusion location was also observed.

AS02

5.5 dpa sample AS02 was strained in three steps stopped at 0.70σy, 0.78σy, and 0.87σy (Figure B.12), resulting in the formation of a crack at the location shown in Figure B.13. Some inclusions formed large corrosion product as shown in Figure B.14a. Two locations with DCs were observed after the second strain step. One of these DC locations (Figure B.14b) was associated with the corroded inclusion site in Figure B.14a. No change in the corrosion product resulted from DC formation. The second DC location (Figure B.15) was ~375 μm to the right of the location in Figure B.14b. BSE images of the area in Figure B.14 are shown in Figure B.16, to highlight their locations.

After 0.87σy, a change occurred at the corroded inclusion site (Figure B.14c and Figure B.16b), while the adjacent slip location shown in Figure B.15 did not. Growth of the corrosion product at this location indicated the opening of a crack. The presence of a crack was confirmed after removal of surface oxidation, shown in Figure B.16c. A drastic increase in the number density of DCs was also observed at the top and bottom of the crack, which extend beyond the area shown

in Figure B.16. Also during this increment, a second small crack was observed adjacent to an inclusion with corrosion product formation, shown in Figure B.17.

ES01

10.7 dpa sample ES01 was strained in 8 steps (Figure B.18), causing deformation beyond the macroscopic yield point and the application of approximately 1.8% strain before failure occurred. The initial test was stopped at 0.68σy. DCs were visible on the bend surface after the first test, which increased in density with strain, as shown in Figure B.19.

A small crack was observed at the sample edge after ~1% plastic strain, shown in Figure B.20. The GB which cracked was almost perfectly normal to the direction of stress, and DCs are visible in the grain adjacent to the crack tip. A final strain increment was applied, resulting in failure ('Failure' in Figure B.18), as the load-deflection curve deviated from linearity at a lower load than in the previous increment. A large IGSCC crack formed during this test, shown in Figure B.22. The initial crack remained unchanged, located ~400 μm to the right of the second crack. The second crack also likely initiated at the sample edge. High magnification images of the initiation site are compared in Figure B.23, before and after the crack had initiated. Only few DCs were visible at the crack location.

No extraordinary corrosion product formation was observed on the sample surface, but corrosion product was observed on IG facets within the crack. Comparing differences between the images of the large crack before and after oxide removal reveal the presence of this corrosion product, shown in Figure B.24.

KS02

9.6 dpa Alloy KS was strained 10 times in NWC to a total of approximately 9.4% strain, Figure B.25. No IG fracture was observed, but similar to the alloy ES sample, DCs were observed even after the initial increment of strain stopped at 0.73σy. DCs increased in density with strain, as shown in Figure B.26.

AS09

47.5 dpa alloy AS was strained in two increments in NWC (0.49σy and 0.55σy), as indicated in Figure B.27. DCs were observed after 0.49σy, shown in Figure B.28. An IGSCC crack nearly 1 mm in length was observed after 0.55σy, as located in Figure B.29. The DCs observed before cracking did not change in appearance after 0.55σy, even with the formation of the large IGSCC crack shown in Figure B.30. The crack formed adjacent to a surface inclusion, with a large amount of corrosion product formation at the widest portion of the crack. This location is shown at high magnification in Figure B.31. Few DCs were observed at the crack initiation site, but more were observed at either end of the crack (Figure B.31b). Figure B.31c and Figure B.31d show the crack after removal of surface oxidation. One large DC extends from the top of the inclusion.

AS07

10.2 dpa sample AS07 was strained in 288 °C Ar in six increments, stopped at 0.62σy, 0.70σy, 0.74σy, 0.78σy, 0.87σy, and 1.16σy, Figure B.32. An effective stress was applied with greater magnitude than the tensile yield stress, however no observable yield had occurred. No cracking was observed on the sample surface. DC and slip transmission site density increased with strain, eventually causing DCs which intersected with surface inclusions. DCs were first observed after 0.70σy causing 17 DCs and 2 slip transmission sites, but none of the initial DCs intersected

surface inclusions. After straining to 1.16σy, a high density of DCs had formed, a small fraction of which intersected surface inclusions. DC intersection with inclusions after this straining increment sometimes caused visible crack formation within in the inclusion, exemplified in Figure B.33.

This sample was exposed to NWC in an un-stressed condition for a period of 24 hours after straining in Ar. The density of inclusion sites with corrosion product formation was no greater than on samples without pre-strain in 288 °C Ar. These corrosion product sites did not preferentially occur at inclusion locations with DC intersections.

AS03

5.5 dpa sample AS03 was strained once in 288 °C Ar to 0.85σy, shown in Figure B.34. 115 DCs and 28 slip transmission sites were observed after this test. 8 of the channels were adjacent to inclusions, although none caused visible cracks in the inclusion (exemplified in Figure B.35).

This sample was exposed to NWC in an un-stressed condition after straining in Ar. Several locations formed corrosion product, but the density of these sites was no greater than on other alloy AS samples.

ES02

10.2 dpa sample ES02 was strained in 288°C Ar to 0.65σy and 0.90σy, as shown in Figure B.36. No cracks formed in this sample, and DCs were characterized after each test.

KS01

9.6 dpa sample KS01 was strained in 288°C Ar to 0.65σy and 0.89σy, as shown in Figure B.37. No cracks formed in this sample, and DCs were characterized after each test.

AS04

5.5 dpa sample AS04 was strained in NWC to 74% of the yield strength (shown in Figure B.38), resulting in the crack as located in Figure B.39. The ~150 μm crack (shown in detail in Figure B.40) appeared similar to previous cracks in alloy AS: a large surface inclusion with corrosion product was present at the initiation site, and few DCs were observed in this area.

AS08

10.2 dpa sample AS08 underwent four strain steps in NWC (Figure B.41). Crack initiation was observed after 0.74σy, located in Figure B.42. DCs were observed prior to crack initiation. BSE and SE images of the IG crack initiation site are shown in Figure B.43.

AS10

47.5 dpa sample AS10 underwent two strain steps in NWC, stopped at 0.47σy and 0.49σy, as shown in Figure B.44. No cracking or DCs were observed after the first increment, but two crack initiation sites formed after 0.49σy, located in Figure B.45. One initiation site was small, and appeared similar to other crack initiation sites in alloy AS, shown in Figure B.46. The second site interacted with the sample edge and was outside the center region of the sample, Figure B.47.

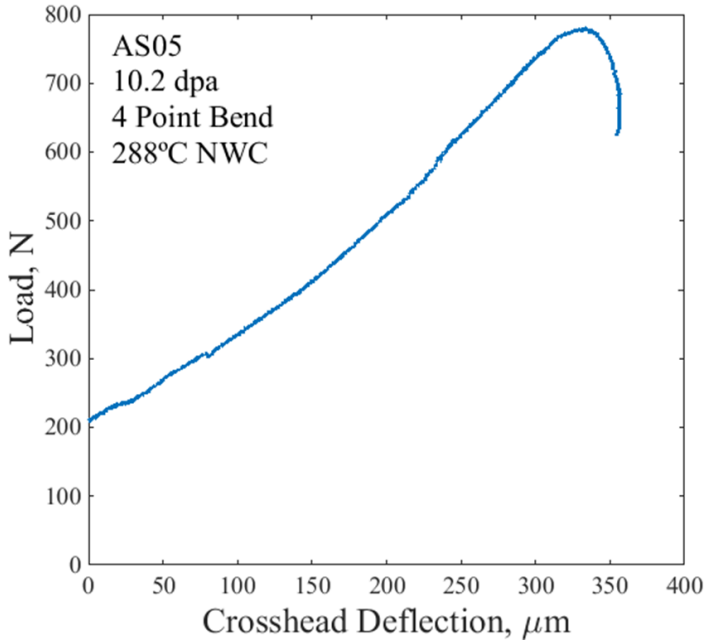

Figure B.1. Load vs. deflection curve for sample AS05.

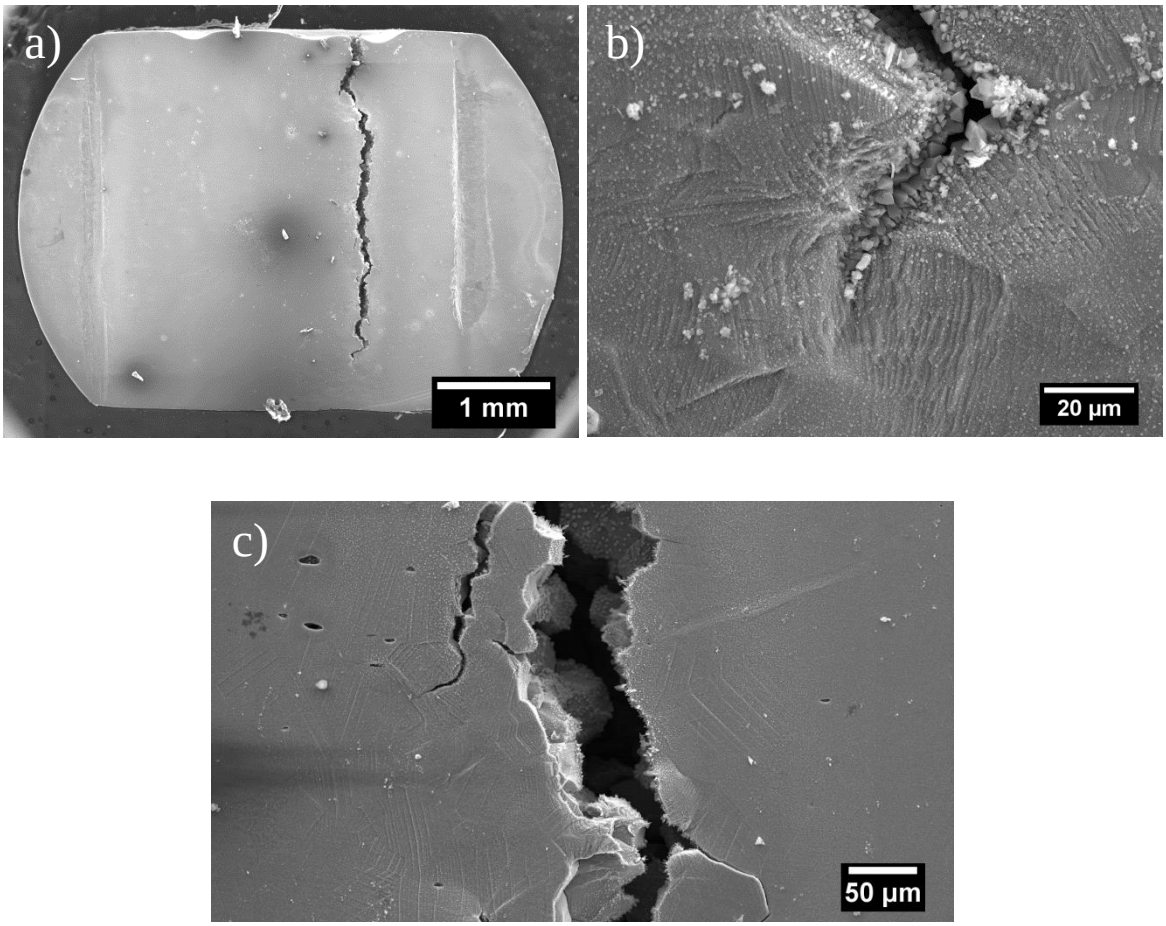

Figure B.2. a) The post-test bend surface of sample AS05, b) the IG crack tip and c) the central region of the IG crack.

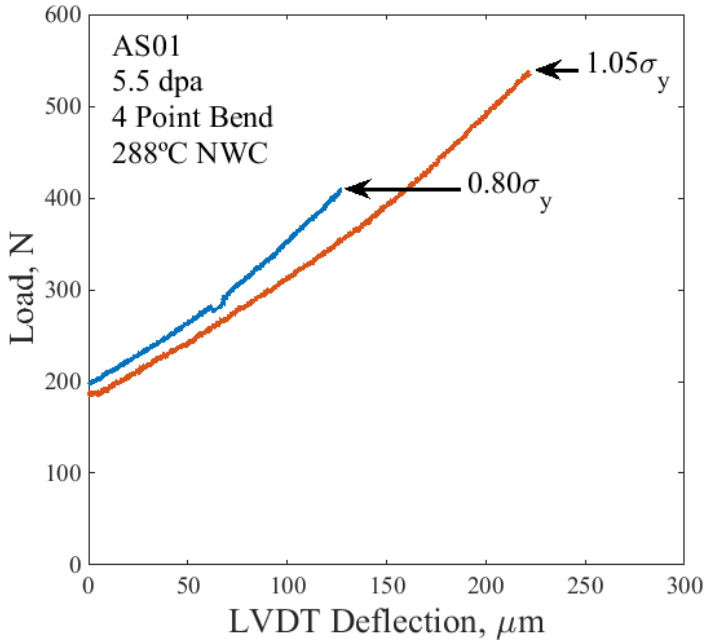

Figure B.3. Load vs. deflection curves for sample AS01.

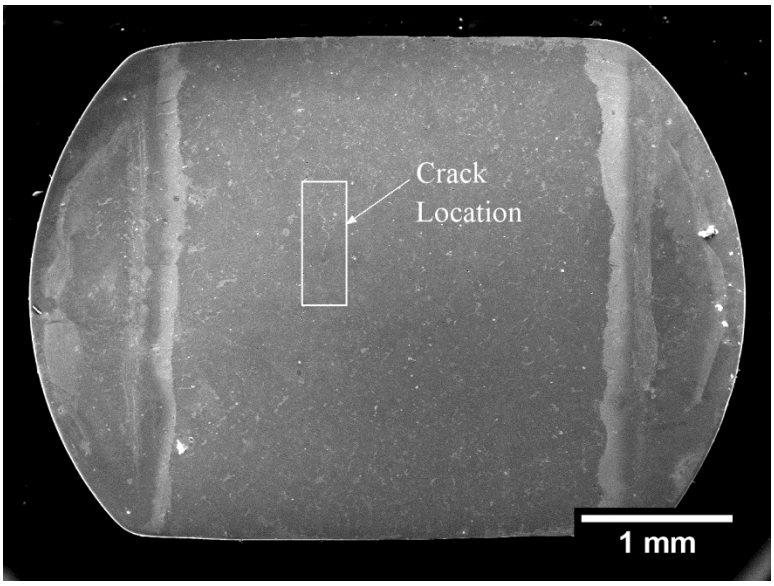

Figure B.3. Crack location on sample AS01.

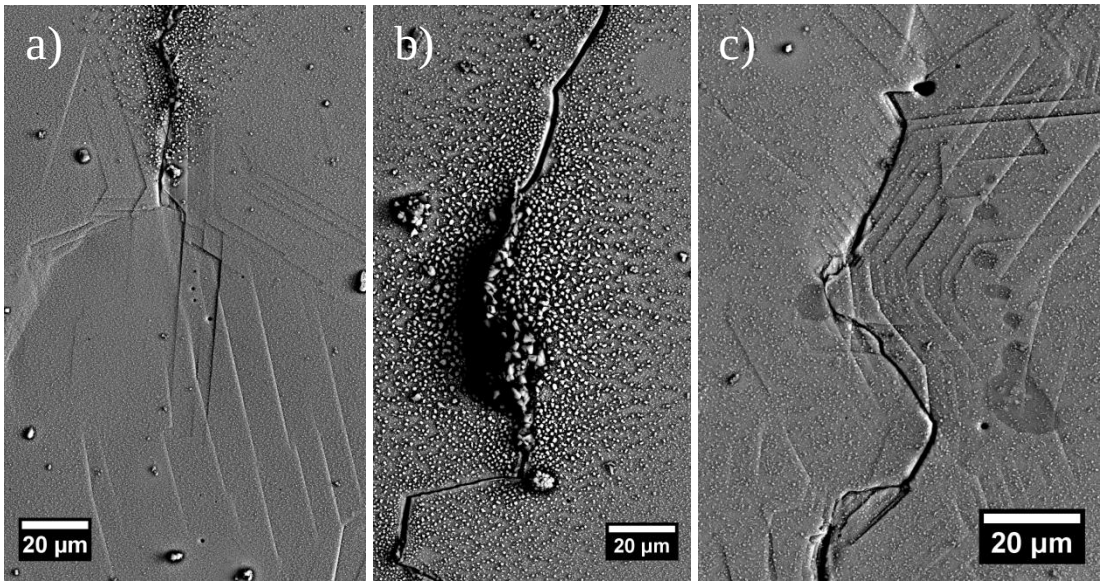

Figure B.5. High magnification BSE images of the a) bottom, b) middle, and c) top of the IGSCC crack in sample AS01.

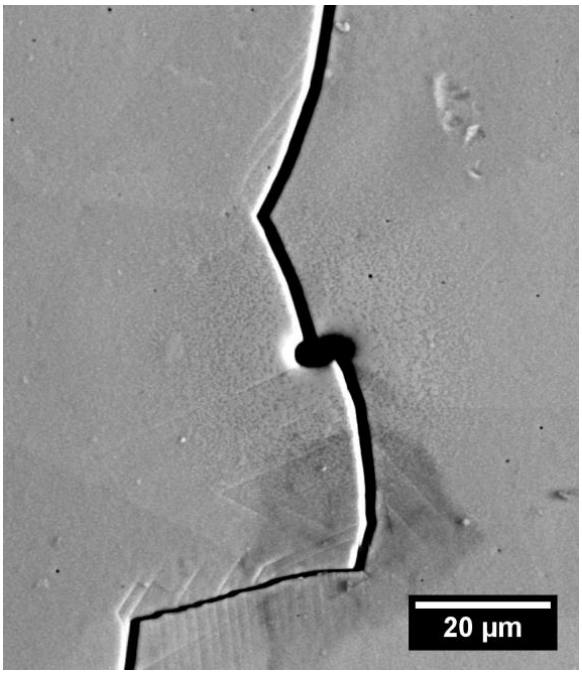

Figure B.6. High magnification BSE image of the middle portion of the IGSCC crack in sample AS01 after oxide removal.

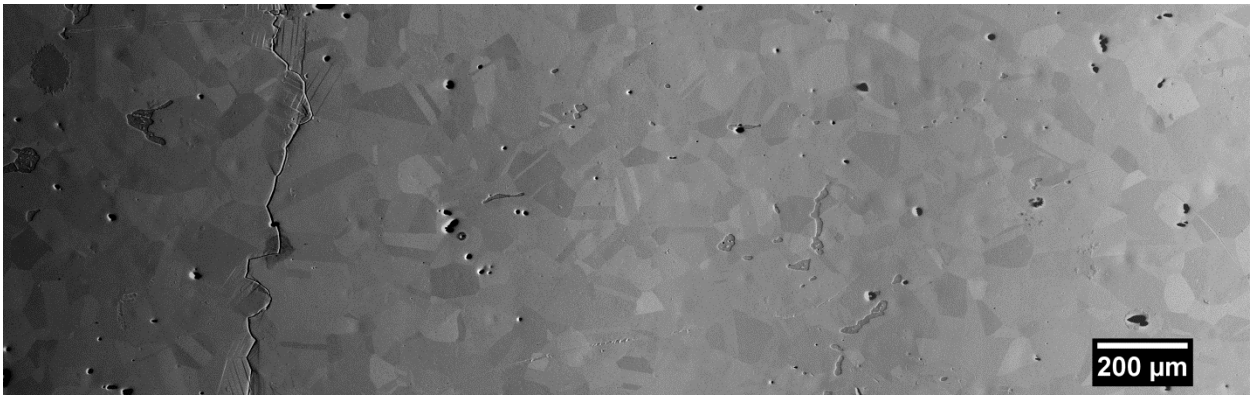

Figure B.7. Center region of sample AS01, showing a lack of slip lines in the same plane as the initiation site of the IGSCC crack. Grain contrast is visible in BSE imaging after oxide removal.

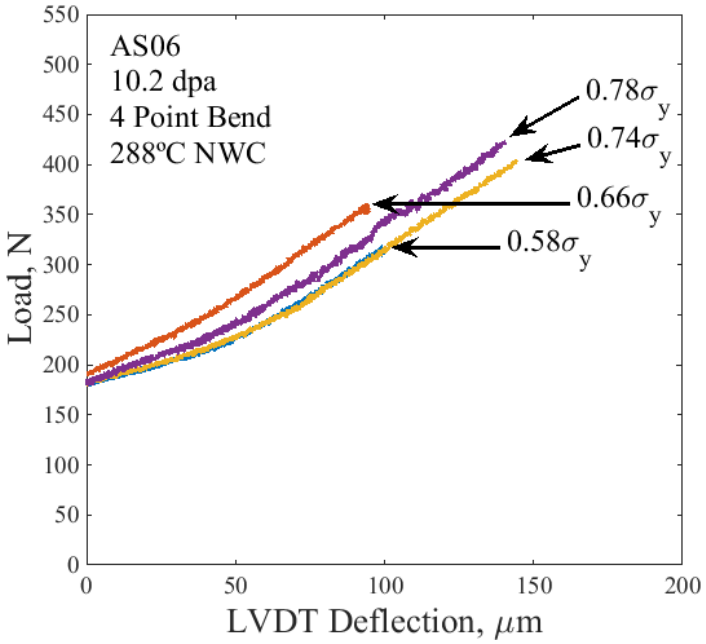

Figure B.8. Load vs. deflection curves for the 4 straining increments conducted on sample AS06.

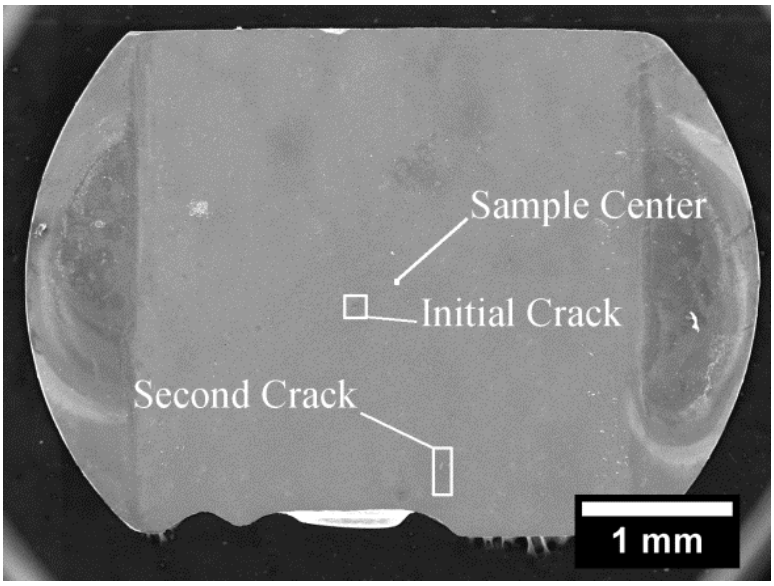

Figure B.9. Locations of cracking on sample AS06.

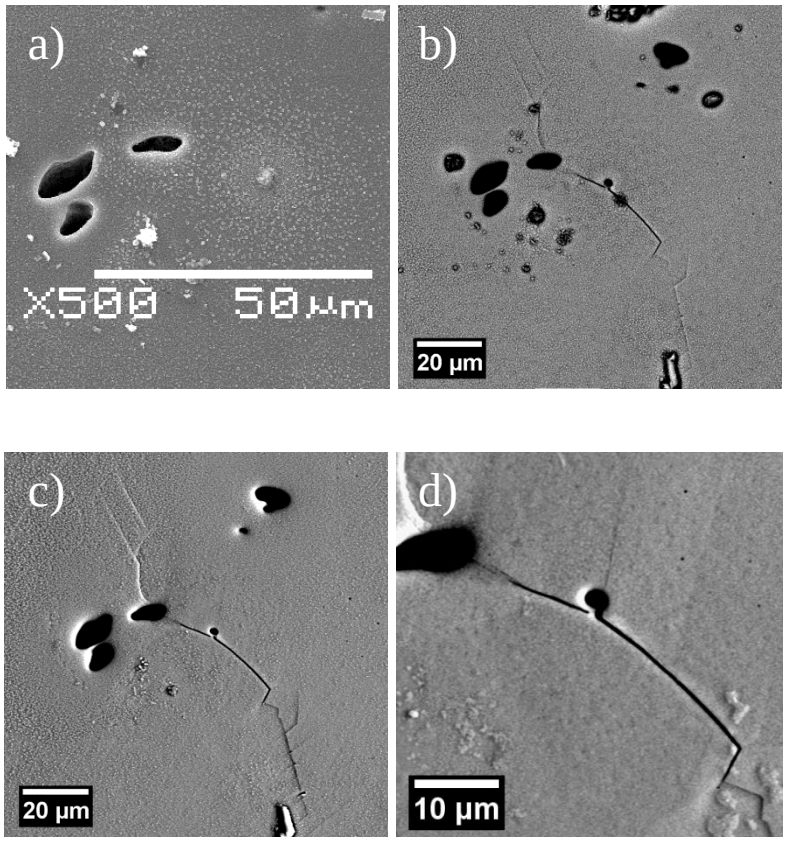

Figure B.10. High magnification images showing the first IGSCC crack on sample AS06: a) $0.66\sigma_y$ (SE), b) $0.74\sigma_y$ (BSE), c) $0.78\sigma_y$ (BSE), and d) $0.78\sigma_y$ after oxide removal (BSE).

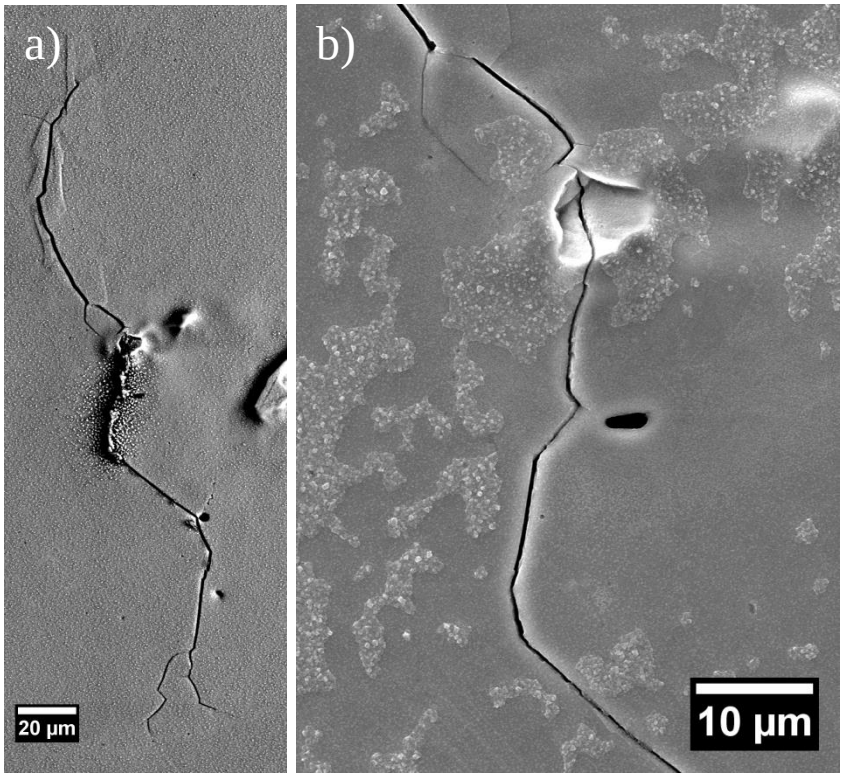

Figure B.11. Images of the second IGSCC crack formed on sample AS06 bend sample after a) $0.78\sigma_y$ (BSE) and b) $0.78\sigma_y$ after oxide removal (SE).

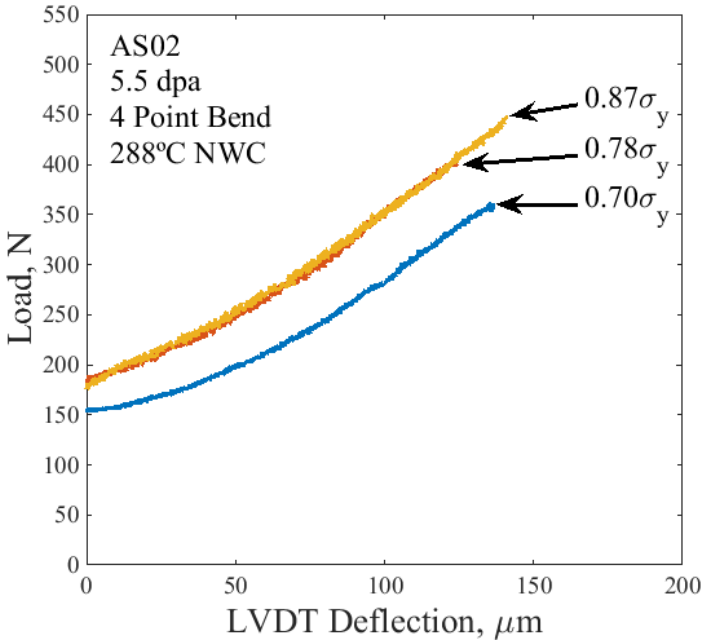

Figure B.12. Load vs. deflection curves for the 3 straining increments conducted on sample AS02.

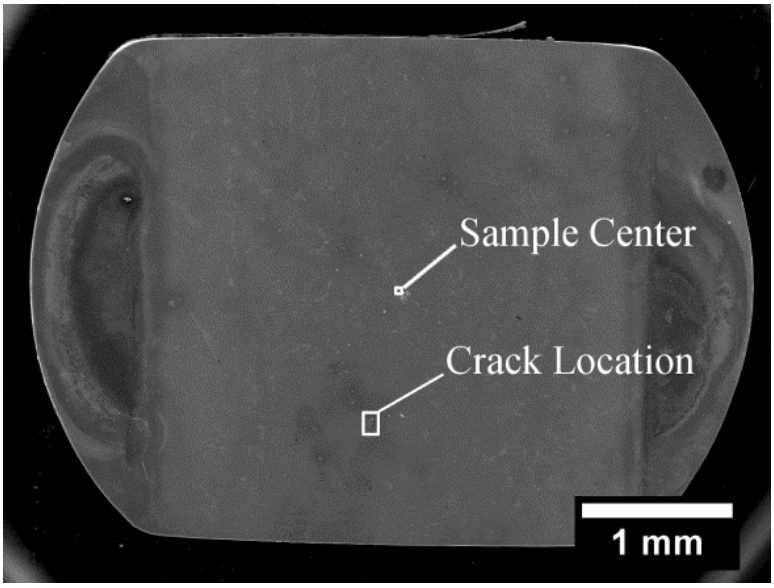

Figure B.13. Crack location on sample AS02.

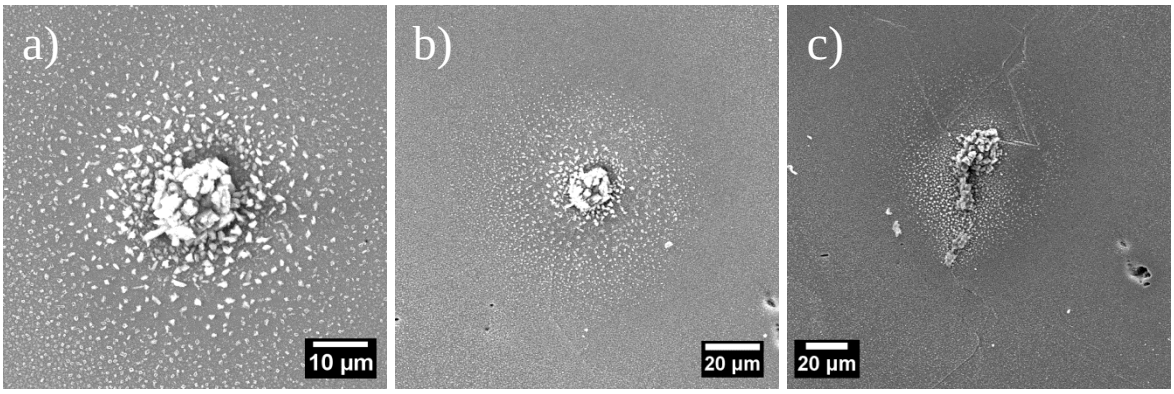

Figure B.14. High magnification SE images showing the location of the IGSCC crack on sample AS02 after a) $0.70\sigma_y$, b) $0.78\sigma_y$, c) and $0.87\sigma_y$.

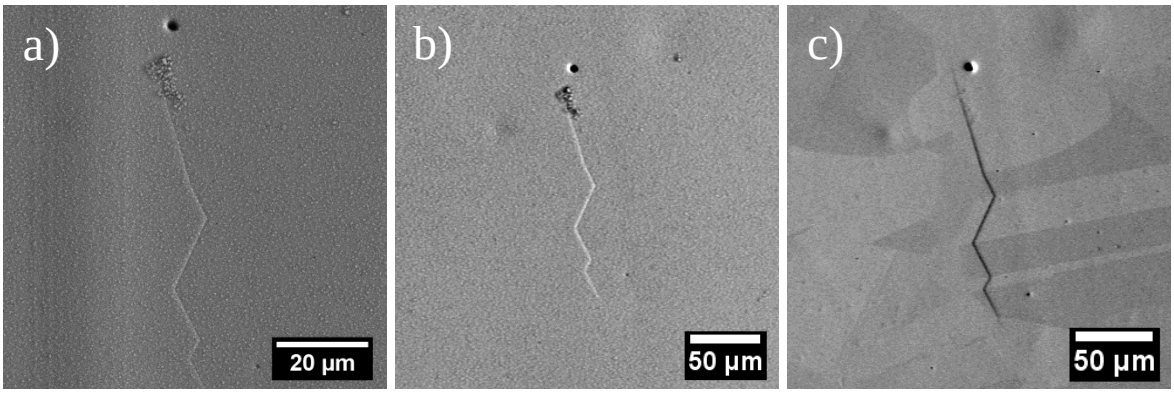

Figure B.15. High magnification BSE images showing the second location of slip lines on sample AS02 after a) $0.78\sigma_y$, b) $0.87\sigma_y$, c) and $0.87\sigma_y$ after oxide removal.

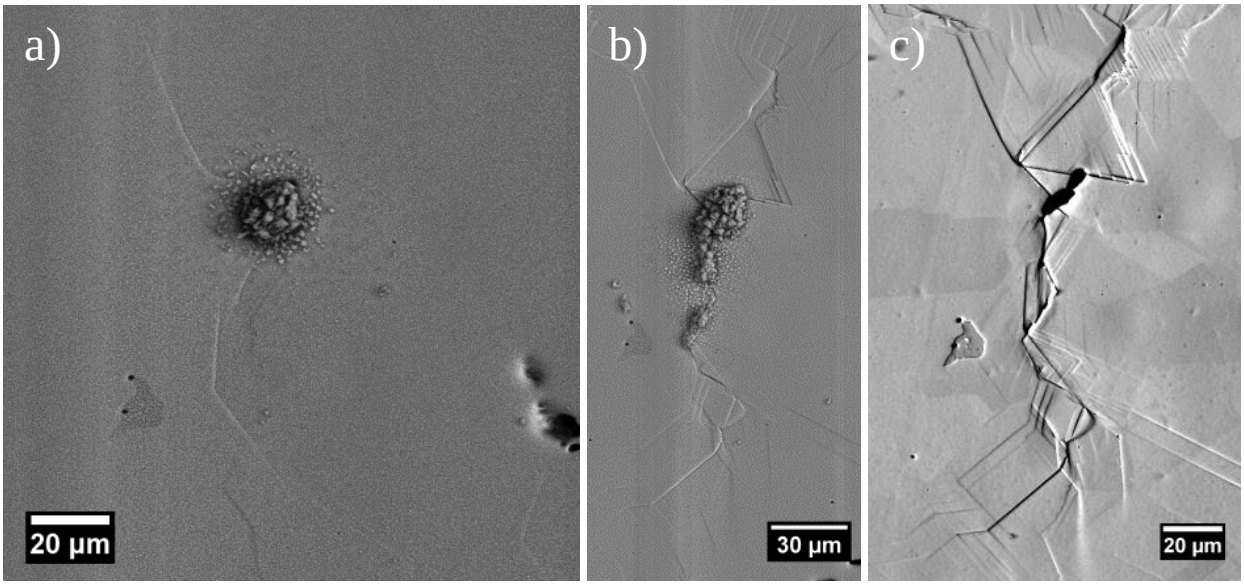

Figure B.16. High magnification BSE images showing the location of the first IGSCC crack on sample AS02 after a) $0.78\sigma_y$, b) $0.87\sigma_y$, c) and $0.87\sigma_y$ after oxide removal.

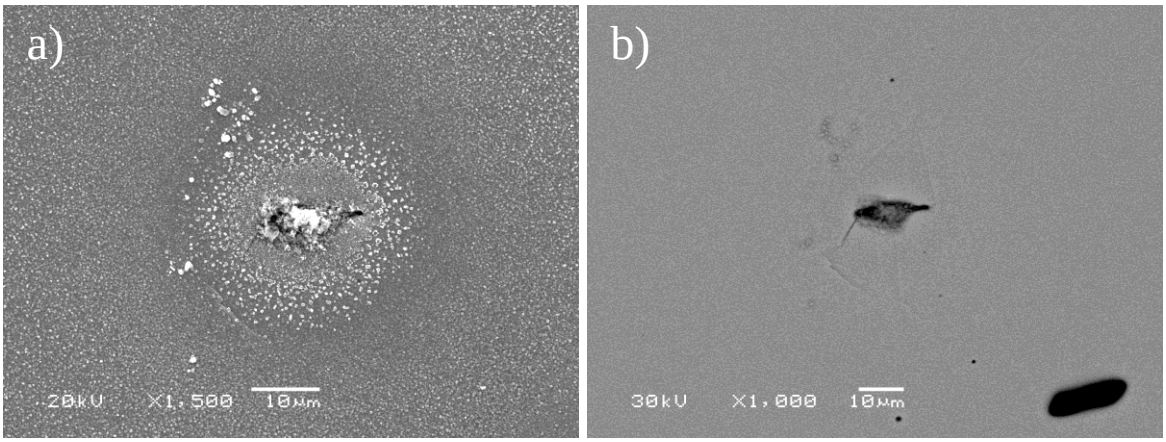

Figure B.17. The second crack observed on sample AS02 after $0.87\sigma_y$, a) SE, b) BSE.

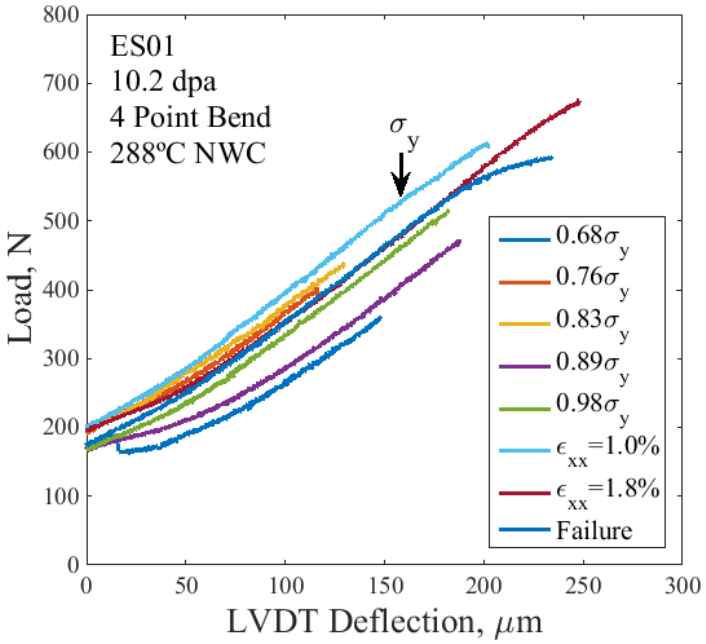

Figure B.18. Load vs. deflection curves for the 8 straining increments applied to sample ES01.

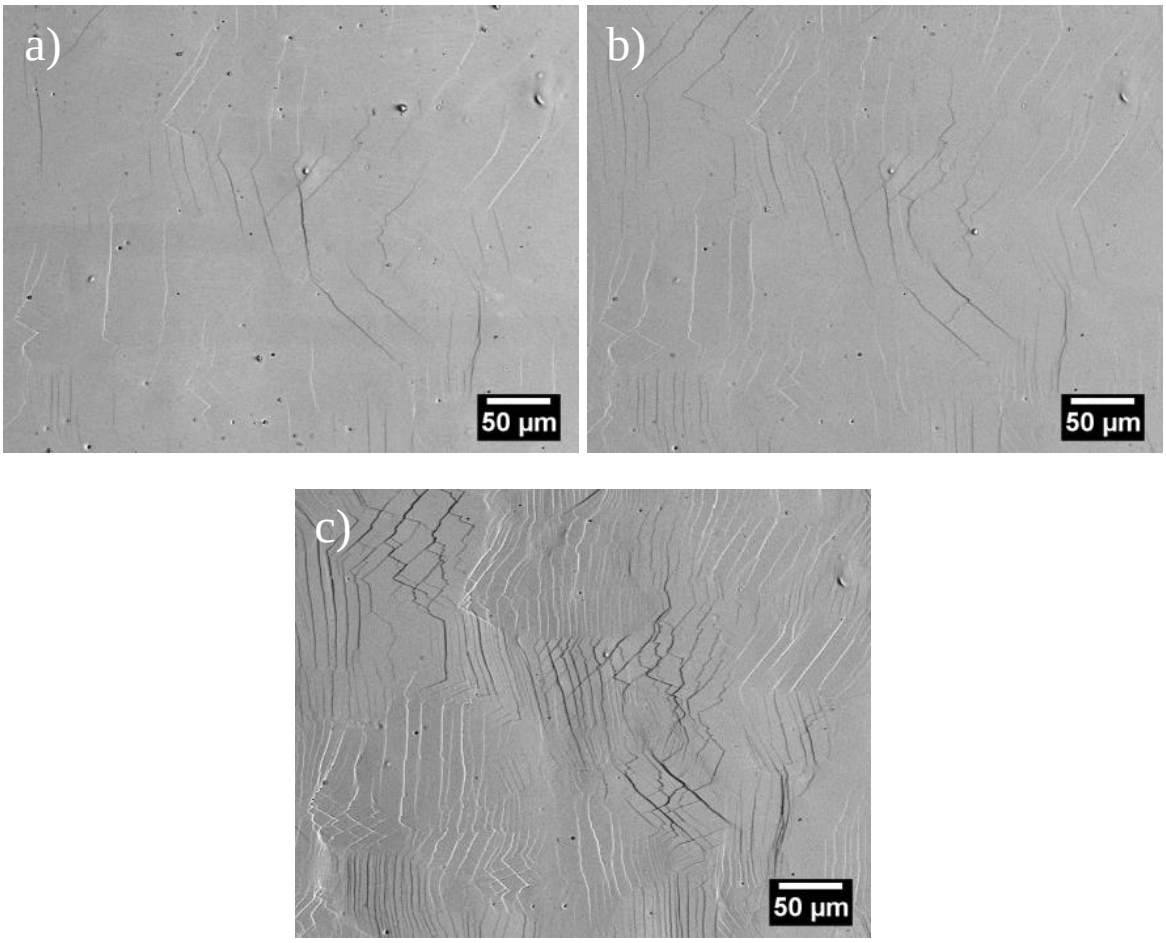

Figure B.19. BSE images of an area of sample ES01 after straining increments stopped at a) $0.68\sigma_y$, b) $0.89\sigma_y$, and c) $\varepsilon_{xx} = 1.8\%$.

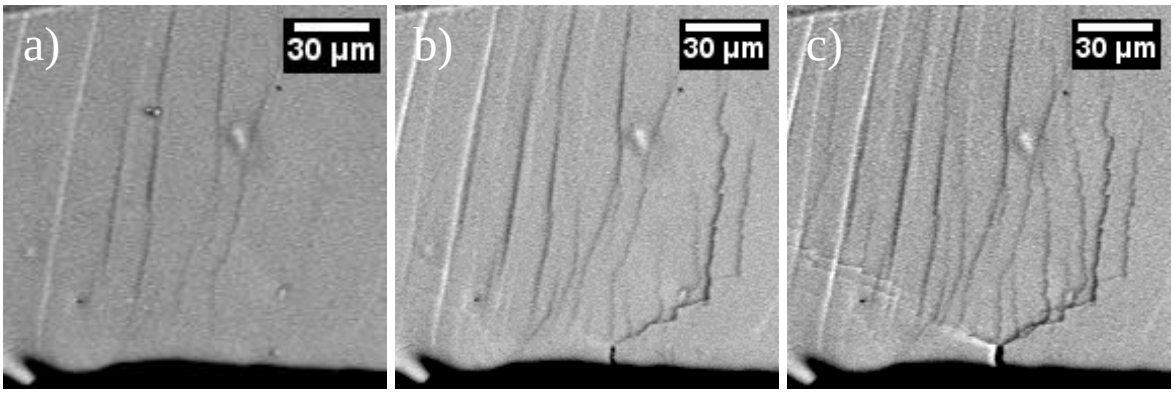

Figure B.20. The region where the small IGSCC crack formed at the edge of sample ES01 a) prior to initiation after straining to $0.98\sigma_y$, b) after crack initiation at $\varepsilon_{xx} = 1.0\%$, and c) after straining to $\varepsilon_{xx} = 1.8\%$.

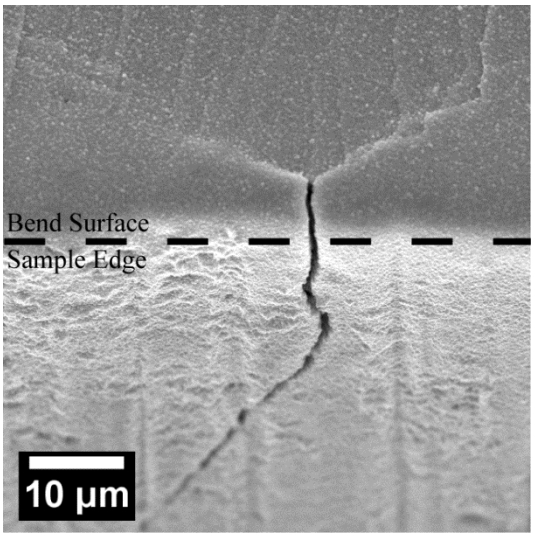

Figure B.21. The small IGSCC crack at the edge of sample ES01 after ε_{xx} = 1.8%.

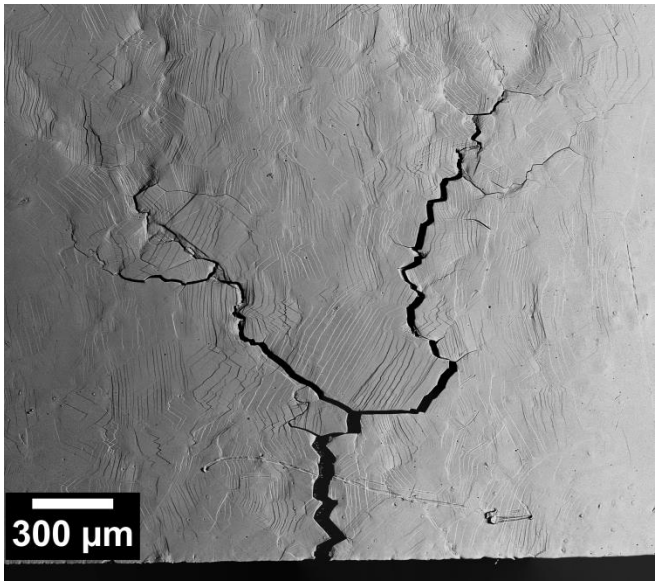

Figure B.22. The second IGSCC crack on sample ES01 after the final straining increment.

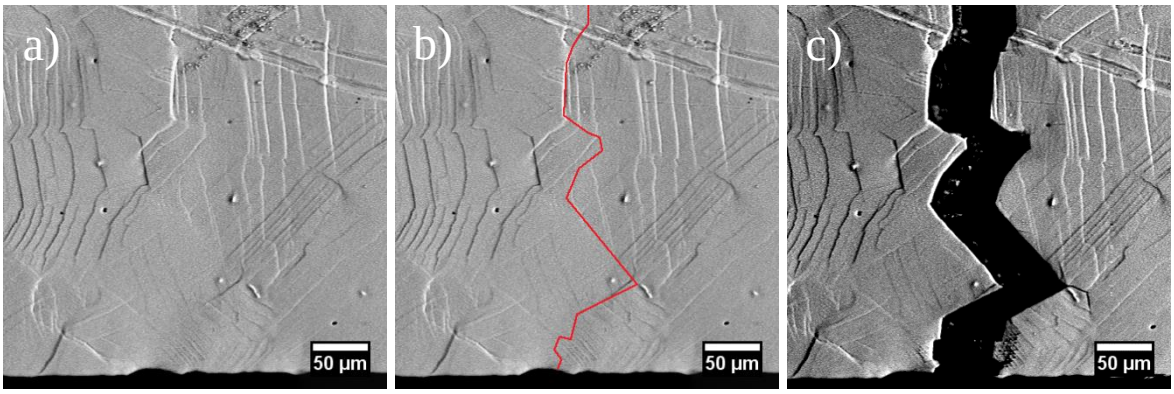

Figure B.23. High magnification BSE images of the failure crack location on sample ES01 a) after ε_{xx} = 1.8%, b) after ε_{xx} = 1.8% with the cracked boundary indicated by a red line, and c) after failure.

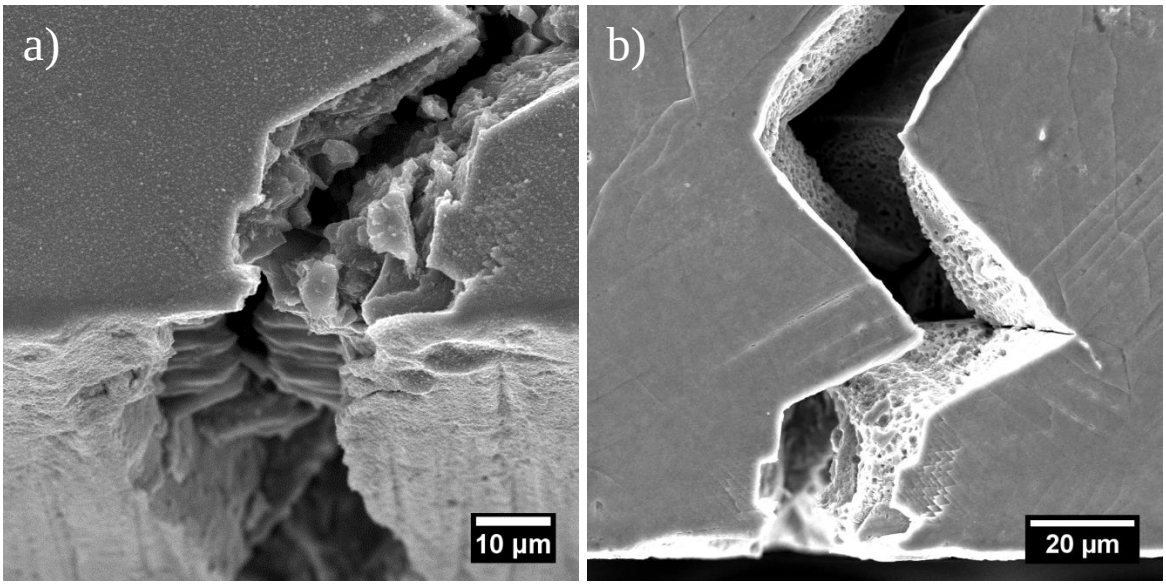

Figure B.24. Additional SE images of the second crack initiation site on sample ES01 a) sample tilted, before oxide removal and b) after oxide removal.

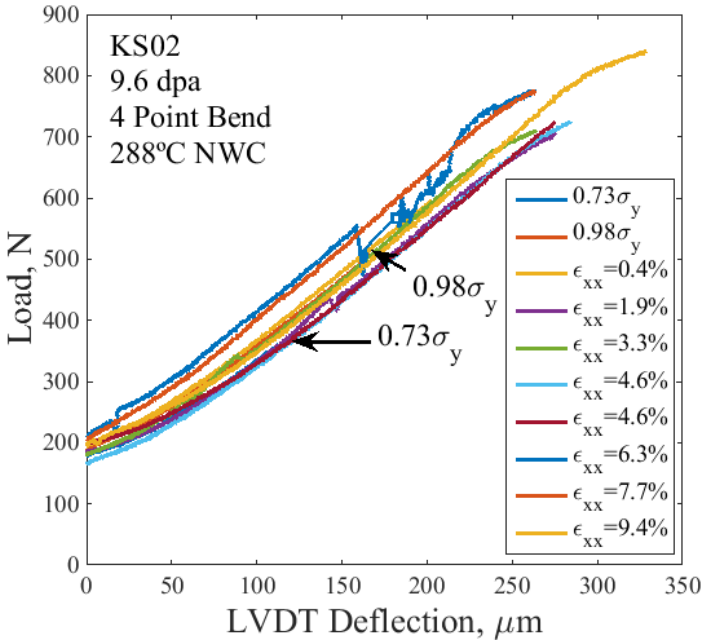

Figure B.25. Load vs. deflection curves for the 10 straining increments conducted on sample KS02.

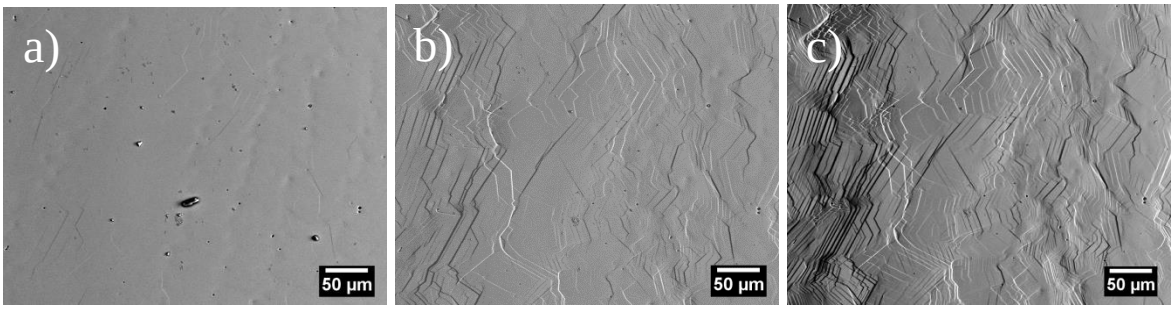

Figure B.26. BSE images of an area of the bend surface on sample KS02 after straining increments stopped at a) $0.73\sigma_y$, b) $\varepsilon_{xx} = 1.9\%$, and c) $\varepsilon_{xx} = 9.4\%$.

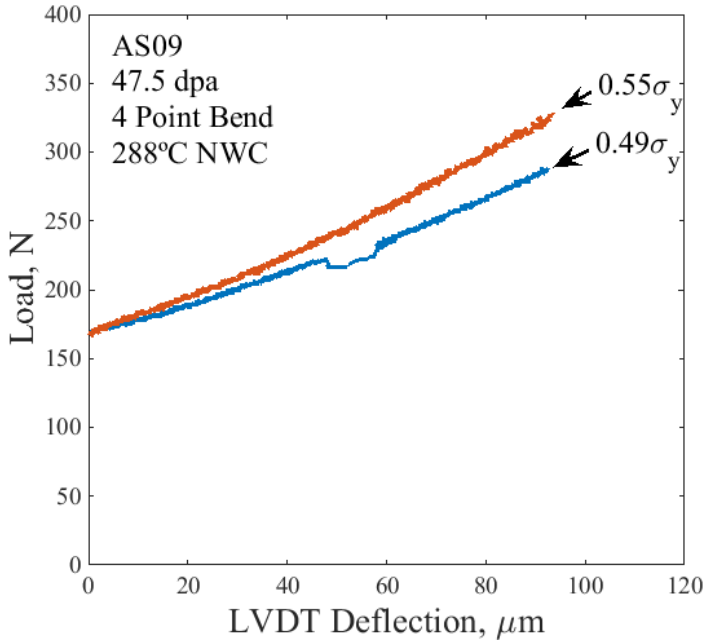

Figure B.27. Load vs. deflection curves for the 2 straining increments applied to sample AS09.

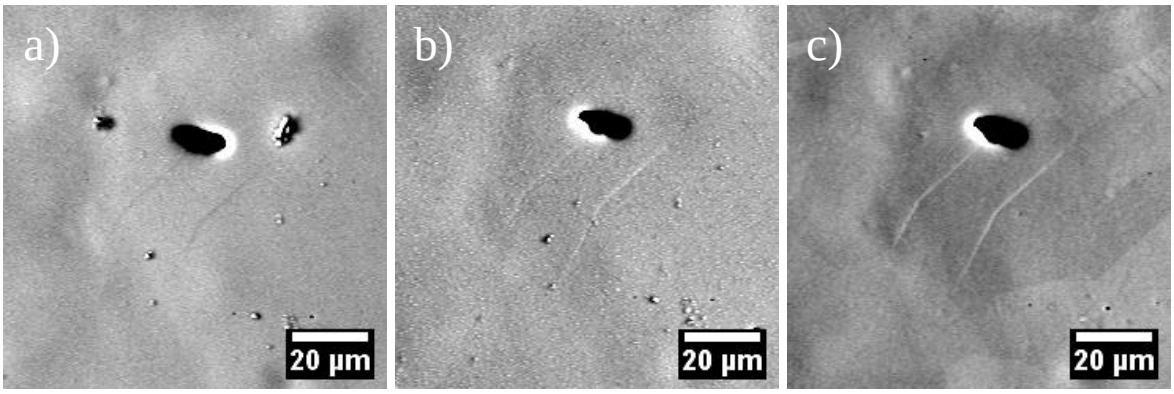

Figure B.28. BSE images of the location of initial DCs formed on sample AS09 after a) $0.49\sigma_y$ b) $0.55\sigma_y$ and c) $0.55\sigma_y$ after oxide removal.

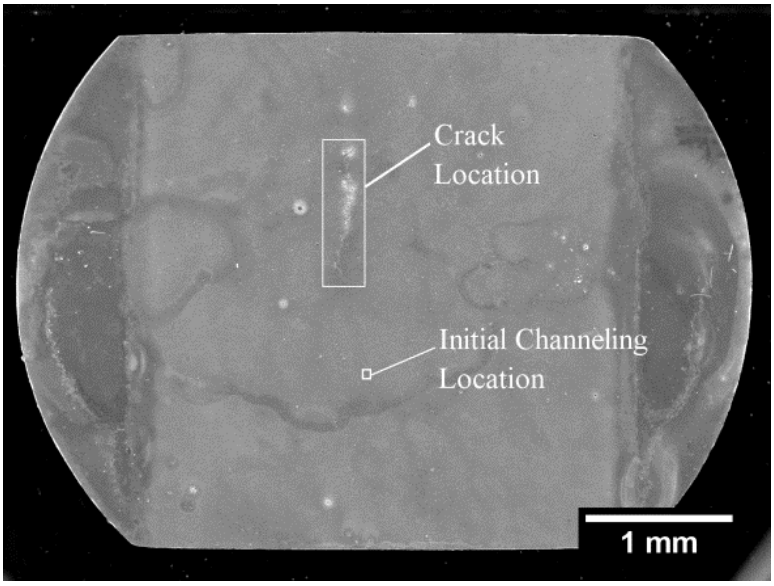

Figure B.29. Locations of cracking and initial deformation on sample AS09.

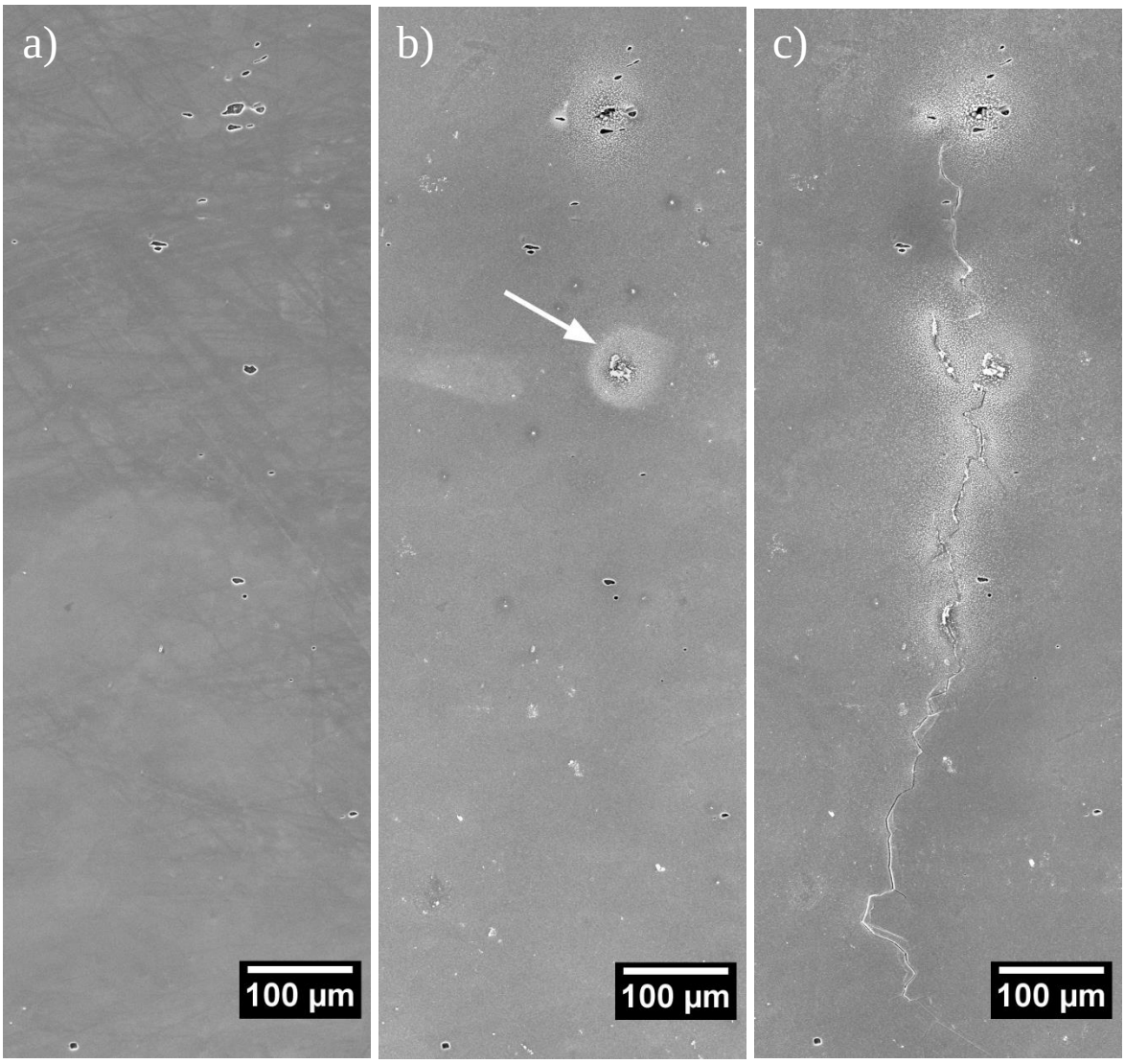

Figure B.30. SE images of the IGSCC location on sample AS09 a) prior to straining, b) after $0.49\sigma_y$, and c) after $0.55\sigma_y$.

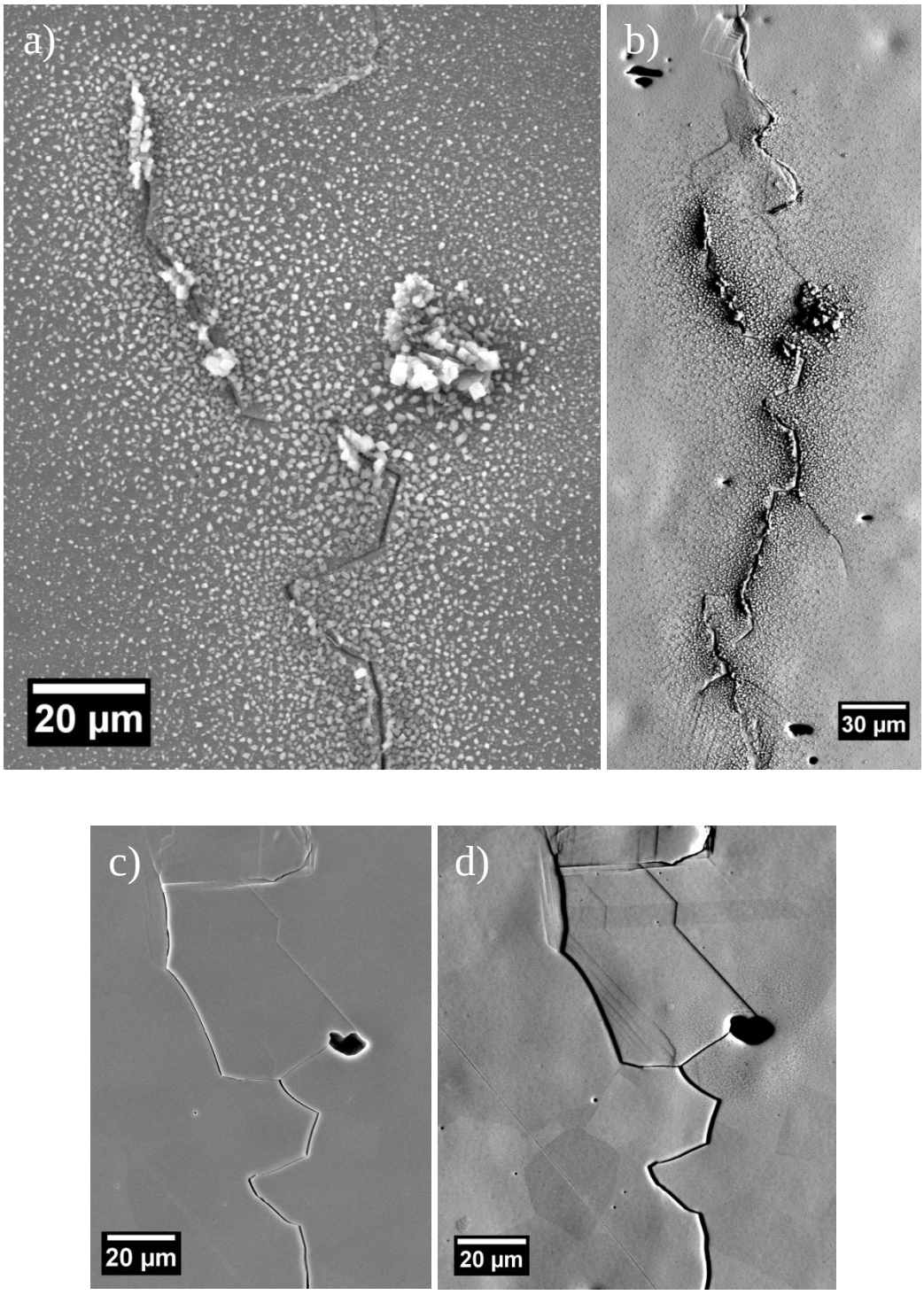

Figure B.31. Images of the crack initiation site on sample AS09 after: a) $0.55\sigma_y$ (SE), b) $0.55\sigma_y$ (BSE), c) $0.55\sigma_y$ with oxide removed (SE), and d) $0.55\sigma_y$ with oxide removed (BSE).

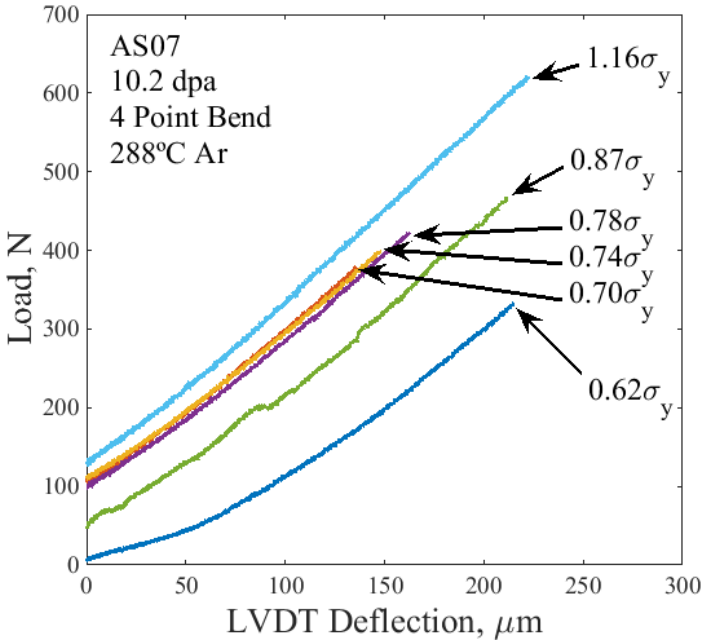

Figure B.32. Load vs. deflection curves for the 6 straining increments conducted on sample AS07, strained in 288°C Ar.

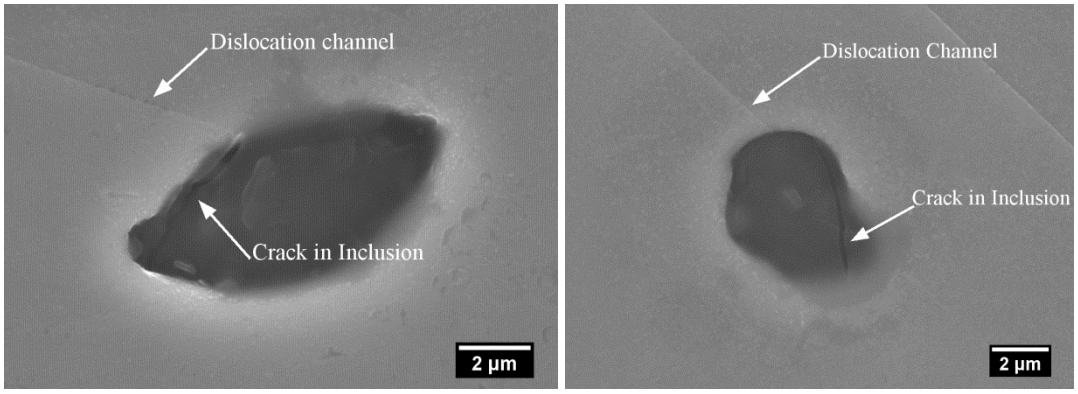

Figure B.33. Dislocation channels intersecting surface inclusions and causing visible cracking in the inclusions in AS07 strained to $1.16\sigma_y$ in 288 °C Ar.

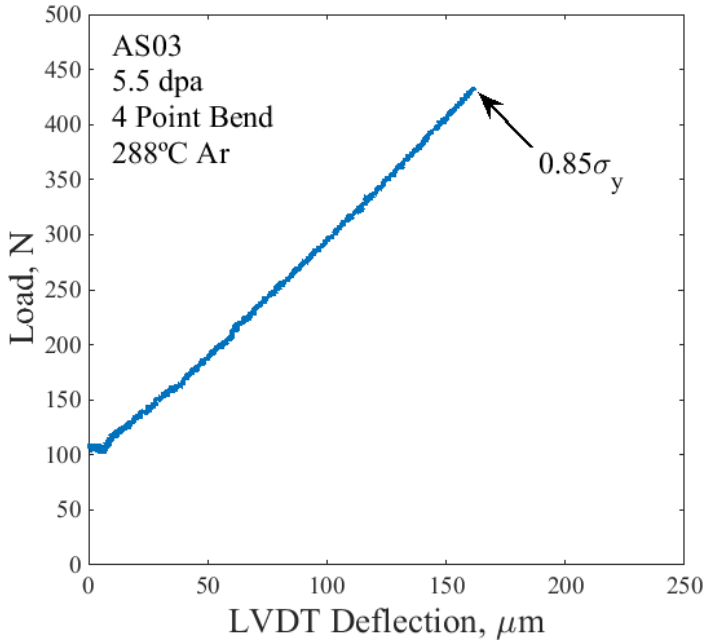

Figure B.34. Load vs. deflection curve for sample AS03, strained in 288°C Ar.

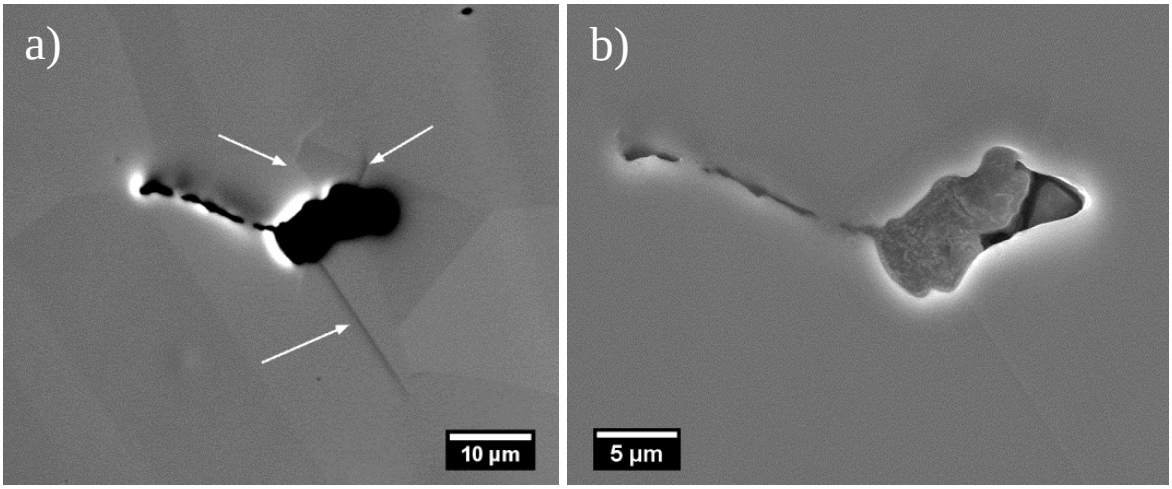

Figure B.35. DC intersection with a surface inclusion on the surface of AS03. a) BSE and b) SE images, indicating dislocation channels with white arrows.

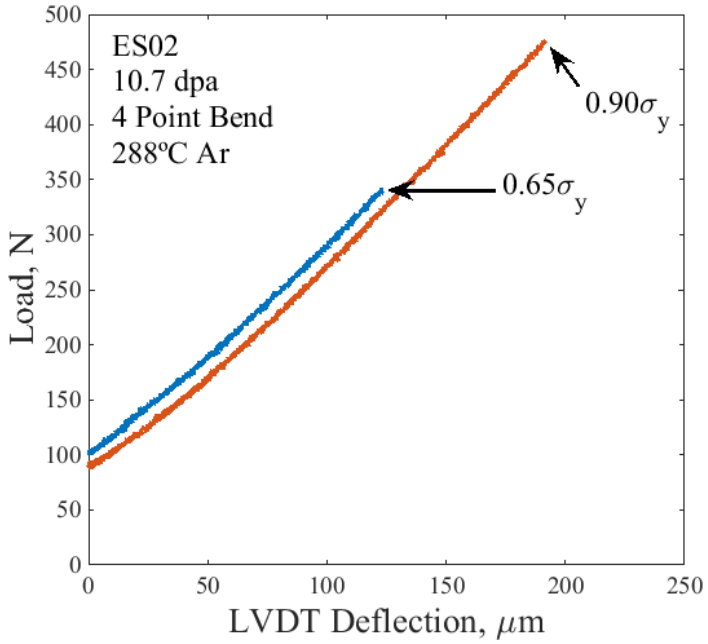

Figure B.36. Load vs. deflection curves for sample ES02 strained in 288 °C Ar.

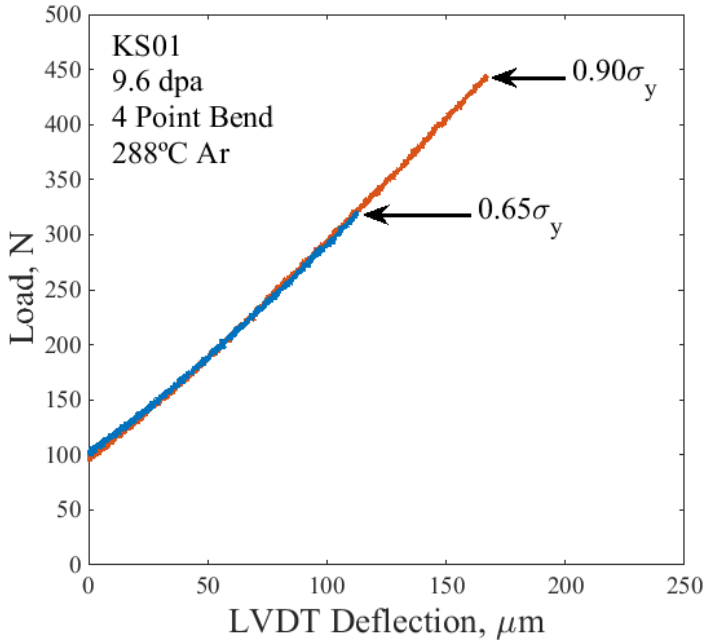

Figure B.37. Load vs. deflection curves for sample KS01 strained in 288 °C Ar.

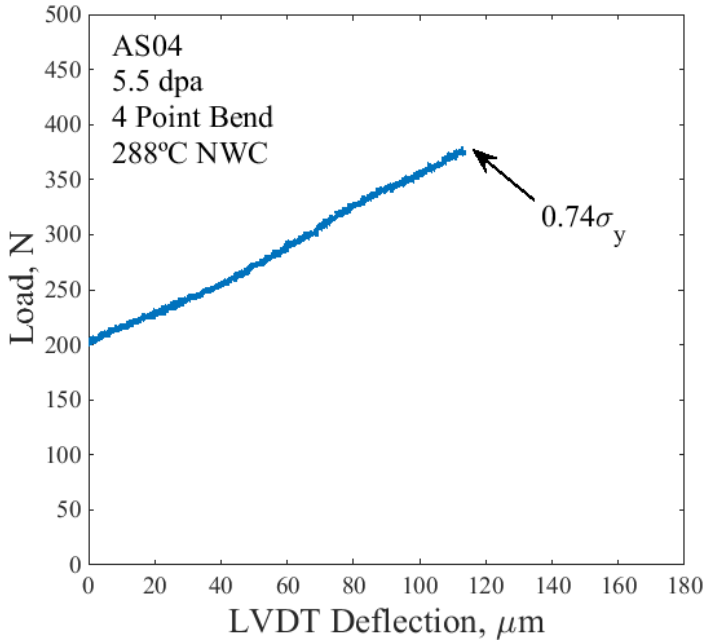

Figure B.38. Load vs. deflection curve for sample AS04 strained in 288°C NWC.

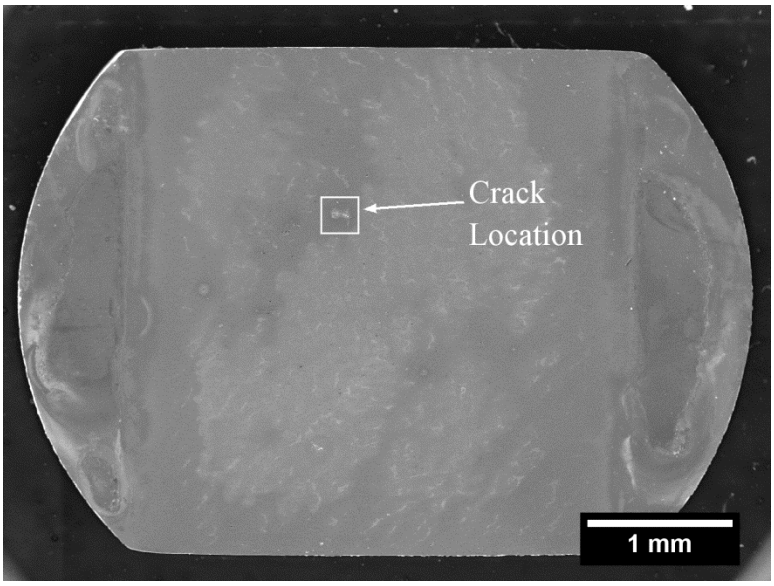

Figure B.39. Location of cracking on sample AS04.

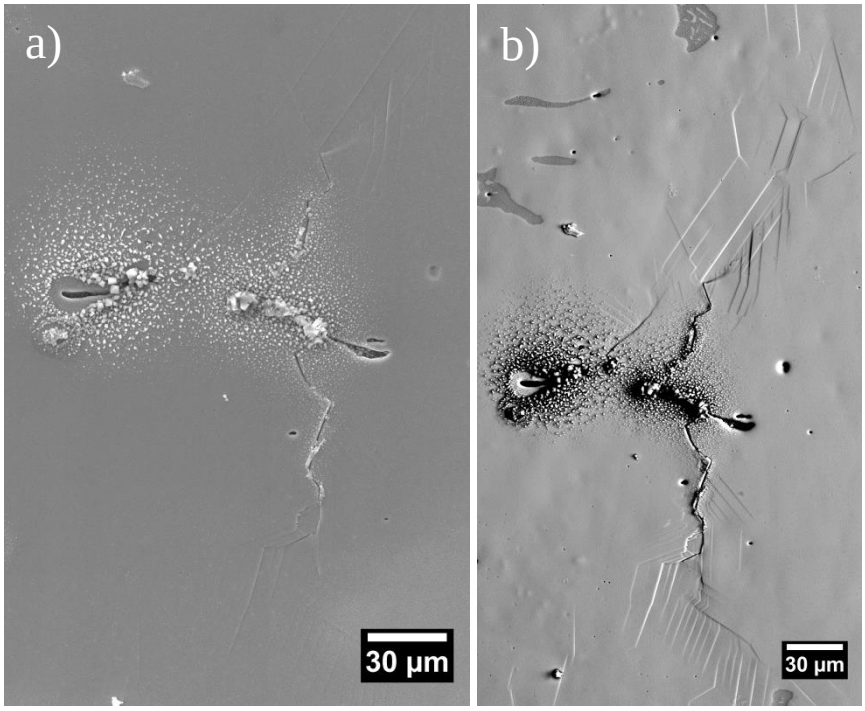

Figure B.40. High magnification a) SE and b) BSE images of the IG crack on sample AS04.

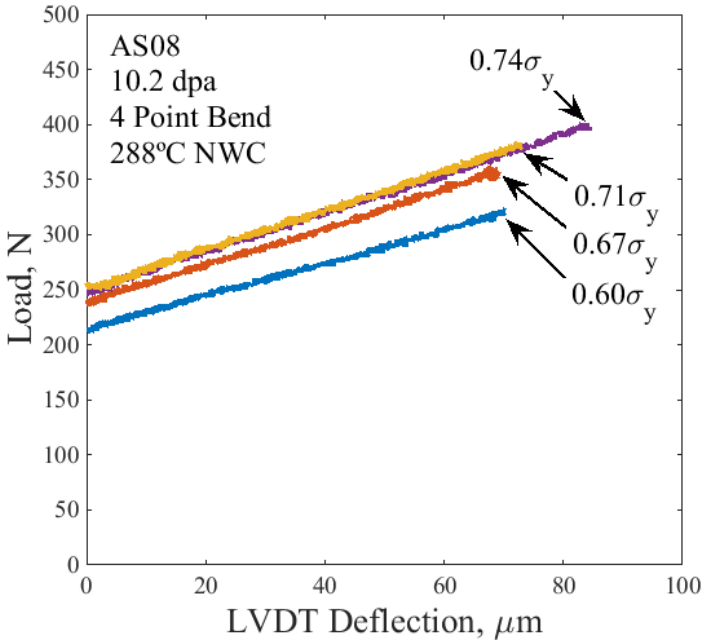

Figure B.41. Load vs. deflection curves for sample AS08 strained in 288°C NWC.

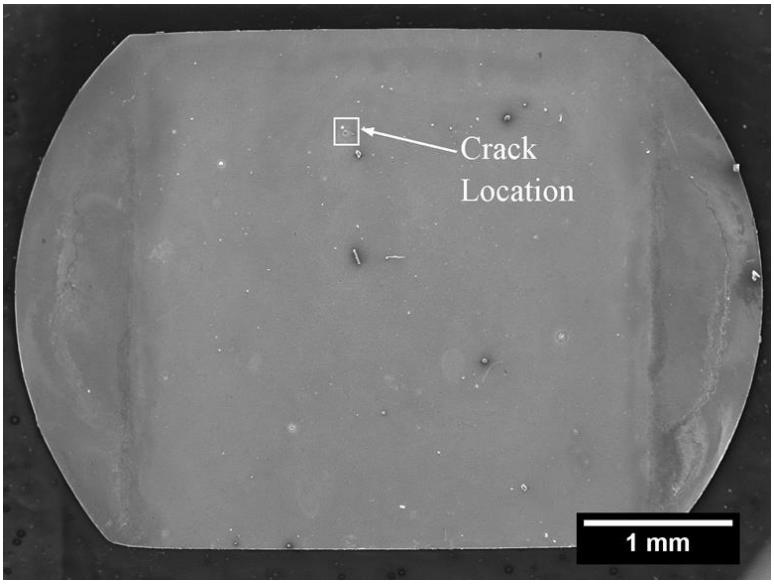

Figure B.42. Location of cracking on sample AS08.

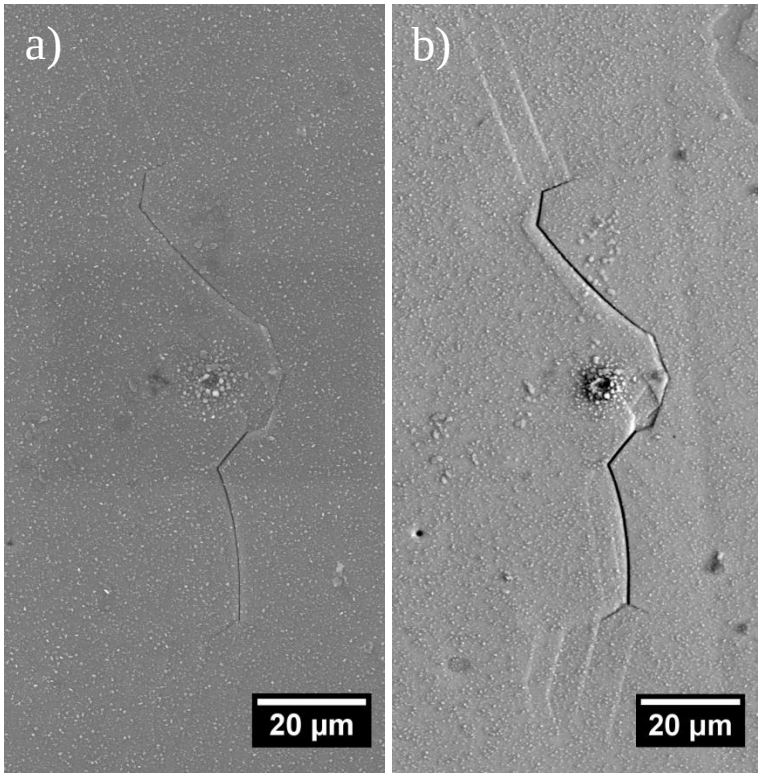

Figure B.43. High magnification a) SE and b) BSE images of the IG crack on sample AS08.

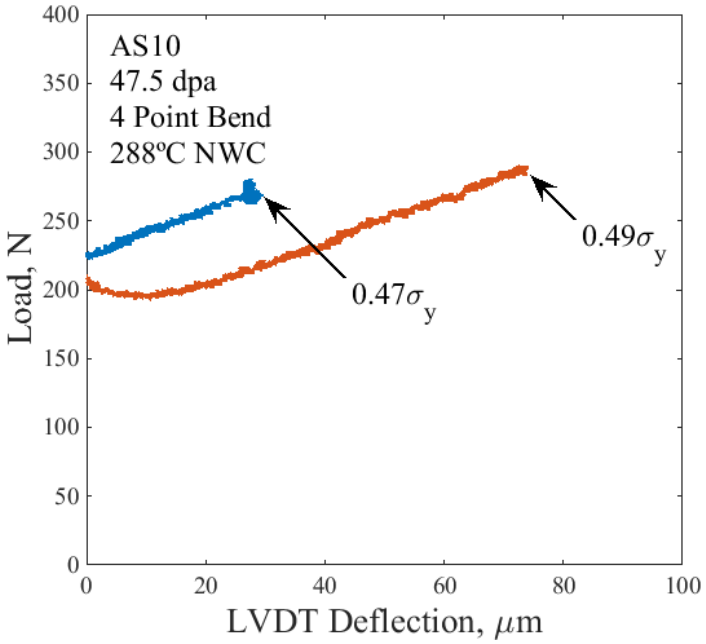

Figure B.44. Load vs. deflection curves for sample AS10 strained in 288 °C NWC.

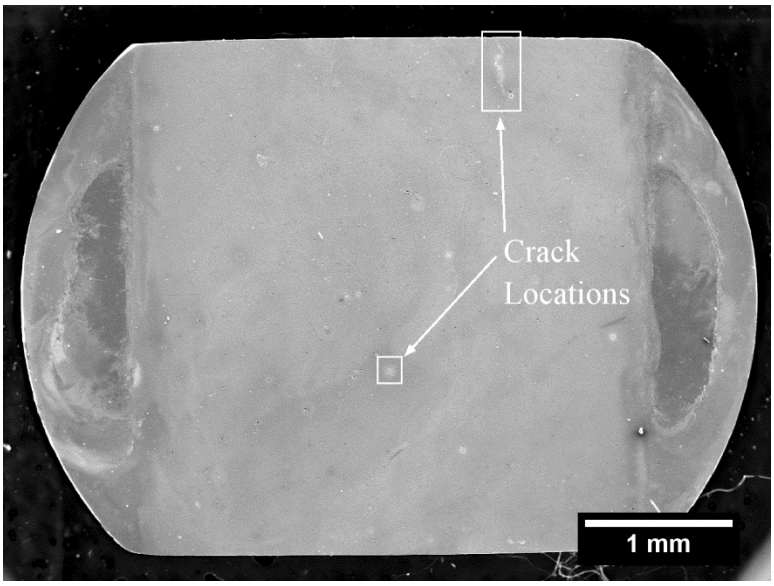

Figure B.45. Locations of cracking on sample AS10.

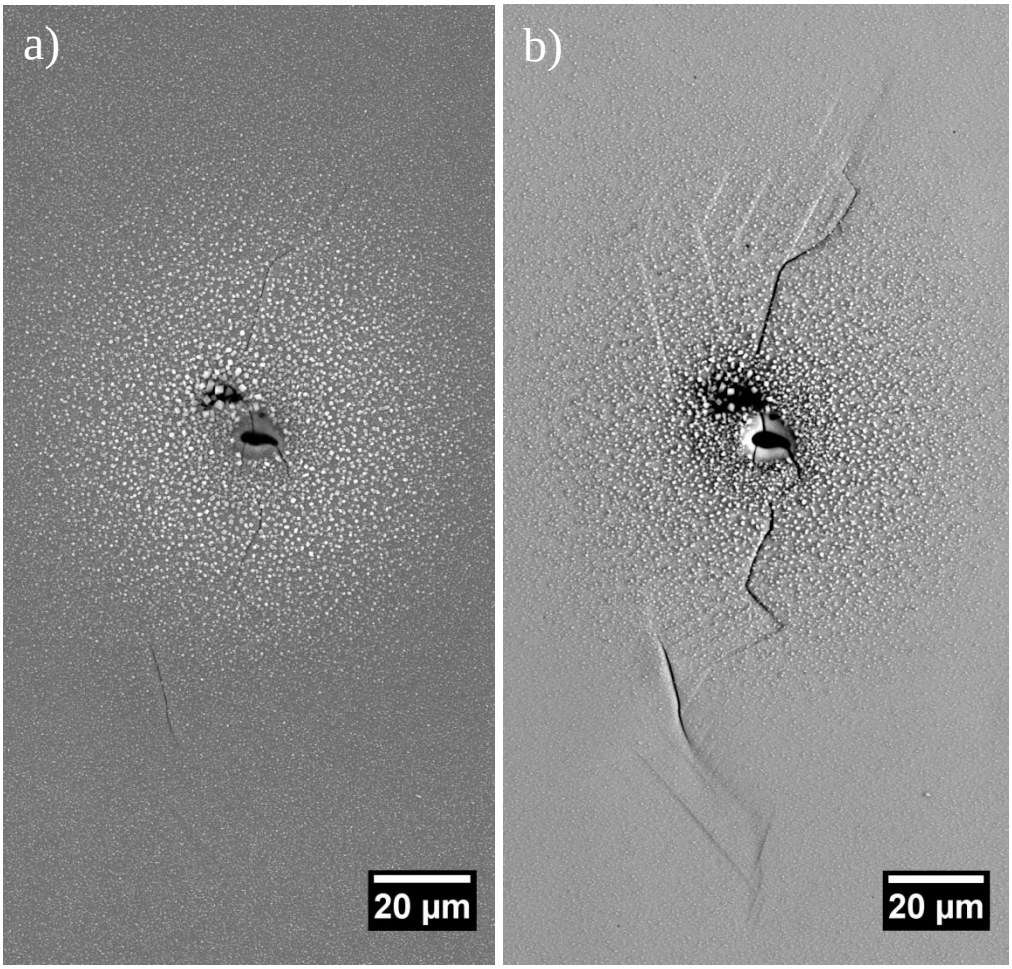

Figure B.46. High magnification a) SE and b) BSE images of the IG crack on sample AS10.

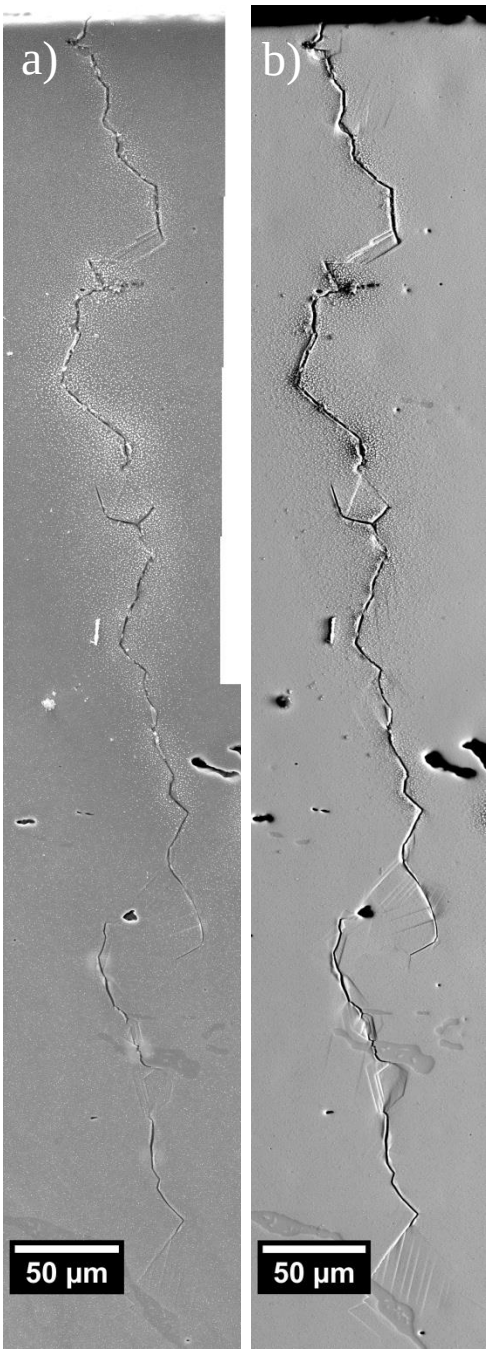

Figure B.47. High magnification a) SE and b) BSE images of the edge-interacting IG crack on sample AS10.

REFERENCES

[1] U.S.Energy Inf. Adm. (2015).

[2] P.L. Andresen, G.S. Was, in:, Compr. Nucl. Mater., Elsevier Inc., 2012, pp. 177–205.

[3] E.A. Kenik, R.H. Jones, G.E.C. Bell, J. Nucl. Mater. 212-215 (1994) 52.

[4] G.S. Was, in:, 11th Int. Conf. Environ. Degrad. Mater. Nucl. Power Syst. - Water React., TMS, Stevenson, WA, 2003.

[5] Z. Jiao, G.S. Was, J. Nucl. Mater. 382 (2008) 203.

[6] K. Fukuya, J. Nucl. Sci. Technol. 50 (2013) 213.

[7] K. Fukuya, K. Fujii, in:, 12th Int. Conf. Environ. Degrad. Mater. Nucl. Power Syst. - Water React., 2005, pp. 389–393.

[8] K. Fukuya, H. Nishioka, K. Fujii, T. Miura, T. Torimaru, J. Nucl. Mater. 417 (2011) 958.

[9] Z. Jiao, G.S. Was, J. Nucl. Mater. 408 (2011) 246.

[10] M.D. McMurtrey, G.S. Was, L. Patrick, D. Farkas, Mater. Sci. Eng. A 528 (2011) 3730.

[11] M.D. McMurtrey, G.S. Was, B. Cui, I. Robertson, L. Smith, D. Farkas, Int. J. Plast. (2014) 1.

[12] H. Nishioka, K. Fukuya, K. Fujii, Y. Kitsunai, J. Nucl. Sci. Technol. 45 (2008) 274.

[13] R.W. Bosch, M. Vankeerberghen, R. Gérard, F. Somville, J. Nucl. Mater. 461 (2015) 112.

[14] K. Fukuya, M. Nakano, K. Fujii, T. Torimaru, J. Nucl. Sci. Technol. 41 (2004) 673.

[15] K. Fukuya, S. Shima, H. Kayano, M. Narui, J. Nucl. Mater. 191-194 (1992) 1007.

[16] M. Kodama, J. Morisawa, S. Nishimura, K. Asano, S. Shima, K. Nakata, J. Nucl. Mater. 212-215 (1994) 1509.

[17] M. Kodama, K. Fukuya, H. Kayano, in:, A.S. Kumar, D.S. Gelles, R.K. Nanstad, E.A. Little (Eds.), American Society for Testing and Materials, Philadelphia, 1993.

[18] G. Furutani, N. Nakajima, T. Konishi, M. Kodama, J. Nucl. Mater. 288 (2001) 179.

[19] K.J. Stephenson, G.S. Was, in:, 17th Int. Conf. Environ. Degrad. Nucl. Power Syst., 2015.

[20] J.T. Busby, G.S. Was, The Use of Proton Irradiation to Determine IASCC Mechanisms in Light Water Reactors: Phase 2: Commercial Alloys 1009898, EPRI, Palo Alto, CA, 2005.

[21] J.T. Busby, G.S. Was, The Use of Proton Irradiation to Determine IASCC Mechanisms in Light Water Reactors: Solute Addition Alloys 1007440, EPRI, Palo Alto, CA, 2003.

[22] J.T. Busby, G.S. Was, The Use of Proton Irradiation to Determine IASCC Mechanisms in Light Water Reactors – Phase 3: Deformation Studies 1013081, EPRI, Palo Alto, CA, 2006.

[23] D.J. Edwards, A. Schemer-Kohrn, S. Bruemmer, Characterization of Neutron-Irradiated 300-Series Stainless Steels 1009896, EPRI, Palo Alto, CA, 2006.

[24] J.P. Massoud, P. Dubuisson, P. Scott, V.K. Chamardine, CIR II Program: Description of the Boris 6 and 7 Experiments in the BOR-60 Fast Breeder Reactor 1011787, EPRI, Palo Alto, CA, 2005.

[25] P. Scott, Materials Reliability Program: A Review of the Cooperative Irradiation Assisted Stress Corrosion Cracking Research Program (MRP-98), 1002807, Palo Alto, CA, 2003.

[26] B.W. Arey, D.G. Atteridge, S.M. Bruemmer, Production of Tailored Alloys to Isolate Metallurgical Variables Promoting IASCC, Palo Alto, CA, 2007.

[27] D.J. Edwards, S.M. Bruemmer, Characterization of CIR II Irradiated Stainless Steels EP-P19021/C9406, Palo Alto, CA, 2008.

[28] K.J. Stephenson, G.S. Was, J. Nucl. Mater. 444 (2014) 331.

[29] J. Beddoes, J.G. Parr, Introduction to Stainless Steels, 3rd ed., ASM International, Materials Park, OH, 1999.

[30] W.F. Hosford, Mechanical Metallurgy, Taylor & Francis Group, Boca Raton, FL, 2005.

[31] S.M. Bruemmer, B.W. Arey, L. a Charlot, Corrosion 48 (1992) 42.

[32] D.J. Kotecki, T. a. Siewert, AWS Annu. Meet. (1992) 171.

[33] F. Hull, Weld. J. (1973).

[34] Met. Handb. Desk Ed., ASM International, 1998, pp. 362–375.

[35] R.A. Lula, Stainless Steel, ASM International, Materials Park, OH, 1986.

[36] K. Arioka, T. Yamada, T. Terachi, R.W. Staehle, Corrosion 62 (2006) 568.

[37] G. Krauss, Mater. Sci. Eng. A 273-275 (1999) 40.

[38] S.M. Bruemmer, G.S. Was, J. Nucl. Mater. 216 (1994) 348.

[39] S. Gulbrandsen, Stress Corrosion Cracking of 316L Austenitic Stainless Steel in High Temperature Ethanol/Water Environments, 2012.

[40] J.E. Castle, R. Ke, Corros. Sci. 30 (1990) 409.

[41] M.A. Baker, J.E. Castle, Corros. Sci. 34 (1993) 667.

[42] G. Wranglen, Corros. Sci. 14 (1974) 331.

[43] M.A. Baker, J.E. Castle, Corros. Sci. 33 (1992) 1295.

[44] T.H. Courtney, Mechanical Behavior of Materials, 2nd ed., McGraw-Hill Publishing Co., 2000.

[45] E.H. Lee, M.H. Yoo, T.S. Byun, J.D. Hunn, K. Farrell, L.K. Mansur, Acta Mater. 49 (2001) 3277.

[46] F.B. Pickering, in:, Proc. Conf. Stainl. Steels 84, The Institute of Metals, Goteborg, 1984, p. 2.

[47] L. Vitos, J.O. Nilsson, B. Johansson, Acta Mater. 54 (2006) 3821.

[48] S.M. Bruemmer, J.I. Cole, J.L. Brimhall, R.D. Carter, G.S. Was, in: R.E. Gold, E.P. Simonen (Eds.), Sixth Int. Symp. Environ. Degrad. Mater. Nucl. Power Syst. - Water React., The Minerals, Metals, and Materials Society, Warrendale, PA, 1993, pp. 537–546.

[49] J.W. Brooks, M.H. Loretto, R.E. Smallman, Acta Metall. 27 (1979) 1829.

[50] T.S. Byun, E.H. Lee, J.D. Hunn, J. Nucl. Mater. 321 (2003) 29.

[51] E.H. Lee, T.S. Byun, J.D. Hunn, M.H. Yoo, K. Farrell, L.K. Mansur, Acta Mater. 49 (2001) 3269.

[52] T. Miura, K. Fujii, K. Fukuya, Y. Ito, J. Nucl. Mater. 386-388 (2009) 210.

[53] T.S. Byun, Acta Mater. 51 (2003) 3063.

[54] J. Talonen, H. Hänninen, Acta Mater. 55 (2007) 6108.

[55] G.I. Taylor, J. Inst. Met. (1938) 307.

[56] M. Kamaya, Y. Kawamura, T. Kitamura, Int. J. Solids Struct. 44 (2007) 3267.

[57] G.E. Dieter, Mechanical Metallurgy, 3rd ed., McGraw-Hill, 1986.

[58] S.J. Zinkle, B.N. Singh, J. Nucl. Mater. 199 (1993) 173.

[59] S.J. Zinkle, P.J. Maziasz, R.E. Stoller, J. Nucl. Mater. 206 (1993) 266.

[60] N. Yoshida, J. Nucl. Mater. 174 (1990) 220.

[61] D.. Edwards, E.. Simonen, S.. Bruemmer, J. Nucl. Mater. 317 (2003) 13.

[62] G.E. Lucas, J. Nucl. Mater. 206 (1993) 287.

[63] Y. V Konobeev, S.I. Rudnev, At. Energy 53 (1983) 107.

[64] T. Muroga, F.A. Garner, T.M. McCarthy, N. Yoshida, in:, R.E. Stoller, A.S. Kumar, D.S. Gelles (Eds.), Eff. Radiat. Mater. 15th Int. Symp. ASTM STP 1125, American Society for Testing and Materials, Philadelphia, 1992, pp. 1015–1033.

[65] D.. Edwards, E.. Simonen, F.. Garner, L.. Greenwood, B.. Oliver, S.. Bruemmer, J. Nucl. Mater. 317 (2003) 32.

[66] C. Cawthorne, C. Brown, J. Nucl. Mater. 66 (1977) 201.

[67] Y. Isobe, M. Sagisaka, F. a. Garner, S. Fujita, T. Okita, J. Nucl. Mater. 386-388 (2009) 661.

[68] Y. Chen, P.H. Chou, E. a. Marquis, J. Nucl. Mater. 451 (2014) 130.

[69] J.T. Busby, Isolation of the Role of Radiation-Induced Segregation in Irradiation-Assisted Stress Corrosion Cracking of Proton-Irradiated Austenitic Stainless Steels, University of Michigan, 2001.

[70] T.R. Allen, J.T. Busby, G.S. Was, E.A. Kenik, J. Nucl. Mater. 255 (1998).

[71] K.G. Field, Y. Yang, T.R. Allen, J.T. Busby, Acta Mater. 89 (2015) 438.

[72] I.M. Robertson, J. Robach, B. Wirth, A. Arsenlis, in:MRS Proceedings, Materials Research Society, 2003.

[73] T.H. Blewitt, R.R. Coltman, R.E. Jamison, J.K. Redman, J. Nucl. Mater. 2 (1960) 277.

[74] S.M. Bruemmer, E.P. Simonen, P.M. Scott, P.L. Andresen, G.S. Was, J.L. Nelson, J. Nucl. Mater. 274 (1999) 299.

[75] A.J.E. Foreman, M.J. Makin, Can. J. Phys. 45 (1967) 511.

[76] E. Orowan, Internal Stresses in Metals and Alloys, Institute of Metals, London, 1948.

[77] P.M. Kelly, Int. Metall. Rev. 18 (1973) 31.

[78] R.E. Stoller, S.J. Zinkle, J. Nucl. Mater. 283-287 (2000) 349.

[79] N. Hashimoto, T.S. Byun, K. Farrell, J. Nucl. Mater. 351 (2006) 295.

[80] L. Vitos, P. Korzhavyi, B. Johansson, Phys. Rev. Lett. 88 (2002) 155501.

[81] S. Chatterjee, H.-S. Wang, J.R. Yang, H.K.D.H. Bhadeshia, Mater. Sci. Technol. 22 (2006) 641.

[82] G.R. Odette, D. Frey, J. Nucl. Mater. 85-86 (1979) 817.

[83] M.L. Grossbeck, P.J. Maziasz, A.F. Rowcliffe, J. Nucl. Mater. 191-194 (1992) 808.

[84] E.A. West, S. Teysseyre, Z. Jiao, G.S. Was, in:, Proc. 13th Environ. Degrad. Mater. Nucl. Power Syst. - Water React., 2007, pp. 1–18.

[85] B.N. Singh, A.J.E. Foreman, H. Trinkaus, J. Nucl. Mater. 249 (1997) 103.

[86] T.S. Byun, N. Hashimoto, K. Farrell, J. Nucl. Mater. 351 (2006) 303.

[87] G.S. Was, Fundamentals of Radiation Materials Science, Springer, New York, NY, 2007.

[88] D.J. Edwards, B.N. Singh, J.B. Bilde-Sorensen, J. Nucl. Mater. 342 (2005) 164.

[89] E. V Esquivel, L.E. Murr, Mater. Sci. Eng. A 409 (2005) 13.

[90] E.H. Lee, T.S. Byun, J.D. Hunn, K. Farrell, L.K. Mansur, J. Nucl. Mater. 296 (2008) 183.

[91] T.D. de la Rubia, H.M. Zbib, T.A. Khraishi, B.D. Wirth, M. Victoria, M.J. Caturla, Nature 406 (2000) 871.

[92] M. Briceño, J. Fenske, M. Dadfarnia, P. Sofronis, I.M. Robertson, J. Nucl. Mater. 409 (2011) 18.

[93] M.S. Wechsler, in:, Inhomogeneity Plast. Deform., American Society for Metals, Metals Park, OH, 1973, pp. 19–54.

[94] K. Farrell, T.S. Byun, N. Hashimoto, J. Nucl. Mater. 335 (2004) 471.

[95] Z. Jiao, G.S. Was, J. Nucl. Mater. 407 (2010) 34.

[96] J.L. Brimhall, J.I. Cole, S.M. Bruemmer, Scr. Metall. Mater. 30 (1994) 1473.

[97] E.P. Simonen, S.M. Bruemmer, in:, Seventh Int. Symp. Environ. Degrad. Mater. Nucl. Power Syst. - Water React., Breckenridge, CO, 1995, pp. 1081–1092.

[98] N. Hashimoto, S.J. Zinkle, A.F. Rowcliffe, J.P. Robertson, S. Jitsukawa, J. Nucl. Mater. 283-287 (2000) 528.

[99] Z. Jiao, J.T. Busby, G.S. Was, J. Nucl. Mater. 361 (2007) 218.

[100] R.D. Kane, ed., Slow Strain Rate Testing for the Evaluation of Environmentally Induced Cracking, ASTM STP 1210, Baltimore, MD, 1993.

[101] T. Onchi, K. Dohi, N. Soneda, M. Navas, M.L. Castano, J. Nucl. Mater. 340 (2005) 219.

[102] H.M. Chung, R. V Strain, W.J. Shack, Nucl. Eng. Des. 208 (2001) 221.

[103] G.S. Was, P.L. Andresen, Corrosion 63 (2007) 19.

[104] J. Conermann, R. Shogan, K. Fujimoto, T. Yonezawa, Y. Yamaguchi, in:, Proc. 12th Environ. Degrad. Mater. Nucl. Power Syst. - Water React., 2005, pp. 277–287.

[105] M.P. Manahan, R. Kohli, J. Santucci, P. Sipush, Nucl. Eng. Des. 113 (1989) 297.

[106] E. a. West, M.D. McMurtrey, Z. Jiao, G.S. Was, Metall. Mater. Trans. A 43 (2011) 136.

[107] S. Teysseyre, Z. Jiao, E. West, G.S. Was, J. Nucl. Mater. 371 (2007) 107.

[108] J.T. Busby, G.S. Was, E.A. Kenik, J. Nucl. Mater. 302 (2002) 20.

[109] K. Fukuya, M. Nakano, K. Fujii, T. Torimaru, Y. Kitsunai, J. Nucl. Sci. Technol. 41 (2004) 1218.

[110] M.C. Hash, J.T. Busby, G.S. Was, in:, M.L. Grossbeck, T.R. Allen, R.G. Lott, A.S. Kumar (Eds.), Eff. Radiat. Mater. 21st Int. Symp. ASTM STP 1447, ASTM International, West Cohshohocken, PA, 2004, pp. 92–104.

[111] J.T. Busby, G.S. Was, in:, T.R. Allen, P.J. King, L. Nelson (Eds.), 12th Int. Conf. Environ. Degrad. Mater. Nucl. Power Syst. - Water React., TMS, 2005, pp. 255–266.

[112] J.S. Armijo, Corros. Sci. 7 (1967) 143.

[113] G.S. Was, Y. Ashida, P.L. Andresen, Corros. Rev. 29 (2011) 7.

[114] T. Yonezawa, K. Fujimoto, T. Iwamura, S. Nishida, in:, R.D. Kane (Ed.), Environ. Assist. Crack. Predict. Methods Risk Assess. Eval. Mater. Equipment, Struct. ASTM 1401, American Society for Testing and Materials, West Conshohocken, PA, 2000, pp. 224–238.

[115] P.L. Andresen, P.H. Chou, M.M. Morra, J. Lawrence Nelson, R.B. Rebak, Metall. Mater. Trans. A 40 (2009) 2824.

[116] T. Yonezawa, H. Kanasaki, M. Taneike, Y. Sakaguchi, S. Ooki, H. Tezuka, K. Takamori, S. Suzuki, in:, Proc. 14th Intl. Conf. Environ. Degrad. Mater. Nucl. Power Syst. - Water React., Virginia Beach, VA, 2009, pp. 1274–1288.

[117] H.M. Chung, W.E. Ruther, J.E. Sanecki, A. Hins, N.J. Zaluzec, T.F. Kassner, J. Nucl. Mater. 239 (1996) 61.

[118] T. Tsukada, Y. Miwa, H. Nakajima, T. Kondo, in:, 8th Int. Symp. Environ. Degrad., Amelia Island, FL, 1997, pp. 795–802.

[119] A.N. Stroh, Philos. Mag. 3 (1958) 625.

[120] T. Onchi, K. Dohi, N. Soneda, J.R. Cowan, R.J. Scowen, M.L. Castano, J. Nucl. Mater. 320 (2003) 194.

[121] B. Alexandreanu, G.S. Was, Corrosion 59 (2003) 705.

[122] D.A. Jones, Corros. Sci. (1996) 356.

[123] J.T. Busby, G.S. Was, in:, Proc. 12th Environ. Degrad. Mater. Nucl. Power Syst. - Water React., 2005, pp. 255–266.

[124] Z. Jiao, G.S. Was, J.T. Busby, in:, 13th Int. Conf. Environ. Degrad. Mater. Nucl. Power Syst. - Water React., Whistler, British Columbia, 2007, pp. 1–11.

[125] Z. Jiao, J.T. Busby, R. Obata, G.S. Was, in: Proc. 12th Int. Symp. Environ. Degrad. Mater. Nucl. Power Syst. - Water React., T.R. Allen, P.J. King, L. Nelson (Eds.), TMS, Salt Lake City, Utah, 2005, pp. 379–388.

[126] C. Bailat, A. Almazouzi, N. Baluc, R. Shaublin, F. Groschel, M. Victoria, J. Nucl. Mater. 283-287 (2000) 446.

[127] K. Fukuya, H. Nishioka, K. Fujii, M. Kamaya, T. Miura, T. Torimaru, J. Nucl. Mater. 378 (2008) 211.

[128] R.B. Dropek, G.S. Was, J. Gan, J.I. Cole, T.R. Allen, E.A. Kenik, in:, Proc. 11th Environ. Degrad. Mater. Nucl. Power Syst. - Water React., 2003, pp. 1132–1141.

[129] E.E. Bloom, in:, N.L. Peterson, S.D. Harkness (Eds.), Radiat. Damage Met., American Society for Metals, Metals Park, OH, 1975.

[130] G.S. Was, B. Alexandreanu, J.T. Busby, Key Eng. Mater. 261-263 (2004) 885.

[131] E.S.P. Das, M.J. Marcinkowski, J. Appl. Phys. 43 (1972) 4425.

[132] W.A.T. Clark, R.H. Wagoner, Z.Y. Shen, T.C. Lee, I.M. Robertson, H.K. Birnbaum, Scr. Metall. Mater. 26 (1992) 203.

[133] L.C. Lim, R. Raj, Acta Metall. 33 (1985) 1577.

[134] A.H. King, D.A. Smith, Acta Crystallogr. A 36 (1980) 335.

[135] R.J. Kurtz, R.G. Hoagland, J.P. Hirth, Philos. Mag. A 79 (1999) 665.

[136] H. Kokawa, T. Watanabe, S. Karashima, J. Mater. Sci. 18 (1983) 1183.

[137] G.R. Kegg, C.A.P. Horton, J.M. Silcock, Philos. Mag. 27 (1973) 1041.

[138] K. Fukuya, H. Nishioka, K. Fujii, T. Miura, Y. Kitsunai, J. Nucl. Mater. 432 (2013) 67.

[139] P. Evrard, M. Sauzay, J. Nucl. Mater. 405 (2010) 83.

[140] E. a. West, G.S. Was, J. Nucl. Mater. 408 (2011) 142.

[141] G.S. Was, S.M. Bruemmer, J. Nucl. Mater. 216 (1994) 326.

[142] J.C. Heap, Thermal Stresses in Concentrically Heated Hollow Cylinders, Argonne, IL, 1960.

[143] D.E. Turek, Polym. Eng. Sci. 33 (1993) 328.

[144] F.I. Baratta, W.T. Matthews, G.D. Quinn, Errors Associated with Flexure Testing of Brittle Materials, Watertown, MA, 1987.

[145] Z. Jiao, J.T. Busby, R. Obata, G.S. Was, in:, Proc. 12th Environ. Degrad. Mater. Nucl. Power Syst. - Water React., 2005, pp. 379–388.

[146] M.D. Mcmurtrey, B. Cui, I. Robertson, D. Farkas, G.S. Was, Curr. Opin. Solid State Mater. Sci. 19 (2015) 305.

[147] S. Nogami, Y. Sato, A. Hasegawa, J. Nucl. Sci. Technol. 48 (2011) 1265.

[148] N. Huin, K. Tsutsumi, T. Couvant, G. Henaff, J. Mendez, J. Press. Vessel Technol. 136 (2014).

[149] M. Kodama, R. Katsura, J. Morisawa, S. Nishimura, S. Suzuki, K. Takamori, S. Shima, T. Kato, in:, Proc. 7th Environ. Degrad. Mater. Nucl. Power Syst. - Water React., Breckenridge, CO, 1995, pp. 1121–1132.

[150] M. Kodama, S. Nishimura, J. Morisawa, S. Shima, S. Suzuki, N. Yamamoto, in:, Proc. 5th Int. Symp. Environ. Degrad. Mater. Nucl. Power Syst. - Water React. Environ. Degrad. Mater. Nucl. Power Syst. - Water React., American Nuclear Society, Monterey, CA, 1992, p. 948.

[151] M.P. Fay, P. a Shaw, J. Stat. Softw. 36 (2010) 1.

[152] D.W. Hosmer, S. Lemeshow, Applied Survival Analysis: Regression Modeling of Time to Event Data, 1999.

[153] The R Project for Statistical Computing. https://www.r-project.org/

[154] O.K. Chopra, a. S. Rao, J. Nucl. Mater. 409 (2011) 235.

[155] L. Tan, J.T. Busby, J. Nucl. Mater. 443 (2013) 351.

[156] M.L. Jenkins, M.A. Kirk, Characterisation of Radiation Damage by Transmission Electron Microscopy, CRC Press, Boca Raton, FL, 2000.

[157] K. Fukuya, K. Fujii, H. Nishioka, Y. Kitsunai, J. Nucl. Sci. Technol. 43 (2006) 159.

[158] P. Hurst, D.A. Appleton, P. Banks, A.S. Raffel, Corros. Sci. 25 (1985) 651.

[159] H. Hanninen, W. Cullen, M. Kemppainen, Corrosion 46 (1990) 563.

[160] J.M. Cookson, The Role of Oxides and Impurities in Proton Irradiation Assisted Stress Corrosion Cracking of Stainless Steels, University of Michigan, 1996.

[161] J. Goodier, J. Appl. Mech 55 (1933) 39.

[162] W.C. Young, R.G. Budynas, Roark's Formulas for Stress and Strain, 7th Edition, McGraw-Hill, 2002.

[163] J. Robertson, M.I. Manning, Mater. Sci. Technol. 6 (1990) 81.

[164] P. Juvonen, Effects of Non-Metallic Inclusions on Fatigue Properties of Calcium Treated Steels, Helsinki University of Technology, 2004.

[165] A. Melander, M. Larsson, Int. J. Fatigue 15 (1993) 119.

[166] R. Mathis, J. Mater. Sci. 22 (1987) 907.

[167] D. Brooksbank, K.W. Andrews, J. Iron Steel Inst. 206 (1968) 593.

[168] M.P. Mueller, Corrosion 38 (1982) 431.

[169] B. Bavarian, Z. Szklarska-Smialowska, D.D. Macdonald, Corrosion 38 (1982) 604.

[170] C. Donik, I. Paulin, M. Jenko, Mater. Technol. 44 (2010) 67.

[171] R. Ke, R. Alkire, J. Electrochem. Soc. 142 (1995) 4056.

[172] D.A. Jones, Principles and Prevention of Corrosion, 2nd ed., Prentice-Hall, Inc., Upper Saddle River, NJ, 1996.

[173] Z. Szklarska-Śmialowska, a Szummer, M. Janik-Czachor, Br. Corros. J. 5 (1970) 159.

[174] X.Y. Zhou, J. Congleton, a. Bahraloloom, Corrosion 54 (1998) 898.

[175] J.D. Hem, Chemical Equilibria and Rates of Manganese Oxidation, Washington, D.C., 1963.

[176] A.J. Jacobs, S. Dumbill, in:, Proc. 7th Environ. Degrad. Mater. Nucl. Power Syst. - Water React., 1995, pp. 1021–1032.

[177] T.P. Hoar, D.C. Mears, G.P. Rothwell, Corros. Sci. 5 (1965) 279.

[178] F.P. Ford, D.F. Taylor, P.L. Andresen, R.G. Ballinger, Corrosion-Assisted Cracking of Stainless and Low-Alloy Steels in LWR Environments, 1987.

[179] P.L. Andresen, C.L. Briant, Corrosion 45 (1989) 448.

[180] F.P. Ford, Corrosion 52 (1996) 375.

[181] P.L. Andresen, I. Vasatis, F.P. Ford, in:, Corros. '90, NACE, 1990.

[182] T. Shoji, H. Takahashi, S. Aizawa, M. Saito, in:, Proc. 3rd Environ. Degrad. Mater. Nucl. Power Syst. - Water React., 1988, pp. 251–259.

[183] T. Tsukada, Y. Miwa, H. Nakajima, in: Proc. 7th Int. Symp. Environ. Degrad. Mater. Nucl. Power Syst. - Water React., 1995, pp. 1009–1018.

[184] F. Meng, J. Wang, E.H. Han, W. Ke, Corros. Sci. 52 (2010) 927.

[185] J. Tan, X. Wu, E. Han, W. Ke, X. Liu, F. Meng, X. Xu, Corros. Sci. 88 (2014) 349.

[186] J.M. Cookson, R.D. Carter Jr., D.L. Damcott, M. Atzmon, G.S. Was, J. Nucl. Mater. 202 (1993) 104.

[187] L. Tan, K. Field, Personal Communication. (2013).

[188] A.J. Jacobs, C.M. Shepherd, G.E.C. Bell, G.P. Wozadlo, in:, Proc. 5th Int. Symp. Environ. Degrad. Mater. Nucl. Power Syst. - Water React., 1991, pp. 917–934.

[189] R. Katsura, J. Morisawa, M. Kodama, S. Nishimura, S. Suzuki, S. Shima, M. Yamamoto, in:, Proc. 6th Int. Symp. Environ. Degrad. Mater. Nucl. Power Syst. - Water React., 1993, pp. 625–632.

[190] B. Cui, J. Kacher, M. McMurtrey, G. Was, I. Robertson, Acta Mater. 65 (2014) 150.

[191] M. Kodama, K. Fukuya, H. Kayano, in:, 16th Int. Symp. No Eff. Radiat. Mater., ASTM International, Aurora, CO, 1994, pp. 889–901.

[192] T.C. Lee, I.M. Robertson, H.K. Birnbaum, Acta Metall. 37 (1989) 407.

[193] M.N. Gussev, K.G. Field, J.T. Busby, K.J. Stephenson, G.S. Was, in:, 17th Int. Conf. Environ. Degrad. Nucl. Power Syst., 2015.

[194] H. Hänninen, K. Törrönen, M. Kemppainen, S. Salonen, Corros. Sci. 23 (1983) 663.